GEMS & GEMOLOGY

SUMMER 2018
VOLUME LIV

THE QUARTERLY JOURNAL OF THE GEMOLOGICAL INSTITUTE OF AMERICA

Characteristics of Natural-Color Blue Diamonds

Black Diamonds from Zimbabwe

Characterization of Yogo Sapphires

Synthetic Diamonds Chart

2018 GIA SYMPOSIUM

NEW CHALLENGES. CREATING OPPORTUNITIES.

OCTOBER 7–9, 2018 • CARLSBAD, CA

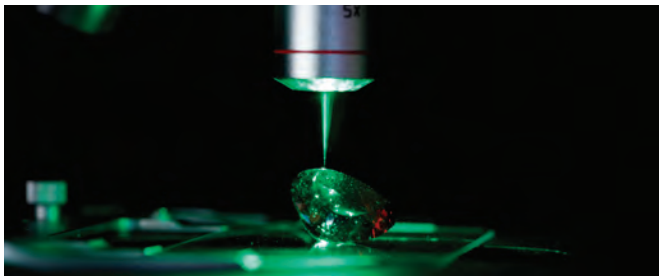

GIA RESEARCH TRACK

Researchers and scientists respected across the industry and from around the world will present their latest findings. **Topics include:** Colored Stones and Pearls, Diamond Geology, Diamond Identification, Gem Characterization, Gem Localities and Formations, General Gemology and Jewelry, and New Technologies and Techniques.

HARVARD BUSINESS TRACK

Harvard Business School professors lead an exploration into *Authentic Leadership, Customer Centricity* and *Disruptive Innovation* utilizing the famed HBS case-study method.

THE MUSIC PARADIGM

An engaging and unforgettable learning experience that translates the unique insights of a symphony orchestra conductor into lessons on leadership and collaboration.

FUTURESCAPE FORUM

Symposium will close with *Futurescape Forum* – a landmark event that will change how you think about the industry's trajectory. An interactive dialogue moderated by David Ager of Harvard Business School, industry leaders will deliberate their unfiltered predictions on the horizon for the gem and jewelry industry.

Bruce Cleaver
De Beers

Gina Drosos
Signet Jewelers

Jason Goldberger
Blue Nile

Andy Johnson
Diamond Cellar

Rahul Kadakia
Christie's

Kent Wong
Chow Tai Fook

DON'T MISS OUT. REGISTER NOW AT SYMPOSIUM.GIA.EDU

INTERNATIONAL GIA GEMOLOGICAL SYMPOSIUM

GEMS & GEMOLOGY
Summer 2018
VOLUME 54, No. 2


pg. 113


pg. 134


pg. 171


pg. 185

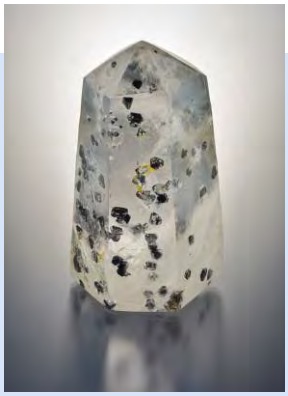
pg. 231


pg. 245

Editorial

Feature Articles

Charts

Regular Features

Editorial Staff

Editor-in-Chief
Duncan Pay
dpay@gia.edu

Managing Editor
Stuart D. Overlin
soverlin@gia.edu

Editor
Jennifer-Lynn Archuleta
jennifer.archuleta@gia.edu

Technical Editors
Tao Z. Hsu
tao.hsu@gia.edu
Jennifer Stone-Sundberg
jstone@gia.edu

Editors, Lab Notes
Thomas M. Moses
Shane F. McClure

Editors, Micro-World
Nathan Renfro
Elise A. Skalwold
John I. Koivula

Editors, Gem News
Emmanuel Fritsch
Gagan Choudhary
Christopher M. Breeding

Editorial Assistants
Brooke Goedert
Erin Hogarth

Contributing Editors
James E. Shigley
Andy Lucas
Donna Beaton

Editor-in-Chief Emeritus
Alice S. Keller

Customer Service
Martha Erickson
(760) 603-4502
gandg@gia.edu

Production Staff

Creative Director
Faizah Bhatti

Production and Multimedia Specialist
Juan Zanahuria

Photographer
Robert Weldon

Photo/Video Producer
Kevin Schumacher

Video Production
Larry Lavitt
Pedro Padua
Nancy Powers
Albert Salvato
Betsy Winans

Editorial Review Board

Ahmadjan Abduriyim, Tokyo, Japan
Timothy Adams, San Diego, California
Edward W. Boehm, Chattanooga, Tennessee
James E. Butler, Washington, DC
Alan T. Collins, London, UK
John L. Emmett, Brush Prairie, Washington
Emmanuel Fritsch, Nantes, France
Eloïse Gaillou, Paris, France
Gaston Giuliani, Nancy, France
Jaroslav Hyršl, Prague, Czech Republic
Dorrit Jacob, Sydney, Australia
A.J.A. (Bram) Janse, Perth, Australia
E. Alan Jobbins, Caterham, UK
Mary L. Johnson, San Diego, California
Anthony R. Kampf, Los Angeles, California
Robert E. Kane, Helena, Montana
Stefanos Karampelas, Manama, Bahrain
Lore Kiefert, Lucerne, Switzerland
Ren Lu, Wuhan, China
Thomas M. Moses, New York, New York
Aaron Palke, Carlsbad, California
Nathan Renfro, Carlsbad, California
Benjamin Rondeau, Nantes, France
George R. Rossman, Pasadena, California
Andy Shen, Wuhan, China
Guanghai Shi, Beijing, China
James E. Shigley, Carlsbad, California
Elisabeth Strack, Hamburg, Germany
Nicholas Sturman, Bangkok, Thailand
Fanus Viljoen, Johannesburg, South Africa
Wuyi Wang, New York, New York
Christopher M. Welbourn, Reading, UK
J.C. (Hanco) Zwaan, Leiden, The Netherlands

GEMS & GEMOLOGY

gia.edu/gems-gemology

Subscriptions
Copies of the current issue may be purchased for $29.95 plus shipping. Subscriptions are $79.99 for one year (4 issues) in the U.S. and $99.99 elsewhere. Canadian subscribers should add GST. Discounts are available for renewals, group subscriptions, GIA alumni, and current GIA students. To purchase print subscriptions, visit store.gia.edu or contact Customer Service. For institutional rates, contact Customer Service.

Database Coverage
G&G is abstracted in Thomson Reuters products (Current Contents: Physical, Chemical & Earth Sciences and Science Citation Index—Expanded, including the Web of Knowledge) and other databases. For a complete list of sources abstracting *G&G*, go to gia.edu/gems-gemology, and click on "Publication Information."

Manuscript Submissions
Gems & Gemology, a peer-reviewed journal, welcomes the submission of articles on all aspects of the field. Please see the Author Guidelines at gia.edu/gems-gemology or contact the Managing Editor. Letters on articles published in *G&G* are also welcome. Please note that Field Reports, Lab Notes, Gem News International, Micro-World, and Charts are not peer-reviewed sections but do undergo technical and editorial review.

Copyright and Reprint Permission
Abstracting is permitted with credit to the source. Libraries are permitted to photocopy beyond the limits of U.S. copyright law for private use of patrons. Instructors are permitted to reproduce isolated articles and photographs/images owned by *G&G* for noncommercial classroom use without fee. Use of photographs/images under copyright by external parties is prohibited without the express permission of the photographer or owner of the image, as listed in the credits. For other copying, reprint, or republication permission, please contact the Managing Editor.

Gems & Gemology is published quarterly by the Gemological Institute of America, a nonprofit educational organization for the gem and jewelry industry.

Postmaster: Return undeliverable copies of *Gems & Gemology* to GIA, The Robert Mouawad Campus, 5345 Armada Drive, Carlsbad, CA 92008.

Our Canadian goods and service registration number is 126142892RT.

Any opinions expressed in signed articles are understood to be opinions of the authors and not of the publisher.

About the Cover

For more than 120 years, Yogo Gulch in central Montana has been one of the world's most illustrious sapphire sources. In this issue, Nathan Renfro, Aaron Palke, and Richard Berg offer a mining history and gemological characterization of Yogo sapphires. The cover photo shows a suite of rough Yogo sapphires atop samples of the ouachatite dike rock in which they are found. The largest rough sapphire weighs 8.49 ct. Photo by Kevin Schumacher; courtesy of Don Baide (The Gem Gallery, Bozeman, Montana).

Printing is by L+L Printers, Carlsbad, CA.
GIA World Headquarters The Robert Mouawad Campus 5345 Armada Drive Carlsbad, CA 92008 USA

© 2018 Gemological Institute of America All rights reserved.

ISSN 0016-626X

FSC www.fsc.org MIX Paper from responsible sources FSC® C006300

Summer Reading: Diamond Research, Yogo Sapphire, and Byzantine Garnet

Characterization of diamond—both natural and synthetic—is a common thread for three of our Summer issue's six papers. This large issue also contains a synthetic diamond chart and our new regular feature "Diamonds from the Deep," which aims to demonstrate the value of the natural gem to science and our understanding of the earth's depths.

However, we have much more besides diamond to offer, including Byzantine garnets, Yogo sapphires—which grace the cover—and cultured freshwater pearls from Japan's Lake Kasumigaura.

First, lead authors Sally Eaton-Magaña, Christopher M. Breeding, and James E. Shigley review the science of naturally colored blue diamonds, which are among nature's rarest and most valuable gems. This is the second in their series of papers focused on natural-color diamonds. Although boron impurities are top of mind for most people, the authors detail other causes of blue color in diamond, including radiation-induced defects and complex defects involving hydrogen.

"Naturally colored blue diamonds are among nature's most rare and valuable gems ..."

Our second paper, by Karen V. Smit, Elina Myagkaya, Stephanie Persaud, and Wuyi Wang, turns the focus to Fancy Dark brown-black diamonds from Zimbabwe's Marange deposits. Their dark appearance is caused by a combination of tiny, methane-associated graphite inclusions, graphite needles, and brown radiation stains resulting from the diamonds' billion-year contact with radioactive minerals in the Umkondo conglomerate.

In our third paper, H. Albert Gilg, Karl Schmetzer, and Ulrich Schüssler tell a fascinating story. Using contemporary nondestructive analytical methods, they trace a Byzantine garnet intaglio back to its geographical source in Telangana State, India. The study reveals much about the ancient trading of Indian garnet.

Our fourth article, by Ahmadjan Abduriyim, profiles Japanese freshwater pearls, first cultivated in Lake Biwa, and then in Lake Kasumigaura, where most farms relocated in 1962. Although the production is limited, "Kasumiga pearls" are very attractive, displaying a variety of hues and very good luster.

Sapphires from Montana's Yogo Gulch are renowned for their vibrant untreated blue color and high clarity. In our fifth article, Nathan D. Renfro, Aaron C. Palke, and Richard B. Berg offer a complete gemological characterization of these unique American gemstones.

Next, Sally Eaton-Magaña and Christopher M. Breeding present a new chart on the growth and characteristics of HPHT and CVD synthetic diamonds, including information on recent advances in technology that enable production of larger, higher-quality synthetics and colorless melee.

I'd also like to draw your attention to our three regular sections. Lab Notes includes entries on advances in the size and quality of synthetic diamonds. Gem News International has something for everyone: a green-blue Maxixe-type beryl, the trace element characteristics of "golden sheen" sapphire, and Ethiopian color-change garnets. *G&G* Micro-World includes a mushroom preserved in copal, microlite crystals in topaz, and a wurtzite phantom in quartz. This issue also presents a new regular column by Karen V. Smit and Steven B. Shirey on the value of natural diamond to science. In their inaugural entry, the authors examine how diamonds help researchers solve the enigma of water's presence in the earth's depths.

Finally, we'd like to remind everyone that we're fast approaching the last chance to register for the GIA Symposium, so please go to symposium.gia.edu if you haven't already.

Enjoy our summer edition!

Duncan Pay | Editor-in-Chief | dpay@gia.edu

Natural-Color Blue, Gray, and Violet Diamonds: Allure of the Deep

Sally Eaton-Magaña, Christopher M. Breeding, and James E. Shigley

Natural-color blue diamonds are among the rarest and most valuable gemstones. Gray and violet diamonds are also included here, as these diamonds can coexist on a color continuum with blue diamonds. More so than most other fancy colors, many diamonds in this color range are sourced from specific locations—the Cullinan mine in South Africa and the Argyle mine in Australia. Although blue color is often associated with boron impurities, the color of diamonds in this range (including gray and violet) also originates from simple structural defects produced by radiation exposure or from more complex defects involving hydrogen. These different mechanisms can be characterized by absorption and luminescence spectroscopy. A fourth mechanism—micro-inclusions of grayish clouds or tiny graphite particles in gray diamonds—can be distinguished through microscopy. In this article, we summarize prior research as well as collected data such as color and carat weight on more than 15,000 naturally colored blue/gray/violet diamonds from the GIA database (along with an analysis of spectroscopic data on a subset of 500 randomly selected samples) to provide an unprecedented description of these beautiful gemstones.

Diamond in its pure form would be an uncomplicated material to study scientifically: a perfectly assembled carbon crystal with no color, no structural imperfections or defects at the atomic lattice level, and no inclusions. But no diamond is perfect, and it is these structural imperfections that can create beautiful colors and provide evidence of the growth history of the diamond. Nature has gifted us with diamonds that span the entire color spectrum. In this second in a series of articles about color in natural diamonds (see Breeding et al., 2018 for a discussion of the green color range), we will summarize the causes of blue/gray/violet hues (figure 1), and supplement information in the published literature by providing a compilation of results drawn from the GIA database.

Among fancy-color diamonds, there is greater awareness of blue diamonds because of the prominent display of the Hope diamond at the Smithsonian Institution in Washington, DC—there is no corresponding public stage for other large colored diamonds. This year, 2018, marks the sixtieth anniversary—the diamond anniversary—of the Hope's permanent exhibition at the Smithsonian. Several other historical blue diamonds are also steeped in legend and royalty (see, e.g., Gaillou et al., 2010). Additionally, recently discovered stones (e.g., Gaillou et al., 2014) capture princely sums at auctions today (see box A). For example, the 12.03 ct Blue Moon of Josephine sold for $48.5 million in 2015 (setting a world record of over $4 million per carat; Sotheby's, 2015).

In Brief

- Almost all blue/gray/violet diamonds owe their color to four different mechanisms.
- The majority of diamonds with unmodified blue color description and deep color saturation are type IIb with their color due to boron impurities.
- Most finds of type IIb diamonds are from the Cullinan mine in South Africa, while many blue/gray/violet diamonds due to hydrogen defects are sourced from the Argyle mine in Australia.
- These four causes of color among the blue/gray/violet diamonds show distinctive gemological properties and spectral features.

During the last decade, GIA has examined over 15,000 naturally colored blue/gray/violet diamonds, including more than 6,000 with unmodified blue

See end of article for About the Authors and Acknowledgments.
Gems & Gemology, Vol. 54, No. 2, pp. 112–131,
http://dx.doi.org/10.5741/GEMS.54.2.112
© 2018 Gemological Institute of America

Figure 1. A few recently discovered blue diamonds are displayed alongside some legendary gems within the blue/gray/violet color range. Clockwise from upper left: the 30.62 ct Blue Heart diamond, photo by Chip Clark, © Smithsonian Institution; a 0.77 ct Fancy Dark gray-violet shield cut, photo by Robert Weldon/GIA; a 1.23 ct Fancy Dark gray diamond, GIA photo; the 45.52 ct Fancy Deep grayish blue Hope diamond and Fancy Deep blue 31.06 ct Wittelsbach-Graff diamond, photo by Robert Weldon/GIA, courtesy of the Smithsonian Institution.

color descriptions (figure 2). While there are a few different causes of blue color in diamond, the most familiar cause, accounting for more than half of the natural unmodified blue diamonds seen at GIA, is measurable quantities of boron accompanied by extremely low levels of nitrogen. The Hope diamond, arguably the most famous colored diamond in the world, derives its color from 360 ppb of neutrally charged boron (Gaillou et al., 2010).

Numerous aspects of gem-quality diamonds in this color range have previously been addressed. Type IIb diamonds were discussed by King et al. (1998), Eaton-Magaña et al. (2008), and Gaillou et al. (2012); hydrogen-defect blue/gray/violet diamonds were explored by Fritsch and Scarratt (1992), Iakoubovskii and Adriaenssens (2002), Fritsch et al. (2007), and van der Bogert et al. (2009). The purpose of this article is to provide a detailed account of the gemological and spectroscopic characteristics of natural blue/gray/violet diamonds colored by various mechanisms in order to help the trade better understand these beautiful and often extremely valuable gems. The description of these diamonds will begin with a discussion of their coloration. As a caveat, we wish to mention that in this series of articles, a good deal of discussion is based on the graded color description of the diamonds (for example, "blue" diamonds are separated from "green-blue" diamonds in later sections and in figures). In the description of color grades, we do not explicitly address that it is more difficult for the eye to interpret subtle hue differences for very light-colored diamonds than it is for more saturated diamonds (King et al., 1994; King, 2006). Therefore, for the lightest color grades, fewer hue names are used and the color description spans a wider portion of the hue wheel. Of the 6,000+ diamonds with unmodified blue color descriptions in this study, 42% were from the lightest color grades (Faint, Very Light, Light; figure 3, right).

CAUSES OF COLOR

Blue/gray/violet color in gem diamonds can span a wide range in the GIA color description terminology (figure 2). For the purposes of this article, we include all natural fancy-color diamonds with blue, gray, or

BOX A: VALUATION OF BLUE DIAMONDS

The record-setting auction prices of blue diamonds over the last few years have attracted considerable attention. While blue diamonds are rare enough to be extremely valuable, they are still abundant enough to create and sustain a market. Additionally, many older blue diamonds have been recently recut. Public awareness of fancy-color diamonds has grown considerably in the past several decades due to high-profile auction sales and media attention. But the market value of larger, more intensely colored blue diamonds means they are generally available only to the wealthiest consumers.

Figure A-1 shows a compilation of sale prices for blue diamonds since 1940—including several noteworthy blue diamonds—and those sold at auction in the last few decades. The chart shows the sale price (in price per carat), and all diamonds are adjusted to 2018 U.S. dollars using the Consumer Price Index conversion. From 1940 to 1990, only a handful of blue diamonds had data available, but we see a clear increase in the value of blue diamonds, particularly in the last few decades.

There are several reasons for the increased awareness of colored diamonds among the public. These include media attention associated with celebrities wearing colored diamonds, Argyle's marketing campaign in the 1990s to create awareness of "champagne" and "cognac" diamonds, and improved cutting styles that enhance the face-up appearance of colored diamonds, thus creating a more marketable product (Shor, 2005). The high volume of treated diamonds in recent years have provided lower-cost options for the majority of the buying public. As long as color treatment is disclosed, these products have a viable place in the gem market.

Figure A-1. This chart chronicles the sale prices for several notable blue diamonds over the last 80 years. The data show the price per carat and normalizes the prices over the time period by adjusting each to May 2018 US dollars using the Consumer Price Index (CPI) conversion. The data show a clear increase in valuation of blue diamonds by several orders of magnitude. The full table of blue diamonds used to produce this chart can be found at https://www.gia.edu/doc/SU18-natural-color-blue-gray-and-violet-diamonds-table.pdf. From left to right: The 30.62 ct Blue Heart diamond, photo by Chip Clark © Smithsonian Institution; a 6.04 ct Fancy Vivid blue diamond, courtesy of Sotheby's Hong Kong; the 10.95 ct Bulgari Blue, courtesy of Christie's Images Ltd.; the 13.22 ct Winston Blue, courtesy of Christie's; the 31.06 ct Wittelsbach-Graff, photo by Robert Weldon/GIA, courtesy of the Smithsonian Institution; the 14.62 ct Oppenheimer Blue, courtesy of Christie's.

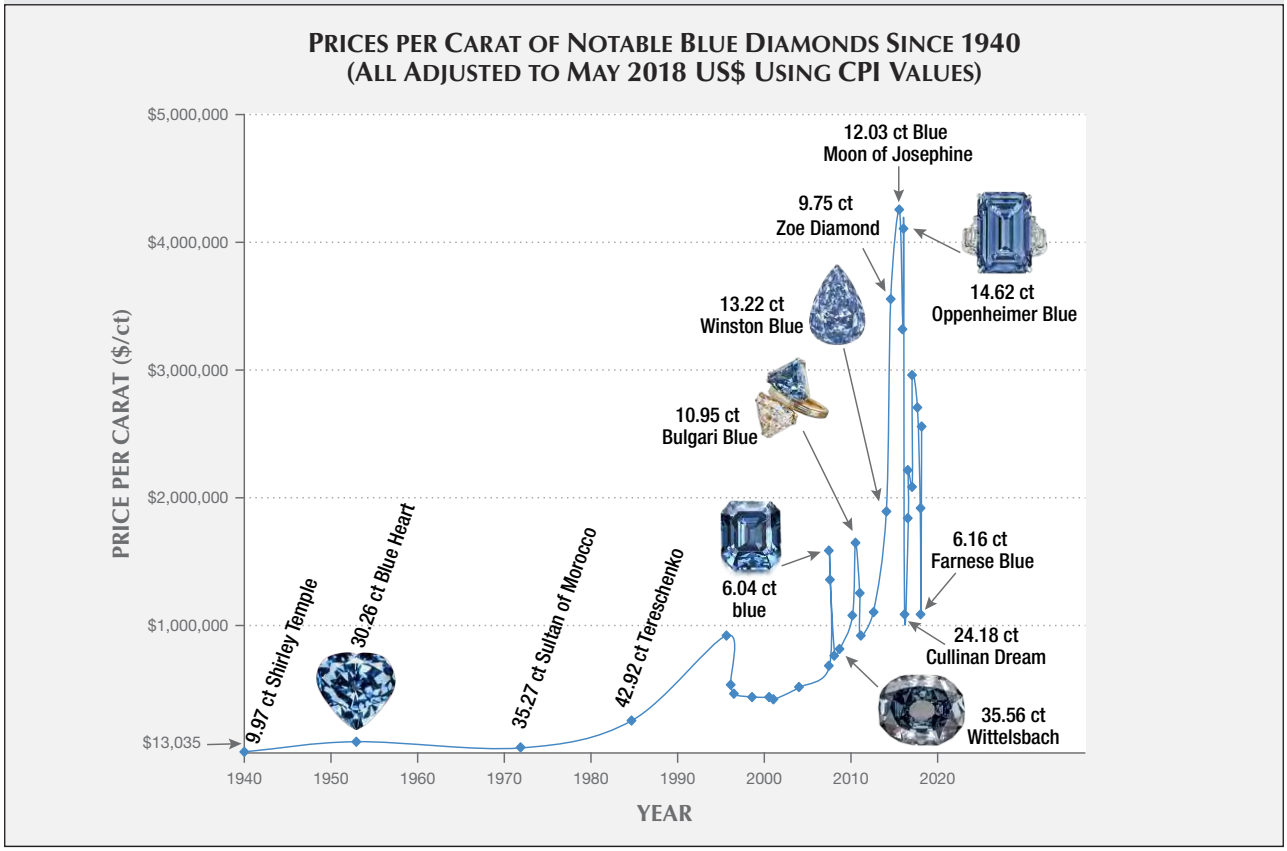

Figure 2. Diamonds with varying hues are shown to represent the color ranges within each of the four causes of color.

violet as the dominant color (i.e., the final name in the color description). Of the full dataset of 15,000+ blue/gray/violet diamonds seen at GIA over the last decade, most were unmodified blue (37.8%) or gray (33.1%). Next in abundance were those of gray-blue to blue-gray coloration, followed by green-blue diamonds. The lowest percentages belonged to those with violet coloration (figure 3, left). Below we chronicle the main causes of color; three are due to the presence of structural defects and one due to the presence of micro-inclusions. Representative diamonds and visible/near-infrared (Vis-NIR) spectra for these four causes of color are shown in figures 2 and 4, respectively.

Boron. Natural type IIb diamonds were studied in the 1950s and '60s (Dean, 1965), and aluminum was originally identified as the impurity responsible for the color (e.g., Crowther et al., 1967). Ultimately, boron was unambiguously identified as the natural dopant causing the observed color and semi-conductivity (Collins and Williams, 1971).

Type IIb diamonds are identified by a characteristic infrared absorption feature at 2800 cm^{-1}. The area

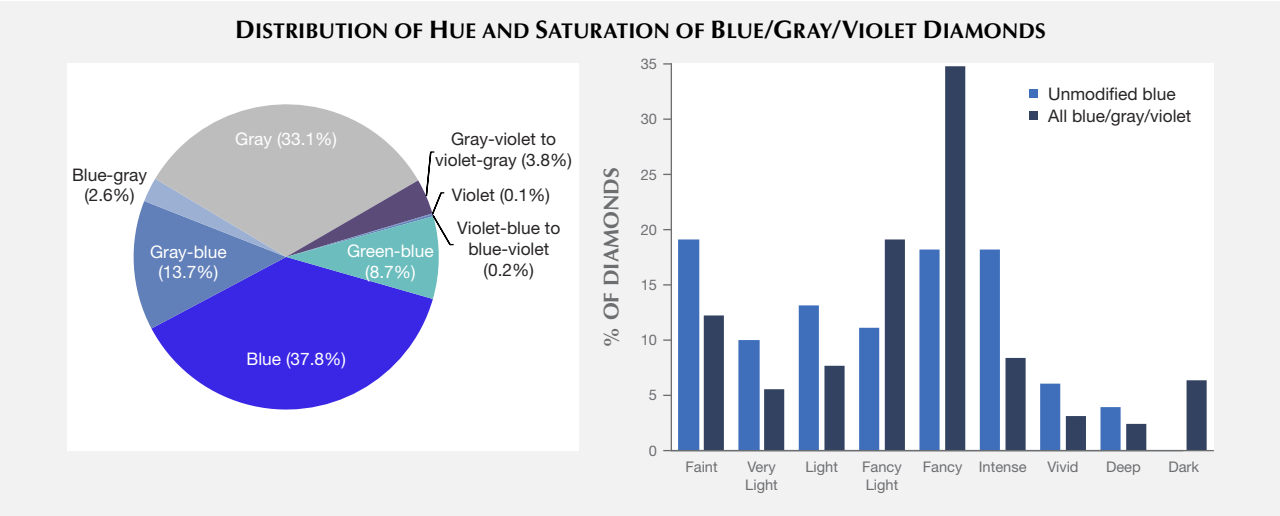

Figure 3. Left: Hue distribution of 15,000+ blue/gray/violet diamonds graded at GIA in the last decade. Unmodified gray and blue diamonds dominated within this color range, while comparatively few diamonds with a violet hue description were submitted. Right: Saturation distribution of blue/gray/violet diamonds. A majority of the unmodified blue diamonds (54%) are in the Faint to Fancy light color range.

under this absorption peak can also be used to calculate the uncompensated boron concentration (Fisher et al., 2009; Collins, 2010), which is the total boron concentration minus any donors such as nitrogen. Compensation occurs when electrical acceptors (such as boron in diamond) and electrical donors (such as nitrogen) cancel out each other's electrical charge. It is this uncompensated boron absorption peak centered at 2800 cm^{-1} in the infrared region that creates the gradually decreasing absorption gradient that extends into the near-infrared and red areas of the visible spectrum and creates the blue coloration (figure 4A and figure 5). In addition to the absorption that boron creates in the red region of the visible spectrum, plastic deformation–related defects of uncertain structure produce absorption at wavelengths less than 500 nm that can add a gray component (Collins et al., 2000). However, higher boron concentration is generally associated with a higher absorption gradient and a stronger blue color (see, e.g., box A in King et al., 1998 and figure 5). Boron content will not create blue color if sufficient competing defects are also present within the diamond. The necessity of both the presence of boron and the absence of detectable nitrogen—among other donors such as irradiation-related defects—creates the (extremely rare) geological conditions that produce natural type IIb diamonds.

Hydrogen. The observed color in hydrogen-defect diamonds results from the contributions of two broad absorption bands creating transmission windows in the blue and red regions of the absorption spectrum (figure 4B; Fritsch et al., 2007; van der Bogert et al., 2009). Two primary broad absorption bands span the range of 500–760 nm (and generally centered at

Figure 4. Representative Vis-NIR absorption spectra for the four major causes of color in blue/gray/violet diamonds. The spectra are offset vertically for clarity. For the first three mechanisms, the spectra are representative of the responsible color centers. For the fourth mechanism (colored by inclusions), this figure shows the spectral features common to most natural type Ia diamonds, namely N2 and N3.

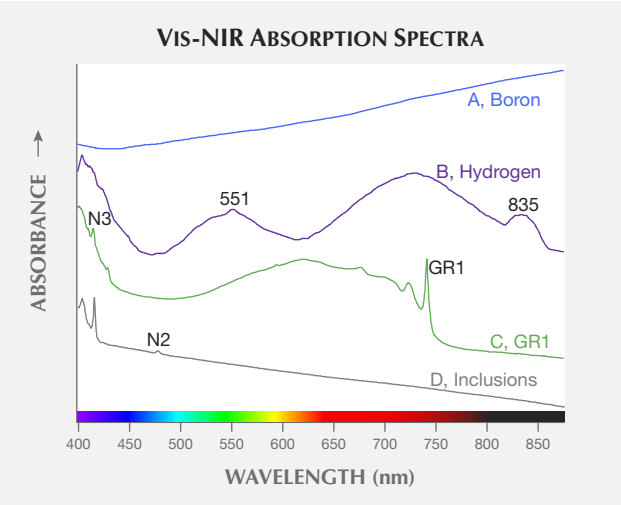

around 530 and 720 nm, though the central positions can vary between diamonds; see figure 4B), along with a characteristic "hydrogen band" at 835 nm. The relative intensity of these two bands creates transmission windows (blue or red) that determine if the resultant color appears more blue or violet (Fritsch et al., 2007; van der Bogert et al., 2009).

The cause of these broad bands, along with the commonly observed narrow feature at 551 nm, is unknown. The possible relationship between the band at approximately 530 nm in blue/gray/violet diamonds and the 550 nm band in pink diamonds is also still a matter of scientific debate (Iakoubovskii and Adriaenssens, 2002; van der Bogert et al., 2009) despite the close proximity in wavelength position and comparable band width, and the fact that diamonds of both colors are predominantly sourced from Australia's Argyle mine. Van der Bogert et al. (2009) determined that the band at approximately 530 nm is likely a composite of several independent peaks, and that there are several other gemological distinctions between pink and blue/gray/violet diamonds.

The best-known hydrogen-related defect in natural diamond is the 3107 cm^{-1} infrared absorption—recently attributed to a hydrogen atom associated with three nitrogen atoms and a vacancy (i.e., a vacant carbon atom position in the lattice; Goss et al., 2014). While the 3107 cm^{-1} peak in the infrared region has been correlated with the hydrogen-related band at 835 nm, the precise mechanism causing the visible coloration is still unknown (Fritsch et al., 2007). There are certainly other as yet unidentified structural defects involved with the diamond coloration. The presence of hydrogen defects in the diamond structure has been known and studied for decades, but very little is known about how the hydrogen impurities affect diamond color. Nevertheless, high hydrogen concentrations have been determined as a necessary condition for the diamonds in this color range (Iakoubovskii and Adriaenssens, 2002).

In Breeding et al. (2018), we discussed hydrogen defects that occasionally create a green color component. Figure 6 shows a distinction between hydrogen-related spectra obtained for green diamonds (upper set) and those for violet-gray diamonds (lower set). Both have a pronounced band at approximately 835 nm. This hydrogen band occurs in both green and blue/gray/violet diamonds containing high quantities of hydrogen, and it was described by Fritsch et al. (2007) as a triple band including absorptions at 829, 837, and 844 nm. However, the green diamonds have much less pronounced bands at 530 and 720 nm, along with more pronounced "cape" features (e.g., N2 at 477.6 nm and N3 peaks at 415.2 nm). In green diamonds, the greater absorption at low wavelengths (below 500 nm), plus a comparatively minor contribution from the 530 and 720 nm bands, shifts the transmission window into the green region of the visible spectrum.

The two absorption bands in these diamonds create two transmission windows (again, see figure 6). This can result in a color shift under two different light sources. This phenomenon is most associated with alexandrite, and occasionally seen in natural di-

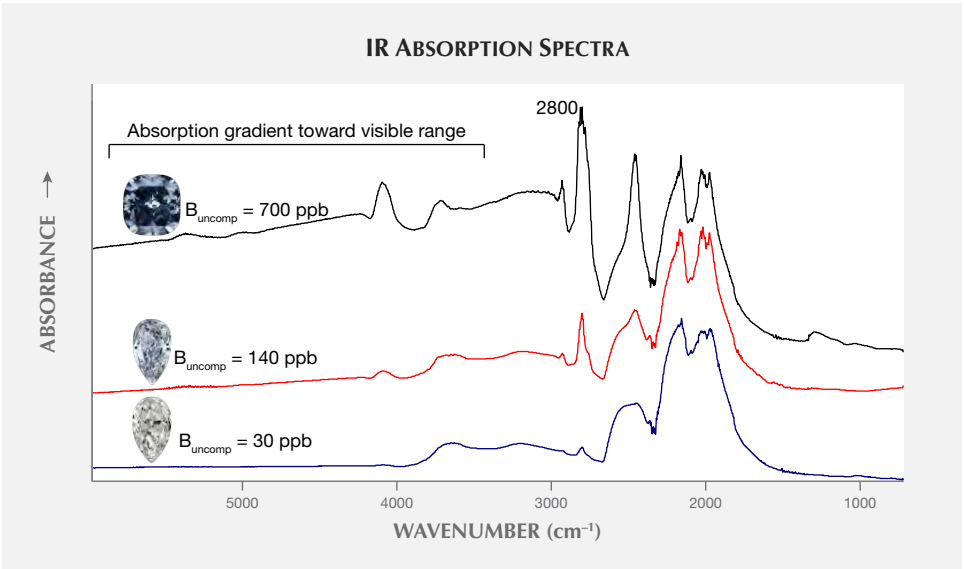

Figure 5. These IR absorption spectra of three type IIb diamonds (top: Fancy Deep blue; middle: Fancy Light blue; bottom: Faint blue) are representative of the range of peak intensities at 2800 cm^{-1} and the corresponding uncompensated boron concentrations that encompass the majority of natural blue diamonds.

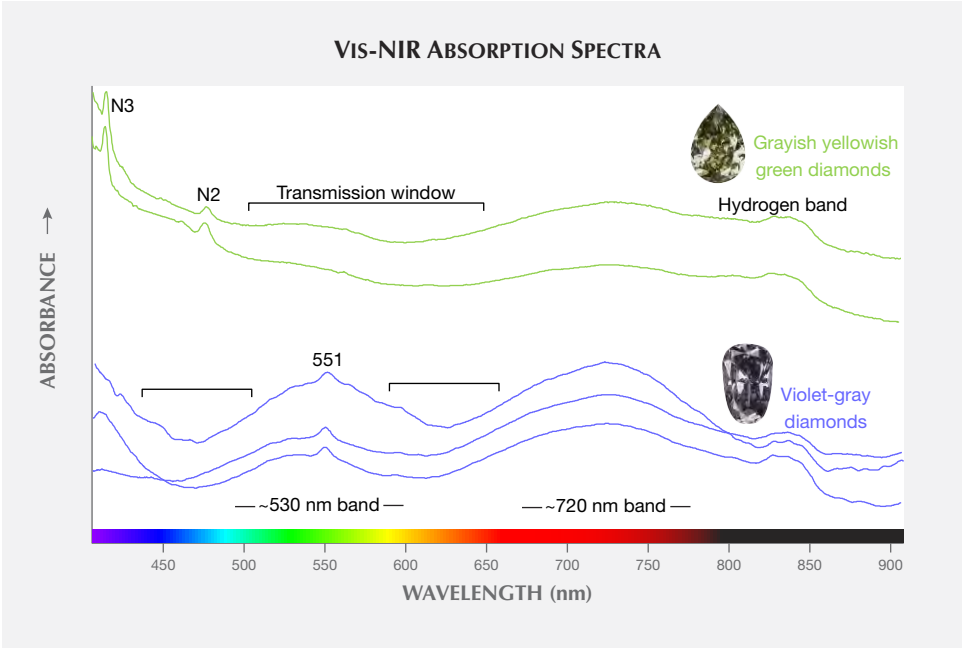

Figure 6. A comparison of Vis-NIR absorption spectra of diamonds colored by hydrogen-related defects highlights the differences within two color families—grayish yellowish green diamonds (Breeding et al., 2018) and violet-gray diamonds (this study). Violet-gray diamonds show much stronger absorption bands at ~530 nm and ~720 nm and exhibit fewer cape-related features than their greenish counterparts. See also Fritsch et al. (2007). Spectra are offset vertically for clarity, and the transmission windows are indicated with brackets.

amonds (Liu et al., 1998) and treated diamonds (Eaton-Magaña, 2016). Many of these hydrogen-defect diamonds receive color grades within the gray-to-blue range when viewed in the GIA color-grading environment (King et al., 1994), but they can often appear violet under other light sources (see figures 2 and 7). Although very few diamonds receive a color grade with a violet component (again, see figure 3, left), there are likely many more diamonds with this cause of color in which violet can be observed under incandescent lighting conditions.

GR1. As discussed extensively in Breeding et al. (2018), GR1 (general radiation 1) defects are empty or vacant lattice positions in the diamond structure, and they serve as the most common mechanism for green to green-blue color in gem diamonds (Shigley and Fritsch, 1990; Collins, 2001; Shigley and Breeding, 2013). Vacancies are created when radiation (both natural and laboratory-induced) provides sufficient energy to displace carbon atoms from their normal positions in the diamond lattice. GR1 vacancies cause the diamond to absorb light in the red part of the visible spectrum (zero phonon line [ZPL] at 741 nm with associated broad absorption extending from approximately 550 to 750 nm; see figure 4C).

Figure 8 compares the Vis-NIR absorption spectra of a blue, a green-blue, and a green diamond. Generally, green diamonds have a greater absorption at lower wavelengths in the UV to blue region of the spectrum (below 500 nm), which shifts the transmission window into the green portion of the visible spectrum. This increased absorption is mostly associated with nitrogen-related defects such as N2 and N3 (Breeding et al., 2018). As naturally irradiated diamonds often have high quantities of these nitrogen-related defects, most of them are green. Green-blue

Figure 7. This 0.13 ct Fancy Light gray-blue diamond (top) and 0.33 ct Fancy grayish blue diamond (bottom) are colored by hydrogen defects and show a different color appearance with different light sources. Color grading occurs under daylight conditions (left), whereas incandescent lighting produces a more violet color (right).

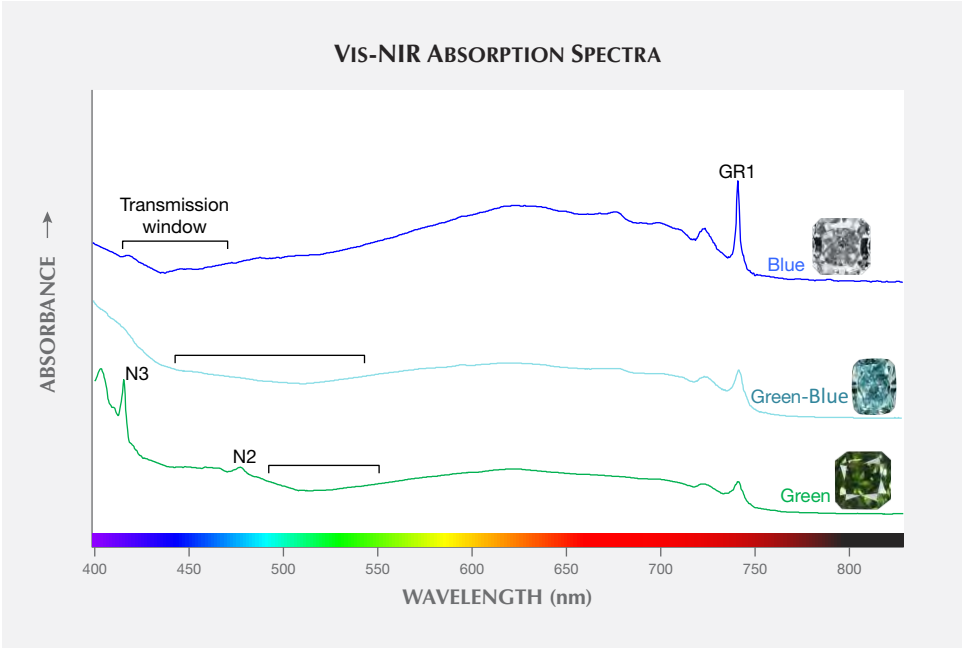

Figure 8. Comparison of Vis-NIR absorption spectra between a green diamond colored by GR1 defects (Breeding et al., 2018) and its green-blue and blue counterparts. The most pronounced and consistent difference is that the green-blue to blue diamonds colored by GR1 have less-pronounced cape peaks, thus allowing a shift in the transmission window from the green into the blue range. Spectra are offset vertically for clarity, and the transmission windows are indicated with brackets.

to blue diamonds often have lower nitrogen-related absorption in the UV to blue region (top two spectra in figure 8), and many are type IIa.

As with green diamonds, jewelers must take great care during jewelry repair processes when heating blue diamonds colored by this mechanism in order to avoid destroying the GR1 defects and losing the blue color.

Inclusions. The micro-inclusions and cloud-like features that cause gray color in diamonds (e.g., figure 9A and 9B)[1] should not be confused with the micro-inclusions often seen in Fancy white diamonds (which are almost always type IaB). The micro-inclusions in Fancy white diamonds provide an opalescent appearance (Moses and Reinitz, 2000; Gu and Wang, 2017).

In contrast, these gray diamonds colored by internal features are typically type IaA±B (determined as type IaA, IaAB, or IaB) or saturated (where the aggregated nitrogen absorption is greater than the detection limits of infrared spectroscopy, generally greater than 500 ppm) type Ia. The observed particle clouds appear whitish to grayish. Except for nitrogen impurities, the Vis-NIR spectrum contains a decreasing absorption gradient toward higher wavelengths (figure 4D). These clouds are sometimes termed "hydrogen clouds" due to the elevated intensity of the 3107 cm^{-1} infrared peak within these areas. However, there is little similarity between these so-called hydrogen-cloud gray diamonds and the hydrogen-related blue-to-violet diamonds discussed previously.

Far more likely is that these gray diamonds are similar to the mixed-habit type IaAB diamonds containing gray/colorless zoning (the term "mixed habit" refers to standard {111} growth accompanied by growth of approximately {100} orientation). These diamonds have been studied extensively due to their simultaneously grown cuboid and octahedral sectors (e.g., Smit et al., 2016). Within the cuboid sectors are many micro-inclusions that have been identified as graphite (Smit et al., 2016; Eaton-Magaña et al., 2016), and those sectors often have a grayish appearance. Analysis of the micro-inclusions within polished flat-plate samples indicated that the individual inclusions are quite small—no more than 1 µm. When those samples were heated to 1200°C, they were still gray, but the graphitic inclusions were en-

[1]Since a variety of hues can appear "gray" at very low color saturation, these diamonds have a variety of subtle color sensations and can appear, for example, as either more bluish or more yellowish and still be graded as the color gray (King et al., 1994, King, 2006). Many of the diamonds that derive their color from inclusions also show a typical cape spectrum (e.g., figure 4D), which can often impart a yellowish (or warm) appearance to these gray diamonds. In contrast, many gray diamonds due to boron impurities will have a bluish (or cool) appearance. The color sensation is not sufficient to affect the color grade but can lead to variations in appearance among diamonds with the same color description.

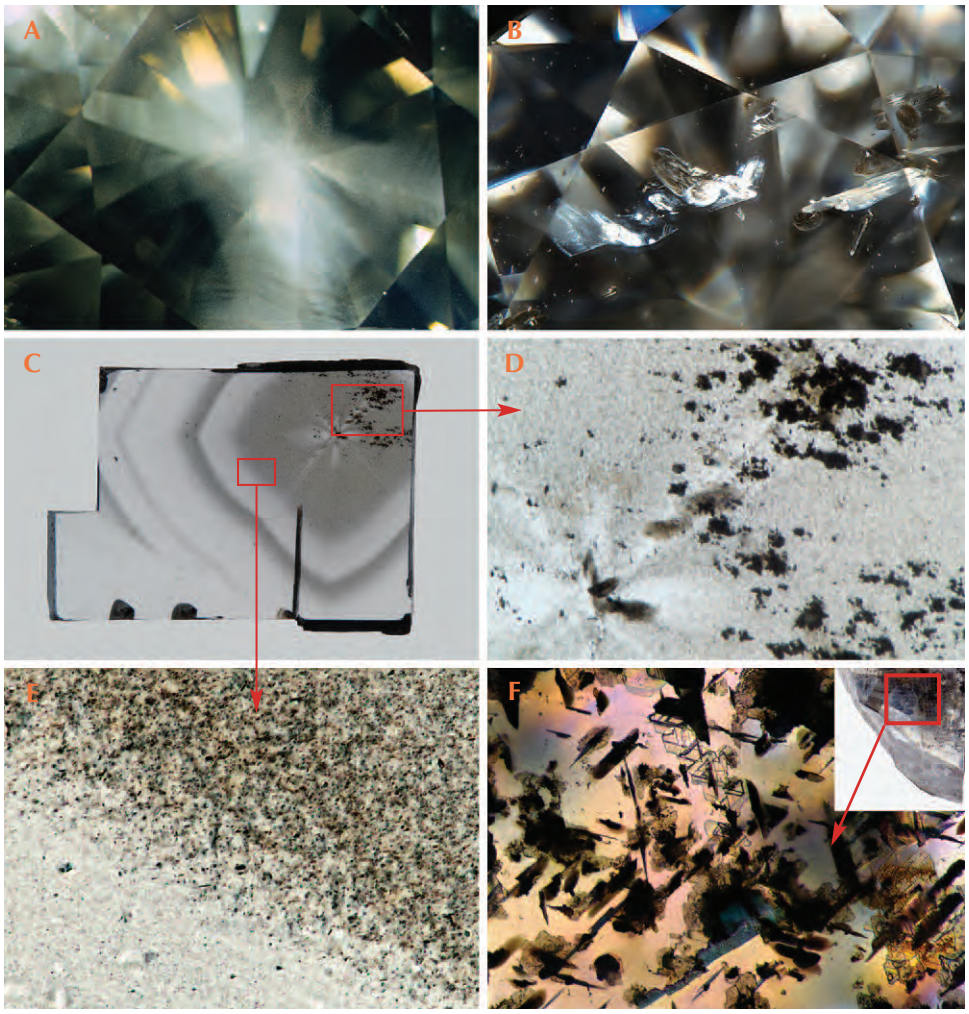

Figure 9. Micro-inclusions resembling clouds are an example in which atomic-scale defects are not responsible for color in gem diamonds. These clouds can appear whitish, light gray, or dark gray under the microscope (A; field of view 5.1 mm). Larger inclusions can also impart a gray color (B; FOV 2.9 mm). The color of the micro-inclusions—along with their density and abundance—contributes to the graded hue and the modifier (i.e., Faint to Fancy Dark). Portions of a flat plate shown in figure 9C (FOV 5.25 mm) are magnified to show graphite inclusions within a gray cloud (D; FOV 900 µm) and the boundary between a gray clouded region and an inclusion-free colorless region (E; FOV 286 µm). Also shown (F; FOV 665 µm) are graphite inclusions oriented along the [111] direction. This photomicrograph was collected from the dark gray portion of the diamond in the inset.

larged to 3–4 µm and appeared dark in the microscope (Eaton-Magaña et al., 2016). This indicates that both the small gray micro-inclusions and the larger, darker micro-inclusions impart a gray bodycolor. Photomicrographs obtained from flat plates of a natural mixed-habit diamond show grayish clouds and graphitic inclusions (figure 9, C–E), and a natural diamond shows noticeable graphitic inclusions (figure 9F). Although the micro-inclusions in several mixed-habit research diamonds have been identified as graphite (e.g., Smit et al., 2016), and likely a good number of the gray diamonds colored by inclusions are due to graphite micro-inclusions, we should not presume that all micro-inclusion and cloud observations within this color category are due to graphite.

OCCURRENCE AND FORMATION

The formation mechanism for blue/gray/violet diamonds in the earth varies significantly depending on the defects responsible for the color. Stones colored by micro-inclusions or by hydrogen- or boron-related defects incorporate these impurities, along with any nitrogen impurities, when they crystallized deep in Earth's mantle. Long residence times at high temperatures and pressures contribute to the final arrangement of structural defects within the diamonds.

The precise formation mechanism that leads to type IIb diamond—measurable boron concentrations accompanied by extremely low nitrogen levels—is still a matter requiring further study. It is unclear what distinguishes the Cullinan mine from other mines and makes it a reliable source for type IIb diamonds; however, recent evidence demonstrates that these are "superdeep" diamonds originating at sublithospheric mantle depths (> 600 km) and that the boron is likely sourced from subducted oceanic lithosphere (Smith et al., 2018). Similarly, the blue/gray/violet diamonds colored by hydrogen defects are almost exclusively from the Argyle mine. Diamonds colored by GR1 defects are generally thought to ob-

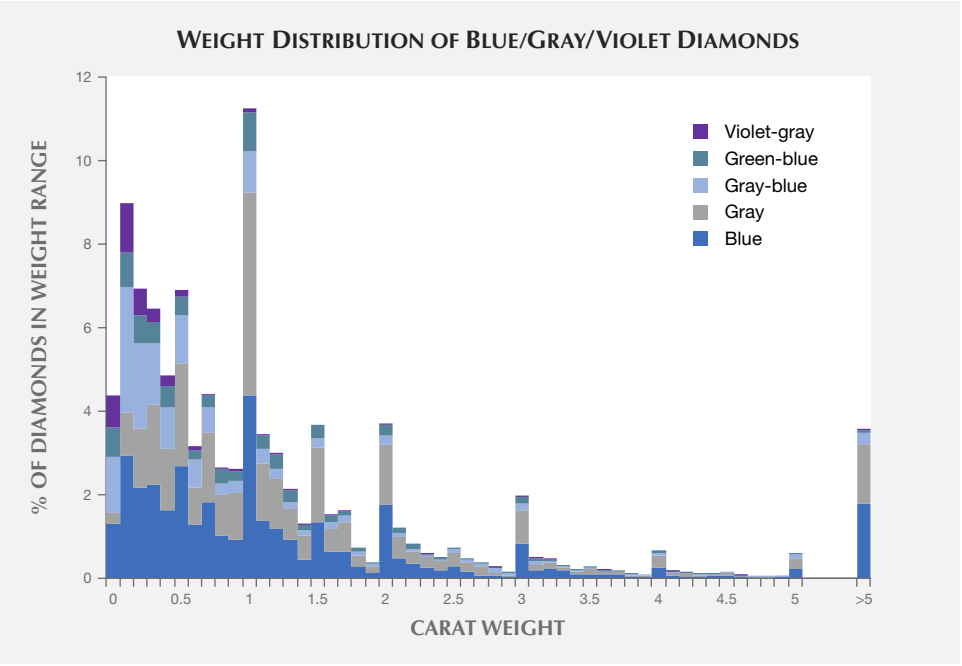

Figure 10. The weight distribution of the 15,000+ natural-color blue/gray/violet diamonds graded by GIA in the last decade. The histogram is divided into 0.1 carat increments between 0 and 5 ct. Also shown are the remaining 4% of graded diamonds larger than 5 ct. The histogram also shows the distribution of the different diamond colors. For example, the violet-gray diamonds are mostly represented at the lower weights and are much less prevalent in larger diamonds, which is consistent with prior observations (e.g., van der Bogert et al., 2009).

tain their color from late-stage interactions with radioactive minerals or fluids in the earth's crust over thousands to millions of years (see Breeding et al., 2018, and references therein). Since elevated temperatures will change their color, this natural irradiation likely occurred in the earth's crust, relatively close to the surface.

The blue/gray/violet diamonds colored by hydrogen-related defects, as well as the gray diamonds colored by inclusions, likely underwent more rapid growth than typical diamond growth, with processes similar to the cuboid growth observed in mixed-habit diamonds (Fritsch et al., 2007; Smit et al., 2016). This faster growth rate would allow the growing diamonds to trap impurity atoms, such as hydrogen and nickel, at much higher concentrations (see the "Luminescence" section below; Fritsch et al., 2007). Similarly, this fast growth model applies to the gray diamonds colored by inclusions, as it allows the diamond to trap high quantities of mineral and fluid inclusions (Smit et al., 2016).

LABORATORY GRADING

Stones weighing up to 1.0 ct comprised 63% of the 15,000+ natural blue/gray/violet diamonds examined at GIA (see figure 10). Noticeable spikes in quantity are observed near important carat-weight thresholds (e.g., 0.5, 1.0, 1.5, and 2.0 ct). This chart shows that faceting and polishing decisions may maximize the face-up color and appearance, but weight thresholds are often important considerations as well. The diamonds in figure 10 are shown according to their general color groups. The data indicate that the diamonds with gray-violet, green-blue, and gray-blue hues are much more prevalent below 1 carat than at higher weights. Above a carat, most are blue or gray.

Although fancy-color diamonds are often fashioned as fancy shapes to enhance their face-up color, round brilliants represent a plurality (44%) of the 15,000+ diamonds (figure 11, left), followed by pears (16%), rectangles (9%), and cushions (8%). The majority of diamonds with pale color (i.e., Faint to Fancy Light) are faceted as rounds (figure 11, right), whereas fancy shapes are dominated by the deeper colors (Fancy to Fancy Dark). Those faceted as round brilliants were likely interpreted as D to Z material during the pre-faceting steps.

To determine the distribution of the four major causes of color, we further analyzed the Vis-NIR and infrared (IR) absorption spectra of a representative sampling of 500 natural blue/gray/violet diamonds (randomly selected from the 15,000+ in our GIA database) and identified the cause of color for each. This subset of data was used to generate figures 12 and 13. For this subset, we observed that 177 (35%) of natural blue/gray/violet diamonds were colored by boron and 132 (27%) by the GR1 defect, 152 (30%) by hydrogen defects, and 37 (7%) by inclusions (figure 12, top). We also determined the boron concentration of the 177 type IIb diamonds (Fisher et al., 2009; Collins, 2010), and the nitrogen aggregate concentration in 48 unsaturated type IaA±B diamonds (Boyd et al., 1994,

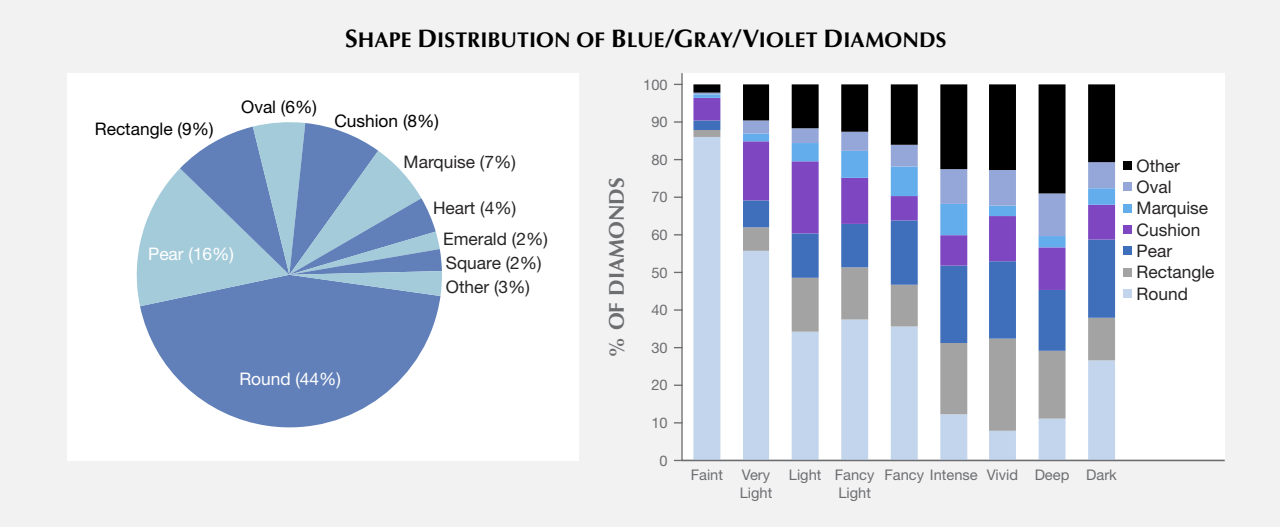

Figure 11. Left: The overall shape distribution of the 15,000+ diamonds graded by GIA in the last decade that fell within the blue/gray/violet color range. Right: The shape distribution can vary dramatically with the tone of the diamond. Many of those with paler colors (such as Faint or Very Light) are faceted as rounds.

1995). Two other diamonds were colored by the 480 nm band and will be discussed in the "Unusual Examples" section.

The data become more illustrative when separated out into color groups. For example, the green-blue color grade is populated exclusively with diamonds colored by GR1, while inclusion-related defects are found solely within the gray color region. The blue-gray to gray-blue region is populated almost evenly with type IIb (boron) and hydrogen-defect diamonds, with a small minority colored by GR1 defects. The violet category is dominated by H defects but also contains a low amount of type IIb diamonds.

The blue category—the most valuable hue within this range—has a majority of diamonds colored by

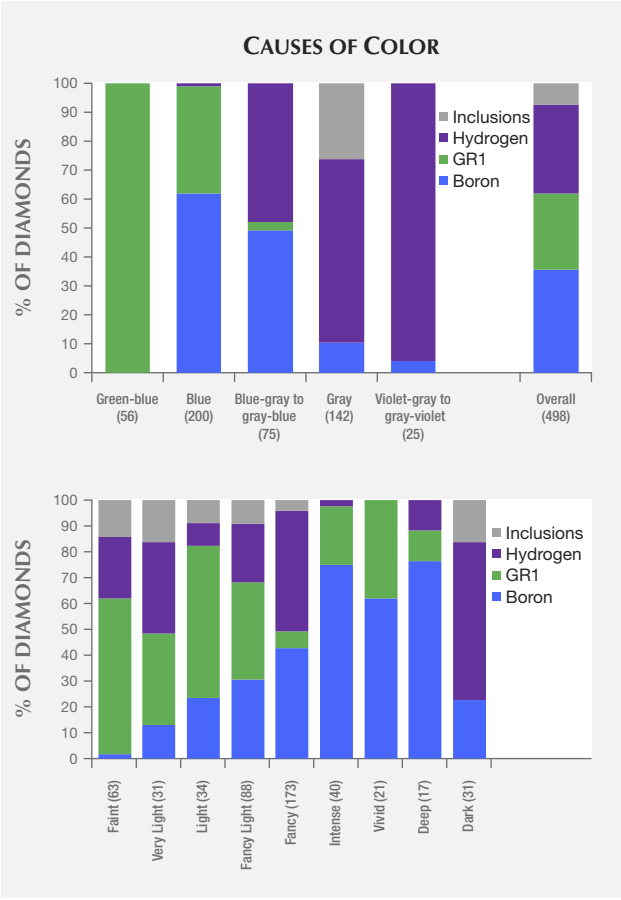

Figure 12. Natural blue/gray/violet diamonds submitted to GIA over the last decade are predominantly colored by four mechanisms. When the randomly selected subset of 500 diamonds are analyzed and divided by hue (top), clear distinctions emerge. Green-blue diamonds are comprised solely of diamonds with color due to GR1 defects, while inclusion-related defects reside only within the gray category. Diamonds with a violet component are almost exclusively due to hydrogen-related defects, and over half of the unmodified blue diamonds are type IIb. When the diamonds are segregated by tone (bottom), H- and GR1-related defects predominate within the more faintly colored diamonds while the type IIb diamonds comprise the majority of the more saturated stones. Also shown along the x-axis are the number of samples within each category.

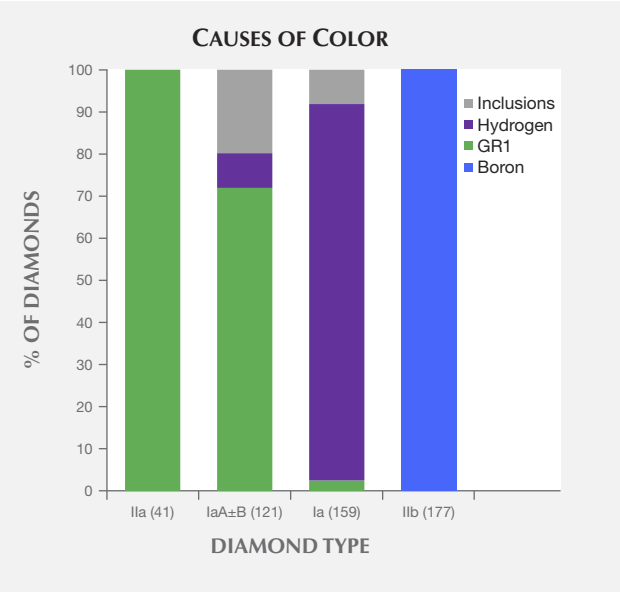

Figure 13. The four dominant causes of color for natural blue/gray/violet diamonds submitted to GIA show clear distinctions when separated by diamond type. Among the subset of 500 diamonds, type IIa diamonds in this color range have GR1 defects as the cause of color while, unsurprisingly, all type IIb diamonds are due to boron. Diamonds with nitrogen aggregates that are at sufficiently low concentration so as not to saturate the IR spectra (termed IaA±B) are mostly colored by GR1-related defects. Saturated type Ia spectra are largely associated with H-related diamonds. Also shown along the x-axis are the number of samples from each category.

boron, with 37% due to GR1 defects (although these generally have low color saturation).

Figure 12 (bottom) shows the distribution of these color centers based on the color saturation from Faint to Fancy Deep. Diamonds colored by GR1 or H defects are usually found among the lighter hues, while type IIb diamonds dominate among the more saturated color descriptions. The GR1-defect diamonds with Intense or Vivid color grades were all green-blue and not an unmodified blue color.

Figure 12 also illustrates the perceived dominance of type IIb diamonds within the blue/gray/violet color range. They frequently have an unmodified blue color description and more often have intense color than any of the other groups. This combination of saturated color and attractive blue hue commands the highest value, especially at the higher weights in which other colors in this range are not well represented. With the exception of a handful of violet diamonds offered at the Argyle mine's annual tender (e.g., King et al., 2014; Rio Tinto, 2017), the most famous and notable of the blue/gray/violet diamonds are type IIb.

GEMOLOGICAL OBSERVATIONS

Blue/gray/violet natural diamonds have numerous interesting features that can be observed with standard gemological equipment. These properties, however, are quite variable depending on the cause of the color. In this section, we review the major observations from diamonds colored by each group of defects.

Colored by Boron. Type IIb diamonds often show visible phosphorescence (figure 14A). The most famous example is probably the vibrant red phosphorescence displayed by the Hope diamond (Eaton-Magaña et al., 2008) which can be observed for up to one minute. Regardless of the observed color of phosphorescence, natural type IIb diamonds generally have two well-defined phosphorescence emission bands (figure 14B), centered at 500 nm (blue phosphorescence) and 660 nm (red). Natural diamonds that show only the 500 nm band are predominantly an unmodified blue, while those type IIb diamonds with gray or violet components typically show the 660 nm band (Eaton-Magaña and Lu, 2011; figure 14C).

The generally accepted mechanism for phosphorescence in type IIb diamonds is "donor–acceptor pair recombination" (DAPR), which is reviewed in depth by Dean (1965). In this mechanism, "holes" bound to acceptor atoms and electrons bound to donor atoms are activated by energy from the ultraviolet source, and they subsequently recombine and emit light equivalent to their energy difference (plus an electrostatic correction). Boron has been positively identified as the acceptor in the mechanism (Collins and Williams, 1971). Since gray coloration is largely caused by defects related to plastic deformation, it is highly likely that the donor corresponding to the 660 nm band is also influenced by plastic deformation, while the donor responsible for the 500 nm phosphorescence band is not (Eaton-Magaña and Lu, 2011).

Colored by Hydrogen-Related Defects. As with green diamonds colored by hydrogen defects (Breeding et al., 2018), diamonds in the blue color range also often contain whitish particle clouds with sharp boundaries and relatively non-included regions. As these clouds can create gray color on their own, their presence can influence the grayish coloration of these diamonds. However, the color contribution of inclusions in these diamonds has not been fully evaluated.

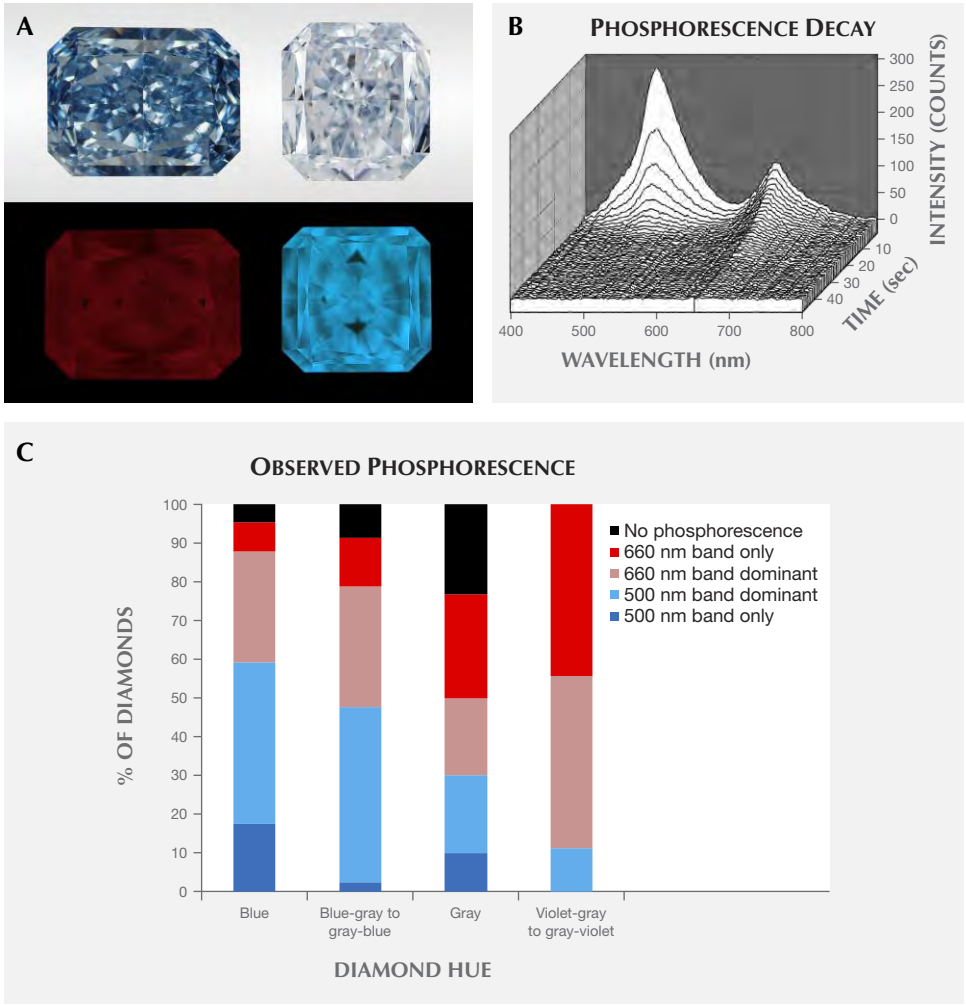

Figure 14. A: A 0.66 ct Fancy Intense blue diamond showing red phosphorescence and a 0.28 ct Fancy Light blue diamond showing blue phosphorescence. B: Phosphorescence spectra showing the decay over 40 seconds of the 500 nm band (blue phosphorescence) and the 660 nm band (red phosphorescence). The plot shows that the blue phosphorescence decreases much more quickly than the red phosphorescence. C: A histogram showing the distribution of phosphorescence reactions for the type IIb diamonds, separated by bodycolor.

When viewed under UV light, many hydrogen-rich diamonds fluoresce yellow. This observation has been consistent for many different colors of diamond, including "chameleon" and green H-defect diamonds (Fritsch et al., 2007; van der Bogert et al., 2009; Breeding et al., 2018). The same observation was true for the 152 blue/gray/violet diamonds colored by hydrogen that were examined for this study—93 (61%) fluoresced yellow under long-wave UV, and 137 (90%) did so under short-wave UV.

Colored by GR1. The most distinctive gemological feature of blue diamonds colored by radiation damage is surficial radiation spots and internal color zonation. Radiation stains occur as either green or brown patches of color on the surface of a rough diamond or within fractures. Polishers will often preserve a portion of these radiation stains after faceting, particularly in the girdle area (again, see figure 11), to provide confirmation that the GR1 defect originated from natural radiation and not laboratory irradiation.

Although the bodycolor is green-blue to blue, the radiation stains are colored green and turn brown if heated above 550–600°C (Nasdala et al., 2013; Eaton-Magaña and Moe, 2016). Radiation stains in these diamonds still appear green (figure 15, left) even when the bodycolor appears blue. In the green radiation stains, optical absorption spectra show GR1-related absorption at high wavelengths and vacancy cluster–related general absorption at lower wavelengths (Nasdala et al., 2013), thus creating a transmission window within the green area. For brown radiation stains, the color is determined solely by the vacancy cluster absorption, as the heating brought about depletion of the GR1 absorption. At low wavelengths, therefore, the absorption within the radiation stains and the absorption within the bulk of the diamond (nitrogen "cape" absorption; figure 8) are brought about by separate causes. If the cape absorption is not present, then the bulk of the diamond appears blue while the radiation stain appears green.

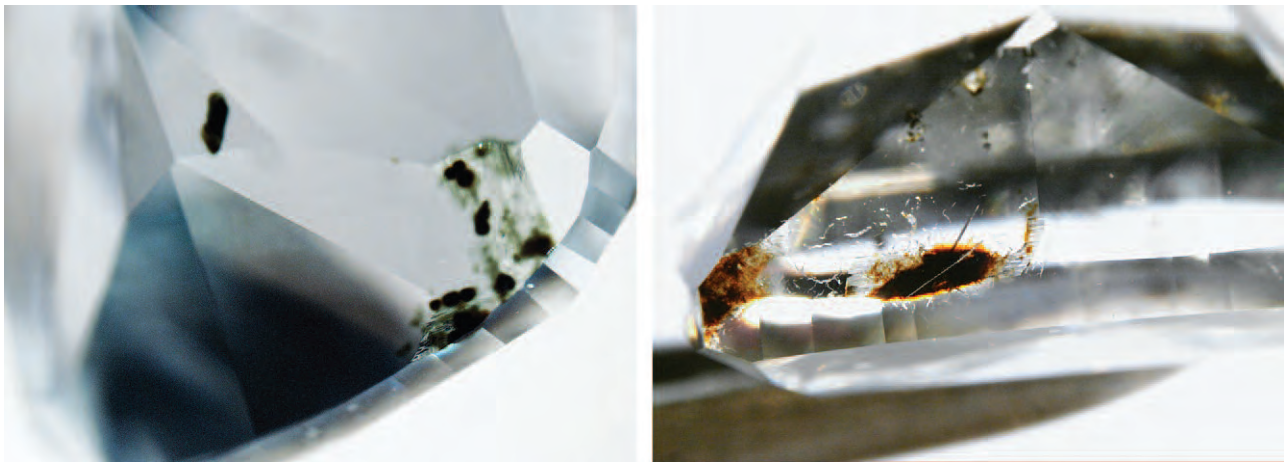

Figure 15. This 0.30 ct Fancy green-blue diamond (left) and 1.18 ct Fancy Light green-blue diamond (right), both colored by GR1 defects, show several green and brown radiation stains.

Colored by Inclusions. Gray diamonds colored by internal inclusions have few indicators regarding cause of color within their absorption spectra, so microscopic observation of cloud-like features or graphitic inclusions is essential for these stones. As there are several possible origins for gray color in diamond, a Vis-NIR spectrum with common features (e.g., figure 4D) in conjunction with the presence of cloud-like inclusions establishes the inclusions as the cause of the gray color. Due to the abundance of color-causing inclusions, these diamonds also have very low clarity grades—typically the Included clarity grades (I_1 to I_3).

ABSORPTION SPECTROSCOPY

Absorption spectroscopy measurements are nondestructive and provide a detailed glimpse of a diamond's atomic structure by passing light of different wavelengths through the stone and measuring what wavelengths (energies) are absorbed by the impurities and defects present. IR absorption gives information about the impurities present in the diamond lattice, while optical absorption reveals the color-producing defects. All of the atomic defect groups of blue/gray/violet diamonds have unique spectroscopy features. Standard testing conditions and instrumentation are applied to all diamonds submitted to GIA. These methods have been detailed in other publications (e.g., D'Haenens-Johansson et al., 2015) and summarized for this series of articles in Breeding et al. (2018).

IR Absorption. Details of the major impurities present, as well as their configuration relative to the rest of the carbon lattice in diamond (diamond type), are directly and quickly determined by IR spectroscopy (Breeding and Shigley, 2009).

For diamonds in this color range, the cause of color can sometimes be inferred from the diamond type (figure 13). Type IIa diamonds are generally colored by irradiation; type IIb, by definition, contain boron impurities. H-defect diamonds in this color range require high concentrations of hydrogen and therefore generally high nitrogen (Iakoubovskii and Adriaenssens, 2002). Most H-defect diamonds studied here were saturated type Ia diamonds.

Boron. The uncompensated boron concentration for 177 type IIb diamonds was determined from the IR spectra. The values ranged from 25 ppb for a Faint blue diamond up to 1500 ppb for a Fancy Vivid blue. Type IIb diamonds with lower boron concentrations would likely receive a grade in the D to F range (King et al., 2008). The range of uncompensated boron concentrations was greatest for unmodified blue type IIb diamonds (several with values above 500 ppb), while gray type IIb diamonds spanned a much narrower range (only up to 400 ppb) and gray-blue and blue-gray were at intermediate ranges.

The highest value (1500 ppb) and median value (300 ppb) were, unsurprisingly, lower than the highest value and median value observed in HPHT synthetic diamonds (4630 ppb and 650 ppb, respectively; Eaton-Magaña et al., 2017b), as manufacturers are able to deliberately introduce large quantities of boron into the growth chamber. Of the 177 type IIb diamonds examined from the 500 diamond subset, 36% had a color grade of Intense, Vivid, Dark, or Deep. Of the type IIb

HPHT synthetics examined in Eaton-Magaña et al. (2017b), 85% had color grades in that range.

Hydrogen Defects. Most of the diamonds colored by hydrogen-related defects had very high concentrations of nitrogen aggregates—the nitrogen-related peaks were saturated within the IR absorption spectra. Generally, there were more than 500 ppm of total nitrogen aggregates for these samples. The diamonds with saturated IR spectra are termed here as "type Ia," as the spectra do not permit us to further specify A or B aggregates. Therefore, relative concentrations (A or B) and total concentrations could not be determined. Diamonds that are termed "type IaA±B" have a sufficiently low concentration of nitrogen aggregates to allow us to evaluate specific aggregates and concentrations. A small percentage (3%) of diamonds colored by H defects were in this category, and most of these were type IaA>B.

GR1. Diamonds colored by GR1 varied greatly in nitrogen concentration from type IIa (no measurable nitrogen) up through a measurable total nitrogen concentration of several hundred ppm; none of those surveyed from the subset of 500 diamonds were saturated type Ia. About one-third (41 of 132) of the diamonds colored by GR1 were type IIa. Of these, 74% were blue (the remaining were green-blue or a few gray). Among the type IaA±B diamonds, most were green-blue (58%). Nitrogen concentrations were calculated for the IaA±B diamonds colored by GR1, and little correlation with bodycolor was noted; however, the highest total nitrogen concentrations were noted for the green-blue diamonds with Fancy Vivid to Fancy Deep color grades. Most of the diamonds were type IaAB with A<B, and most had a total nitrogen concentration ranging from 100 to 300 ppm.

Inclusions. The diamonds colored by inclusions spanned all nitrogen aggregation combinations (type IaA, IaAB, or IaB). In contrast, Fancy white diamonds are almost always type IaB.

Optical Absorption. Visible/near-infrared spectroscopy measures the color center absorptions that produce the color we see in a diamond. In the "Causes of Color" section, we discussed the primary visible absorption features responsible for color in these diamonds due to boron, GR1, and hydrogen-related defects.

The optical absorption spectra for diamonds colored by boron or inclusions generally have minimal usefulness (figures 4A and 4D). Type IIb diamonds show only a slope of decreasing absorption from the IR to UV regions, while diamonds colored by inclusions will typically just show cape-related features (e.g., N2 and N3), which do not explain the gray coloration. In these cases, the optical absorption spectra serve to eliminate other potential causes of color and to provide confirmation of separate gemological observations (e.g., IR absorption, PL spectra, and phosphorescence for type IIb diamonds, as well as microscopy for inclusion-related diamond color).

Hydrogen Defects. For H-rich diamonds, several peaks are commonly observed in addition to the major absorption bands discussed earlier. Most of the unmodified gray diamonds in this category (70%) showed N2/N3 peaks, even in those with pronounced bands at around 530 and 720 nm; however, N2/N3 peaks were seen in very few diamonds with a blue or violet color (figure 4B and figure 6). The 551 nm feature was seen in most diamonds with blue or violet coloration (94%), and in very few gray diamonds (13%). A few diamonds also showed a narrow peak at about 594 nm and weak peaks at 503, 615, 620, 631, and 671 nm.

GR1. Radiation damage in diamond produces a number of defect centers in optical spectra in addition to the primary GR1 color center. The most commonly observed defects occur at 595 and 667 nm. The 595 nm center is a defect of uncertain structure consisting of nitrogen atoms and vacancies and is no longer detected after annealing above 1000°C (figure 4C). The 667 nm center consists of a carbon interstitial (a term used for an atom within the crystal structure that is not positioned at a standard lattice position; Green, 2013; Breeding et al., 2018) that anneals out at 400–500°C (Zaitsev, 2003).

PHOTOLUMINESCENCE SPECTROSCOPY

Photoluminescence (PL) spectroscopy is one of the most sensitive and useful techniques for defect characterization in diamond. This method uses lasers of different wavelengths to produce emission spectra that reveal the defects present in a stone. Defects occurring at concentrations as low as the ppb level can easily be detected using this method (Eaton-Magaña and Breeding, 2016).

Boron. The PL spectra of type IIb diamonds have peaks that are generally not detected in diamonds without boron. These include features at 648.2 nm

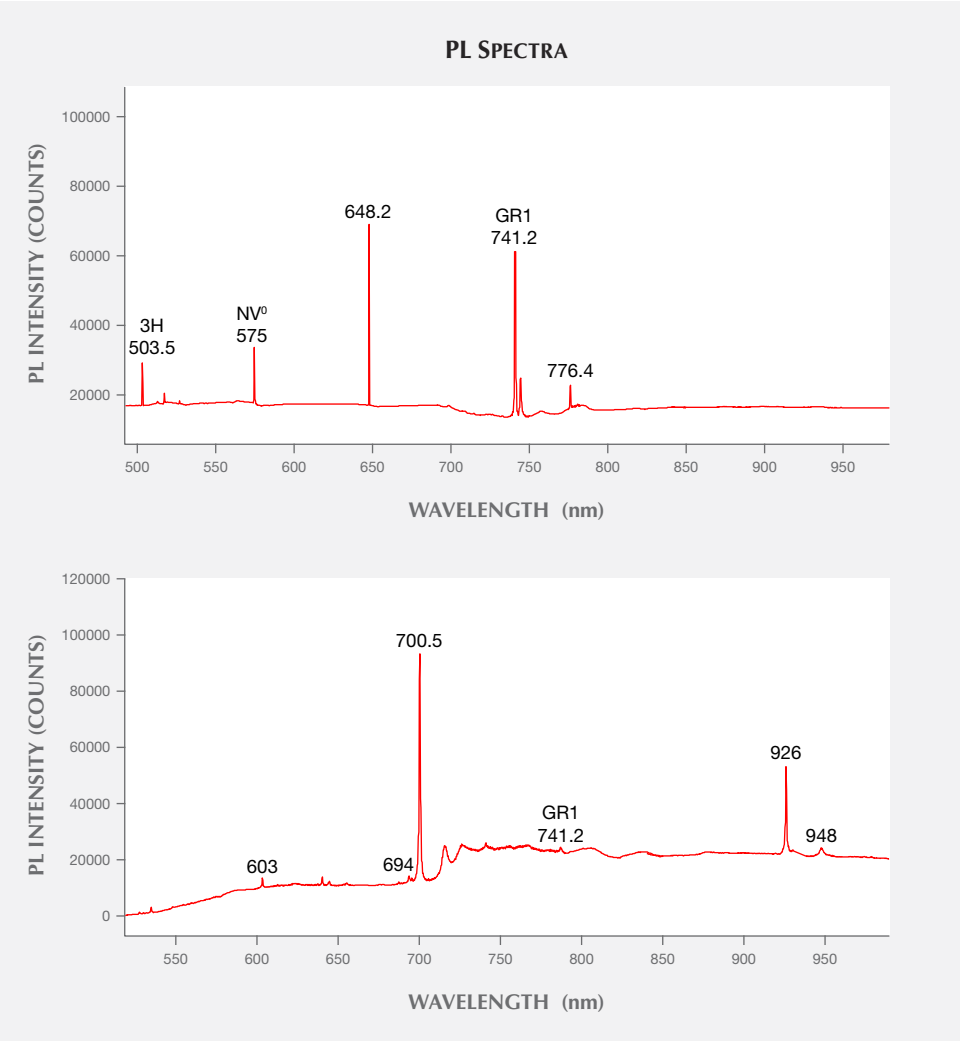

Figure 16. PL spectra from type IIb diamonds (top) and hydrogen-rich (bottom) blue/gray/violet diamonds aid in identification. Among type IIb diamonds (top), the 3H, 648.2 nm, GR1, and 776.4 nm peaks are common, while nitrogen-related peaks (such as NV^0) are less often observed. Among H-defect diamonds (bottom), nickel-related peaks dominate the PL spectra. Intrinsic diamond Raman lines have been removed for clarity.

(identified as boron-interstitial; Green, 2013) and 776.4 nm (tentatively assigned as a boron-vacancy complex; Eaton-Magaña and Ardon, 2016). Additionally, nearly all natural type IIb diamonds have the interstitial-related 3H peak (ZPL at 503.5 nm). Nitrogen-related defects are only rarely observed, and generally only as NV^0 at 575 nm (figure 16, top).

Hydrogen Defects. The PL spectra for diamonds colored by hydrogen defects generally show a high number of nickel-related peaks (figure 16, bottom) Iakoubovskii and Adriaenssens, 2002; Fritsch et al., 2007; van der Bogert et al., 2009). Similar Ni-related PL spectra are commonly seen in chameleon diamonds (Hainschwang et al., 2005) and mixed-habit diamonds (Lang et al., 2004; Yelisseyev and Kanda, 2007; Eaton-Magaña et al., 2017a). The nickel-related peaks occur at 523.4, 603, 694, 700, 926, and 948 nm; those with greatest intensity occur at 700 and 926 nm. Although these peaks are ascribed to nickel—and some, such as the 926 nm peak, are proposed as Ni-N defects (e.g., Hainschwang et al., 2005)—the specific composition, charge state, and interrelationships between the various detected peaks are currently unknown.

GR1. PL spectra collected from diamonds colored by GR1 can be quite variable due to irregular distributions of radiation damage across a stone's surface and interior. PL features related to radiation damage are also dramatically affected by heating, even to relatively low temperatures of a few hundred degrees (Eaton-Magaña and Moe, 2016). The strongest PL peaks in these green-blue to blue diamonds are vacancy-related defects such as GR1 (ZPL at 741.2 nm), interstitial-related peaks such as 3H (503.5 nm), and nitrogen-related defects such as H4 (495.9 nm), H3 (503.2 nm), NV^0 (575 nm), and NV^- (637 nm).

Inclusions. PL spectra of gray diamonds colored by inclusions can vary depending on whether or not the spectra were collected from an included region. Typically, most PL centers are found to have higher intensity in the gray, inclusion-rich sectors than in the colorless, inclusion-poor sectors (Eaton-Magaña et al., 2017a). These include nitrogen- and/or vacancy-related centers such as S3, H3, 612.4 nm, GR1, and H2, along with the nickel-related centers with peaks at 523.4, 603, 694, 700, 926, and 948 nm. Although these latter peaks are correlated with nickel, the specific compositions are currently unknown. In contrast, the NV^- (637 nm) center is stronger in colorless, inclusion-poor sectors.

IDENTIFICATION CONCERNS

Boron. Type IIb diamonds may be subjected to HPHT treatment to reduce the grayish component (comparable to HPHT treatment that reduces the brownish component in type IIa diamonds; Fisher et al., 2009). Blue HPHT synthetic diamonds are commonly produced at large sizes (Moe et al., 2016). However, there are very few difficulties separating natural-color blue diamonds from type IIb treated or synthetic diamonds, and they are reliably distinguished based on DiamondView imaging and/or PL spectroscopy.

GR1. Like their green counterparts, blue diamonds colored by GR1 receive a higher than standard incidence of "Undetermined" color origin reports from gemological laboratories. As with green diamonds colored by GR1, the presence of radiation stains is helpful in establishing a natural origin for irradiated blue diamonds.

Hydrogen Defects. There is no known method of treatment to mimic H-related defects in natural diamonds in this color range. The hydrogen-related peak at 3107 cm^{-1} in the IR region has been correlated with the optical absorption defects causing these colors. While the 3107 cm^{-1} peak can be increased with annealing or introduced in synthetic diamonds, those laboratory processes do not create the associated absorption of the hydrogen band at 835 nm in optical absorption spectroscopy or the other features seen in these blue/gray/violet diamonds.

Inclusions. There is no known method of treatment to mimic the micro-inclusions in natural diamonds in this color range. Heating of mixed-habit type IaAB diamonds containing micro-inclusions of graphite causes these inclusions to enlarge; the diamonds become darker gray and ultimately black. The graphite inclusions in such heated black diamonds often have a distinctive hexagonal morphology (Eaton-Magaña et al., 2017a). Low-quality CVD synthetic diamonds can have graphitic inclusions along with pinpoint inclusions resembling clouds; additionally, many have a gray color grade (Eaton-Magaña and Shigley, 2016). But CVD synthetics in this color range are always type IIa with distinctive DiamondView features and PL spectra.

In the last few years, GIA's laboratory has seen a much higher quantity of these diamonds. When we examined 500 of the blue/gray/violet diamonds in greater detail, 37 of them owed their color to inclusions. Of these, 31 were submitted between 2013 and 2016, with the remaining six submitted from 2008 to 2012.

UNUSUAL EXAMPLES

Less than 1% of the diamonds in the blue/gray/violet range attributed their color to a weak 480 nm band. All of these diamonds were gray. Typically, diamonds with a 480 nm band show chameleon behavior or a yellow-orange coloration. A majority of chameleon diamonds have gray as a color modifier (Breeding et al., 2018). These few gray diamonds are likely on the extremely low end of color saturation for chameleons, and they have insufficient visible absorption features to present any color besides gray. As with the gray diamonds colored by inclusions, these gray chameleon diamonds also tend toward warmer tones instead of the cooler, bluish tones of gray type IIb diamonds.

Generally, diamonds that show a 480 nm band in their optical absorption spectra have strong yellow fluorescence to both long- and short-wave UV radiation and weak yellow phosphorescence to short-wave UV. The gray diamonds with a 480 nm band studied here did as well. Very little is known about the defect causing this band.

OUTLOOK

In this article we have discussed the four major causes of blue/gray/violet color in gem diamonds. Based on the results obtained for the randomly selected subset of 500 diamonds from the 15,000+ diamonds in this color range, these four groups comprise over 99% of the natural-color blue diamonds seen at GIA's laboratories in the last decade. As with all natural diamonds, these gems act as messengers from deep within the earth. The type IIb diamonds in par-

ticular, which include several with large size and saturated hue, have captivated royalty and other gem connoisseurs for centuries.

Although many famous and historical blue diamonds were once found in India, today most type IIb diamonds are sourced from South Africa's Cullinan mine, and most hydrogen-defect diamonds come from the Argyle mine of Australia. As the Argyle mine is set to close within the next few years and the Cullinan mine is projected to close in 2030 (Petra Diamonds, n.d.), it will be interesting to monitor the future of these blue/gray/violet diamonds. These already rare diamonds may themselves become consigned to legend.

ABOUT THE AUTHORS

Dr. Eaton-Magaña and Dr. Breeding are senior research scientists, and Dr. Shigley is a distinguished research fellow, at GIA in Carlsbad, California.

ACKNOWLEDGMENTS

Discussions with John King (GIA, New York) contributed to some of the ideas presented here.

REFERENCES

Associated Press (2015) Rare blue diamond sells for record $48.5 million at auction. *NBC News*, Nov. 11, www.nbcnews.com/business/markets/rare-blue-diamond-sells-record-48-5-million-auction-n461836

Breeding C.M. (2011) Hydrogen-rich diamonds from Zimbabwe with natural radiation features. *G&G*, Vol. 47, No. 2, pp. 129–130.

Breeding C.M., Shigley J.E. (2009) The "type" classification system of diamonds and its importance in gemology. *G&G*, Vol. 45, No. 2, pp. 96–111, http://dx.doi.org/10.5741/GEMS.45.2.96

Breeding C.M., Shen A.H., Eaton-Magaña S., Rossman G.R., Shigley J.E., Gilbertson A. (2010) Developments in gemstone analysis techniques and instrumentation during the 2000s. *G&G*, Vol. 46, No. 3, pp. 241–257, http://dx.doi.org/10.5741/GEMS.46.3.241

Breeding C.M., Eaton-Magaña S.C., Shigley J.E. (2018) Natural-color green gem diamonds: A beautiful conundrum. *G&G*, Vol. 54, No. 1, pp. 2–27, http://dx.doi.org/10.5741/GEMS.53.4.2

Boyd S.R., Kiflawi I., Woods G.S. (1994) The relationship between infrared absorption and the A defect concentration in diamond. *Philosophical Magazine B*, Vol. 69, No. 6, pp. 1149–1153, http://dx.doi.org/10.1080/01418639408240185

——— (1995) Infrared absorption by the B nitrogen aggregation in diamond. *Philosophical Magazine B*, Vol. 72, No. 3, pp. 351–361, http://dx.doi.org/10.1080/13642819508239089

Christie's (2007) Magnificent jewels. Lot 291, an extremely rate colored diamond ring. Oct. 16, www.christies.com/lotfinder/jewelry/an-extremely-rare-colored-diamond-ring-4970551-details.aspx?from=salesummery&intObjectID=4970551&sid=d785b076-4194-478c-98a8-0a12ffb2c62e

—— (2008) Jewels: The Geneva sale (evening glamour). Lot 393: An extraordinary coloured diamond ring. May 14, www.christies.com/lotfinder/jewelry/an-extraordinary-coloured-diamond-ring-5076879-details.aspx?from=searchresults&intObjectID=5076879&sid=232203b1-3318-4885-be5c-24843bb45bf8

—— (2010) Jewels: The Hong Kong sale. Lot 2482: A superb coloured diamond and diamond ring. Jun. 1, www.christies.com/lotfinder/jewelry/a-superb-coloured-diamond-and-diamond-ring-5318702-details.aspx?from=salesummery&intObjectID=5318702&sid=dcc01d3f-2a50-410c-b01a-94f8884d8d38

—— (2011a) New York magnificent jewels. Lot 292: A colored diamond ring. Apr. 12, www.christies.com/lotfinder/jewelry/a-colored-diamond-ring-5423207-details.aspx?from=salesummery&intObjectID=5423207&sid=878e253d-e97c-407c-b649-b354e8ab70e7

—— (2011b) Geneva magnificent jewels. Lot 320: A coloured diamond ring. May 18, www.christies.com/lotfinder/jewelry/a-coloured-diamond-ring-5436555-details.aspx?from=searchresults&intObjectID=5436555&sid=bd06983d-7dfc-4ff7-88af-d65b4fa57e31

—— (2016) Magnificent jewels & the Cullinan Dream. Lot 261: A magnificent colored diamond ring. Jun. 9, www.christies.com/lotfinder/jewelry/a-magnificent-colored-diamond-ring-6006060-details.aspx?from=salesummary&intObjectID=6006060&sid=d2fd7428-240f-456b-baca-a3b1a5b50355

Collins A.T. (2001) The colour of diamond and how it may be changed. *Journal of Gemmology*, Vol. 18, No. 1, pp. 341–359, http://dx.doi.org/10.15506/JoG.2001.27.6.341

—— (2010) Determination of the boron concentration in diamond using optical spectroscopy. *Proceedings of the 61st Diamond Conference*, Warwick, UK.

Collins A.T., Williams A.W.S. (1971) The nature of the acceptor centre in semiconducting diamond. *Journal of Physics C: Solid State Physics*, Vol. 4, No. 13, pp. 1789–1800.

Collins A.T., Kanda H., Kitawaki H. (2000) Colour changes produced in natural brown diamonds by high-pressure, high-temperature treatment. *Diamond and Related Materials*, Vol. 9, No. 2, pp. 113–122.

Crowther P.A., Dean P.J., Sherman W.F. (1967) Excitation spectrum of aluminum acceptors in diamond under uniaxial stress, *Physical Review B*, Vol. 154, pp. 772–785.

Dean P.J. (1965) Bound excitons and donor-acceptor pairs in natural and synthetic diamond. *Physical Review*, Vol. 139, No. 2A, p. A588, http://dx.doi.org/10.1103/PhysRev.139.A588

De Marco A. (2014) Harry Winston names world's largest flawless vivid blue diamond, 'The Winston Blue.' *Forbes.com*, May 15, www.forbes.com/sites/anthonydemarco/2014/05/15/harry-winston-renames-worlds-largest-flawless-vivid-blue-diamond-the-winston-blue/#2aa122005715

——— (2016) No buyer for the Shirley Temple blue diamond. Forbes.com, Apr. 19, www.forbes.com/sites/anthonydemarco/2016/04/19/no-buyer-for-the-shirley-temple-blue-diamond/#6af18e942040

D'Haenens-Johansson U.F.S., Katrusha A., Moe K.S., Johnson P., Wang W. (2015) Large colorless HPHT-grown synthetic gem diamonds from New Diamond Technology. *G&G*, Vol. 51, No. 3, pp. 260–279, http://dx.doi.org/10.5741/GEMS.51.3.260

Eaton-Magaña S.C. (2016) Lab Notes: Treated pink type IIa diamond colored by red luminescence. *G&G*, Vol. 52, No. 3, pp. 299–301.

Eaton-Magaña S.C., Breeding C.M. (2016) An introduction to photoluminescence spectroscopy for diamond and its applications in gemology. *G&G*, Vol. 52, No. 1, pp. 2–17, http://dx.doi.org/10.5741/GEMS.52.1.2

Eaton-Magaña S.C., Lu R. (2011) Phosphorescence in type IIb diamonds. *Diamond and Related Materials*, Vol. 20, No. 7, pp. 983–989, http://dx.doi.org/10.1016/j.diamond.2011.05.007

Eaton-Magaña S.C., Moe K.S. (2016) Temperature effects on radiation stains in natural diamonds. *Diamond and Related Materials*, Vol. 64, pp. 130–142, http://dx.doi.org/10.1016/j.diamond.2016.02.009

Eaton-Magaña S.C., Shigley J.E. (2016) Observations on CVD-grown synthetic diamonds: A review. *G&G*, Vol. 52, No. 3, pp. 222–245, http://dx.doi.org/10.5741/GEMS.52.3.222

Eaton-Magaña S., Post J.E., Heaney P.J., Freitas J., Klein P., Walters P., Butler J.E. (2008) Using phosphorescence as a fingerprint for the Hope and other blue diamonds. *Geology*, Vol. 36, No. 1, pp. 83–86, http://dx.doi.org/10.1130/G24170A.1

Eaton-Magaña S.C., Ardon T., Zaitsev A. (2017a) Inclusion and point defect characteristics of Marange graphite-bearing diamonds after high temperature annealing. *Diamond and Related Materials*, Vol. 71, pp. 20–29, http://dx.doi.org/10.1016/j.diamond.2016.11.011

Eaton-Magaña S.C., Shigley J.E., Breeding C.M. (2017b) Observations on HPHT-grown synthetic diamonds: A review. *G&G*, Vol. 53, No. 3, pp. 262–284, http://dx.doi.org/10.5741/GEMS.53.3.262

Fisher D., Sibley S.J., Kelly C.J. (2009) Brown colour in natural diamond and interaction between the brown related and other colour-inducing defects. *Journal of Physics: Condensed Matter*, Vol. 21, No. 36, Article 364213, 10 pp., http://dx.doi.org/10.1088/0953-8984/21/36/364213

Frank R. (2016) 'Oppenheimer Blue' diamond sells at auction for $57.5 million. *NBC News*, May 19, www.nbcnews.com/business/business-news/oppenheimer-blue-diamond-sells-auction-57-5-million-n576781

Fritsch E., Scarratt K. (1992) Natural-color nonconductive gray-to-blue diamonds. *G&G*, Vol. 28, No. 1, pp. 35–42, http://dx.doi.org/10.5741/GEMS.28.1.35

Fritsch E., Shigley J.E., Moses T., Rossman G.R., Zucker B., Balfour I. (1995) Examination of the twenty-two carat green chameleon diamond. In D. J. Content, Ed., *A Green Diamond: A Study of Chameleonism*. W. S. Maney & Son, Leeds, England, 42 pp.

Fritsch E., Massi L., Rossman G.R., Hainschwang T., Jobic S., Dessapt R. (2007) Thermochromic and photochromic behavior of "chameleon" diamonds. *Diamond and Related Materials*, Vol. 16, No. 2, pp. 401–408, http://dx.doi.org/10.1016/j.diamond.2006.08.014

Fritsch E., Hainschwang T., Massi L., Rondeau B. (2007) Hydrogen-related optical centers in natural diamond: An update. *New Diamond and Frontier Carbon Technology*, Vol. 17, No. 2, pp. 63–89.

Gaillou E., Wang W., Post J.E., King J.M., Butler J.E., Collins A.T., Moses T.M. (2010) The Wittelsbach-Graff and Hope diamonds: Not cut from the same rough. *G&G*, Vol. 46, No. 2, pp. 80–88, http://dx.doi.org/10.5741/GEMS.46.2.80

Gaillou E., Post J.E., Rost D., Butler J.E. (2012) Boron in natural type IIb blue diamonds: Chemical and spectroscopic measurements. *American Mineralogist*, Vol. 97, No. 1, pp. 1–18, http://dx.doi.org/10.2138/am.2012.3925

Gaillou E., Post J.E., Byrne K.S., Butler J.E. (2014) Study of the Blue Moon diamond. *G&G*, Vol. 50, No. 4, pp. 280–286, http://dx.doi.org/10.5741/GEMS.50.4.280

Goss J.P., Briddon P.R., Hill V., Jones R., Rayson M.J. (2014) Identification of the structure of the 3107 cm^{-1} H-related defect in diamond. *Journal of Physics: Condensed Matter*, Vol. 26, No. 14, pp. 1–6, http://dx.doi.org/10.1088/0953-8984/26/14/145801

Green B.L. (2013) Thesis: Optical and magnetic resonance studies of point defects in single crystal diamond, University of Warwick.

Gu T., Wang W. (2017) IaB diamond and its geological implications. 11th International Kimberlite Conference, Extended Abstract No. 11IKC-4494.

Hainschwang T., Simic D., Fritsch E., Deljanin B., Woodring S., DelRe N. (2005) A gemological study of a collection of chameleon diamonds. *G&G*, Vol. 41, No. 1, pp. 20–35, http://dx.doi.org/10.5741/GEMS.41.1.20

Iakoubovskii K., Adriaenssens G.J. (2002) Optical characterization of natural Argyle diamonds. *Diamond and Related Materials*, Vol. 11, No. 1, pp. 125–131, http://dx.doi.org/10.1016/S0925-9635(01)00533-7

King J.M. (2006) *GIA Colored Diamonds Color Reference Charts*. Gemological Institute of America, Carlsbad, California.

——— (2008) Color grading "D-to-Z" diamonds at the GIA Laboratory. *G&G*, Vol. 44, No. 4, pp. 296–321, http://dx.doi.org/10.5741/GEMS.44.4.296

King J.M., Moses T.M., Shigley J.E., Liu Y. (1994) Color grading of colored diamonds in the GIA Gem Trade Laboratory. *G&G*, Vol. 30, No. 4, pp. 220–242, http://dx.doi.org/10.5741/GEMS.30.4.220

King J.M., Moses T.M., Shigley J.E., Welbourn C.M., Lawson S.C., Cooper M. (1998) Characterizing natural-color type IIb blue diamonds. *G&G*, Vol. 34, No. 4, pp. 246–268, http://dx.doi.org/10.5741/GEMS.34.4.246

King J.M., Shigley J.E., Jannucci C. (2014) Exceptional pink to red diamonds: A celebration of the 30th Argyle diamond tender. *G&G*, Vol. 50, No. 4, pp. 268–279, http://dx.doi.org/10.5741/GEMS.50.4.268

Lang A.R., Yelisseyev A.P., Pokhilenko N.P., Steeds J.W., Wotherspoon A. (2004) Is dispersed nickel in natural diamonds associated with cuboid growth sectors in diamonds, that exhibit a history of mixed-habit growth? *Journal of Crystal Growth*, Vol. 263, pp. 575–589, http://dx.doi.org/10.1016/j.jcrysgro.2003.11.116

Liu Y., Shigley J.E., Moses T., Reinitz I. (1998) The alexandrite effect of the Tavernier diamond caused by fluorescence. *Color Research and Application*, Vol. 23, No. 5, pp. 323–327.

Luo Y., Breeding C.M. (2013) Fluorescence produced by optical defects in diamond. *G&G*, Vol. 49, No. 2, pp. 82–97, http://dx.doi.org/10.5741/GEMS.49.2.82

Moe K.S., Johnson P., D'Haenens-Johansson U., Wang W. (2016) Lab Notes: Largest blue HPHT synthetic diamond. *G&G*, Vol. 52, No. 1, pp. 74–75.

Moses T., Reinitz I. (2000) Lab Notes: Fancy white diamonds. *G&G*, Vol. 36, No. 2, p. 156.

Nasdala L., Grambole D., Wildner M., Gigler A.M., Hainschwang T., Zaitsev A.M., Harris J.W., Milledge J., Schulze D., Hofmeister W., Balmer W.A. (2013) Radio-colouration of diamond: A spectroscopic study. *Contributions to Mineralogy and Petrol-*

ogy, Vol. 165, No. 5, pp. 843–861, http://dx.doi.org/10.1007/s00410-012-0838-1
Ogden J. (2016) The tale of the Mouawad-Tereschenko blue diamond. *Gems & Jewellery*, Vol. 25, No. 2, pp. 32–33, gem-a.com/component/k2/from/mouawad-tereschenko-diamond-second-largest-blue-diamond
Petra Diamonds (n.d.) Cullinan. www.petradiamonds.com/our-operations/our-mines/cullinan/
——— (2017) Important blue diamonds of the world. www.petradiamonds.com/wp-content/uploads/Important-Blue-Diamonds-July-2017.pdf
Reuters (2018) Farnese blue diamond, with 300-year royal history, fetches $6.7 mln. May 15, www.reuters.com/article/us-auction-diamond-farnese/farnese-blue-diamond-with-300-year-royal-history-fetches-6-7-mln-idUSKCN1IG35B
Rio Tinto (2017) Rio Tinto reveals its largest red diamond at world exclusive preview in New York, Jul. 27, http://www.riotinto.com/media/media-releases-237_22892.aspx
Rondeau B., Fritsch E., Guiraud M., Chalain J-P., Notari F. (2004) Three historical "asteriated" hydrogen-rich diamonds: Growth history and sector-dependent impurity incorporation. *Diamond and Related Materials*, Vol. 13, No. 9, pp. 1658–1673, http://dx.doi.org/10.1016/j.diamond.2004.02.002
Segarra L.M. (2017) These diamond earrings just sold for a record-breaking $57 million at auction. Fortune.com, May 16, http://fortune.com/2017/05/16/apollo-blue-artemis-pink-diamond-earrings/
Shor R. (2005) A review of the political and economic forces shaping today's diamond industry. *G&G*, Vol. 41, No. 3, pp. 202–233, http://dx.doi.org/10.5741/GEMS.41.3.202
——— (2007) Gem News International: Colored diamonds break $1 million per carat with record auction prices. *G&G*, Vol. 43, No. 4, pp. 366–367.
——— (2013) Auction houses: A powerful market influence on major diamonds and colored gemstones. *G&G*, Vol. 49, No. 1, pp. 2–15, http://dx.doi.org/10.5741/GEMS.49.1.2
Smit K.V., Shirey S.B., Stern R.A., Steele A., Wang W. (2016) Diamond growth from C–H–N–O recycled fluids in the lithosphere: Evidence from CH_4 micro-inclusions and $\delta^{13}C$–$\delta^{15}N$–N content in Marange mixed-habit diamonds. *Lithos*, Vol. 265, pp. 68–81, http://dx.doi.org/10.1016/j.lithos.2016.03.015
Smith E.M., Shirey S.B., Richardson S.H., Nestola F., Bullock E.S., Wang J., Wang W. (2018) Blue boron-bearing diamonds from Earth's lower mantle. *Nature*, in press. http://dx.doi.org/10.1038/s41586-018-0334-5
Sotheby's (2012) Magnificent jewels 555. Magnificent and exceptionally rare fancy deep blue diamond. Nov. 14, http://www.sothebys.com/en/auctions/ecatalogue/2012/magnificent-jewels-ge1205/lot.555.html
——— (2015) http://www.sothebys.com/en/news-video/blogs/all-blogs/all-that-glitters/2015/11/record-setting-blue-diamond.html
——— (2016a) Magnificent jewels and noble jewels 298A. Magnificent fancy deep blue diamond ring. Nov. 16-17, www.sothebys.com/en/auctions/ecatalogue/2016/magnificent-jewels-and-noble-jewels-ge1605/lot.298A.html
——— (2016b) Magnificent jewels and noble jewels 337. The Sky Blue diamond superb fancy vivid blue diamond ring, Cartier. Nov. 16–17, http://www.sothebys.com/en/auctions/ecatalogue/2016/magnificent-jewels-and-noble-jewels-ge1605/lot.337.html
——— (2017a) Magnificent jewels and noble jewels, session 3, 363A. Important fancy vivid blue diamond ring. May 16, http://www.sothebys.com/en/auctions/ecatalogue/2017/magnificent-jewels-and-noble-jewels-eve-ge1709/lot.363A.html
——— (2017b) Magnificent jewels 211. Exquisite fancy vivid blue diamond and diamond ring. Dec. 5, www.sothebys.com/en/auctions/ecatalogue/2017/magnificent-jewels-n09694/lot.211.html
——— (2018a) The rarest of the rare: Multimillion-dollar blue diamonds. Mar.23, www.sothebys.com/en/news-video/blogs/all-blogs/all-that-glitters/2018/03/impessive-blue-diamonds-sold-at-auction.html
——— (2018b) Magnificent jewels 138. A rare fancy intense blue diamond ring. Apr. 18, www.sothebys.com/en/auctions/ecatalogue/2018/magnificent-jewels-n09846/lot.138.html
Van der Bogert C.H., Smith C.P., Hainschwang T., McClure S.F. (2009) Gray-to-blue-violet hydrogen-rich diamonds from the Argyle mine, Australia. *G&G*, Vol. 45, No. 1, pp. 20–37, http://dx.doi.org/10.5741/GEMS.45.1.20
Welbourn C.M., Cooper M., Spear P.M. (1996) De Beers natural versus synthetic diamond verification instruments. *G&G*, Vol. 32, No. 3, pp. 156–169, http://dx.doi.org/10.5741/GEMS.32.3.156
Yelisseyev A., Kanda H. (2007) Optical centers related to 3d transition metals in diamond. *New Diamond and Frontier Carbon Technology*. Vol. 17, pp. 127–178.
Zaitsev A.M. (2003) *Optical Properties of Diamond: A Data Handbook*. Springer.

For online access to all issues of GEMS & GEMOLOGY from 1934 to the present, visit:

gia.edu/gems-gemology

Black Diamonds from Marange (Zimbabwe): A Result of Natural Irradiation and Graphite Inclusions

Karen V. Smit, Elina Myagkaya, Stephanie Persaud, and Wuyi Wang

This study investigates the color origin of 40 natural Fancy Dark brown-black round brilliant diamonds from the Marange alluvial deposits in eastern Zimbabwe. Visual observations show that the dark appearance of the Marange diamonds is due to a combination of graphite micro-inclusions (associated with methane), graphite needles, and dark brown radiation stains that occur along internal fractures. The GR1 (V^0) defect, typically formed during natural and artificial irradiation, is observed in the optical spectra of 43% of the diamonds, although its intensity is too low to significantly impact the bodycolor. Natural irradiation in these diamonds is likely related to their billion-year residence in the Umkondo conglomerate, which is known to contain radioactive minerals such as zircon. Aside from radiation staining, irradiation-damaged diamond appears non-luminescent in DiamondView images and shows a weaker, broader diamond peak (at 1332 cm^{-1}) in Raman spectroscopy. Brown coloration of the radiation stains is due to heating of the diamonds during later regional metamorphism, which also facilitated the formation of the H3 (NVN^0) and NiN complexes.

Diamonds with Fancy black color grades can have either natural or treated color origin. *Natural* black diamonds are usually colored by inclusions of sulfides, graphite, magnetite, hematite, or iron-bearing inclusions (e.g., Titkov et al., 2003). A rare natural diamond (of undisclosed geographic origin) colored by abundant brown radiation stains has previously been examined by GIA's Carlsbad laboratory (Ardon, 2013). *Treated* black diamonds are often those that are heavily fractured naturally and then treated at low-pressure and high-temperature (LPHT) conditions to graphitize the fractures and turn them black (Hall and Moses, 2001; Notari, 2002). Artificial irradiation can also produce dark colors that appear black (Collins, 1982; Kitawaki, 2007).

The Marange locality in eastern Zimbabwe is well known for producing diamonds that contain both octahedral and cuboid sectors (mixed-habit diamonds) where the cuboid sectors are visible to the eye due to abundant micro-inclusions of graphite (Rakovan et al., 2014; Smit et al., 2016). These micro-inclusions, informally known in the gem trade as "clouds," give the diamonds a brown-gray appearance that lowers their value. Heat treatment of these lower-quality graphite-containing Marange diamonds has the potential to introduce gem-quality treated black diamonds into the market. In natural diamonds, these graphite micro-inclusions are around 1 µm in diameter; during heating above 1200°C, they become larger. After annealing at 1700°C, the grain size increases to 11–16 µm, causing the cuboid sectors to appear opaque black (Eaton-Magaña et al., 2017). The challenge for gem laboratories is to confidently distinguish these treated black diamonds from naturally occurring black diamonds.

Here our goal was to document a suite of untreated Marange diamonds, all with Fancy Dark brown to Fancy black GIA color grades, so that their characteristics could be distinguished from any suspected treated black diamonds. When viewing the samples, however, it became clear that the appearance of the these dark Marange diamonds was due not only to graphite clouds but also to abundant graphite needles and dark brown radiation stains occurring within surface-reaching fractures.

See end of article for About the Authors and Acknowledgments.
Gems & Gemology, Vol. 54, No. 2, pp. 132–148,
http://dx.doi.org/10.5741/GEMS.54.2.132
© 2018 Gemological Institute of America

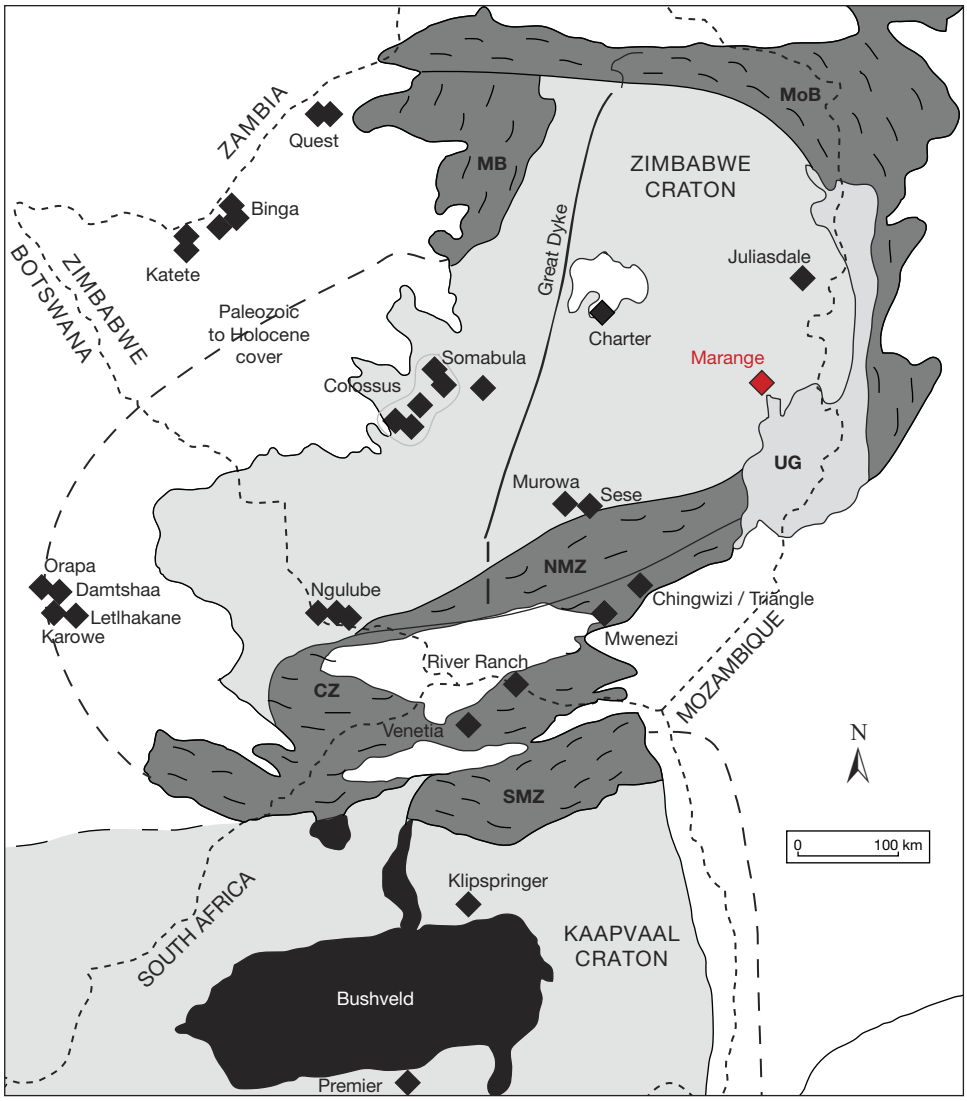

Figure 1. Geological map of Zimbabwe, northern South Africa, and eastern Botswana that shows the Kaapvaal and Zimbabwe cratons and their bounding mobile belts. Image taken from Smit et al. (2016), which is adapted from Hanson et al. (2011) and McCourt et al. (2004). Kimberlite localities (indicated here as diamonds) from Moore et al. (2009) and Google Maps. Marange alluvial diamonds occur in eastern Zimbabwe in sediments that were reworked from the basal conglomerate of the ~1.1 Ga Umkondo Group (UG; Hanson et al., 2004; Moore et al., 2009, and references therein). The 2.7–2.6 Ga Limpopo Belt is divided into the CZ (Central Zone), NMZ (Northern Marginal Zone), and SMZ (Southern Marginal Zone). MB is the 2.1–1.8 Ga Magondi Belt (Stowe, 1989; Jacobs et al., 2008), and MoB is the 0.55 Ga Mozambique Belt.

MARANGE ALLUVIAL DIAMOND LOCALITY

Primary diamond deposits are always found in association with extremely old portions of the earth's crust known as cratons (e.g., Clifford, 1966). The combined Kaapvaal and Zimbabwe cratons in Botswana, South Africa, and Zimbabwe host many of the world's famous diamond mines. For example, the Kimberley mines on the southwestern Kaapvaal craton are famous as the type locality for kimberlite, the primary source rock for diamonds. Also, the Karowe mine in central Botswana is an exciting new source for super-large colorless diamonds near the western margin of the Zimbabwe craton (www.lucaradiamond.com).

The Marange alluvial diamonds occur on the Zimbabwe craton near the Zimbabwe-Mozambique border. The Zimbabwe craton comprises 3.6 to 3.5 Ga basement granite-greenstone terranes (Wilson, 1990, and references therein), although an older Paleoarchean heritage is suggested by ~3.9 Ga detrital zircons (Dodson et al., 1988; Zeh et al., 2014) and 3.97 to 3.75 Ga chromites from ultramafic intrusions (Nägler et al., 1997). The Zimbabwe craton amalgamated with the Kaapvaal craton to the south, through successive terrane accretions that included the Central Zone of the Limpopo Mobile Belt between 2.70 and 2.61 Ga (figure 1; Zeh et al., 2009, 2013).

The Marange diamonds were discovered by De Beers in 2001 in >1.1 Ga Umkondo Group conglomerates near the eastern edge of the Zimbabwe craton (figure 1; Hanson et al., 2004; Moore et al., 2009). These conglomerates were deposited into the Umkondo Foreland Basin, through fluvial erosion of diamondiferous kimberlites in the more westerly

Figure 2. Rough Marange diamonds previously examined at GIA. These are not the same rough from which the black diamonds in this study were cut, but are shown as examples of typical rough Marange diamond morphologies. These diamonds are generally large (5–7 ct each), with resorbed morphologies and non-transparent coatings. Rather than arising from fibrous growth, these coatings are thought to be the result of radiation damage combined with metamorphic heating (Moore et al., 2009, and references therein). Photos by Wuyi Wang.

parts of the Zimbabwe craton, and have been locally weathered to much softer Quaternary sediments (Moore et al., 2009). The primary source kimberlites for the Marange diamonds have not been found and, due to a lack of studies focusing on mineral inclusions from these diamonds, their age and source paragenesis (eclogitic vs. peridotitic) is unknown.

Diamonds from Marange first entered the market in 2006, and early artisanal mining focused on the softer Quaternary sediments. Mining has since been mechanized, and several mining companies have operated in the Marange fields—including Anjin Investments, Diamond Mining Company, Gye Nyame Resources, Jinan Mining, Kusena Diamonds, Marange Resources, and Mbada Diamonds. In 2016, many of these operations were acquired by the government-controlled Zimbabwe Consolidated Diamond Company (ZCDC).

Marange diamonds are typically large (5–7 ct apiece; figure 2) and abundant (with grades ranging between 1 and >30 carats per ton), which means they were discovered *in situ* in the conglomerate during exploration field work (M. de Wit, pers. comm., 2016). A unique characteristic of Marange diamonds is their thin, non-transparent coating (figure 2). Rather than arising from fibrous growth, this coating is thought to be the result of radiation damage combined with metamorphic heating (Moore et al., 2009, and references therein).

METHODS

Optical Absorption Spectroscopy. Optical absorption spectra were collected using an Ocean Optics HR4000 spectrometer equipped with a charge-coupled device (CCD) array, a 10 μm entrance slit, and 300 lines/mm grating. The resulting spectral resolution is 1.4 nm. Spectra were collected between 380 and 980 nm while the diamonds were cooled to liquid nitrogen temperatures (77 K). Integration time for each spectrum was 0.5 seconds with 30 accumulations.

Fourier-Transform Infrared (FTIR) Spectroscopy. FTIR absorption spectra were collected over the 400–6000 cm^{-1} range using a Thermo Nicolet Nexus 6700 spectrometer furnished with KBr and quartz beam splitters and a diffuse-reflectance infrared Fourier-transform (DRIFT) accessory. Spectra were collected with a resolution of 1 cm^{-1} and over 32 scans. During analyses, the instrument and sample chambers were

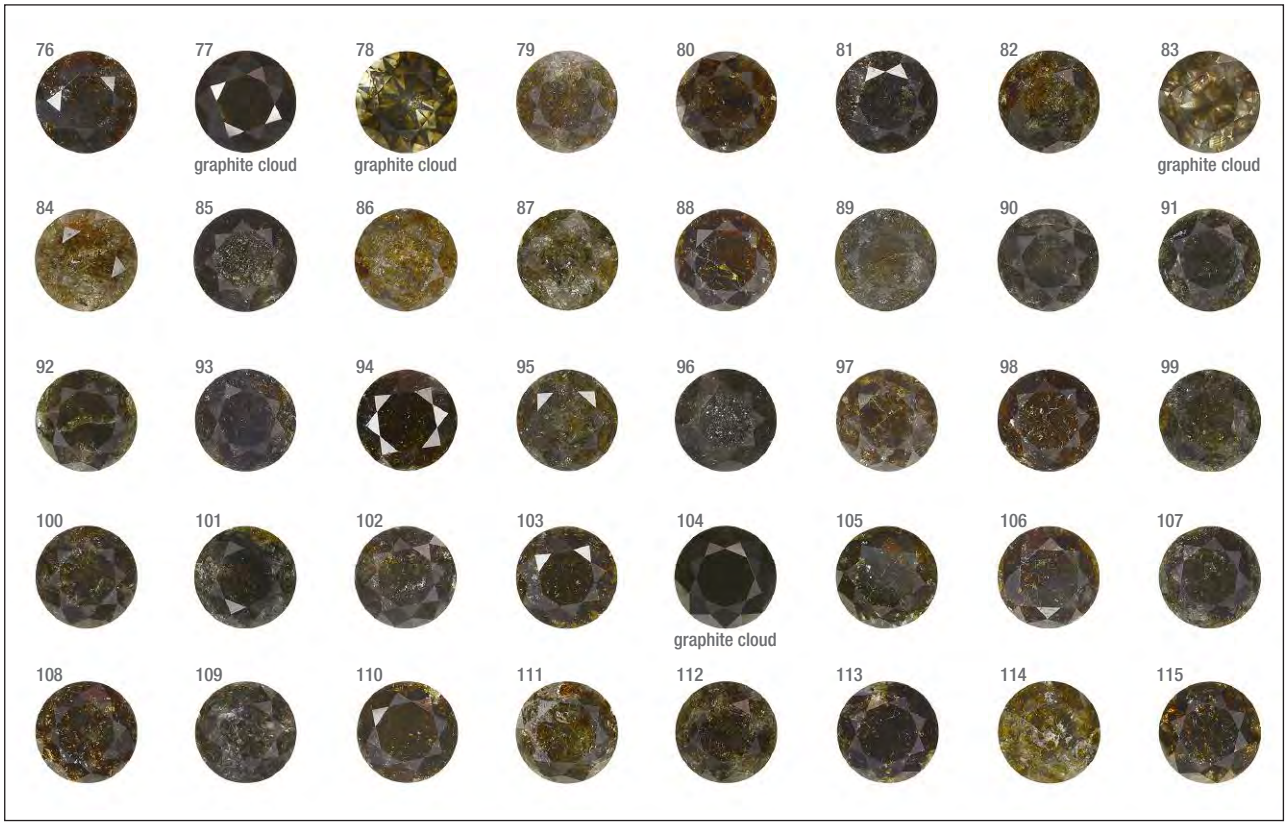

Figure 3. Table-up images of the 40 natural Fancy Dark brown to Fancy black Marange diamonds from this study. The diamonds range between 0.39 and 3.11 ct, and between 4.47 and 8.75 mm in diameter (see table 1). All the diamonds have a dark appearance due to graphite needles and abundant radiation stains, except for four with dark clouds comprised of micron-sized inclusions of graphite. Photos by Jian Xin (Jae) Liao.

continuously purged with dry air to minimize atmospheric contamination.

DiamondView Imaging. Images of the internal growth zoning were obtained using an International Institute of Diamond Grading and Research (IIDGR) DiamondView instrument, which uses broadband ultraviolet radiation (filtered for $\lambda < 230$ nm) to induce luminescence in diamond (Welbourn et al., 1996). Integration time, aperture size, and gain settings were all adjusted between samples to obtain optimal brightness and contrast for each image.

Photoluminescence (PL) Spectroscopy. Photoluminescence spectra were collected using a Renishaw InVia Raman confocal microspectrometer equipped with a CCD detector. PL spectra were taken using three different laser excitation wavelengths: 488 nm (Ar-ion laser), 632.8 nm (He-Ne laser), and 830 nm (diode laser). All diamonds were cooled to 77 K by direct immersion in liquid nitrogen to improve the intensity and sharpness of any observed peaks. Spectra were recorded over the ranges of 490 to 650 nm (488 nm excitation), 635 to 850 nm (632.8 nm excitation), and 837 to 1000 nm (830 nm excitation). Integration times for all spectra were 10 seconds, with 1 accumulation. Spectra were collected on a RenCam air-cooled CCD detector after passing through a spectrometer using an 1800 lines/mm grating (488 and 633 nm excitation) and a 1200 lines/mm grating (830 nm excitation).

RESULTS

Sample Characteristics. This study is based on 40 natural round brilliant diamonds from the Marange mining operations in Zimbabwe (figure 3). The diamonds all received Fancy Dark brown to Fancy black color grades from GIA, and they ranged between 0.39 and 3.11 ct (table 1). These samples were obtained from the trade and had undergone no heat or irradiation treatments. The overwhelming majority (36 out of 40 samples) were heavily fractured and contained numerous dark graphitic needle-like inclusions. These diamonds had various degrees of brown radiation stains that were localized along the surface-

TABLE 1. Physical and spectroscopic characteristics of the 40 natural brown-black Marange diamonds analyzed in this study.

Sample no.	Dimensions (mm)	Weight (carat)	GIA color grade	3050 cm^{-1} CH_4 peak in FTIR	GR1 in optical absorption	GR1 in 633 nm PL	H3 in 488 nm PL	H2 in 830 nm PL	700.5 Ni peak in 633 nm PL	926 nm Ni peak in 830 nm PL
76	4.47–4.49 × 3.03	0.39	Fancy black	×					×	×
77	5.99–6.00 × 3.69	0.83	Fancy black	×					×	×
78	5.96–5.97 × 3.71	0.85	Fancy Dark brown	×			×	×	×	×
79	6.15–6.17 × 4.03	0.99	Fancy black			×	×		×	×
80	6.06–6.08 × 4.17	1.00	Fancy black				×	×		×
81	6.18–6.20 × 4.02	1.00	Fancy black			×	×		×	×
82	6.24–6.27 × 4.01	1.00	Fancy black	×		×	×		×	×
83	6.13–6.16 × 4.12	1.01	Fancy Dark brown	×			×		×	×
84	6.31–6.36 × 4.17	1.09	Fancy Dark brown		×	×	×	×	×	×
85	6.10–6.13 × 4.06	1.03	Fancy black				×		×	×
86	6.14–6.17 × 4.14	1.03	Fancy Dark brown		×	×	×	×	×	×
87	6.23–6.26 × 4.11	1.03	Fancy Dark gray	×			×	×	×	×
88	6.06–6.10 × 4.19	1.05	Fancy black		×	×	×			×
89	6.46–6.50 × 4.06	1.06	Fancy black	×			×		×	×
90	6.32–6.34 × 4.16	1.06	Fancy black	×			×		×	×
91	6.34–6.37 × 4.04	1.06	Fancy black	×					×	×
92	6.32–6.34 × 4.08	1.07	Fancy black						×	×
93	6.55–6.58 × 4.07	1.10	Fancy black				×		×	×
94	6.53–6.54 × 3.98	1.09	Fancy black		×	×	×			×
95	6.35–6.42 × 4.08	1.09	Fancy black	×			×		×	×
96	6.32–6.33 × 4.25	1.10	Fancy black	×			×		×	×
97	6.43–6.46 × 4.07	1.12	Fancy black			×	×	×	×	×
98	6.41–6.45 × 4.10	1.11	Fancy black		×	×	×	×		×
99	6.25–6.26 × 4.29	1.12	Fancy black	×	×	×	×		×	×
100	6.33–6.36 × 4.28	1.12	Fancy black	×	×	×	×		×	×
101	6.41–6.42 × 4.27	1.14	Fancy black				×		×	×
102	6.35–6.41 × 4.26	1.14	Fancy black	×			×		×	×
103	6.58–6.60 × 4.28	1.18	Fancy black		×	×	×			×
104	6.51–6.55 × 4.29	1.19	Fancy black	×					×	×
105	6.62–6.64 × 4.40	1.27	Fancy black		×	×	×		×	×
106	6.58–6.62 × 4.27	1.26	Fancy black		×	×	×		×	×
107	6.46–6.49 × 4.50	1.27	Fancy black	×			×		×	×
108	6.67–6.68 × 4.55	1.34	Fancy black		×		×		×	×
109	6.72–6.73 × 4.53	1.35	Fancy black				×		×	×
110	7.16–7.21 × 4.26	1.44	Fancy black		×	×	×		×	×
111	7.02–7.03 × 4.57	1.50	Fancy black	×	×	×	×		×	×
112	7.00–7.04 × 4.70	1.52	Fancy black		×	×	×		×	×
113	7.45–7.48 × 4.62	1.71	Fancy black		×	×	×			×
114	8.20–8.26 × 5.21	2.24	Fancy black		×	×	×		×	×
115	8.71–8.75 × 6.07	3.11	Fancy black		×	×	×	×		×
			Number		17	20	35	8	33	40
			Percentage		42.5	50	87.5	20	82.5	100

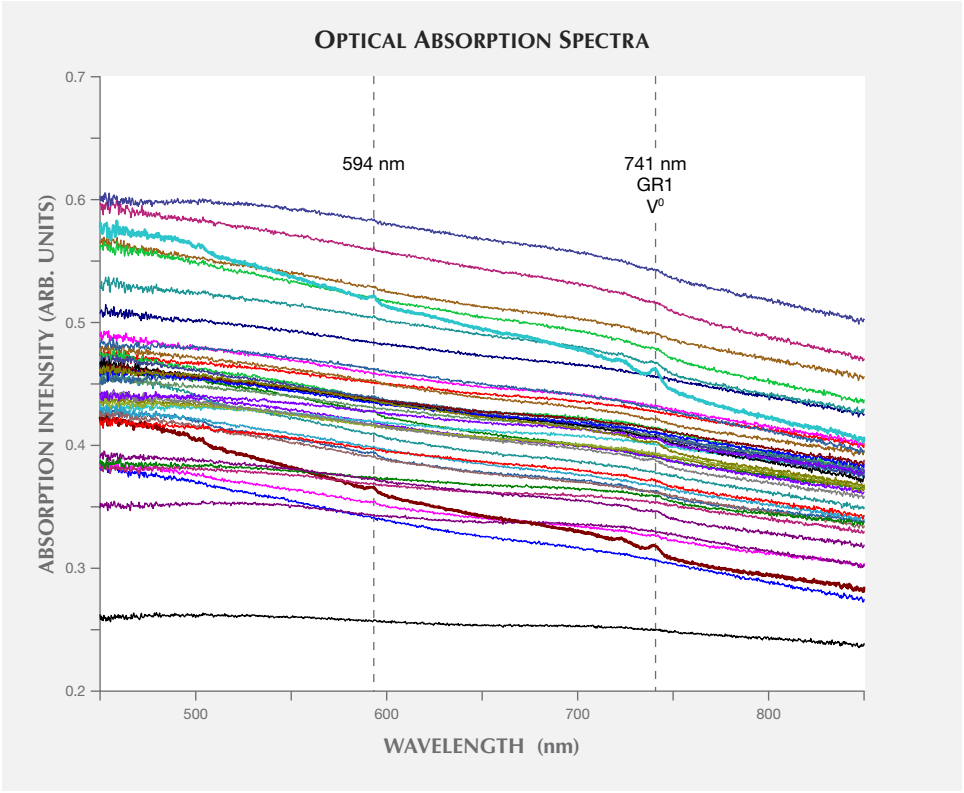

Figure 4. Optical absorption spectra (77 K) of all the samples in the suite. Weak GR1 (V^0 at 741 nm) was observed in 43% of the samples. Two samples with the highest-intensity GR1 are 84 (maroon spectrum) and 114 (teal spectrum). GR1 was accompanied by the 594 nm peak associated with annealing after irradiation (Collins et al., 1986). All samples have an absorption continuum with an increasing slope toward the ultraviolet. This may be intrinsic in part and due to vacancy clusters, but analytical artifacts cannot be ruled out (see text for further details).

reaching fractures. The original bodycolor of the diamonds was obscured by the presence of fractures, dark inclusions, and radiation stains. Four samples (77, 78, 83, and 104; see figure 3) were not heavily fractured and instead contained clouds of dark pinpoint (or micro-) inclusions.

Origin of Dark Appearance and Color. Any defects that are present in the visible spectrum (390 to 700 nm) and in sufficient concentration to be detected by optical absorption spectroscopy can influence the bodycolor of a diamond.

The optical absorption spectra for all the samples had a slight absorption continuum with an increasing slope toward the ultraviolet (figure 4). Brown diamonds typically have such an absorption slope, which is attributed to vacancy clusters formed along deformation lamellae (Fisher et al., 2009). However, the spectra for this study were obtained on faceted diamonds, and the instrument's integrating sphere made accurate baseline subtraction a challenge. This means that while we cannot discount that there may be an intrinsic absorption continuum in some samples, any observed slope may also be an analytical artifact.

Very weak GR1 (741 nm) was visible in 17 out of the 40 diamonds (43%) (figure 4). The two diamonds with the highest-intensity GR1 in optical absorption were samples 84 and 114 (maroon and teal in figure 4). GR1 is the neutral vacancy defect (V^0), produced during both natural and artificial irradiation (Clark et al., 1956). Where GR1 is present in the optical absorption spectra, the 594 nm peak is also seen (figure 4), indicating that natural annealing and associated vacancy migration occurred (Collins et al., 1986). These features are most likely related to the brown radiation stains visible on the surface of the diamonds. Typically, these stains do not penetrate deep into the diamond (<30 µm; see Crookes, 1904; Wagner, 1914; Lind and Barwell, 1923). With optical absorption spec-

In Brief

- The Marange alluvial deposits in Zimbabwe produce many naturally irradiated diamonds.
- The abundance of brown radiation stains combined with the intense fracturing impart a dark bodycolor to the diamond.
- Some Marange diamonds are colored by "clouds" of graphite micro-inclusions that are restricted to cuboid growth sectors.

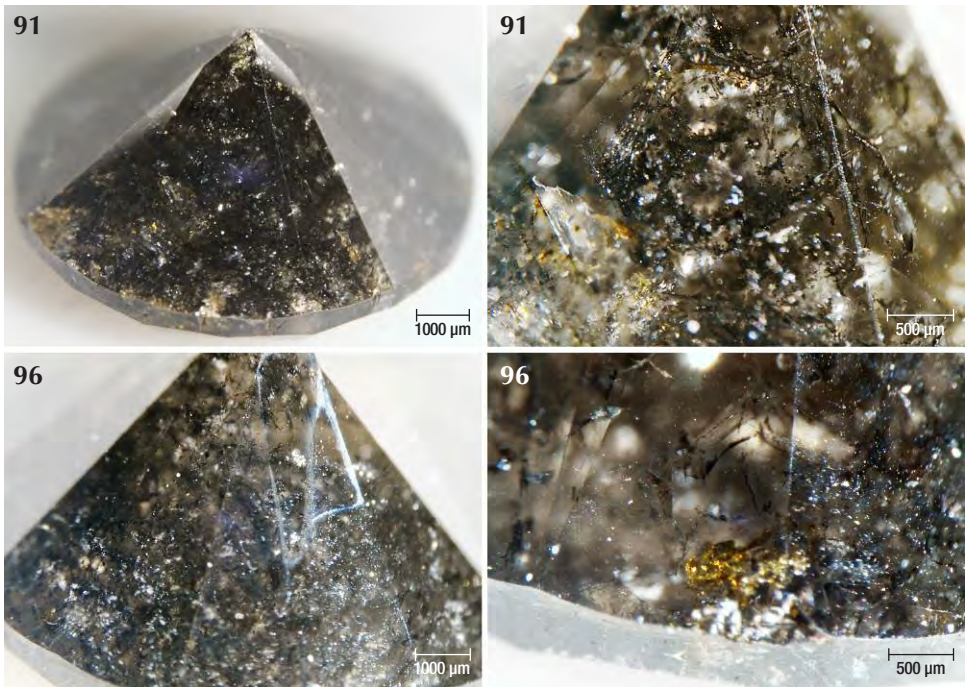

Figure 5. The appearance of these two diamonds is dominated by black graphitic needles, with very few brown radiation stains. These graphite needles are all significantly larger than the micron-sized graphite inclusions forming the dark clouds in figure 9. Photos by Karen Smit.

troscopy, the entire thickness of the diamond is sampled, so the signal from irradiation-related defects is diluted. This may explain why the peak intensities of GR1 and 594 nm are low, whereas there are abundant radiation spots visible on the surface and along fractures. The dark appearance of the diamonds is therefore related to the combined presence of dark mineral inclusions and abundant brown radiation stains.

The majority of samples were colored by graphite needles (figure 5) along with brown radiation stains occurring along surface-reaching internal fractures (figures 6 and 7). Marange diamonds have previously

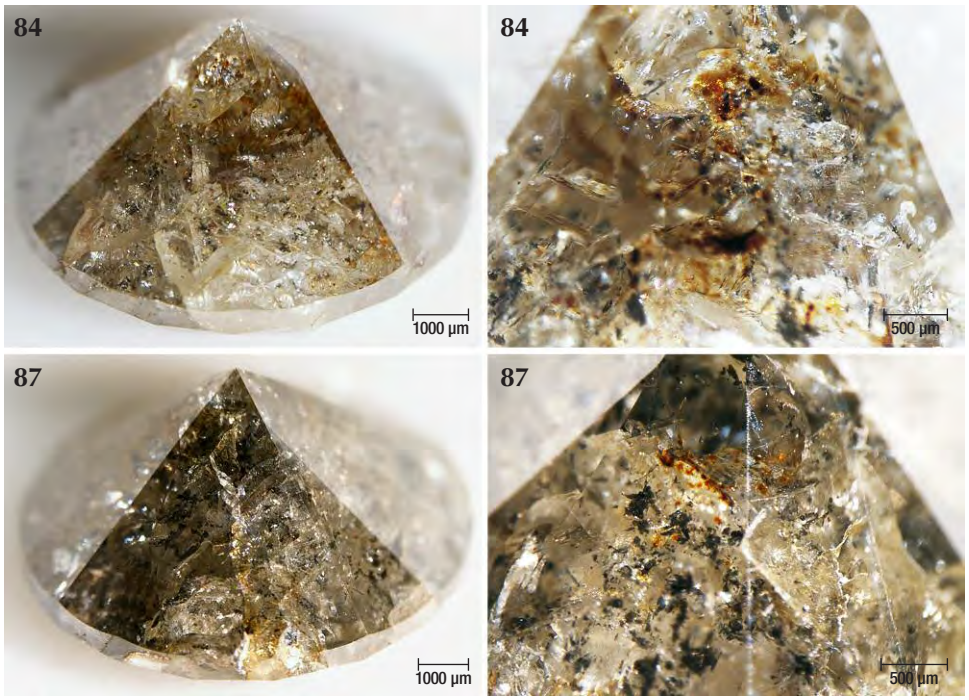

Figure 6. Images of two diamonds that are only lightly colored by brown radiation stains along internal fractures, but also contain abundant graphite needles. These graphite needles are all significantly larger than the micron-sized graphite inclusions forming the dark clouds in figure 9. Photos by Karen Smit.

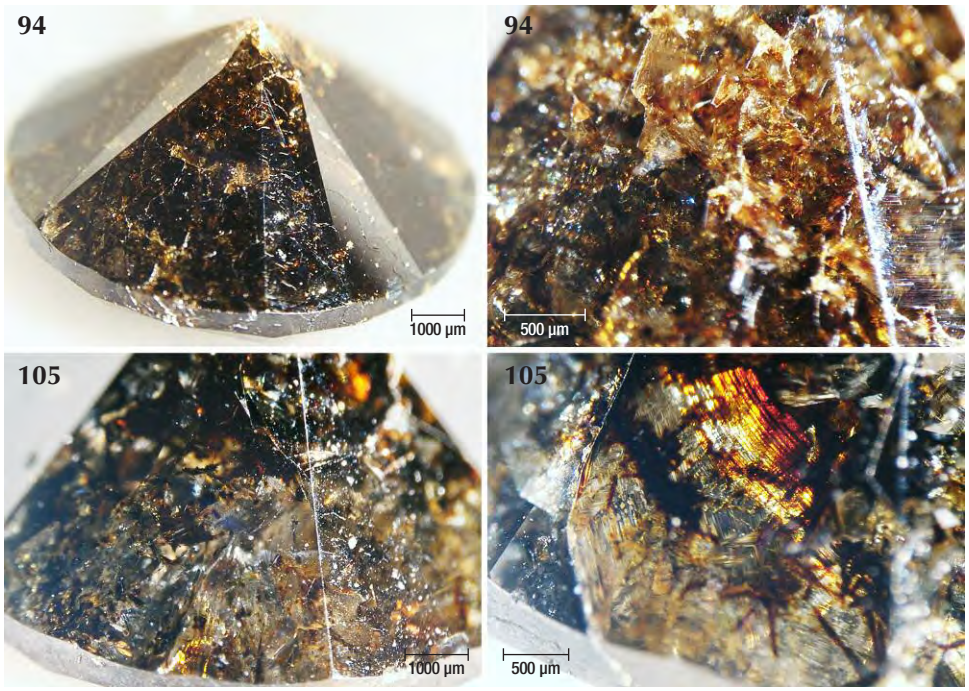

Figure 7. These two diamonds have the darkest appearance due to abundant brown radiation stains, combined with graphite needles. These graphite needles are all significantly larger than the micron-sized graphite inclusions forming the dark gray to black clouds in figure 9. Photos by Karen Smit.

been described with both green and brown radiation stains (Breeding and Wang, 2014; Eaton-Magaña et al., 2017; and unpublished GIA data). In all 40 samples described for this study, however, only brown radiation stains were observed (figure 8).

Four of the diamonds were not colored by graphite needles or brown radiation stains. Instead, their dark appearance was due to clouds of graphitic micro-inclusions (figures 3 and 9), similar to Marange diamond samples described in Smit et al. (2016) and Eaton-Magaña et al. (2017). These clouds appear to correlate with growth zones within the diamonds (figures 9 and 10). These four samples did appear to have a brown bodycolor that might have been due to the absorption continuum seen in the optical absorption spectra (again, see figure 4) and was likely related to vacancy clusters formed in the diamond lattice through deformation (Fisher et al., 2009).

Nitrogen and Other Defects Observed in FTIR Spectra. Due to high amounts of nitrogen, the nitrogen concentration and nitrogen aggregation characteristics of the Marange diamonds in this study could not be

Figure 8. Individual brown radiation stains visible within fractures. This feature is most consistent with natural radioactive fluids infiltrating the diamond along the fractures, and it would not be produced by artificial irradiation. Photos by Karen Smit.

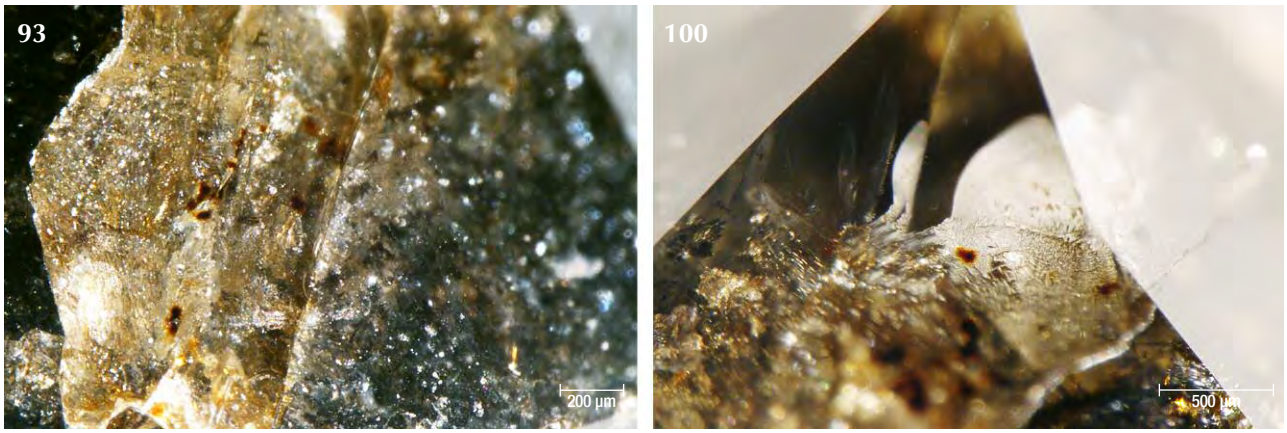

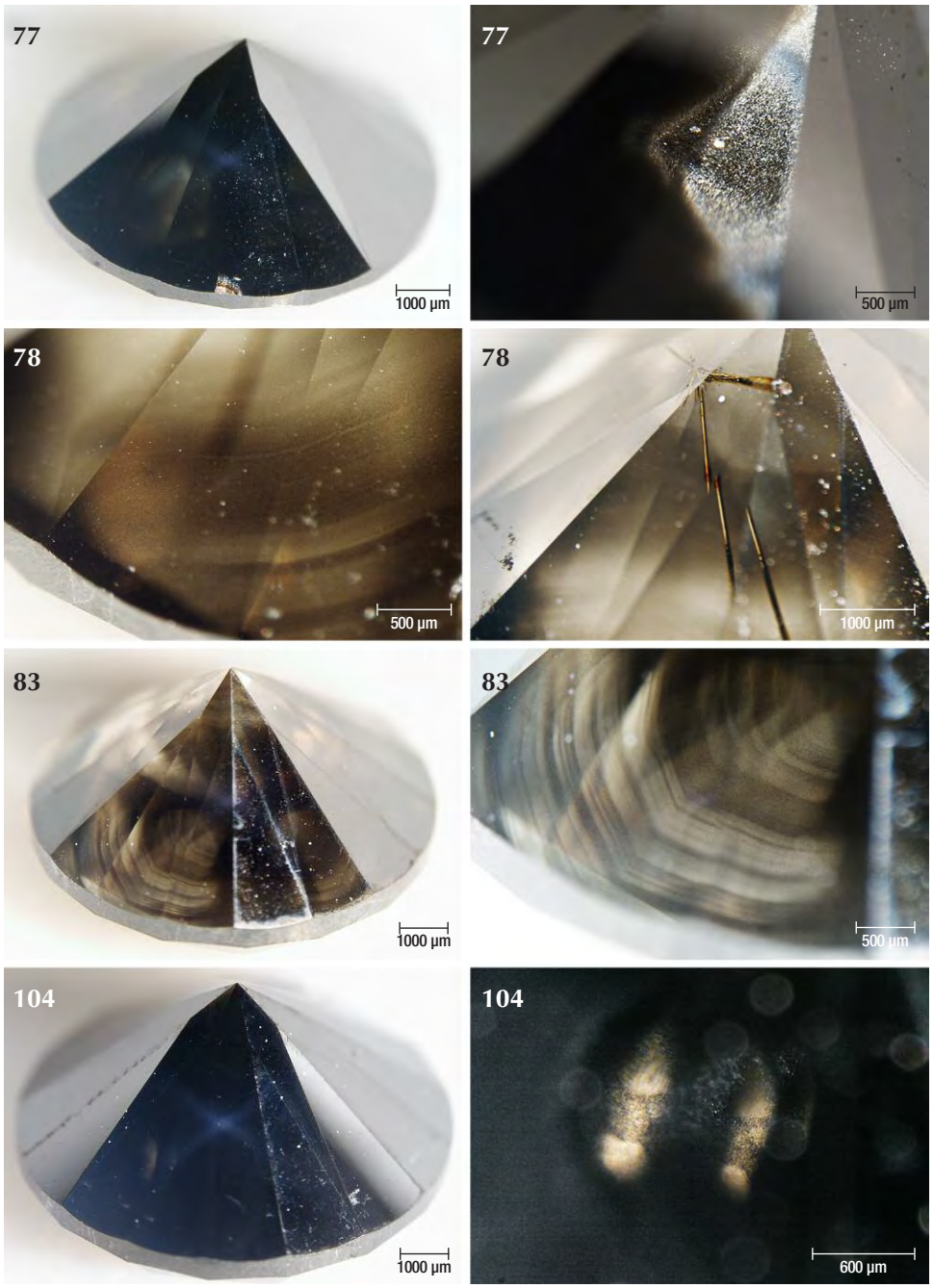

Figure 9. Images of the four diamonds that contain clouds of micron-sized inclusions of graphite that impart a dark appearance to the diamonds. Graphite in Marange diamonds has previously been found to occur in association with methane fluid inclusions (Smit et al., 2016). Also visible in sample 78 are radiation stains along the fractures in the diamond. Photos by Karen Smit.

quantified. Previously, FTIR mapping across thin (0.5 mm) Marange diamond plates has allowed for quantification of nitrogen in the one phonon region. Smit et al. (2016) reported FTIR-determined nitrogen concentrations between 971 ppma and 2628 ppma, all with less than 30% of nitrogen occurring as B centers (N_4V, where V is a vacancy). All 40 diamonds in this current study had strong VN_3H peaks (Goss et al., 2014) at 3107 cm^{-1} (stretching mode) and 1405 cm^{-1} (bending mode), as well as many other hydrogen-related defects in the 3050–3311 cm^{-1} region (figure 11). A small 3050 cm^{-1} peak seen in 17 of the 40 diamonds (42.5%) is indicative of methane (Benedetti et al., 1999; Teinturier et al., 2002; see figure 11).

Previous studies have noted the spatial association of methane and graphite micro-inclusions exclusively in the cuboid sectors of Marange diamonds (e.g., Smit et al., 2016). All diamonds in this study that contain methane peaks in FTIR also contain graphitic micro-inclusions (figure 9 and table 1). Based on our previous

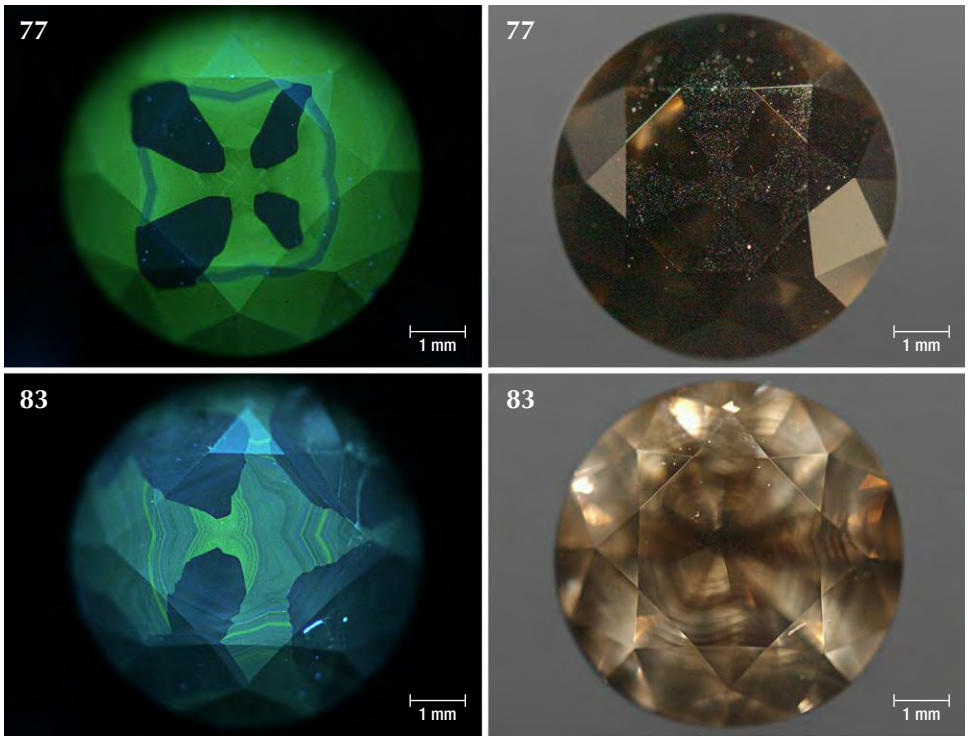

Figure 10. DiamondView and visible-light images of two diamonds that are colored exclusively by clouds comprised of micron-sized inclusions of graphite (causing the dark appearance). These diamonds display cuboctahedral growth, with graphite micro-inclusions (clouds) that occur only within the cuboid sectors. Graphite in Marange diamonds is associated with methane fluid inclusions (Smit et al., 2016) as well as Ni-N defects that luminesce a green-yellow color with UV excitation (Rondeau et al., 2004; Lang et al., 2004; Howell et al., 2013; Rakovan et al., 2014). Photos and images by Karen Smit.

work on Marange diamonds, graphite is reasonably assumed to occur in the cuboid sectors. Additionally, high nitrogen contents, the presence of methane, and the other hydrogen-related FTIR features are all consistent with previously described Marange diamonds (Smit et al., 2016; Eaton-Magaña et al., 2017).

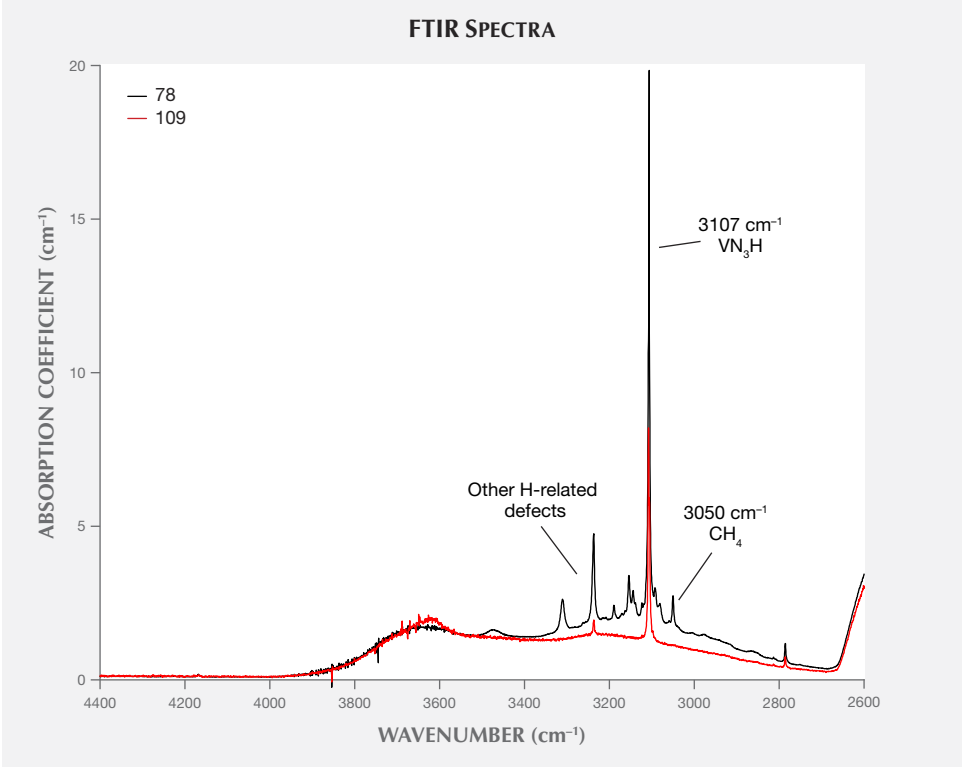

Figure 11. FTIR spectra for two representative samples that show the presence and absence of CH_4 at 3050 cm^{-1}. The sample containing CH_4 also shows other hydrogen-related peaks in the vicinity of the VN_3H peak at 3107 cm^{-1} (Goss et al., 2014). Previous work on other Marange diamonds showed that CH_4 inclusions are restricted to cuboid sectors and closely associated with the clouds of graphitic micro-inclusions (Smit et al., 2016).

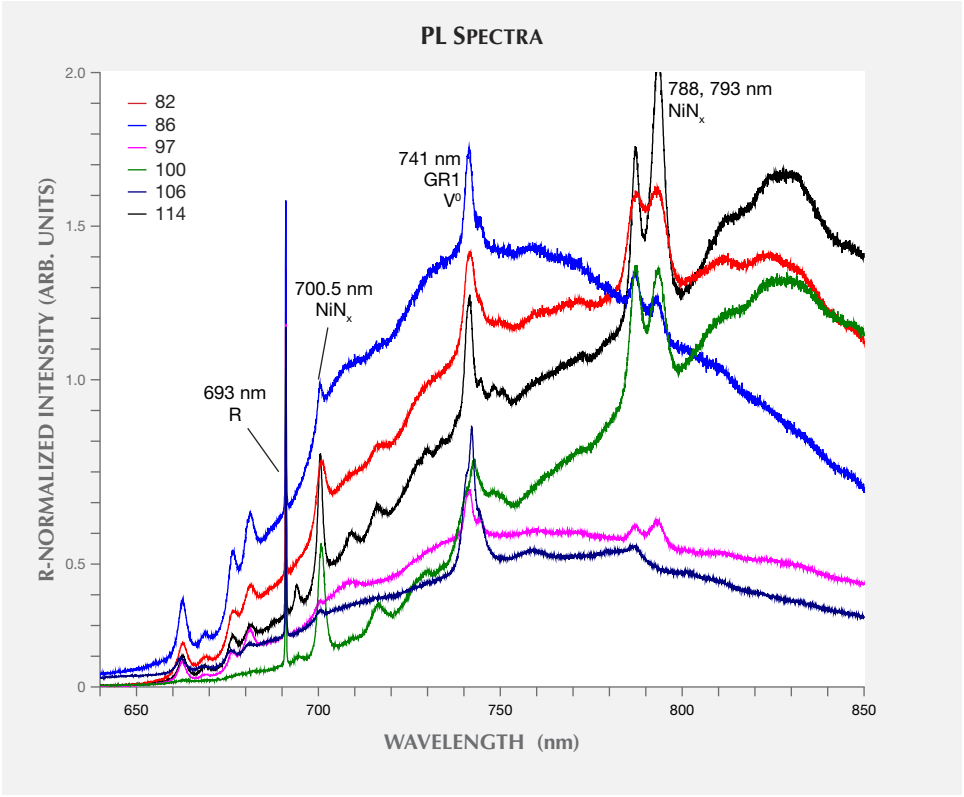

Figure 12. PL spectra (77 K) taken with a 633 nm laser excitation source. In all spectra, the diamond Raman peak (R) is normalized to an intensity of 1 so that the intensities of PL peaks in different samples are comparable. GR1 (741 nm) is observed in 50% of the 633 nm PL spectra compared to 43% of optical absorption spectra, due to the enhanced sensitivity of the PL technique. Also shown are peaks related to NiN_x at 700.5, 788, and 793 nm.

Defects Observed in PL Spectra. Defects that are only detectable by PL spectroscopy and not present in sufficient quantities to be detected through optical absorption spectroscopy have no influence on the bodycolor of diamonds. Nevertheless, these defects can provide important information on the diamonds' geological history.

Nickel-Related Defects. Nickel-related defects were observed in all 40 samples in this suite (again, see table 1). Previous studies of Marange and other mixed-habit diamonds have shown that these Ni-related defects only occur in the cuboid sectors (Lang et al., 2004; Rondeau et al., 2004; Howell et al., 2013; Smit et al., 2016). In this study, PL spectra were collected randomly, and as such are representative of the bulk diamond, so sector-dependent Ni incorporation was not evaluated. However, the observation of Ni-related defects in all 40 samples suggests at least some cuboid growth in all of the samples. Peaks at 700.5, 788, and 793 nm (observed using 633 nm laser excitation) as well as 926 nm (830 nm laser excitation) relate to NiN_x complexes that can form during high-temperature annealing (Iakoubvskii and Adriaenssens, 2002; Hainschwang et al., 2005; Yelisseyev and Kanda, 2007; Dischler, 2012; see figures 12 and 13). These NiN_x complexes (where x = 1–4) have a basic structure as Ni^+ in a divacancy interstitial position with six carbon neighbors (NE4 EPR center correlating with 1.4 eV/883 nm optical center; Nazaré et al., 1991; Collins, 2000; Lang et al., 2004). When N substitutes for the carbon atoms that surround Ni, the NE1–NE8 EPR centers are created (e.g., NE1 = NiN_2 and NE8 = NiN_4; Nadolinny et al., 1999; Johnston and Mainwood, 2003).

Defects Related to Irradiation and Annealing. Since PL spectroscopy is more sensitive than optical absorption spectroscopy, GR1 (V^0) was observed in 50% of the 633 nm PL spectra compared to 43% of the optical absorption spectra (figure 12 and table 1). H3—NVN^0 at 503.2 nm—occurred in 35 out of the 40 Marange diamonds we analyzed for this study (figure 14). H3 can form through high-temperature annealing of diamonds and forms when vacancies migrate through the diamond lattice and become trapped at A centers (N pairs). H2 is the negative charge state of H3—NVN^- at 986 nm—and can form by accepting an electron from isolated substitutional nitrogen (N_S^0). Weak H2 was observed in only eight diamonds in this suite (20%; see figure 13 and table 1). Although Marange diamonds are type IaAB and do not have sufficient N_S^0 to be detected through FTIR spectroscopy, natural diamonds are known to contain trace amounts of N_S^0 that could contribute to H2 for-

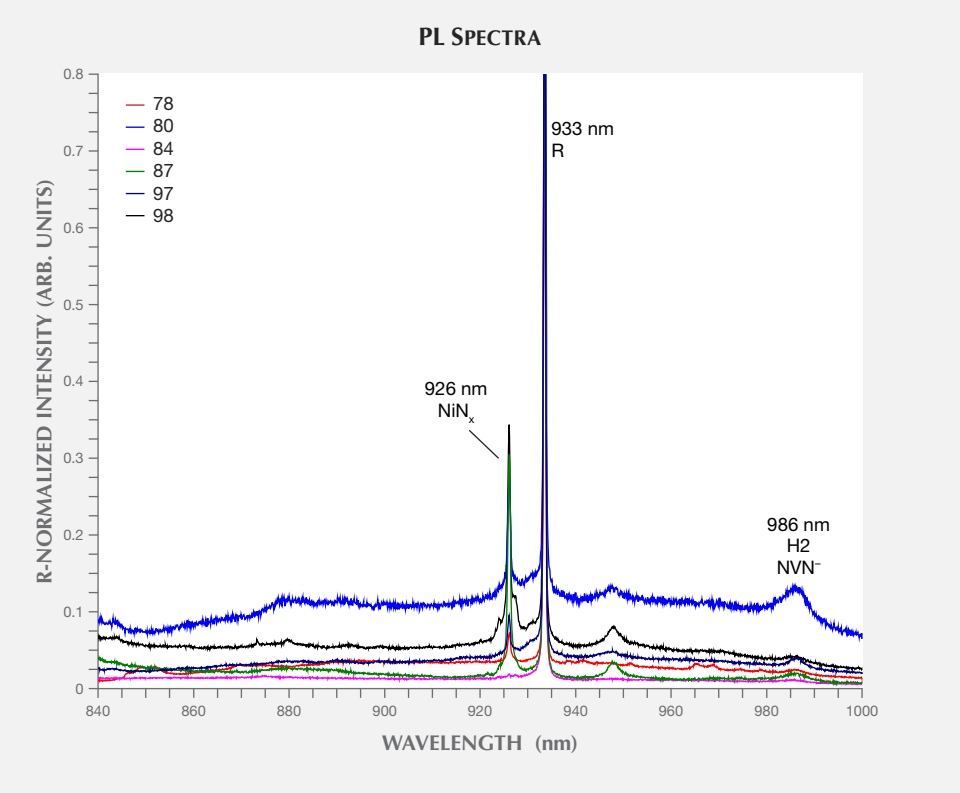

Figure 13. PL spectra (77 K) taken with an 830 nm laser excitation source show the 926 nm peak related to NiN_x defects and H2 at 986 nm. In all spectra, the diamond Raman peak (R) is normalized to an intensity of 1 so that the intensities of PL peaks in different samples are comparable.

mation (e.g., type IaB diamonds contain 4 ± 2.5 ppb N_S^0 detected through EPR spectroscopy (Newton, 2011). For comparison, the detection limit in FTIR spectroscopy is typically around 1 ppma.

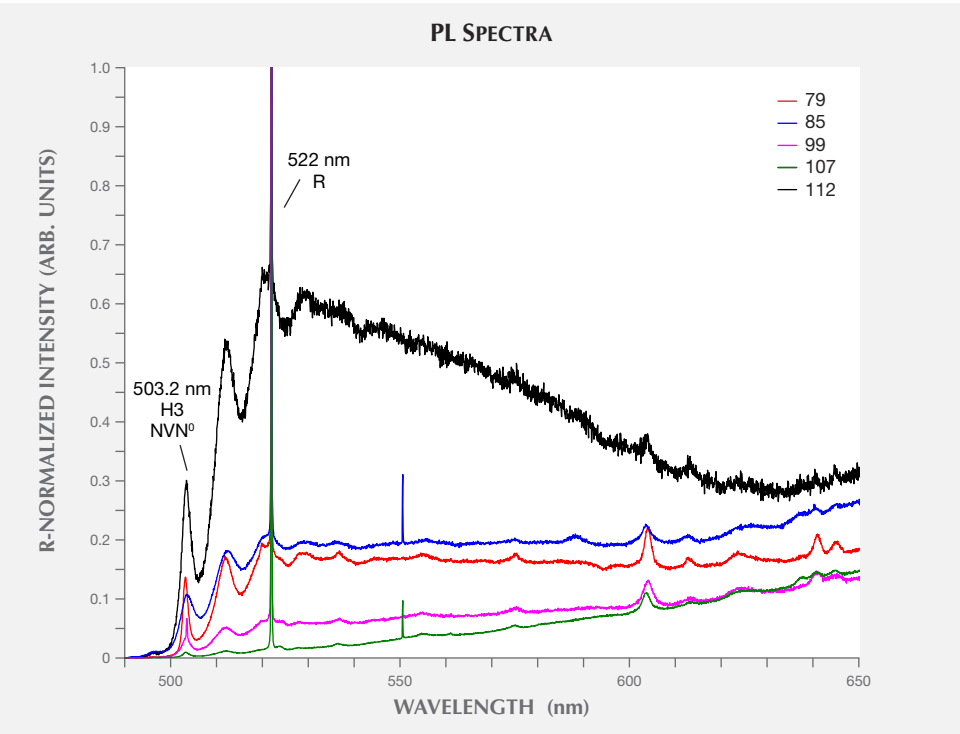

Figure 14. PL spectra (77 K) taken with a 488 nm laser excitation source, with the zero phonon line (ZPL) of H3 observed at 503 nm, along with its vibronic structure up to around 520 nm. In all spectra, the diamond Raman peak (R) is normalized to an intensity of 1 so that the intensities of PL peaks in different samples are comparable. The sharp line visible at around 550 nm in two samples is from the liquid nitrogen used to cool the diamonds.

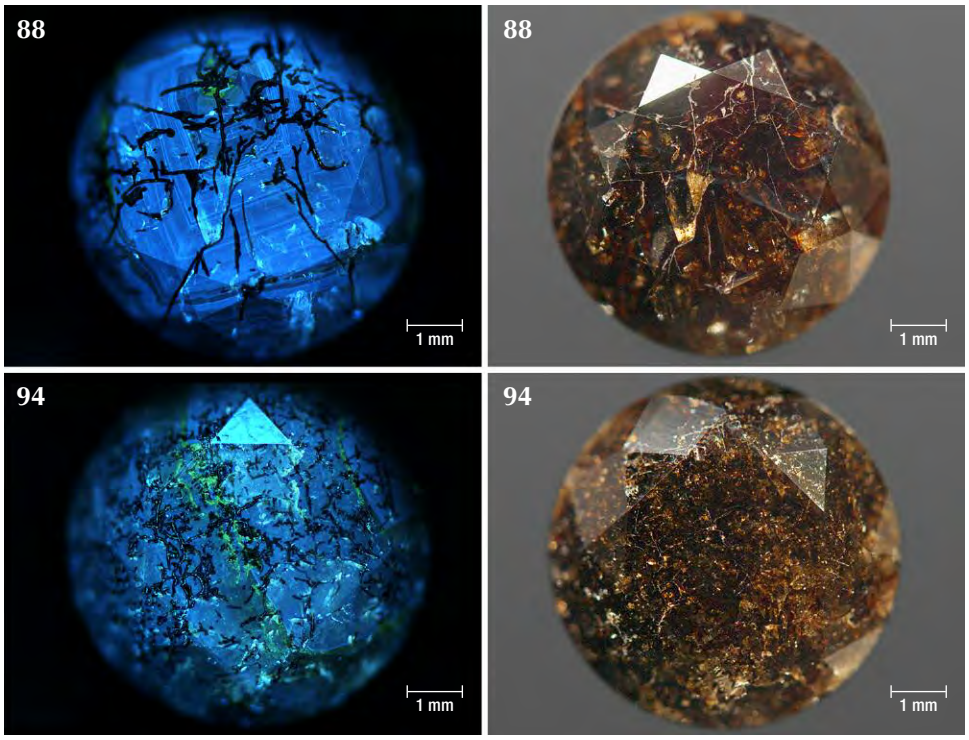

Figure 15. DiamondView and visible light images of two diamonds that show radiation stains within fractures in the diamond. Non-luminescent regions in the DiamondView images are associated with extensive radiation damage along fractures in the diamonds. Photos and images by Karen Smit.

Features Observed in DiamondView Images. The DiamondView uses a UV source to excite luminescent defects in the diamond lattice. Similar to cathodoluminescence, growth zones within diamond are visible if they contain different concentrations of defects that may produce different color responses. DiamondView images of the Marange diamonds are dominated by blue and yellowish green luminescence, where blue luminescence can be related to both "Band A" and/or the N3 (VN_3) center (van Wyk, 1982; Collins, 1992; Welbourn et al., 1996) and the yellowish green luminescence could be due to H3 (NVN^0) and/or the NiN-related defects observed in PL spectra (e.g., Welbourn et al., 1989, 1996).

Cuboctahedral (mixed-habit) growth sectors were visible in some samples and most obvious in the diamonds colored exclusively by clouds of graphitic micro-inclusions (figures 9 and 10). Following observations on a different suite of Marange diamonds, as well as mixed-habit diamonds from other localities (Lang et al., 2004; Rondeau et al., 2004; Howell et al., 2013), cuboid sectors always contain the graphite clouds and Ni-related defects, whereas the octahedral sectors are free of any inclusions and Ni-related defects (Smit et al., 2016). Based on the close spatial association of graphite and methane in other Marange diamonds, the cuboid sectors containing graphite clouds in this study can also reasonably be expected to contain methane (as identified through bulk FTIR analyses; figure 11).

Areas of irradiation damage on the Marange diamonds showed no luminescence and appeared darker than the bulk of the stone (figure 15), features that were also observed in diamonds from the Grib mine (Arkhangelsk region, Baltic shield; Rubanova et al., 2009). These non-luminescent areas generally correlate with brown radiation stains that occur both in fractures and on the surface, although this is not always the case.

DISCUSSION

Effect of Irradiation on Marange Diamonds. Alpha particles (^{4}He ions) produced during ^{238}U, ^{235}U, and ^{232}Th decay result in radiation damage when they impact a diamond. These alpha particles have short penetration depths, so any damage is typically less than 30 µm into the diamond and results in green coloration (Crookes, 1904; Wagner, 1914; Lind and Barwell, 1923). Where this radiation damage and associated vacancy formation (V^0/GR1) are localized, green radiation stains (or spots) occur (Eaton-Magaña and Moe, 2016).

Diamonds with lower nitrogen content may be more likely to be damaged by radiation, as vacancy concentration has been shown to correlate with nitrogen content (Kiflawi et al., 2007). All 40 Marange

diamonds had high nitrogen contents, so any correlation between nitrogen content and vacancy concentration within this suite is unlikely.

Abundant radiation stains on the surfaces and within fractures indicate that the Marange diamonds were exposed to a radioactive source, likely during their >1 billion-year residency at the earth's surface. In natural diamonds, green radiation stains result when the diamond surface is in contact with minerals rich in uranium and thorium, such as uraninite (UO_2), for around 10 million years (Vance and Milledge, 1972). Zircons ($ZrSiO_4$) contain only trace amounts of uranium and would need to be in contact with diamond for significantly longer, around one billion years, to cause significant radiation damage to the diamond lattice (Nasdala et al., 2013).

Brown color in the radiation stains (figures 6 and 7) further indicates that these diamonds were heated to at least 600°C during their surface residency. Green radiation stains start changing to an olive color at 500–550°C and turn brown when heated to 600°C in the laboratory (Vance et al., 1973; Nasdala et al., 2013; Eaton-Magaña and Moe, 2016). Color change of the radiation stains from green to brown at 600°C is associated with loss of GR1, although the diamond lattice is expected to remain disordered and damaged (Nasdala et al., 2013).

Origin of Radiation and Metamorphism in the Marange Alluvial Deposit. Marange diamonds occur in Mesoproterozoic (>1.1 Ga) basal conglomerates of the Umkondo Group that comprise compositionally mature quartz pebble and cobble conglomerate (de Wit and Ward, 2014). The conglomerate also contains zircon and gold (de Wit and Ward, 2014). Given the long residency time of these diamonds at the surface, irradiation could have originated from either the Meso- to Paleoarchean basement gneisses of the Zimbabwe craton or from radioactive minerals (such as zircon) in the host Umkondo conglomerate. Although zircon contains significantly less uranium than uraninite, the billion-year residency of the diamonds in the conglomerate would be sufficient to cause green radiation stains (e.g., Nasdala et al., 2013). The Umkondo Group experienced greenschist to amphibolite facies metamorphism (Goodwin, 1996)—likely related to tectonic activity in the 0.55 Ga Mozambique Belt (see location in figure 1)—which would provide the requisite temperatures to change these green radiation spots to brown (Vance et al., 1973). Heating during metamorphism likely also facilitated the formation of the 594 nm and H3 (NVN^0) defects through vacancy migration, as well as formation of the NiN complexes (Lawson and Kanda, 1993).

Other Natural Diamonds with Abundant Radiation Stains. Apart from Marange, natural diamonds from many other localities show abundant radiation damage. Diamonds from the 2.8–2.9 Ga Central Rand Group of the Witwatersrand Basin (Kaapvaal craton, South Africa) show both green and brown radiation stains (Williams, 1932). Radiation damage to form the initially green radiation stains is consistent with these diamonds' occurrence in uraninite-rich conglomerate (Gittus, 1963; Raal and Robinson, 1980). Later heating events in the crust must have raised the temperatures to at least 600°C for these green stains to turn brown (Vance et al., 1973). These events could be related to either large-scale Bushveld magmatism at 2.1 Ga (see location on figure 1) or Karoo magmatism at the time of Gondwana breakup (~180 Ma).

Similarly, the majority of Guaniamo placer diamonds that occur in the alluvium of the Quebrada Grande River (Venezuela) have green radiation stains on their surface (Kaminsky et al., 2000; Schulze and Nasdala, 2016). The primary source for these diamonds are ~700 Ma kimberlite sills in the area (Kaminsky et al., 2000, 2004), and the lack of abundant brown radiation stains indicates there were no significant events that heated the crust more than 600°C. The source of radiation is still unknown, and radioactive grains could be related to Archean crust that is a potential source for monazite and zircon, or otherwise to the Guaniamo kimberlites that contain radioactive pyrochlore (Sharygin et al., 2009).

SUMMARY AND CONCLUSIONS

Although there are other occurrences of diamonds with natural radiation damage, the Marange locality may be unique in its high proportion of diamonds with abundant brown radiation stains that give them an almost black appearance. This could be due to their long residency (>1 Ga) in crustal conglomerates that contain highly radioactive minerals, followed by high-temperature metamorphism associated with the Mozambique belt (Goodwin, 1996).

Natural diamonds with Fancy black color grades and abundant radiation stains (such as the Marange samples studied here) are relatively easy to distinguish from any heat-treated or irradiated diamonds with similar color grades. Low-clarity diamonds that are highly fractured, such as the ones studied here, are not expected to survive HPHT treatment. However,

these fractured diamonds can be treated at LPHT conditions to graphitize the fractures and turn them into more valuable black diamonds (Hall and Moses, 2001; Notari, 2002). Such treatment would cause abundant graphitization along internal fractures, which is not visible in these Marange diamonds. Artificial irradiation is not expected to produce the radiation staining seen along the fractures, as this feature is most consistent with natural radioactive fluids infiltrating the fractures (figures 6 and 7).

Radiation stains and graphite needles are not the only cause of the dark appearance. A subset of the Marange diamonds contain abundant clouds of graphitic (+ methane) micro-inclusions in their cuboid sectors that impart a dark appearance to the bulk diamond, and these need to be distinguished from heated black diamonds that may have a similar appearance. Experiments by Eaton-Magaña et al. (2017) showed that the grain size of graphitic micro-inclusions in Marange diamonds increases during heat treatment, coinciding with the disappearance of any associated methane micro-inclusions. Accordingly, visual observations of graphite grain size, along with FTIR and Raman spectroscopy to detect methane, are required to distinguish natural from heat-treated Marange graphite-bearing diamonds.

ABOUT THE AUTHORS

Dr. Smit is a research scientist, and Ms. Myagkaya and Ms. Persaud are analytical technicians, at GIA in New York. Dr. Wang is GIA's vice president of research and development.

ACKNOWLEDGMENTS

We are grateful to Ulrika D'Haenens-Johansson for many useful discussions. Comments by Troy Ardon, Sally Eaton-Magaña, and Kyaw Soe Moe on an earlier version of this manuscript are appreciated. Eloïse Gaillou, Russell Shor, and Christopher Welbourn are thanked for constructive reviews that improved the final version of the manuscript. We are grateful to the DEYI Jewelry Company for making these samples available for study. Mike de Wit is thanked for informal discussions about the Marange diamond deposits.

REFERENCES

Ardon T. (2013) Lab Notes: Black diamond with unusual color origin. *G&G*, Vol. 49, No. 4, p. 252.

Benedetti L.R., Nguyen J.H., Caldwell W.A., Liu H., Kruger M., Jeanloz R. (1999) Dissociation of CH_4 at high pressures and temperatures: Diamond formation in giant planet interiors. *Science*, Vol. 286, pp. 100–102, http://dx.doi.org/10.1126/science.286.5437.100

Breeding C.M., Wang W. (2014) Characterization of gem diamonds from eastern Zimbabwe. Poster presentation at the 21st General Meeting of the International Mineralogical Association, Johannesburg.

Clark C.D., Ditchburn R.W., Dyer H.B. (1956) The absorption spectra of irradiated diamonds after heat treatment. *Proceedings of the Royal Society of London. Series A, Mathematical and Physical Sciences*, Vol. 237, No. 1208, pp. 75–89, http://dx.doi.org/10.1098/rspa.1956.0163

Clifford T.N. (1966) Tectono-metallogenic units and metallogenic provinces of Africa. *Earth and Planetary Science Letters*, Vol. 1, No. 6, pp. 421–434, http://dx.doi.org/10.1016/0012-821X(66)90039-2

Collins A.T. (1982) Colour centres in diamond. *Journal of Gemmology*, Vol. 18, No. 1, pp. 37–75, http://dx.doi.org/10.15506/JoG.1982.18.1.37

——— (1992) The characterisation of point defects in diamond by luminescence spectroscopy. *Diamond and Related Materials*, Vol. 1, No. 5-6, pp. 457–469, http://dx.doi.org/10.1016/0925-9635(92)90146-F

——— (2000) Spectroscopy of defects and transition metals in diamond. *Diamond and Related Materials*, Vol. 9, No. 3-6, pp. 417–423, http://dx.doi.org/10.1016/S0925-9635(99)00314-3

Collins A.T., Davies G., Woods G.S. (1986) Spectroscopic studies of the H1b and H1c absorption lines in irradiated, annealed type-Ia diamonds. *Journal of Physics C: Solid State Physics*, Vol. 19, No. 20, pp. 3933–3944, http://dx.doi.org/10.1088/0022-3719/19/20/026

Crookes W. (1904) On the action of radium emanation on diamonds. *Proceedings of the Royal Society of London*, Vol. 74, No. 497-506, pp. 47–49, http://dx.doi.org/10.1098/rspl.1904.0077

Dischler B. (2012) *Handbook of Spectral Lines in Diamond*. Springer, Berlin.

Dodson M.H., Compston W., Williams I.S., Wilson J.F. (1988) A search for ancient detrital zircons in Zimbabwean sediments. *Journal of the Geological Society, London*, Vol. 145, No. 6, pp. 977–983, http://dx.doi.org/10.1144/gsjgs.145.6.0977

Eaton-Magaña S.C., Moe K. (2016) Temperature effects on radiation stains in natural diamonds. *Diamond and Related Materials*, Vol. 64, pp. 130–142, http://dx.doi.org/10.1016/j.diamond.2016.02.009

Eaton-Magaña S., Ardon T., Zaitsev A.M. (2017) Inclusion and point defect characteristics of Marange graphite-bearing diamonds after high temperature annealing. *Diamond and Related Materials*, Vol. 71, pp. 20–29, http://dx.doi.org/10.1016/j.diamond.2016.11.011

Fisher D., Sibley S.J., Kelly C.J. (2009) Brown colour in natural di-

amond and interaction between the brown related and other colour-inducing defects. *Journal of Physics: Condensed Matter*, Vol. 21, No. 36, p. 364213, https://doi.org/10.1088/0953-8984/21/36/364213
Gittus J.H. (1963) *Metallurgy of the Rarer Metals-8. Uranium*. Butterworths, London.
Goodwin A. (1996) *Principles of Precambrian Geology*. Academic Press, London.
Goss J.P., Briddon P.R., Hill V., Jones R., Rayson M.J. (2014) Identification of the structure of the 3107 cm^{-1} H-related defect in diamond. *Journal of Physics: Condensed Matter*, Vol. 26, No. 14, 145801, http://dx.doi.org/10.1088/0953-8984/26/14/145801
Hainschwang T., Simic D., Fritsch E., Deljanin B., Woodring S., DelRe N. (2005) A gemological study of a collection of chameleon diamonds. *G&G*, Vol. 41, No. 1, pp. 20–35, http://dx.doi.org/10.5741/GEMS.41.1.20
Hall M., Moses T. (2001) Lab Notes: Heat-treated black diamond: Before and after. *G&G*, Vol. 37, No. 3, pp. 214–215.
Hanson R.E., Crowley J.L., Bowring S.A., Ramezani J., Gose W.A., Dalziel I.W.D., Pancake J.A., Siedel E.K., Blenkinsop T.G., Mukwakwami J. (2004) Coeval large-scale magmatism in the Kalahari and Laurentian cratons during Rodinia assembly. *Science*, Vol. 304, No. 5674, pp. 1126–1129, http://dx.doi.org/10.1126/science.1096329
Hanson R.E., Rioux M., Gose W.A., Blackburn T.J., Bowring S.A., Mukwakwami J., Jones D.L. (2011) Paleomagnetic and geochronological evidence for large-scale post-1.88 Ga displacement between the Zimbabwe and Kaapvaal cratons along the Limpopo belt. *Geology*, Vol. 39, No. 5, pp. 487–490, http://dx.doi.org/10.1130/G31698.1
Howell D., Griffin W.L., Piazolo S., Say J.M., Stern R.A., Stachel T., Nasdala L., Rabeau J.R., Pearson N.J., O'Reilly S.Y. (2013) A spectroscopic and carbon-isotope study of mixed-habit diamonds: Impurity characteristics and growth environment. *American Mineralogist*, Vol. 98, No. 1, pp. 66–77, http://dx.doi.org/10.2138/am.2013.4179
Iakoubvskii K., Adriaenssens G.J. (2002) Optical characterization of natural Argyle diamonds. *Diamond and Related Materials*, Vol. 11, No. 1, pp. 125–131, http://dx.doi.org/10.1016/S0925-9635(01)00533-7
Jacobs J., Pisarevsky S., Thomas R.J., Becker T. (2008) The Kalahari Craton during the assembly and dispersal of Rodinia. *Precambrian Research*, Vol. 160, No. 1-2, pp. 142–158, http://dx.doi.org/10.1016/j.precamres.2007.04.022
Johnston K., Mainwood A. (2003) Properties of nickel nitrogen complexes in diamond: stability and electronic structure. *Diamond and Related Materials*, Vol. 12, No. 3-7, pp. 516–520, http://dx.doi.org/10.1016/S0925-9635(02)00389-8
Kaminsky F.V., Zakharchenko O.D., Griffin W.L., Channer D.M.D.R., Khachatryan-Blinova G.K. (2000) Diamond from the Guaniamo area, Venezuela. *Canadian Mineralogist*, Vol. 38, No. 6, pp. 1347–1370, http://dx.doi.org/10.2113/gscanmin.38.6.1347
Kaminsky F.V., Sablukov S.M., Sablukova L.I., Channer D.M.D.R. (2004) Neoproterozoic 'anomalous' kimberlites of Guaniamo, Venezuela: mica kimberlites of 'isotopic transitional' type. *Lithos*, Vol. 76, No. 1-4, pp. 565–590, http://dx.doi.org/10.1016/j.lithos.2004.03.035
Kiflawi I., Collins A.T., Iakoubvskii K., Fisher D. (2007) Electron irradiation and the formation of vacancy-interstitial pairs in diamond. *Journal of Physics: Condensed Matter*, Vol. 19, No. 4, 046216, http://dx.doi.org/10.1088/0953-8984/19/4/046216
Kitawaki H. (2007) Gem diamonds: Causes and colors. *New Diamond and Frontier Carbon Technology*, Vol. 17, pp. 119–126.
Lang A.R., Yelisseyev A.P., Pokhilenko N.P., Steeds J.W., Wotherspoon A. (2004) Is dispersed nickel in natural diamonds associated with cuboid growth sectors in diamonds that exhibit a history of mixed-habit growth? *Journal of Crystal Growth*, Vol. 263, No. 1-4, pp. 575–589, http://dx.doi.org/10.1016/j.jcrysgro.2003.11.116
Lawson S.C., Kanda H. (1993) An annealing study of nickel point defects in high-pressure synthetic diamond. *Journal of Applied Physics*, Vol. 73, No. 8, pp. 3967–3973, http://dx.doi.org/10.1063/1.352861
Lind S.C., Barwell D.C. (1923) The coloring and thermophosphorescence produced in transparent minerals and gems by radium radiation. *American Mineralogist*, Vol. 8, pp. 171–180.
McCourt S., Kampunzu A.B., Bagai Z., Armstrong R.A. (2004) The crustal architecture of Archaean terranes in northeastern Botswana. *South African Journal of Geology*, Vol. 107, No. 1-2, pp. 147–158, http://dx.doi.org/10.2113/107.1-2.147
Moore A.E., Cotterill F.P.D., Broderick T., Plowes D. (2009) Landscape evolution in Zimbabwe from the Permian to present, with implications for kimberlite prospecting. South African *Journal of Geology*, Vol. 112, No. 1, pp. 65–88, http://dx.doi.org/10.2113/gssajg.112.1.65
Nadolinny V.A., Yelisseyev A.P., Baker J.M., Newton M.E., Twitchen D.J., Lawson, S.C., Yuryeva O.P., Feigelson B.N. (1999) A study of ^{13}C hyperfine structure in the EPR of nickel-nitrogen-containing centres in diamond and correlation with their optical properties. *Journal of Physics: Condensed Matter*, Vol. 11, No. 38, pp. 7357–7376, http://dx.doi.org/10.1088/0953-8984/11/38/314
Nägler T.F., Kramers J.D., Kamber B.S., Frei R., Prendergast M.D.A. (1997) Growth of subcontinental lithospheric mantle beneath Zimbabwe started at or before 3.8 Ga: Re-Os study on chromites. *Geology*, Vol. 25, No. 11, pp. 983–986, http://dx.doi.org/10.1130/0091-7613(1997)025%3C0983:GOSLMB%3E2.3.CO;2
Nasdala L., Grambole D., Wildner M., Gigler A.M., Hainschwang T., Zaitsev A.M., Harris J.W., Milledge J., Schulze D.J., Hofmeister W., Balmer W.A. (2013) Radio-colouration of diamond: a spectroscopic study. *Contributions to Mineralogy and Petrology*, Vol. 165, No. 5, pp. 843–861, http://dx.doi.org/10.1007/s00410-012-0838-1
Nazaré M.H., Neves A.J., Davies G. (1991) Optical studies of the 1.40 eV Ni center in diamond. *Physical Review B*, Vol. 43, No. 17, pp. 14196–14205, http://dx.doi.org/10.1103/PhysRevB.43.14196
Newton M. (2011) Treated diamond identification. *G&G*, Vol. 47, No. 2, p. 106.
Notari F. (2002) Traitement du diamant noir por graphitation "interne" [Treatment of black diamond by internal graphitization]. *Revue de Gemmologie a.f.g.*, No. 145-146, pp. 42–60.
Raal F.A., Robinson D.N. (1980) Green for rarity. *Nuclear Active*, Vol. 23, pp. 5–8.
Rakovan J., Gaillou E., Post J E., Jaszczak J.A., Betts J.H. (2014) Optically sector-zoned (star) diamonds from Zimbabwe. *Rocks and Minerals*, Vol. 89, No. 2, pp. 173–178, http://dx.doi.org/10.1080/00357529.2014.842844
Rondeau B., Fritsch E., Guiraud M., Chalain J.-P., Notari F. (2004) Three historical 'asteriated' hydrogen-rich diamonds: growth history and sector-dependent impurity incorporation. *Diamond and Related Materials*, Vol. 13, No. 9, pp. 1658–1673, http://dx.doi.org/10.1016/j.diamond.2004.02.002
Rubanova E.V., Palazhchenko O.V., Garanin V.K. (2009) Diamonds from the V. Grib pipe, Arkhangelsk kimberlite province, Russia. *Lithos*, Vol. 112S, pp. 880–885, http://dx.doi.org/10.1016/j.lithos.2009.04.044
Schulze D.J., Nasdala L. (2016) Unusual paired pattern of radiohaloes on a diamond crystal from Guaniamo (Venezuela). *Lithos*, Vol. 265, http://dx.doi.org/10.1016/j.lithos.2016.09.024
Sharygin V.V., Sobolev N.V., Channer D.M.D.R. (2009) Oscillatory-zoned crystals of pyrochlore-group minerals from the Guaniamo kimberlites. *Lithos*, Vol. 112S, pp. 976–985, http://dx.doi.org/10.1016/j.lithos.2009.03.049
Smit K.V., Shirey S.B., Stern R.A., Steele A., Wang W. (2016) Diamond growth from C–H–N–O recycled fluids in the lithosphere: Evidence from CH_4 micro-inclusions and $\delta^{13}C$–$\delta^{15}N$–N content in Zimbabwe mixed-habit diamonds. *Lithos*, Vol. 265,

pp. 68–81, http://doi.org/10.1016/j.lithos.2016.03.015
Stowe C.W. (1989) The Proterozoic Magondi mobile belt in Zimbabwe; discussion. *South African Journal of Geology*, Vol. 92, No. 1, pp. 69–71.
Teinturier S., Pironon J., Walgenwitz F. (2002) Fluid inclusions and PVTX modelling: examples from the Garn Formation in well 6507/2-2, Haltenbanken, Mid-Norway. *Marine and Petroleum Geology*, Vol. 19, No. 6, pp. 755–765, http://dx.doi.org/10.1016/S0264-8172(02)00055-7
Titkov S.V., Zudin N.G., Gorshkov A.I., Sivtsov A.V., Magazina L.O. (2003) An investigation into the cause of color in natural black diamonds from Siberia. *G&G*, Vol. 39, No. 3, pp. 200–209, http://dx.doi.org/10.5741/GEMS.39.3.200
Vance E.R., Milledge H.J. (1972) Natural and laboratory α-particle irradiation of diamond. *Mineralogical Magazine*, Vol. 38, No. 299, pp. 878–881, http://dx.doi.org/10.1180/minmag.1972.038.299.11
Vance E.R., Harris J.W., Milledge H.J. (1973) Possible origins of α-damage in diamonds from kimberlite and alluvial sources. *Mineralogical Magazine*, Vol. 39, No. 303, pp. 349–360, http://dx.doi.org/10.1180/minmag.1973.039.303.12
Wagner P.A. (1914) *The Diamond Fields of Southern Africa*. Transvaal Leader, Johannesburg.
Welbourn C.M., Rooney M.T., Evans D.J.F. (1989) A study of diamonds of cube and cube-related shape from the Jwaneng mine. *Journal of Crystal Growth*, Vol. 94, pp. 229–252, http://dx.doi.org/10.1016/0022-0248(89)90622-2
Welbourn C.M., Cooper M., Spear P.M. (1996) De Beers natural versus synthetic diamond verification instruments. *G&G*, Vol. 32, No. 3, pp. 156–169, http://dx.doi.org/10.5741/GEMS.32.3.156
Williams A.F. (1932) *The Genesis of the Diamond II*. Ernest Benn Ltd., London.
Wilson J.F. (1990) A craton and its cracks: some of the behaviour of the Zimbabwe block from the Late Archaean to the Mesozoic in response to horizontal movements, and the significance of some of its mafic dyke fracture patterns. *Journal of African Earth Sciences*, Vol. 10, No. 3, pp. 483–501, http://dx.doi.org/10.1016/0899-5362(90)90101-J
de Wit M., Ward J. (2014) The Proterozoic Marange alluvial diamond deposit in eastern Zimbabwe: Is this a Mega-placer? Vancouver Kimberlite Cluster seminar, University of British Columbia, March 7.
van Wyk J.A. (1982) Carbon-12 hyperfine interaction of the unique carbon of the P2 (ESR) or N3 (optical) centre in diamond. *Journal of Physics C: Solid State Physics*, Vol. 15, No. 27, pp. L981–L983, http://dx.doi.org/10.1088/0022-3719/15/27/007
Yelisseyev A., Kanda H. (2007) Optical centers related to 3d transition metals in diamond. *New Diamond and Frontier Carbon Technology*, Vol. 17, No. 3, 127–178.
Zeh A., Gerdes A., Barton J.M. (2009) Archean accretion and crustal evolution of the Kalahari craton—the zircon age and Hf isotope record of granitic rocks from Barberton/Swaziland to the Francistown Arc. *Journal of Petrology*, Vol. 50, No. 5, pp. 933–966, http://dx.doi.org/10.1093/petrology/egp027
Zeh A., Jaguin J., Poujol M., Boulvais P., Block S., Paquette J.-L. (2013) Juvenile crust formation in the northeastern Kaapvaal Craton at 2.97 Ga—Implications for Archean terrane accretion, and the source of the Pietersburg gold. *Precambrian Research*, Vol. 233, pp. 20–43, http://dx.doi.org/10.1016/j.precamres.2013.04.013
Zeh A., Stern R.A., Gerdes A. (2014) The oldest zircons of Africa—Their U–Pb–Hf–O isotope and trace element systematics, and implications for Hadean to Archean crust–mantle evolution. *Precambrian Research*, Vol. 241, pp. 203–230, http://dx.doi.org/10.1016/j.precamres.2013.11.006

For online access to all issues of GEMS & GEMOLOGY from 1934 to the present, visit:

gia.edu/gems-gemology

An Early Byzantine Engraved Almandine from the Garibpet Deposit, Telangana State, India: Evidence for Garnet Trade Along the Ancient Maritime Silk Road

H. Albert Gilg, Karl Schmetzer, and Ulrich Schüssler

An Early Byzantine almandine garnet engraved with a Christian motif and dated to the late sixth to eighth century offers insight into trade practices in antiquity. The gemstone was characterized by a combination of nondestructive analytical methods including electron microprobe, portable X-ray fluorescence, Raman spectroscopy, and optical microscopy. The chemical composition and zoning, in combination with the inclusion assemblage and the distinct distribution of inclusions between an inclusion-rich core and an inclusion-poor rim, indicated that the sample most likely originated from the large Garibpet deposit in Telangana State, India. The Byzantine intaglio thus furnishes evidence of garnet transport from the eastern Indian coast to the Mediterranean world during Early Medieval times. In so doing, it supports the interpretation of a sixth-century text by the Greek merchant and traveler Cosmas Indicopleustes, which describes the export of "alabandenum," a reference to garnet, from harbors on the southeast Indian shore along the ancient Maritime Silk Road. This idea is further buttressed by considering that garnet from the Garibpet deposit was used for bead production at the archaeological site of Arikamedu, one of the historical ports on the Coromandel Coast in southeast India. Conversely, a comparison with properties of the two predominant types of almandine used in Merovingian cloisonné jewelry shows that the characteristic mineralogical features and therefore the sources of these garnets set in Early Medieval jewelry were different.

Red to purple garnets of predominantly pyrope, pyrope-almandine, and almandine compositions were highly esteemed and frequently employed for gemstone purposes in Hellenistic and Early Roman Imperial times, from about 300 BCE to 200 CE (e.g., Spier, 1989; Zwierlein-Diehl, 2007; Adams, 2011; Thoresen, 2017). With regard to fashioning, engraved gems were prominent during this era but became much rarer during Late Roman Imperial times of the third and fourth century CE (figure 1), signaling a decline in the art of gem engraving (e.g., Entwistle and Adams, 2011).

An apparent resurgence in the use of engraved gemstones occurred in the middle of the fifth century (Spier, 2007, 2011), and the period from the fifth to the seventh century saw developments spread across multiple localities and cultures. Depending on the focus and context, this period may be variously referred to as Early Byzantine, Early Medieval, or Merovingian, among others. Spier (2011), for instance, suggested the existence of a prolific garnet workshop associated with the Early Byzantine imperial court in Constantinople that specialized in engraving the hard red stone, as well as sapphire, during the fifth to the seventh century. The Early Byzantine garnets might thus serve to suggest a revival in the Hellenistic to Early Roman Imperial tradition of gem engraving. The earliest and finest examples displayed beautiful portraits, for example of Theodosius II, while the quality of later ob-

See end of article for About the Authors and Acknowledgments.
Gems & Gemology, Vol. 54, No. 2, pp. 149–165,
http://dx.doi.org/10.5741/GEMS.54.2.149
© 2018 Gemological Institute of America

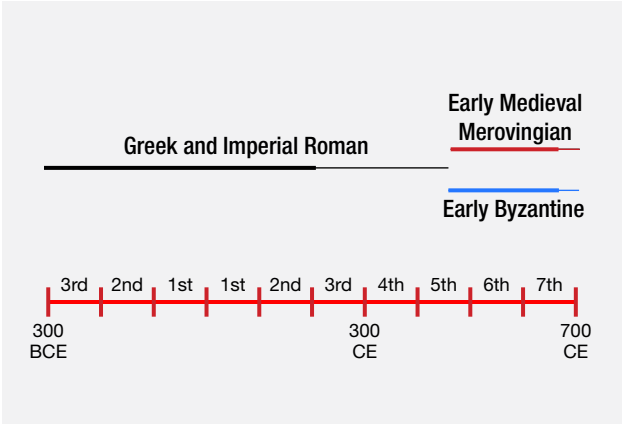

Figure 1. This schematic timeline shows the use of garnets in different eras within the so-called garnet millennium, from 300 BCE to 700 CE.

jects embellished with doves, eagles, dolphins, and religious images or symbols varied substantially. Notably, Early Byzantine engraved garnet seal stones comprised a significant proportion of Early Christian gems (Spier, 2007).

Garnets also played a significant role in Early Medieval (including Merovingian) cloisonné jewelry of the fifth to seventh century (e.g., Arrhenius, 1985; Calligaro et al., 2002; Gilg et al., 2010; Adams, 2014). Largely contemporaneous use of garnet during these centuries can likewise be seen with seal stones in pre-Islamic Persia and Central Asia (Adams, 2011; Adams et al., 2011; Ritter, 2017) and with transparent red beads produced for the Indo-Pacific trade network in the first millennium CE (Francis, 2002; Carter, 2012, 2013, 2016; Borell, 2017; Schmetzer et al., 2017). Evidence further suggests that manufacture of cloisonné jewelry may have begun with the use of non-engraved flat ring stones as garnet inlays for polychrome jewelry in the Black Sea region (Adams, 2011, 2014).

More than 4,000 individual garnets from Early Medieval cloisonné jewelry have been analyzed chemically, with the resultant data indicating classification into at least six garnet types, clusters, or groups with generally distinct features: three of almandine, two of pyrope, and one of intermediate pyrope-almandine with more variable chemical and inclusion characteristics (Quast and Schüssler, 2000; Calligaro et al., 2002, 2006-2007; Mannerstrand and Lundqvist, 2003; Périn and Calligaro, 2007; Mathis et al., 2008; Gilg et al., 2010; Horváth and Bendö, 2011; Gilg and Gast, 2012; Gast et al., 2013; Šmit et al., 2014; Bugoi et al., 2016; Périn and Calligaro, 2016). In contrast, less than 40 full chemical analyses of Hellenistic, Etruscan, and Roman garnets, mostly intaglios and cameos along with a few beads, have been published to date; these data were summarized by Thoresen and Schmetzer (2013). A portion of these stones demonstrated compositions that overlapped with some types found in Early Medieval cloisonné jewelry, but others reflected different chemistries, in particular a Ca- and Mn-rich, Mg-poor almandine (a fourth type or cluster of almandine), and likely derived from sources not used to supply the Medieval examples. Garnets from the Early Byzantine seal stones have not yet been analyzed or assigned to specific garnet types or clusters.

More recently, a detailed study on garnet beads from the Arikamedu archaeological site in Tamil Nadu State, India, identified a new (fifth) type of almandine used in antiquity (figure 2). The archaeological context of that site is described in detail by Schmetzer et al. (2017). The garnets were characterized by a distinct chemical composition with a conspicuous chemical zoning and a zonal distribution of inclusions. These features were shown to correspond with those of almandines from the alluvial Garibpet deposit in Telangana State, India (Schmetzer et al., 2017). The Garibpet locality was first described by Voysey (1833), and Bauer (1896) similarly mentioned it as a secondary occurrence of better-quality gem garnets in India. Production figures were then reported by Mirza (1937), covering a period from 1910 to 1929. In the current era, the prolific nature of the deposit has continued to be recognized, with literature describing a garnet-bearing schist that "constitutes an entire hill at Garibpet, in the Khammam

In Brief

- An engraved almandine garnet, dated to the late sixth to eighth century by art historians through comparison of its stepped-cross motif with Byzantine coinage, provides insight into trading practices in antiquity.
- Chemical composition and inclusion characteristics indicate that the gemstone originated from the Garibpet deposit in India. Garibpet has also been shown to have supplied the rough material for bead production at Arikamedu, an early port and trade center on the southeast Indian coast.
- A sixth-century Greek text describing export of "alabandenum" from the port of Caber, near Arikamedu, has been interpreted as a contemporaneous reference to shipping of almandine from the Coromandel Coast.
- The Byzantine gem serves as tangible evidence of garnet trade between India and the Mediterranean world along the Maritime Silk Road.

Figure 2. This map of southern India shows the locations of Garibpet and Arikamedu on the subcontinent, together with the ancient harbor of Kaveripattinam.

district" of Telangana State (Phani, 2014). Taken together, such references thus chronicle centuries of ongoing use of garnets from the deposit.

An extensive historical role can likewise be documented for Arikamedu, an important port, bead production site, and trading center along the Indian Ocean during the first millennium CE (Wheeler et al., 1946; Casal, 1949; Begley et al., 1996, 2004; Francis, 2004). Some have even equated Arikamedu with the harbor of Podouke (Podukê) mentioned in the *Periplus Maris Erythraei*, a sailing guide for merchants written by an anonymous author in the first century CE (Raman, 1991). Another important ancient harbor on the Indian east coast (the Coromandel Coast), south of Arikamedu, was Kaveripattinam (Rao, 1991a,b; Gaur and Sundaresh, 2006; Sundaresh and Gaur, 2011). The Kaveripattinam port has been associated with the Kaberis Emporium cited by Ptolemy (Raman, 1991) and with a locality referred to as "Caber" by the Greek traveler and merchant Cosmas Indicopleustes in his mid-sixth century CE text known as *Christian Topography* (Banaji, 2015; an English translation is available from Winstedt, 1909, and a modern edition with commentary from Schneider, 2011). It has been speculated that the text mentioning "Caber, which exports alabandenum" refers to shipment of almandine

Figure 3. Early Byzantine garnet intaglio with a stepped-cross motif, dated from the late sixth to eighth century CE. The stone measures 10.1 × 6.1 mm and weighs 1.95 ct. Reflected light. Photo by K. Schmetzer.

garnet (Roth, 1980; Kessler, 2001) on the ancient Maritime Silk Road (see Ptak, 2007).

To date, interpretation of the above-cited sixth-century text has remained obscure, principally because no direct evidence of Garibpet garnets being used in the Mediterranean world during the fifth to seventh or even eighth century CE has been reported. With the aim of probing this question, the present study of an Early Byzantine garnet intaglio (figure 3) was undertaken. Chemical composition and inclusion characteristics were examined using nondestructive methods. Properties from this sample were then compared with those of rough garnets from the Garibpet secondary deposit and fashioned almandines from Merovingian cloisonné jewelry.

MATERIAL AND METHODS

The subject intaglio has been maintained in a private collection (Christian Schmidt, Munich, inventory number 2847) and is said to be from Israel. The sample was previously described by Spier (2011) as catalogue addition No. 58, plate 37. It came to the attention of author HAG while investigating a series of engraved historical garnets from various collections. After a preliminary examination of the sample's inclusion pattern that revealed features typical of garnets from the Garibpet deposit, a more detailed study followed. As all analyses of the engraved gemstone had to be performed by nondestructive methods, only portable X-ray fluorescence (p-XRF) and electron microprobe analysis were employed for determining the major, minor, and trace-element contents. Application of micro-destructive techniques, such as laser ablation–inductively coupled plasma–mass spectrometry (LA-ICP-MS), was not possible.

Chemical analysis was initially achieved with a handheld Niton XL3t XRF analyzer by Thermo Fisher Scientific, which was equipped with a silver anode and a helium purging system. The analysis was performed in the bulk mode ("mining mode") with a collection time of 120 s, using four different settings for acceleration voltage and beam current. The analytical spot size of the primary X-ray beam was in the range of 4 × 3 mm, with the beam directed toward the inclusion-poor side of the gem. The data provided by the automated software were calibrated using a set of approximately 30 gem-quality garnets that had previously been analyzed by electron microprobe, particle-induced X-ray emission (PIXE), and LA-ICP-MS, normalized to 100 wt.%. The detection limits were ~1 wt.% for MgO; ~100 ppm for Ti, Cr, and V; ~50 ppm for Zn; and ~25 ppm for Zr and Y.

Electron microprobe analysis was carried out on a JEOL JXA 8800L microprobe with wavelength-dispersive channels. Analytical conditions were as follows: 15 kV accelerating voltage, 20 nA beam current, 1 µm beam diameter, and counting times of 20 s for peak positions and 20 s for background. Natural and synthetic silicate and oxide mineral standards or pure element standards supplied by Cameca were used for calibration (i.e., andradite for Si and Ca, hematite for Fe, Cr_2O_3 for Cr, corundum for Al, $MnTiO_3$ for Mn and Ti, and MgO for Mg). Kα radiation was utilized in the process. Matrix correction was performed by a ZAF procedure. Under these conditions, the detection limit was ~0.05 wt.% for most elements, and the analytical precision was better than 1% relative for all major elements. The proportion of end members was calculated from the chemical analyses using the methods of Locock (2008).

Optical investigations and documentation were performed with a Schneider immersion microscope with Zeiss optics, a Leica DM LM polarizing micro-

Figure 4. The Early Byzantine garnet intaglio displays an inclusion-rich core, slightly decentered to the right side of the stepped cross, and a more transparent rim. Three areas analyzed by electron microprobe are marked C (core), R (rim), and I (intermediate zone). Transmitted light. Photo by H.A. Gilg.

scope with transmitted and reflected light sources, and an Olympus stereomicroscope, the latter two both equipped with an Olympus DP25 digital camera and Olympus Stream Motion software. Selected mineral phases were identified by micro-Raman spectroscopy using a Horiba Jobin Yvon XploRA PLUS confocal Raman microscope. The spectrometer was equipped with a frequency-doubled Nd:YAG laser (532 nm, with a maximum power of 22.5 mW) and an Olympus LMPLFLN 100× long-working-distance objective with a numerical aperture of 0.9.

PROPERTIES OF THE ENGRAVED ALMANDINE AND COMPARISON WITH GARNETS FROM THE GARIBPET DEPOSIT

Visual Appearance. The historical garnet (figure 3) was red and had been fashioned as an oval, strongly convex cabochon with a concave back. The cabochon measured 10.1 × 6.1 mm, with a height of 4.4 mm from the base to the tip of the dome, and weighed 1.95 ct. The gemstone depicted a simple cross with three steps, and the presence of specific grooves indicated that the design had been engraved using a wheel. This stepped-cross motif—probably depicting the bejeweled cross of Theodosius II at Golgotha—first appeared in Byzantine coinage at the end of the sixth century, in solidi of Roman Emperor Tiberius II Constantine, but the design was also common in the seventh and eighth centuries (Brubaker and Haldon, 2001; Brubaker, 2012). Accordingly, gemstones engraved with this motif can be dated to the period from the late sixth to the eighth century (Spier, 2011). The main usage of garnets in this period, however, is related to the sixth and seventh century, with a decline in the second half of the seventh and a rapid decline in the eighth century (J. Spier, pers. comm., 2018).

The garnet showed a slightly decentered inclusion-rich area (core) that was surrounded by an inclusion-poor, more transparent zone (rim). A small fracture with brownish secondary staining was also seen (figures 3 and 4).

Chemical Composition. Three areas on the convex side of the intaglio were examined chemically via electron microprobe, with several point analyses in each area. Analysis positions are indicated in figure 4. These included the central part of the inclusion-rich core (C); the inner part of the more transparent, inclusion-poor rim (R); and an intermediate area (I) located between the core and the rim. Due to the uneven form of the cabochon, a separate mounting of the garnet was necessary for each sequence. Analyses of a given area that totaled between 98 and 101 wt.% oxides signaled acceptable analytical results, despite the difficult measurement geometry of the curved surface. Analyses below 98 wt.% oxides, stemming either from the uneven surface or from inclusions struck by the electron beam, were rejected. The results are summarized in table 1 and compared with chemical properties of garnets from Garibpet and from Merovingian cloisonné jewelry (see below) in table 2.

The electron microprobe analyses revealed that the engraved gem was a member of the pyrope-almandine

TABLE 1. Chemical properties of the Early Byzantine engraved gemstone from this study.

Sample	Position, electron microprobe analyses			Position, portable X-ray fluorescence analysis
	Major and minor element content, compositional ranges (oxides in wt.%)			
Details	Core, 3 analyses	Intermediate Zone, 9 analyses	Rim, 5 analyses	Rim, 1 analysis
SiO_2	34.96–36.06	35.03–36.50	35.80–36.51	35 ± 2
TiO_2	0.01–0.02	0.00–0.04	0.00–0.05	<0.1
Al_2O_3	20.92–21.67	20.73–21.85	21.26–21.85	20 ± 2
Cr_2O_3	0.02–0.06	0.00–0.04	0.01–0.07	<0.1
Fe_2O_3*	2.57–4.08	1.57–3.03	1.31–2.46	
MnO	1.30–1.35	1.20–1.33	1.13–1.22	1.3 ± 0.3
MgO	2.48–2.63	2.49–2.69	2.56–2.67	<3
CaO	0.68–0.69	0.66–0.70	0.61–0.65	0.9 ± 0.3
FeO*	35.20–36.20	35.71–36.90	36.22–36.87	
FeO_{total}	37.98–38.62	37.69–38.55	38.05–38.60	45 ± 7
	Molecular percentages of end members (ranges, in mol.%)**			
Almandine	80.07–81.49	81.03–82.18	81.49–82.41	
Pyrope	10.12–10.48	10.31–10.72	10.29–10.64	
Spessartine	3.03–3.12	2.74–3.01	2.59–2.70	
Grossular	1.75–1.92	1.53–1.94	1.44–1.80	
Andradite	0.20–1.51	0.10–0.24	0.21–0.44	
	Trace-element content (ppm)			
Y				312
Zn				111
Zr				<25
V				<100
Cr				<100
Ti				<100

** Fe_2O_3 and FeO calculated from stoichiometry*
*** Using the scheme of Locock (2008), the calculated remainder is between 2.4 and 3.8%.*

solid solution series, with almandine between 80.1 and 82.2 mol.% and relatively low pyrope between 10.1 and 10.7 mol.%. Minor percentages of spessartine between 2.6 and 3.1 mol.% and of grossular between 1.4 and 1.9 mol.% were also found (table 1). Ti and Cr were below the detection limit of the electron microprobe. The chemical composition was within the compositional field for garnets from Garibpet (table 2 and figure 5).

The intaglio was chemically zoned, with slightly elevated Mn and thus higher spessartine percentages in the core than in the rim (figure 5, right). A similar Mn zoning was characteristic of Garibpet almandines. A weak zoning of Ca, also observed in some of the Garibpet garnets, was apparent in the engraved gemstone, with slightly higher values in the core and in the intermediate zone than in the rim (figure 5, left). These data on major element zoning were indicative of prograde metamorphic growth (see, e.g., Spear, 1993).

X-ray fluorescence analysis provided meaningful results only for the inclusion-poor rim of the engraved garnet. The data confirmed the average major elemental composition as determined by electron microprobe, especially the low Ca and moderate Mn, but showed considerable uncertainties with respect to Mg, Si, Al, and Fe due to the unfavorable geometry during analysis. The XRF analysis also demonstrated high concentrations of Y (~300 ppm) and Zn (~100 ppm), while Zr, V, Cr, and Ti were below the detection limit of the instrument (table 1). Due to the large spot size and the abundance of inclusions in the core, it was not possible to detect any trace-element zon-

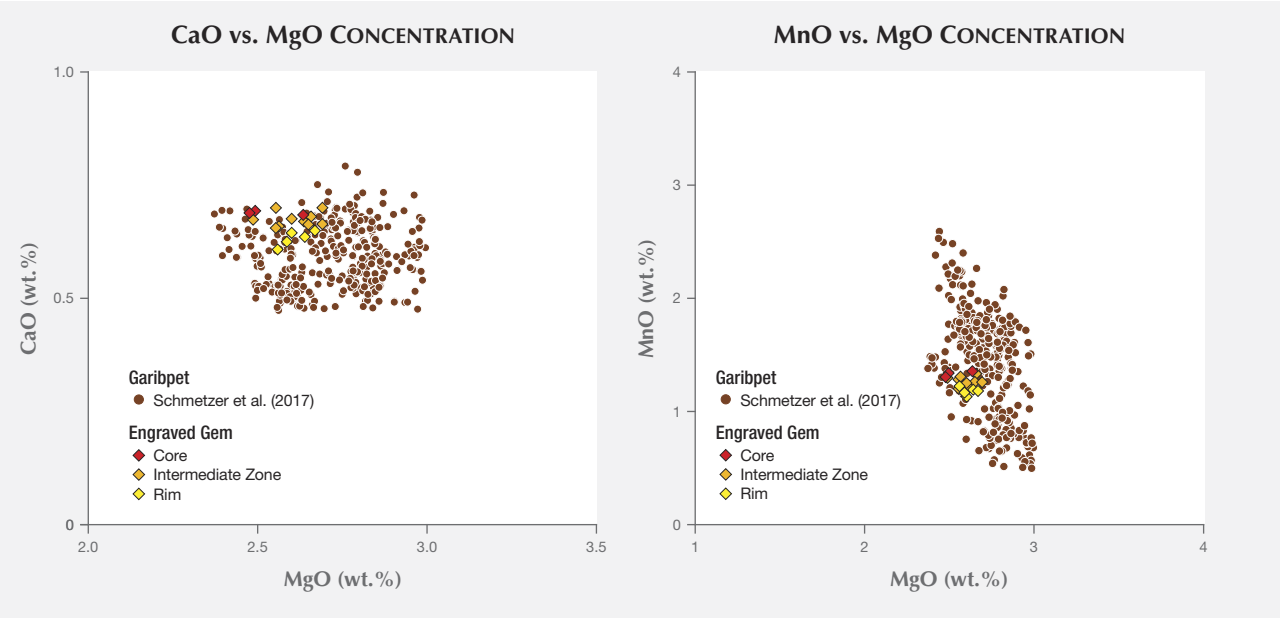

Figure 5. Binary plots showing the chemical composition of the engraved Byzantine garnet and samples from Garibpet as MgO, CaO, and MnO weight percentages.

ing. The high Y and Zn contents and low Zr, V, Cr, and Ti concentrations of the engraved gem were fully consistent with the values reported for Garibpet garnets on the basis of LA-ICP-MS data (table 2).

Microscopic Characteristics. Characteristic inclusions observed in the engraved gem, as well as those seen in garnets from the Garibpet deposit and detailed by Schmetzer et al. (2017), are presented in figures 6 and 8; an overview is provided in table 3.

The gem displayed conspicuous zoning with an inclusion-poor, transparent rim and an inclusion-rich translucent core that was slightly decentered to the right side of the oval (figures 3, 4, and 6A). The translucent core encapsulated a variety of minerals, some of which were opaque and hindered the visibility of the core zone and occasionally the identification of the minerals.

Four types of inclusions proved dominant. A particularly characteristic inclusion feature was the presence of aggregates of curved colorless sillimanite fibers at the border between the inclusion-rich core and the inclusion-poor rim (figure 8E). The other three dominant inclusion types were seen principally within the core, as described below.

Opaque, mostly anhedral elongate crystals (figure 6C) were a prominent core feature and were in part aligned following a schistosity. These irregularly shaped minerals with rounded surfaces were identified as ilmenite by their Raman spectrum. Some Raman spectroscopic measurements also yielded bands characteristic of rutile (444 and 607 cm^{-1}), indicating rutile overgrowth on the ilmenite.

Another common core inclusion was a transparent, colorless, isometric to slightly elongate or irregularly shaped mineral that showed a maximum size of up to several hundred µm (figure 6E). The crystals were identified as quartz by a typical Raman spectrum with a main band at approximately 464 cm^{-1}. Quartz also occurred rarely in the inclusion-poor rim.

Other common inclusions in the core were long-prismatic, partially segmented apatite crystals with rounded edges that could reach a length of more than 200 µm. Included within these crystals were abundant opaque flakes (figure 6G). The small euhedral flakes, approximately 10 µm in diameter, were identified by Raman spectroscopy as graphite (figure 7). The prominent G band at 1580 cm^{-1} in the first-order region and the second-order bands between 2400 and 3300 cm^{-1} were very sharp, while the D1 band was poorly developed, thus signaling high-temperature growth conditions of at least 600°C (Wopenka and Pasteris, 1993; Beyssac et al., 2002).

Notably, the four dominant features just described matched those found in Garibpet garnets (see Schmetzer et al., 2017). The sillimanite fibers between the core and rim were the signature inclusion feature observed in Garibpet garnets and in beads from Arikamedu (Schmetzer et al., 2017), with an

TABLE 2. Comparison of chemical features in the Early Byzantine engraved gemstone, garnets from the Garibpet deposit, and Cluster A and B almandines from Merovingian cloisonné jewelry.

Sample	Engraved gem	Garibpet	Cluster A [Type II]	Cluster B [Type I]
Major and minor elements	**Mean values with standard deviation [ranges], in wt.%**			
Analytical technique, number of analyses	EMPA, n = 17[1]	EMPA, n = 329[2]	EMPA, n = 28[3] PIXE, n = 175[5]	EMPA, n = 85[3] PIXE, n = 491[5]
SiO_2	35.82 ± 0.48 [34.96–36.51]	36.05 ± 0.34 [34.74–36.84]	37.78 ± 1.04 [34.19–39.62]	37.26 ± 0.55 [35.77–38.61]
			37.52 ± 0.66 [36.09–39.84]	36.83 ± 0.48 [36.00–37.98]
Al_2O_3	21.43 ± 0.35 [20.73–21.85]	21.54 ± 0.22 [20.55–22.24]	21.62 ± 0.64 [19.14–22.73]	21.14 ± 0.37 [20.36–22.31]
			21.65 ± 0.44 [20.36–23.35]	21.28 ± 0.33 [20.28–22.36]
MnO	1.25 ± 0.07 [1.16–1.35]	1.44 ± 0.45 [0.50–2.58]	1.26 ± 0.76 [0.13–3.17]	0.30 ± 0.24 [0.00–1.10]
			1.50 ± 0.85 [0.00–4.42]	0.25 ± 0.22 [0.00–1.28]
MgO	2.59 ± 0.07 [2.48–2.69]	2.72 ± 0.15 [2.37–2.99]	6.83 ± 1.00 [5.05–8.87]	4.71 ± 0.67 [3.29–6.26]
			6.49 ± 0.74 [4.46–9.07]	4.69 ± 0.66 [3.04–6.53]
CaO	0.66 ± 0.02 [0.61–0.69]	0.59 ± 0.07 [0.47–0.73]	1.46 ± 0.21 [0.96–2.01]	0.63 ± 0.16 [0.32–1.03]
			1.30 ± 0.20 [0.72–2.01]	0.63 ± 0.15 [0.32–1.03]
FeO_{total}	38.22 ± 0.26 [37.69–38.62]	37.72 ± 0.52 [36.30–39.21]	31.00 ± 1.02 [28.41–31.94]	36.11 ± 1.00 [33.49–37.75]
			31.24 ± 1.39) [26.52–35.63]	36.10 ± 1.13 [32.98–38.35]
Trace elements	**Mean values with standard deviation [ranges], in ppm**			
Analytical technique, number of analyses	p-XRF, n = 1[1]	LA-ICP-MS, n = 31[2]	PIXE, n = 175[5]	PIXE, n = 491[5]
Y	312	213 ± 70 [45–401]	534 ± 325 [57–1478]	57 ± 56 [0–416]
Zn	111	107 ± 15 [77–129]	34 ± 31 [0–369]	14 ± 30 [0–432]
Zr	<50	4 ± 2 [1–11]	26 ± 96 [0–1084]	7 ± 7 [0–34]
V	<100	28 ± 6 [17–44]	72 ± 30 [0–159]	10 ± 14 [0–86]
Cr	<100	55 ± 42 [25–255]	444 ± 165 [101–995]	7 ± 15 [0–121]
Ti	<150	38 ± 9 [18–55]	126 ± 75 [0–441]	74 ± 43 [0–257]
Chemical zoning	**Yes** **[Mn,Ca][1]**	**Yes** **[Mn,Ca,Zn][2]**	**Yes** **[Y][4]**	**Not described**

[1]*This study*
[2]*Schmetzer et al. (2017)*
[3]*Quast and Schüssler (2000)*
[4]*Calligaro et al. (2006-2007)*
[5]*Gilg et al. (2010)*

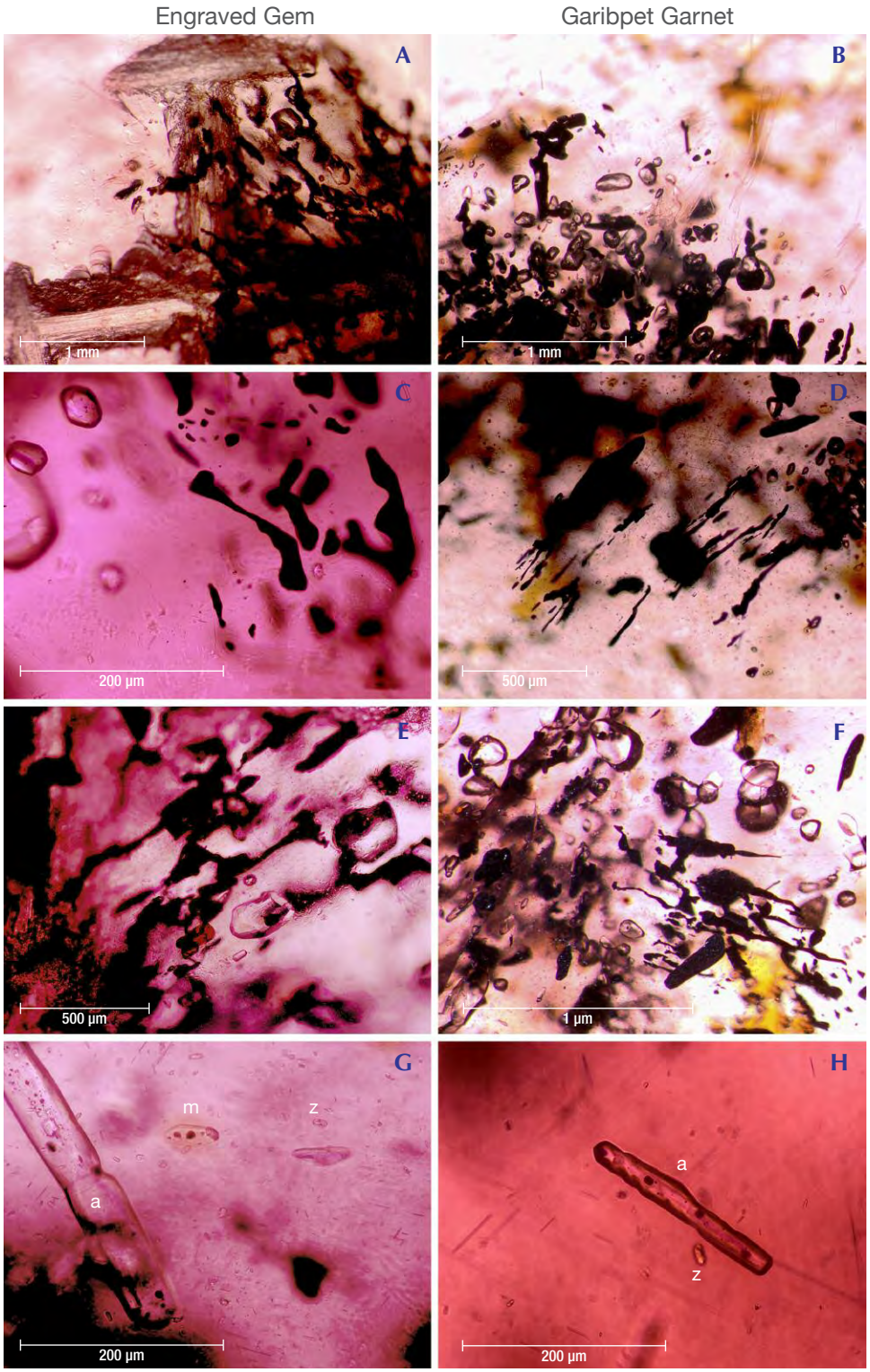

Figure 6. Comparison of inclusions in the Early Byzantine engraved gem (left) with garnets from the Garibpet deposit (right). A and B: Inclusion-rich core and inclusion-poor rim with sillimanite fibers at the boundary. C and D: Irregularly shaped ilmenite. E and F: Subrounded quartz crystals. G and H: Large long-prismatic apatite crystal (a) with characteristic graphite inclusions, along with short-prismatic zircon (z) and monazite (m) crystals. Photomicrographs by H.A. Gilg.

identical distribution and shape (figures 6B, 8F). The ilmenite, quartz, and long-prismatic graphite-bearing apatite were also typical for Garibpet stones (figure 6D, F, H; Schmetzer et al., 2017).

Turning to less dominant but still frequent inclusions in the engraved gemstone core, two types should be mentioned. One consisted of very small, transparent short-prismatic zircon crystals that

TABLE 3. Comparison of inclusion characteristics in the Early Byzantine engraved gemstone, garnets from the Garibpet deposit, and Cluster A and B almandines from Merovingian cloisonné jewelry.

Sample	Engraved gem (this study)	Garibpet (Schmetzer et al., 2017)	Cluster A [Type II][1]	Cluster B [Type I][1]
Inclusions	**Frequency**			
Ilmenite	+++	+++	+++	
Quartz	+++	+++	+++	
Biotite	+	+	+	
Chlorite in fluid inclusions		+	+	++
Apatite, euhedral, inclusion-rich	+++	+++		
Apatite, anhedral, green				+++
Rutile, needle network, coarse			+++	
Rutile, needle network, patchy	+	+		+
Rutile, short prismatic	+	+	+	
Sillimanite bundles at core-rim boundary	+++	+++		
Sillimanite, individual coarse needles		+	++	
Monazite	++	++	++	++
Zircon	++	++	+++	+
Uraninite				++
Graphite in apatite	+++	+++		
Graphite in monazite	++	++	++	++
Graphite	+		+	
Goethite in fractures	+	+	+	+

+++ dominant, ++ frequently present, + occasionally observed
[1]Gilg et al. (2010), Horváth and Bendö (2011), Gilg and Hommrichhausen, unpublished research

caused tension cracks in the host garnet (figure 6G). Another was found as irregularly shaped monazite crystals less than 50 µm in diameter and surrounded by distinctive brownish halos related to radiation damage. The monazites often contained opaque graphite and quartz inclusions as well (figures 6G, 8A). Both zircon and monazite, which are radioactive minerals, were also common in Garibpet garnets and displayed similar habits in that material (figures 6H, 8B).

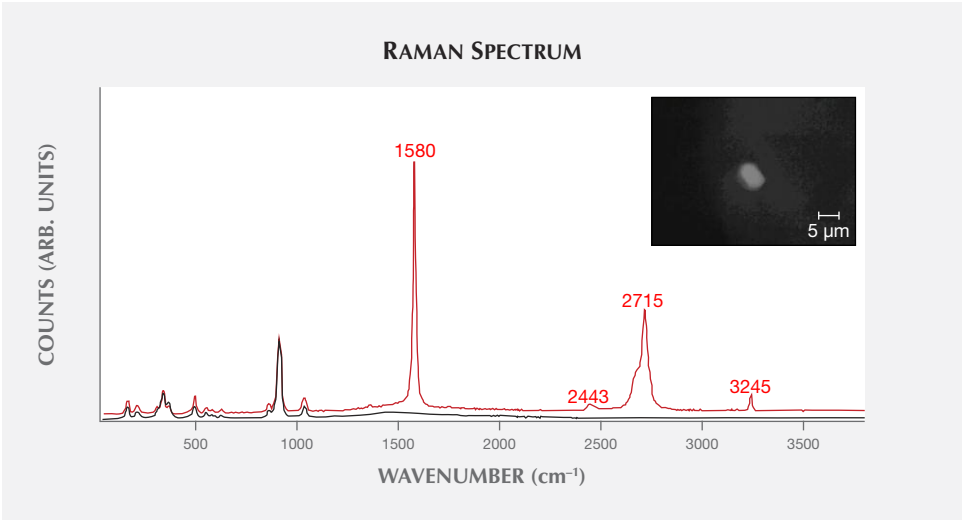

Figure 7. Raman spectrum of a graphite inclusion (red) and the host garnet (black) in the core of the engraved gem. The inset shows the size and shape of the graphite, appearing as a bright crystal in the center, in reflected light. Photomicrograph by H.A. Gilg.

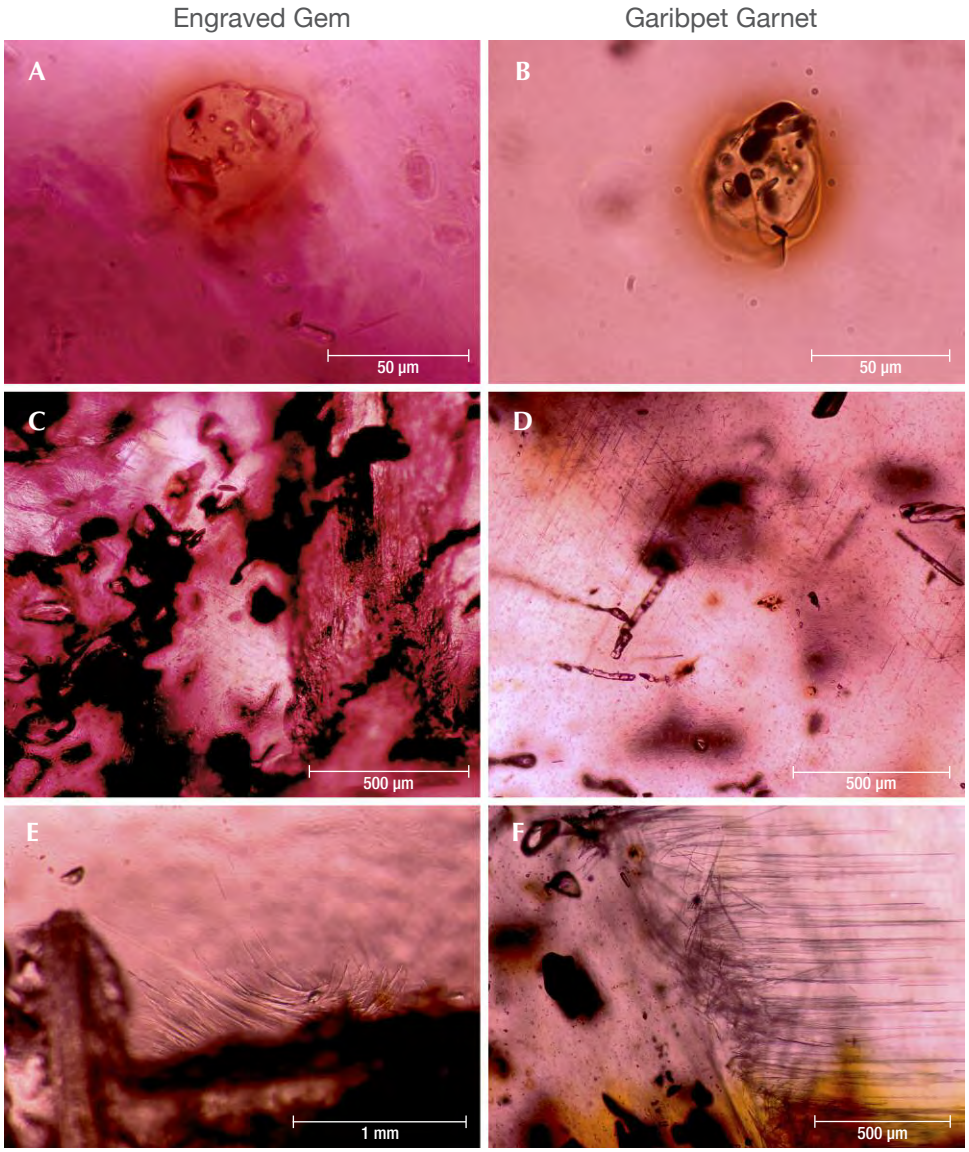

Figure 8. Comparison of additional inclusions in the Early Byzantine engraved gem (left) with garnets from Garibpet (right). A and B: Monazite with graphite and quartz inclusions. C and D: Patchy network of oriented rutile needles. E and F: Sillimanite fibers at the boundary between the inclusion-rich core and the inclusion-poor rim. Photomicrographs by H.A. Gilg.

Less frequently, a three-dimensional network of very thin rutile needles ("silk") was irregularly distributed in a patchy manner within the core zone of the engraved garnet (figure 8C). Such distribution of rutile needles was similar to a feature observed in about 10–15% of the Garibpet garnets (figure 8D).

A rare brown platy crystal approximately 150 µm in length was attached to an ilmenite crystal in the engraved Byzantine garnet (figure 9, top). It resembled short prismatic rutile crystals found overgrown on ilmenite in some Garibpet garnets (see figure 26D in Schmetzer et al., 2017), but the mineral was identified here as biotite on the basis of its Raman spectrum, with an OH-stretching band at about 3664 cm^{-1} (figure 9A; Wang et al., 2015). Meanwhile, with some further study of inclusion characteristics, biotite flakes have also been identified in samples from both Garibpet and Arikamedu (figure 9, bottom). Biotite is considered a less common accessory inclusion mineral found in Garibpet materials.

In the inclusion-poor rim of the engraved garnet, only a few quartz and zircon crystals and a brownish goethite-bearing fracture were observed (figure 4).

COMPARISON WITH CALCIUM-POOR ALMANDINES USED IN CLOISONNÉ JEWELRY

In contrast to the broad equivalence between the chemical and inclusion features of the Early Byzantine engraved garnet and garnets from the Garibpet deposit, comparison with the two dominant Ca-poor almandine types in Merovingian cloisonné jewelry

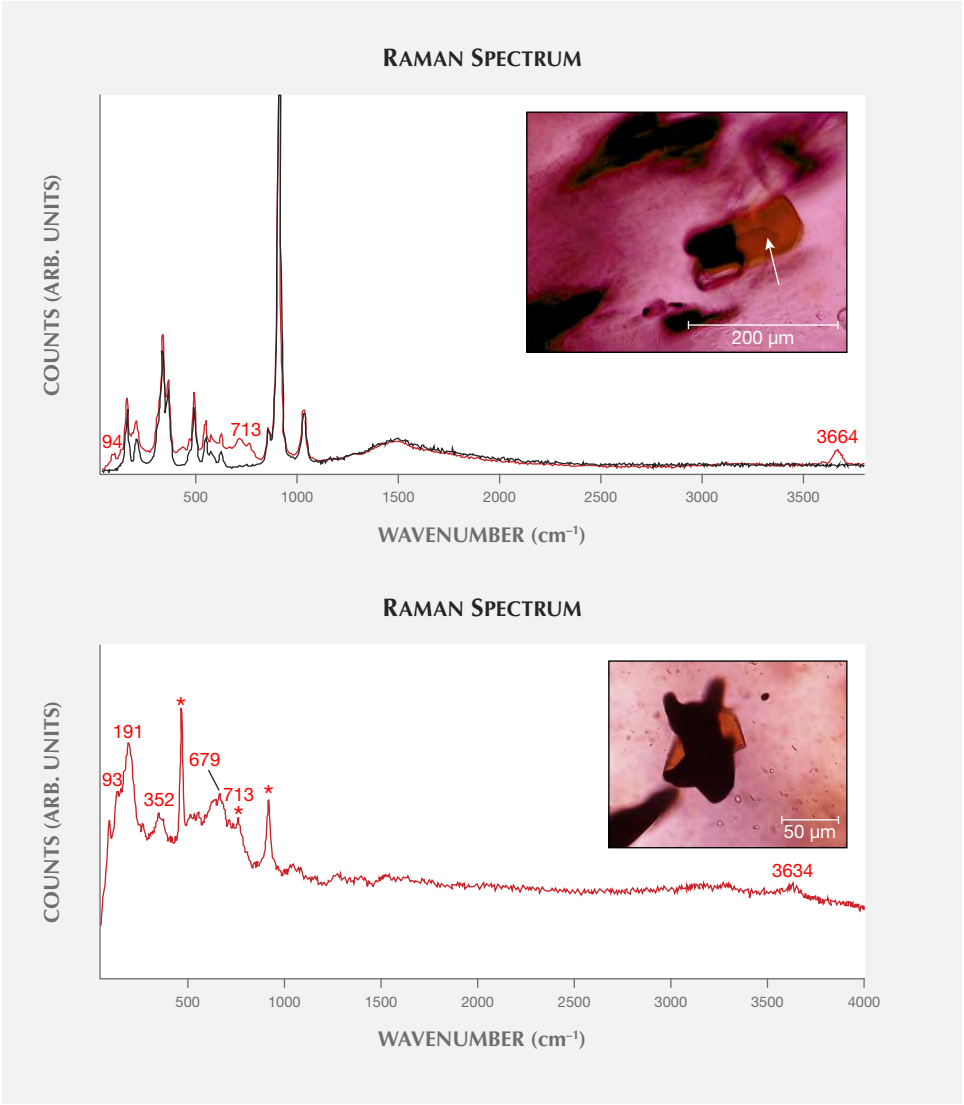

Figure 9. Top: Raman spectrum of a brownish biotite inclusion (red) and the host garnet (black) in the core of the engraved gem. The inset shows the size and shape of the biotite crystal, which is attached to an opaque ilmenite flake; the tip of the arrow shows the analysis spot. Bottom: Raman spectrum of a brownish biotite inclusion (red, the three peaks marked with an asterisk (*) are related to the host garnet) in a garnet from Garibpet, India. The inset shows the size and shape of the biotite crystal, which is attached to an opaque ilmenite. Photomicrographs by H.A. Gilg.

(Cluster A and Cluster B of Gilg et al., 2010, which are identical to Type II and Type I, respectively, of Calligaro et al., 2002) revealed substantially greater divergence. Again, tables 2 and 3 summarize these results.

Chemical Composition. As explained above, the composition of the Early Byzantine gemstone overlapped for all elements with the Ca-poor garnets from the Garibpet deposit. Conversely, considerably lower almandine and higher pyrope contents were measured for the two Ca-poor almandine types (Cluster A and Cluster B) in cloisonné jewelry (figures 10 and 11). Moreover, the high MnO, Y, and Zn levels found in the intaglio demonstrated inconsistency with Cluster B garnets, while the lower CaO, low Cr, and high Zn were incompatible with Cluster A garnets.

The low Ca content of the engraved gem further excluded any meaningful similarity with Ca-rich almandines, such as the Cluster C garnets observed in Scandinavian Early Medieval cloisonné jewelry (Löfgren, 1973; Mannerstrand and Lundqvist, 2003; Gilg and Hyršl, 2014) or the Ca- and Mn-rich almandines commonly encountered among Hellenistic or Early Roman engraved gems (Gilg and Gast, 2012; Thoresen and Schmetzer, 2013).

Microscopic Characteristics. A zonal arrangement of inclusions with an inclusion-rich core and an inclusion-poor rim has not been reported for either of the two Ca-poor Merovingian almandine types. Likewise, bundles of sillimanite fibers at a boundary between the core and rim portions have not been observed in either Cluster A or Cluster B garnets. Coarse silliman-

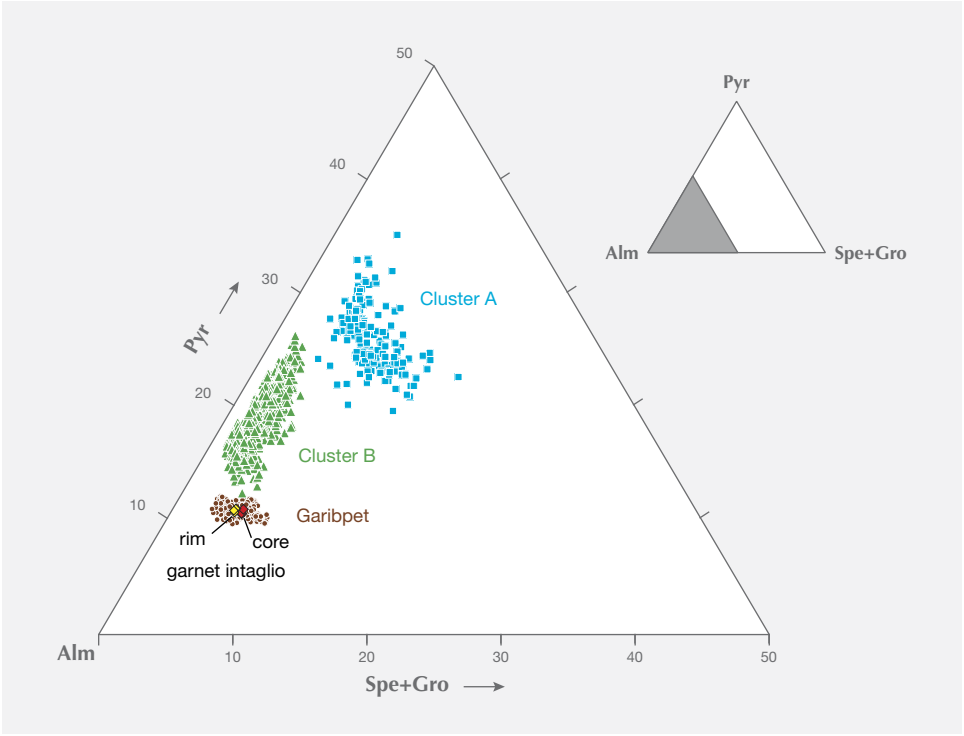

Figure 10. Triangular diagram of the chemical composition in molecular percentages (mol.%) of the core (red diamonds) and the rim (yellow diamonds) of the Early Byzantine garnet intaglio, in comparison with rough from the Garibpet deposit (brown circles, data from Schmetzer et al., 2017) and Cluster A and B almandines from Early Medieval cloisonné jewelry (blue squares and green triangles, respectively; data from Quast and Schüssler, 2000, and Gilg et al., 2010). Alm = almandine, Pyr = pyrope, Spe = spessartine, Gro = grossular.

ite needles, however, have been described for Cluster A almandines (figure 12C), but they were located within rather than bordering inclusion-rich zones, and none have been seen in Cluster B almandines (Calligaro et al., 2006-2007; Horváth and Bendö, 2011; Gast et al., 2013).

Two other dominant inclusions found in both the engraved garnet and the Garibpet material, ilmenite

Figure 11. Binary plots comparing the chemical composition of the garnet intaglio, with Garibpet rough and Cluster A and B almandines as MgO, CaO, and MnO weight percentages.

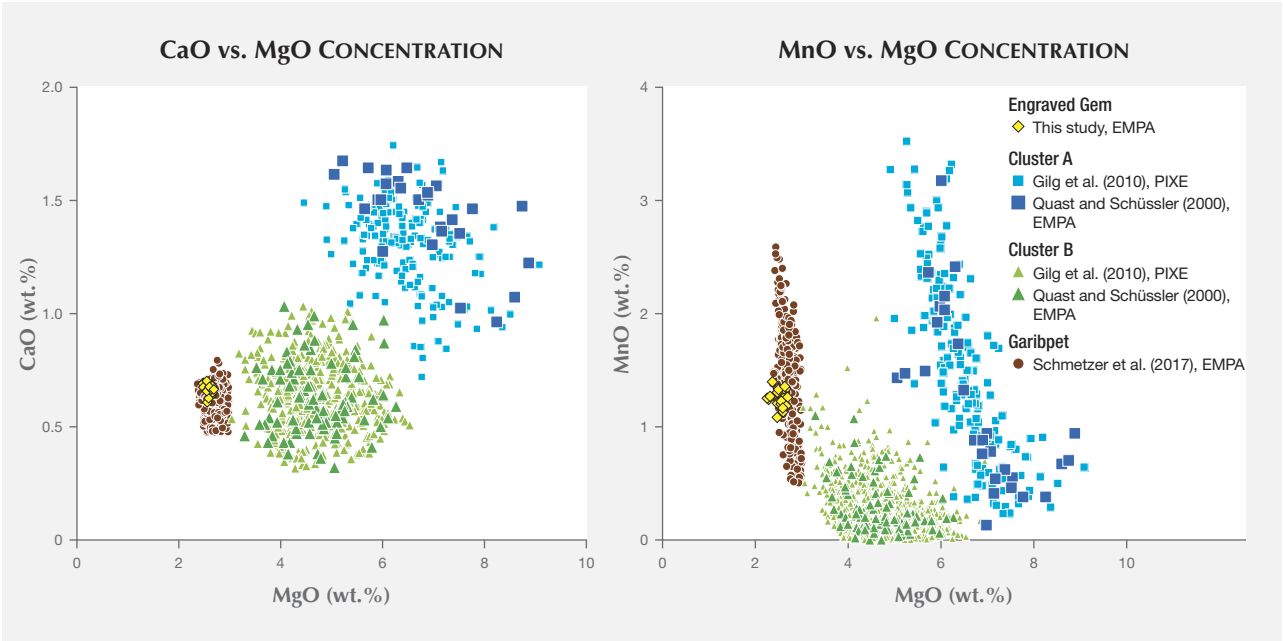

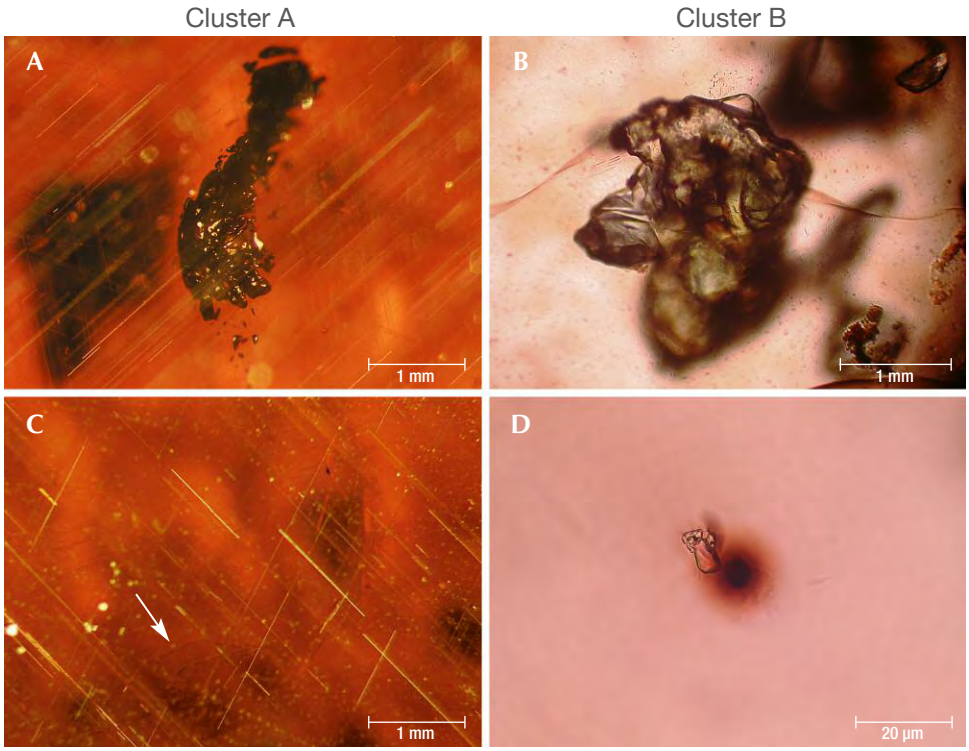

Figure 12. Characteristic inclusions in Ca-poor almandines from Merovingian jewelry of Cluster A (left) and Cluster B (right). A: Irregularly shaped ilmenite and acicular rutile network. B: Greenish xenomorphic apatite. C: Curved sillimanite needles (arrow) and rutile network. D: Black uraninite inclusion with brown radiation halo, along with colorless crystals of apatite (largest grain) and zircon (small grains with tension cracks). Photomicrographs by N. Hommrichhausen (A and C) and H.A. Gilg (B and D).

and quartz, have been reported with similar habits in Cluster A garnets (figure 12A) but have not been seen in Cluster B samples (Calligaro et al., 2002, 2006-2007; Gilg et al., 2010).

Apatite has been identified as a dominant inclusion in Cluster B garnets but has proven extremely rare in Cluster A samples (Calligaro et al., 2002, 2006-2007; Gilg et al., 2010). Nonetheless, apatite crystals in Cluster B garnets (figure 12B) have shown a characteristic greenish color, xenomorphic shape, and lack of graphite inclusions (Gilg et al., 2010), an appearance distinct from that of apatite in the engraved gem and the Garibpet garnets.

Monazite and zircon inclusions have been noted in all different types of almandines discussed in this paper. A three-dimensional network of rutile inclusions (figure 12A,C) has only very rarely been observed in Cluster B garnets but has occurred commonly in Cluster A garnets (Calligaro et al., 2002, 2006-2007; Gilg et al., 2010; Gast et al., 2013). Brownish biotite inclusions have so far only been detected in Cluster A garnets by scanning electron microscopy (Horváth and Bendö, 2011). Uraninite inclusions have been reported as a typical feature only of Cluster B garnets (figure 12D; Calligaro et al., 2002, 2006-2007).

Although certain mineral inclusion features of the engraved gem can be observed in either of the two Ca-poor almandine types in Merovingian jewelry, on balance the combination of features is quite distinctive and consistent only with garnets from the Garibpet deposit. In particular, the sillimanite fibers at the border between an inclusion-rich core and an inclusion-poor rim and the long-prismatic graphite-bearing apatite crystals can be considered the most distinguishing inclusion characteristics.

DISCUSSION AND CONCLUSIONS

Schmetzer et al. (2017) proposed that assignment of garnet samples from a historical context to a specific garnet type or cluster used in antiquity should ideally be based on a series of criteria. For instance:

1. Major element chemical composition, including proportions of garnet end members
2. Chemical zoning for major and minor elements within the crystals from core to rim
3. Trace-element contents
4. Zoning of trace elements from core to rim
5. General inclusion assemblage
6. Appearance of individual inclusions
7. Distribution and zoning of inclusions

It was emphasized that a detailed correlation of several features, rather than merely one or two, should

be considered a prerequisite for assigning a sample to an established garnet type or cluster.

Here, the present study has demonstrated that the engraved gemstone and samples from the Garibpet deposit are consistent with respect to six of the seven criteria just mentioned, namely 1–3 and 5–7. Examining trace-element zoning in the gem was not possible due to experimental restrictions.

Only one inclusion characteristic was not entirely congruent: the absence of thick acicular sillimanite needles in the engraved gemstone. The thick acicular sillimanite needles were observed only in about 10% of Garibpet garnets, however. This is understandable, since garnets from different areas of the large deposit, mined during different historical eras, might also show a degree of variability.

Thus, being unaware of any other known deposit with garnets showing the characteristic features described for the Garibpet material, the authors conclude that the Early Byzantine garnet engraved with a Christian motif originated from this secondary deposit. Garnets from the Garibpet deposit were used extensively for the historical bead-making industry of Arikamedu, in Tamil Nadu State. The bead enterprise flourished from the second century BCE at least until the end of the first millennium CE and probably even to the early seventeenth century (Begley et al., 2004; Francis, 2002, 2004; Schmetzer et al., 2017). The examined spherical and faceted bicone garnet beads from the Arikamedu archaeological site had diameters of less than 5.5 mm, in contrast to the 11 mm length of the engraved gemstone. Nonetheless, rough fragments from Arikamedu reaching 11 mm in size were observed during the 2017 investigation, and material even exceeding that size was found at the Garibpet deposit (Schmetzer et al., 2017).

Accordingly, the present study can be considered to offer the first strong, tangible evidence of garnet trading from the eastern coast of India to the Mediterranean realm, including the Byzantine Empire, in the late sixth to eighth century CE, even as use of garnet for cloisonné jewelry in central Europe declined (for details see Schmetzer et al., 2017, p. 599). When such evidence is combined with the recent work demonstrating use of Garibpet material for bead-making at Arikamedu, the shipment of garnet rough or beads from Arikamedu or nearby harbors on the Coromandel Coast can logically be assumed. Doing so is also consistent with prior interpretation of the sixth-century text by Cosmas Indicopleustes regarding export of "alabandenum" to the Mediterranean region from a port named "Caber," as referring to garnets shipped from Kaveripattinam, close to Arikamedu. Hence, the idea that garnets were transported and traded from Indian ports along the so-called Maritime Silk Road, which connected China with the Western world, becomes a supportable proposition.

It should be noted, however, that the vast majority of almandine garnets that were used for Merovingian cloisonné jewelry and supposedly derived from an Indian source (Greiff, 1998; Quast and Schüssler, 2000; Calligaro et al., 2002, 2006-2007; Gilg et al., 2010; Périn and Calligaro, 2016) must have originated from different localities and likely were not traded from the Coromandel Coast.

Lastly, as a practical point, this study further demonstrates that chemical analysis of ancient garnets using a portable X-ray fluorescence instrument with helium flow mode, in combination with microscopic investigations, can be sufficient to assign a gemstone to a known almandine type or cluster, despite the relatively low precision of the XRF technique for some major elements, (e.g., Fe, Si, Al, and Mg). Specifically, the capability of the device to measure important minor elements including Mn, Ca, and to a lesser extent Mg, as well as the characteristic trace elements Y, Cr, and Zn, provides adequate data. Thus, this research may encourage other scientists to augment the information compiled to date on historical gemstones and their trading.

ABOUT THE AUTHORS

Prof. Gilg is a professor at the Chair of Engineering Geology, Technical University of Munich, Germany. Dr. Schmetzer is an independent researcher living in Petershausen, near Munich. Prof. Schüssler is affiliated with the Institute for Geography and Geology, Würzburg University, Germany.

ACKNOWLEDGMENTS

The authors would like to thank Dr. Christian Schmidt of Munich for the opportunity to analyze engraved garnets from his collection with non-destructive methods. Prof. R. Gebhard (Archäologische Staatssammlung, Munich) provided access to the portable X-ray fluorescence instrument.

REFERENCES

Adams N. (2011) The garnet millennium: The role of seal stones in garnet studies. In C. Entwistle and N. Adams, Eds., *'Gems of Heaven': Recent Research on Engraved Gemstones in Late Antiquity c. AD 200–600*. British Museum Research Publication 177, The British Museum, London, pp. 10–24.

——— (2014) *Bright Lights in the Dark Ages: The Thaw Collection of Early Medieval Ornaments*. D. Giles Ltd, London, 408 pp.

Adams N., Lüle C., Passmore E. (2011) Lithois Indikois: Preliminary characterisation of some garnet seal stones from Central and South Asia. In C. Entwistle and N. Adams, Eds., *'Gems of Heaven': Recent Research on Engraved Gemstones in Late Antiquity c. AD 200–600*. British Museum Research Publication 177, The British Museum, London, pp. 25–38.

Arrhenius B. (1985) *Merovingian Garnet Jewellery: Emergence and Social Implications*. Almqvist och Wiksell International, Stockholm, 229 pp.

Banaji J. (2015) "Regions that look seaward": Changing fortunes, submerged histories and the slow capitalism of the sea. In M. Maiuro and F. De Romanis, Eds., *Across the Ocean: Nine Chapters on Indo-Mediterranean Trade*. Brill, Leiden, the Netherlands pp. 114–126.

Bauer M. (1896) *Edelsteinkunde*. Chr. Herm. Tauchnitz, Leipzig, Germany pp. 400–404.

Begley V., Francis P., Jr., Mahadevan I., Raman K.V., Sidebotham S.E., Slane K.W., Will E.L. (1996) *The Ancient Port of Arikamedu. New Excavations and Researches 1989-1992, Volume One*. École Française d'Extrême-Orient, Pondicherry, India, 400 pp.

Begley V., Francis P., Jr., Raman K.V., Sidebotham S.E., Will E.L. (2004) *The Ancient Port of Arikamedu: New Excavations and Researches, 1989-1992, Vol. 2*. École Française d'Extrême-Orient, Paris, 644 pp.

Beyssac O., Goffé B., Chopin C., Rouzaud J.N. (2002) Raman spectra of carbonaceous material in metasediments: A new geothermometer. *Journal of Metamorphic Geology*, Vol. 20, No. 9, pp. 859–871, http://dx.doi.org/10.1046/j.1525-1314.2002.00408.x

Borell B. (2017) Gemstones in southeast Asia and beyond: Trade along the maritime networks. In A. Hilgner, D. Quast, and S. Greiff, Eds., *Gemstones in the First Millennium AD: Mines, Trade, Workshops and Symbolism*. RGZM Tagungen Vol. 30, Verlag des Römisch-Germanischen Zentralmuseums, Mainz, pp. 21–44.

Brubaker L. (2012) *Inventing Byzantine Iconoclasm*. Bristol Classical Press, London, 134 pp.

Brubaker L., Haldon J. (2001) *Byzantium in the Iconoclast Era (ca 680–850): The Sources: An Annotated Survey*. Ashgate Publishing, Aldershot, UK, 324 pp.

Bugoi R., Oanţâ-Marghitu R., Calligaro T. (2016) IBA investigations of loose garnets from Pietroasa, Apahida and Cluj-Someşeni treasures (5th century AD). *Nuclear Instruments and Methods in Physics Research B*, Vol. 371, pp. 401–406, http://dx.doi.org/10.1016/j.nimb.2015.09.038

Calligaro T., Colinart S., Poirot J.-P., Sudres C. (2002) Combined external-beam PIXE and μ-Raman characterisation of garnets used in Merovingian jewellery. *Nuclear Instruments and Methods in Physics Research B*, Vol. 189, No. 1-4, pp. 320–327, http://dx.doi.org/10.1016/S0168-583X(01)01078-3

Calligaro T., Périn P., Vallet F., Poirot J.-P. (2006-2007) Contribution á l'étude des grenats mérovingiens (Basilique de Saint-Denis et autres collections du musée d'Archéologie nationale, diverses collections publiques et objects de fouilles récentes). *Antiquités Nationales*, Vol. 38, pp. 111–144.

Carter A.K. (2012) Garnet beads in Southeast Asia: Evidence for local production? In M.-L. Tjoa-Bonatz, A. Reinecke, and D. Bonatz, Eds., *Crossing Borders: Selected Papers from the 13th International Conference of the European Association of Southeast Asian Archaeologists, Volume 1*. NUS Press, Singapore, pp. 296–306.

——— (2013) Trade, exchange, and socio-political development in Iron Age (500 BC–AD 500) mainland southeast Asia: An examination of stone and glass beads from Cambodia and Thailand. Unpublished PhD dissertation, Department of Anthropology, University of Wisconsin-Madison.

——— (2016) Determining the provenience of garnet beads using LA-ICP-MS. In L. Dussubieux, M. Golitko, and B. Gratuze, Eds., *Recent Advances in Laser Ablation ICP-MS for Archaeology*. Springer, Vienna, pp. 235–266.

Casal J.M. (1949) *Fouilles de Virampatnam-Arikamedu*. Imprimerie Nationale, Paris, 71 pp.

Entwistle C., Adams N. (2011) *'Gems of Heaven': Recent Research on Engraved Gemstones in Late Antiquity c. AD 200–600*. British Museum Research Publication 177, The British Museum, London.

Francis P., Jr. (2002) *Asia's Maritime Bead Trade: 300 B.C. to the Present*. University of Hawai'i Press, Honolulu, 305 pp.

——— (2004) Beads and selected small finds from the 1989-92 excavations. In V. Begley et al., Eds., *The Ancient Port of Arikamedu: New Excavations and Researches, 1989-1992, Volume Two*. École Française d'Extrême-Orient, Paris, pp. 447–604.

Gast N., Calligaro T., Gilg H.A., Macknapp K., Schmahl W.W., Stark R. (2013) Die Funde: Farbige Einlagen. In R. Gebhard and B. Haas-Gebhard, Eds., *Unterhaching. Eine Grabgruppe der Zeit um 500 n. Chr. bei München*. Abhandlungen und Bestandskataloge der Archäologischen Staatssammlung München, Vol. 1, pp. 50–74.

Gaur A.S., Sundaresh (2006) Onshore and near shore explorations along the southern Tamilnadu coast: With a view to locating ancient ports and submerged sites. In P.C. Reddy, Ed., *Mahasenasiri: Riches of Indian Archaeological and Cultural Studies*. Sharda Publishing House, New Delhi, pp. 122–130.

Gilg H.A., Gast N. (2012) Naturwissenschaftliche Untersuchungen an Granatgemmen der Sammlung James Loeb. In F. Knauß, Ed., *Die Gemmen der Sammlung James Loeb, Forschungen der Staatlichen Antikensammlung und Glyptothek*, Supplement zu Band 1. Kunstverlag J. Fink, Lindenberg im Allgäu, pp. 48–57, 62–63.

Gilg H.A., Hyršl J. (2014) Garnet deposits in Europe. In J. Toussaint, Ed., *Rouges et Noirs. Rubies, grenat, onyx, obsidienne et autres minéraux rouges et noirs dans l'art et l'archéologie*. Monographies du Musée Provincial des Arts du Namurois-Trésor d'Oignies (TreM.a), Société Archéologique de Namur, Namur, pp. 144–173.

Gilg H.A., Gast N., Calligaro T. (2010) Vom Karfunkelstein. In L. Wamser, Ed., *Karfunkelstein und Seide*. Ausstellungskataloge der Archäologischen Staatssammlung (München), Band 37, pp. 87–100.

Greiff S. (1998) Naturwissenschaftliche Untersuchungen zur Frage der Rohsteinquellen für frühmittelalterlichen Almandingranatschmuck rheinfränkischer Provenienz. *Jahrbuch des Römisch-Germanischen Zentralmuseums Mainz*, Vol. 45, No. 2, pp. 599–646.

Horváth E., Bendö Z. (2011) Provenance study on a collection of loose garnets from a Gepidic period grave in Northeast Hungary. *Archeometriai Mühely*, Vol. 2011, No. 1, pp. 17–32.

Kessler O. (2001) Der spätantik-frühmittelalterliche Handel zwischen Europa und Asien und die Bedeutung des Almandins als Fernhandelsgut. In *Archäologisches Zellwerk: Beiträge zur Kulturgeschichte in Europa und Asien*; Internationale Archäologie: Studia honoraria, Vol. 16, Verlag Marie Leidorf, Rahden, pp. 113–128.

Locock A.J. (2008) An Excel spreadsheet to recast analyses of garnet into end-member components, and a synopsis of the crystal

chemistry of natural silicate garnets. *Computers & Geosciences*, Vol. 34, No. 12, pp. 1769–1780, http://dx.doi.org/10.1016/j.cageo.2007.12.013
Löfgren J. (1973) Die mineralogische Untersuchung der Granaten von Paviken auf Gotland. *Early Medieval Studies*, Vol. 6, No. 9, pp. 78–96.
Mannerstrand M., Lundqvist L. (2003) Garnet chemistry from the Slöinge excavation, Halland and additional Swedish and Danish excavations—Comparisons with garnet occurring in a rock context. *Journal of Archaeological Science*, Vol. 30, No. 2, pp. 169–183, http://dx.doi.org/10.1006/jasc.2000.0583
Mathis F., Vrielynck O., Laclavetine K., Chêne G., Strivay D. (2008) Study of the provenance of Belgian Merovingian garnets by PIXE at IPNAS cyclotron. *Nuclear Instruments and Methods in Physics Research B*, Vol. 266, No. 10, pp. 2348–2352, http://dx.doi.org/10.1016/j.nimb.2008.03.055
Mirza K. (1937) A brief outline of Hyderabad State with a reference to its mineral resources. *Hyderabad Geological Series Bulletin*, No. 2, p. 39.
Périn P., Calligaro T. (2007) Neue Erkenntnisse zum Arnegundegrab. Ergebnisse der Metallanalysen und der Untersuchungen organischer Überreste aus Sarkophag 49 aus der Basilika von Saint-Denis. *Acta Praehistorica et Archaeologica*, Vol. 39, pp. 147–179.
——— (2016) Note sur l'origine des grenats utilises par les orfèvres du haut Moyen Âge occidental européen. In Á. Bollók, G. Csiky, and T. Vida, Eds., *Between Byzantium and the Steppe: Archaeological and Historical Studies in Honour of Csanád Bálint on the Occasion of His 70th Birthday*. MTA BTK Régészeti Intézet, Budapest, pp. 75–85.
Phani P.R. (2014) Mineral resources of Telangana State, India: The way forward. *International Journal of Innovative Research in Science, Engineering and Technology*, Vol. 3, No. 8, pp. 15450–15459, http://dx.doi.org/10.15680/IJIRSET.2014.0308052
Ptak R. (2007) *Die maritime Seidenstrasse*. Verlag C.H. Beck, Munich, 368 pp.
Quast D., Schüssler U. (2000) Mineralogische Untersuchungen zur Herkunft der Granate merowingerzeitlicher Cloisonnéarbeiten. *Germania*, Vol. 78, No. 1, pp. 75–96.
Raman K.V. (1991) Further evidence of Roman trade from costal sites in Tamil Nadu. In V. Begley and R.D. De Puma, Eds., *Rome and India: The Ancient Sea Trade*. University of Wisconsin Press, Madison, pp. 125–133.
Rao S.R (1991a) Underwater exploration of submerged towns near Tranquebar (Tarangambadi) on Tamilnadu coast. In S.R. Rao, Ed., *Recent Advances in Marine Archaeology*. Society for Marine Archaeology, Goa, India pp. 60–64.
——— (1991b) Marine archaeological explorations of Tranquebar-Poompuhar region on Tamil Nadu coast. *Marine Archaeology*, Vol. 2, pp. 5–20.
Ritter N.C. (2017) Gemstones in pre-Islamic Persia: social and symbolic meanings of Sasanian seals. In A. Hilgner, D. Quast, and S. Greiff, Eds., *Gemstones in the First Millennium AD: Mines, Trade, Workshops and Symbolism*. RGZM Tagungen Vol. 30, Verlag des Römisch-Germanischen Zentralmuseums, Mainz, Germany, pp. 277–292.
Roth H. (1980) Almandinhandel und -verarbeitung im Bereich des Mittelmeeres. *Allgemeine und vergleichende Archaeologie*, Vol. 2, pp. 309–333.
Schmetzer K., Gilg H.A., Schüssler U., Panjikar J., Calligaro T., Périn P. (2017) The linkage between garnets found in India at the Arikamedu archaeological site and their source at the Garibpet deposit. *Journal of Gemmology*, Vol. 35, No. 7, pp. 598–627.
Schneider H. (2011) K*osmas Indikopleustes, Christliche Topographie: Textkritische Analysen. Übersetzung. Kommentar*. Brepols Publishers, Turnhout, Belgium, 298 pp.
Šmit Ž., Fajfar H., Jeršek M., Knific T., Lux J. (2014) Analysis of garnets from the archaeological sites in Slovenia. *Nuclear Instruments and Methods in Physics Research B*, Vol. 328, pp. 89–94, https//dx.doi.org/10.1016/j.nimb.2014.02.121
Spear F.S. (1993) *Metamorphic Phase Equilibria and Pressure-Temperature-Time Paths*. Mineralogical Society of America, Washington, DC, 799 pp.
Spier J. (1989) A group of Ptolemaic engraved garnets. *Journal of the Walters Art Gallery*, Vol. 47, pp. 67–80.
——— (2007) *Late Antique and Early Christian Gems*. Reichert Verlag, Wiesbaden, 221 pp.
——— (2011) Late antique gems: Some unpublished examples. In C. Entwistle and N. Adams, Eds., *'Gems of Heaven': Recent Research on Engraved Gemstones in Late Antiquity c. AD 200–600*. British Museum Research Publication 177, The British Museum, London, pp. 193–207.
Sundaresh, Gaur A.S. (2011) Marine archaeological investigations on Tamil Nadu coast, India: An overview. In M. Staniforth et al., Eds., *Proceedings of the 2011 Asia-Pacific Regional Conference on Underwater Cultural Heritage*. Asian Academy for Heritage Management, pp. 233–248.
Thoresen L. (2017) Archeogemmology and ancient literary sources on gems and their origins. In A. Hilgner, D. Quast, and S. Greiff, Eds., *Gemstones in the First Millennium AD: Mines, Trade, Workshops and Symbolism*. RGZM Tagungen Vol. 30, Verlag des Römisch-Germanischen Zentralmuseums, Mainz, Germany, pp. 155–218.
Thoresen L., Schmetzer K. (2013) Greek, Etruscan and Roman garnets in the antiquities collection of the J. Paul Getty Museum. *Journal of Gemmology*, Vol. 33, No. 7-8, pp. 201–222.
Voysey H.W. (1833) Second report on the geology of Hyderabad. *Journal of the Asiatic Society of Bengal*, Vol. 2, No. 20, pp. 392–405.
Wang A., Freeman J.J., Jolliff, B.L. (2015) Understanding the Raman spectral features of phyllosilicates. *Journal of Raman Spectroscopy*, Vol. 46, No. 10, pp. 829–845, http://dx.doi.org/10.1002/jrs.4680
Wheeler R.E.M., Ghosh A., Deva K. (1946) Arikamedu: An Indo-Roman trading-station on the east coast of India. *Ancient India*, No. 2, pp. 17–124.
Winstedt E.O. (1909) *The Christian Topography of Cosmas Indicopleustes*. Cambridge University Press, Edinburgh, UK, 376 pp.
Wopenka B., Pasteris J.D. (1993) Structural characterization of kerogens to granulite-facies graphite: Applicability of Raman microprobe spectroscopy. *American Mineralogist*, Vol. 78, No. 5-6, pp. 533–557
Zwierlein-Diehl E. (2007) *Antike Gemmen und ihr Nachleben*. Walter de Gruyter, Berlin/New York, 567 pp.

Cultured Pearls from Lake Kasumigaura: Production and Gemological Characteristics

Ahmadjan Abduriyim

Although today's global freshwater cultured pearl market is mostly dominated by Chinese products, Japanese freshwater pearl cultivation started in 1935. Lake Biwa in Shiga Prefecture supplied pearls in a wide variety of colors to the domestic and international markets until 1982. Due to water pollution and the depletion of *Hyriopsis schlegelii*, some of the pearl farms relocated to Lake Kasumigaura in Ibaraki Prefecture starting in 1962. Today the annual production of large nucleated cultured pearls at Lake Kasumigaura is below 40 kg, a small portion of which are supplied to the international market. This report investigates "Kasumiga pearl" culturing and describes the quality and production volume. UV-visible spectroscopy, fluorescence testing, and chemical analysis were performed on pearls in six different colors collected from the *Hyriopsis schlegelii* × *Hyriopsis cumingii* hybrid mollusk farmed at Kasumigaura.

Since the initial success of culturing round pearls using the akoya oyster in the early twentieth century, there has been a consumer demand for pearls in a variety of colors, shapes, and sizes. Freshwater pearl culturing in Japan began in 1935, with commercial production of nucleated (beaded) pearls at Lake Biwa, Japan's largest lake. These were produced using *Hyriopsis schlegelii* mollusks grown in Lake Biwa. After World War II, cultivation was shifted from beaded pearls to non-nucleated pearls. The annual production of freshwater pearls in Japan peaked at seven tons per year between 1970 and 1980 ("Statistics of fishery and cultivation," 2000), at the same time Chinese freshwater pearls were entering the market.

In 1962, with natural resources of *Hyriopsis schlegelii* in Lake Biwa facing depletion, some Japanese freshwater pearl farmers started moving to the Lake Kasumigaura region in Ibaraki Prefecture to set up a new cultivation base (figure 1). With the need for stronger pearl-producing oysters, *Hyriopsis schlegelii* and *Hyriopsis cumingii* were crossbred to produce a *Hyriopsis* hybrid (figure 2). This oyster can grow larger and more lustrous nucleated cultured pearls in various colors (figure 3). Current annual production of freshwater cultured pearls in Lake Kasumigaura—Japan's second-largest lake—remains low, at less than 40 kg, but these "Kasumiga pearls" are quite popular among buyers from Europe and the United States. This report examines current Japanese freshwater pearl culturing and the characteristics of the pearls produced at Lake Kasumigaura.

Figure 1. This map shows the location of the freshwater nucleated pearl culture farm in Lake Kasumigaura, Japan's second-largest lake, located 60 km northeast of Tokyo.

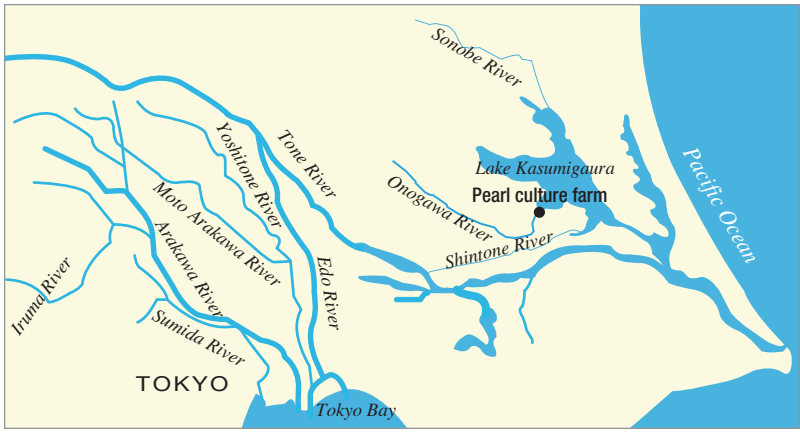

See end of article for About the Author and Acknowledgments.
GEMS & GEMOLOGY, Vol. 54, No. 2, pp. 166–183,
http://dx.doi.org/10.5741/GEMS.54.2.166
© 2018 Gemological Institute of America

Figure 2. Several pearl culturing farms in Lake Kasumigaura use a Hyriopsis schegelii × Hyriopsis cumingii *hybrid that was developed in 1962. An 8.0–8.5 mm freshwater shell bead nucleus is seeded to the gonad of the mussel and cultivated 3.5 to 4 years to produce large pearls up to 15 mm in diameter. The shell shown here measures 220 × 160 cm, and the pearl is 14 mm round. Photo by Ahmadjan Abduriyim.*

In Brief

- Commercial freshwater pearl cultivation started at Lake Biwa in 1935. Between 1970 and 1980, seven tons of non-nucleated pearls were produced each year using *Hyriopsis schegelii* mollusks.
- In 1962, a *Hyriopsis* hybrid mollusk was developed by crossbreeding *Hyriopsis schegelii* and *Hyriopsis cumingii*. Since then, a variety of colored nucleated pearls have been cultured at Lake Kasumigaura, though in limited quantity.
- Cream, yellow, pink, purple, orange and golden with orient are the major colors, and these are sold in the United States and Europe without bleaching or dyeing.
- The six color categories showed different Raman spectral features. "Kasumiga pearls" produced by the *Hyriopsis* hybrid can be differentiated from Chinese nucleated freshwater pearls from the same species through the use of trace-element analysis.

HISTORY OF FRESHWATER PEARL CULTURING IN JAPAN

Lake Biwa. Freshwater pearl culturing dates as far back as the thirteenth century, when pearls bearing Buddhist images and hemispherical pearls were produced from *Cristaria plicata* in China (Ward, 1985). In Japan, freshwater pearl culturing started during the Meiji era (1904–1912) with Tatsuhei Mise using *Cristaria plicata* at Lake Kasumigaura followed by Tokujiro Koshida's experiments with *Margaritifera laevis* at Chitose River in Hokkaido, but both trials ended in failure. Masao Fujita tried a number of experiments in and around Lake Biwa and succeeded in commercial freshwater pearl cultivation using *Hyriopsis schlegelii* in 1935. His breakthrough was interrupted by World War II, and with the resump-

Figure 3. Left: A high-luster round Kasumiga pearl necklace showing various hues of pink, purple, orange, light yellow, and cream. The pearls have diameters of 14 to 16 mm. Right: Recently harvested nucleated pearls from the Hyriopsis *hybrid. The sizes (excluding the undergrown pearl specimen) range from 11 to 17 mm. Photos by Tetsuya Chikayama (left) and Ahmadjan Abduriyim (right).*

Figure 4. These Biwa pearls show a good luster and unusual color and shape. The Hyriopsis schlegelii *mollusk was used to culture non-nucleated freshwater cultured pearls in Lake Biwa since 1935. Photo by Satoshi Furuya.*

tion of culturing operations came a shift from nucleated to non-nucleated pearls, which eventually formed the foundation for modern freshwater pearl cultivation (Wada, 1974; Akamatsu et al., 2001).

Due to war, the first year of recorded production at Lake Biwa was 1955. In that year, the Japan Ministry of Agriculture, Forestry, and Fisheries reported 0.1 tons of freshwater cultured pearls. This figure increased to between six and seven tons during the 1970s, with exports going mainly to the Middle East and India (Toyama, 1991). More than 99% consisted of non-nucleated pearls, and less than 1% were beaded pearls. Farmers in Lake Biwa successfully produced different shapes (figure 4) such as "dragon," cross, triangle, long stick, or triplet, in addition to conventional round or baroque shapes (Wada, 1999). In addition, large nucleated pearls over 10 mm in diameter were cultured in very limited quantities. A wide variety of colors such as pink, purple, orange, brown, and blue, which were not possible by the traditional culturing method using *Hyriopsis schlegelii*, were achieved by grafting a piece of *Anodonta calipygos kobelt* mantle tissue into *Hyriopsis schlegelii*.

In the 1970s, freshwater non-nucleated pearl culturing began along the Chang Jiang River in central mainland China, utilizing its favorable natural environment and abundant freshwater mussel resources. About 13 tons were exported to Japan in 1980, based on statistics published by the Japanese Ministry of Finance. This greatly surpassed the total amount being produced in Japan (about seven tons per year), and Chinese annual production volume has grown larger every year, reportedly surpassing 1,000 tons (Akamatsu et al., 2001).

Meanwhile, pearl culturing at Lake Biwa went into steep decline. Natural resources of *Hyriopsis schlegelii* were overharvested to depletion, and there has been no stable supply since around 1982, despite the development of an artificial seed oyster production technique in 1975. The adverse effects of inbreeding, water pollution, and ecosystem change are some of the causes of poor growth of the artificial seed oysters (Toyama, 1991; Strack, 2006).

Lake Kasumigaura. Kazuhisa Yanase began pioneering work to cultivate 10 mm nucleated freshwater pearls at Kasumigaura in 1946. He personally tested the water, cultivated the mussels, and conducted a variety of studies, making it his life's work to harvest pearls with wonderful color, shape, and size. In 1962, after the pearl cultivation in Lake Biwa was in decline, 10 small pearl farms moved to Lake Kasumigaura and started to culture the non-nucleated freshwater pearls (called Kasumiga *keshi* pearls) by using an artificial seedling *Hyriopsis schlegelii* mussel in a laboratory setting. The yearly production would eventually increase from a few hundred kilograms in the 1970s to more than 750 kg in the 1980s.

Also in 1962, a few pearl farmers challenged themselves to produce high-quality bead-cultured pearls over 10 mm to rival South Sea pearls and, later, to compete with mass-produced Chinese freshwater pearls, an effort which began in the late 1960s. After a thorough investigation of potential for pearl farming, their experiments proved successful in culturing spherical beaded pearls by using a new *Hyriopsis* hybrid, produced by crossbreeding *Hyriopsis schlegelii* and *Hyriopsis cumingii*. Initial production was only

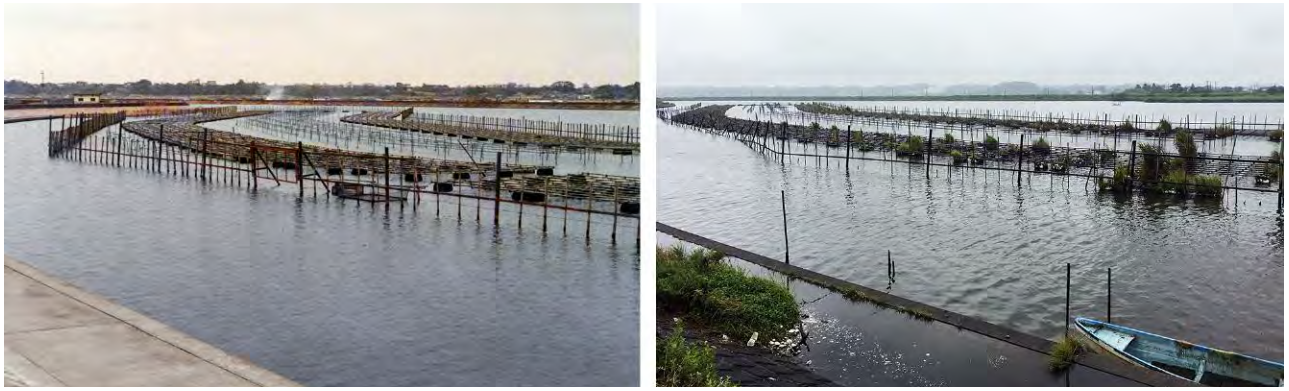

Figure 5. From the 1970s into the 1990s, more than 10 farms cultured the Kasumiga freshwater pearls at the estuaries of the Onogawa, Sonobe, and Shintone Rivers, which empty into Lake Kasumigaura. The photos show the same location of the Toda Pearl farm at the Onogawa River, as seen in 1980 (left) and 2018 (right). Photos by Ryuichi Toda (left) and Ahmadjan Abduriyim (right).

a few dozen grams per year. To minimize the risk of environmental damage to the mussels, the farms were located at estuaries of the Shintone, Sonobe, and Onogawa Rivers, which empty into Lake Kasumigaura (figure 5). The culturing of non-nucleated pearls stopped at Lake Kasumigaura at the end of the 1980s and shifted to solely nucleated culturing in 1991. From that year until 2013, average yearly production was 40–50 kg. Since 2013, production has decreased, with annual yields of less than 40 kg (R. Toda, pers. comm., 2017).

Only beaded pearls are currently produced at Lake Kasumigaura. A small mantle tissue, usually inserted into a drill hole in the bead nucleus, is inserted in each mussel, forming a sac in which a pearl starts to grow. The nacre thickness of pearls that have been cultured for longer periods (3.5–4 years) reaches 3 mm, which is much thicker than the nacre of akoya cultured pearls. The size of Kasumiga pearls typically ranges from 11 to 15 mm.

One of the characteristic features seen in Kasumiga pearls produced by the hybrid mollusk is their coloration. The variety of bodycolors includes white, pink, purple, yellow, purple-red, orange, and brown with an iridescence (Komatsu et al., 1989) that is frequently referred to as "rainbow." Bodycolor preferences for these products differ between countries, and pink and purple colors command higher prices. In the U.S. and Europe, Kasumiga pearl is highly valued for its luster, variety of colors, and size, and the supply cannot keep up with demand.

Unfortunately, only a few pearl farms are active at Lake Kasumigaura (R. Toda, pers. comm., 2017), and the pearl farmers who operate there today do not appear to have any successors. But the Kasumiga pearl, a source of Japanese pride, will surely be able to once again thrive if the farms are able to foster successors and environmental protection measures are adopted, optimally with the government's assistance.

PEARL CULTURING PROCESS AT LAKE KASUMIGAURA

Preparing the Donor Mantle. The farmers at Kasumigaura grow *Hyriopsis cumingii* × *Hyriopsis schlegelii* hybrid larvae in specially constructed pools for two years to protect them from any possible diseases or threats (figure 6). A scalpel is inserted into the

Figure 6. At Lake Kasumigaura, mollusk larvae are grown in specially constructed pools for two years to protect them from disease. Photo by Ahmadjan Abduriyim.

Figure 7. A piece of tissue, measuring about 4 × 4 mm, is cut from the outer part of the mantle lobe of a one-year-old Hyriopsis *hybrid donor mollusk to produce pink-colored pearls. Photo by Yosuke Sasaki.*

ventral margin of the donor shell of *Hyriopsis* hybrid, and the anterior and posterior adductor muscles are removed to open the shell wide. Next, a long slice of mantle is cut along the pallial line using scissors. The margins are trimmed to remove pallial mantle and shape it into ribbons 3 to 4 mm wide, which are further cut into 4 × 4 mm squares (figure 7). Another method of preparing the piece, called "stripping," was developed specifically for pearl culturing using *Hyriopsis schlegelii*. This method involves stripping either outer tissue that is in contact with the shell ("rear stripping") or inner tissue that is deeper within the mussel ("front stripping" from the slice of mantle or directly from the pallial mantle). The mantle obtained by front stripping is thinner compared to rear stripping. A pearl cultured through front stripping grows faster, but the surface of the pearl shows a wrinkled appearance. Therefore, the Kasumiga pearl farms now prepare pieces mainly through rear stripping to produce pink pearls with good luster, even though they tend to take longer to grow.

Operation. Operating on freshwater cultured pearls does not require the preparation that is usually performed in saltwater pearl culturing using akoya oysters, such as high-pressure waterjet cleaning to remove any extraneous material from the surface. The shells for freshwater pearl culturing are simply washed to remove the mud from the surface the day before the operation. A nucleation operation to culture spherical pearls over 10 mm in diameter is performed by inserting a piece of mantle tissue and bead nucleus (from a U.S. freshwater mollusk of the *Anodonta* species, 8–8.5 mm in diameter) into a gonad that is either connected to the bottom of a digestive diverticulum or attached below a pericardial cavity. As the insertion area is not visible, the operator uses a bead that is drilled through. A metal pin is pushed through the bead with a piece of the mantle placed on the tip, to maintain a close contact between the mantle and the bead (figure 8). The operations generally take place in the winter season between October and March. They are suspended between May and

Figure 8. The bead nucleus is drilled. A metal pin is pushed through the hole and a mantle "piece" is placed on the end to maintain a close contact between the piece and nucleus during the insertion process. Photo by Yosuke Sasaki.

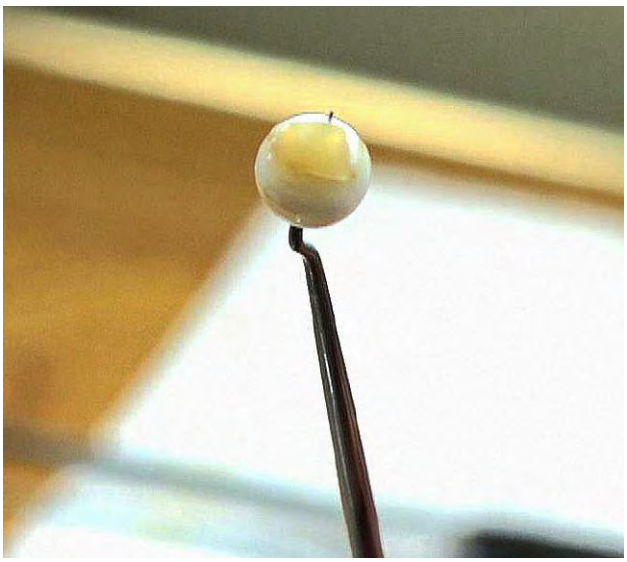

September, when the water temperature exceeds 20°C or during the fertile phase, as these conditions may result in higher mortality of the mollusks. Recently, however, the mortality rate has been lowered by using antibiotics during the procedure, enabling nucleation throughout the year for some farmers.

Growing Pearl Mussels. After the operation, the shells are hung for a couple of days to recover, and then they are placed in a layered net-cage and transferred to the pearl farm. The cage may have two or three layers, in which shells are neatly placed in groups of two to four with their hinges facing down (figure 9). The net-cages are hung from horizontal bamboo sticks at two-meter intervals between 70 and 100 cm below the water surface. The culturing period lasts about three to four years in general. Pearls grow between April and December, when water temperature is above 15°C. Harvesting starts gradually in the summer, in July or August, and enters the peak season in October and November, when the pearls show the most lustrous color.

Figure 9. During cultivation, two to four shells are placed into two layered cage nets and suspended in the water at 70 cm to 1 meter depths. Photo by Ahmadjan Abduriyim.

SAMPLES AND ANALYTICAL METHODS

For this study, the author extracted 25 bead-cultured freshwater pearls directly from *Hyriopsis* hybrid shells at the Toda Shinju company's pearl farm at Lake Kasumigaura (see table 1). The pearls ranged from round to baroque shapes with a width of 9.5–19.6 mm and a weight of 6.0–20.5 ct (figure 10). The

Figure 10. Representative Kasumiga pearls from this study show a color range of cream, light yellow, pink, purple, orange, and golden with orient, in sizes ranging from 9.5 to 19.6 mm and with round and baroque shapes. They were produced after a culturing period of two to four years. Photos by Tetsuya Chikayama.

TABLE 1. Characteristics of freshwater nucleated cultured pearls and shells from Lake Kasumigaura, Japan.

Sample no.	Shape	Color	Weight (ct)	Overtone	Diameter (mm)	LWUV/SWUV reaction	LA-ICP-MS	X-radiography
KSM-W-001	Round	Cream	6.08	None	9.48 × 9.41	Weak chalky green-blue/ Very weak green-blue	x	x
KSM-W-002	Round	Cream	6.67	Pink	9.70 × 9.60	Weak chalky green-blue/ Very weak green-blue	x	-
KSM-W-003	Baroque	Cream	7.74	None	11.69 × 9.98	Weak chalky green-blue/ Very weak green-blue	x	-
KSM-W-004	Baroque	Cream	11.33	None	12.65 × 12.07	Weak chalky green-blue/ Very weak green-blue	x	-
KSM-MW-005	Semi-round	Light yellow	9.52	None	11.30 × 10.55	Weak chalky green-blue/ Very weak green-blue	x	-
KSM-MW-006	Semi-round	Light yellow	12.71	None	12.39 × 12.10	Weak chalky green-blue/ Very weak green-blue	x	-
KSM-MW-007	Baroque	Light yellow	11.64	None	13.34 × 11.75	Weak chalky green-blue/ Very weak green-blue	x	x
KSM-MY-008	Round	Light yellow	14.86	None	12.89 × 12.79	Weak chalky green-blue/ Very weak green-blue	x	-
KSM-Pink-009	Semi-round	Pink	8.52	Yellow	10.89 × 10.13	Very weak chalky green/ Very very weak chalky green	x	-
KSM-Pink-010	Baroque	Pink	12.02	Yellow	12.24 × 11.04	Very weak chalky green/ Very very weak chalky green	x	-
KSM-Pink-011	Baroque	Pink	13.47	Yellow	13.23 × 11.48	Very weak chalky green/ Very very weak chalky green	x	-
KSM-Pink-012	Baroque	Pink	15.43	Yellow	13.65 × 12.06	Very weak chalky bluish green/ Very very weak chalky bluish green	-	-
KSM-Pink-013	Semi-round	Pink	22.19	None	15.43 × 14.28	Very weak chalky bluish green/ Very very weak chalky bluish green	-	x
KSM-Ora-014	Round	Orange	12.72	None	12.34 × 12.08	Inert	x	x
KSM-Pur-015	Baroque	Purple	10.02	Pink	12.20 × 10.75	Very weak chalky green/ Very very weak chalky green	x	-
KSM-pPur-016	Round	Pinkish purple	12.07	Pink	12.23 × 12.03	Very weak chalky green/ Very very weak chalky green	x	-
KSM-Pur-017	Semi-round	Purple	14.24	None	13.27 × 12.15	Weak chalky green/ Very weak chalky green	x	x
KSM-Pur-018	Round	Purple	14.92	None	13.03 × 12.80	Very weak chalky green/ Very very weak chalky green	-	-
KSM-Pur-TD	Semi-round	Purple	12.30	None	12.49 × 11.46	Very weak chalky green/ Very very weak chalky green	-	-
KSM-GY-019	Baroque	Golden with orient	11.83	Pink	13.76 × 10.62	Very weak chalky green/ Very very weak chalky green	-	-
KSM-GY-020	Baroque	Golden with orient	12.92	Pink	14.89 × 12.09	Inert/Very very weak chalky green	x	-
KSM-GY-021	Baroque	Golden with orient	15.55	Purple	18.42 × 12.33	Inert/Very very weak chalky green	x	x
KSM-GY-022	Baroque	Golden with orient	20.52	Purple	19.64 × 14.37	Inert/Very very weak chalky green	x	x
KSM-GY-023	Baroque	Golden with orient	7.44	Purple	10.26 × 10.10	Inert/Very very weak chalky green	-	-
KSM-Ora-half-024	Semi-round	Light orange	20.20	None	15.48 × 14.40	Weak chalky green blue/ Very weak green blue	x	-
KSM-SHELL-001	Section	Yellow	819 (one side)	Purple	190 × 135	Inert	x	-
KSM-SHELL-002	Section	Cream	859 (one side)	Pink	195 × 135	Very weak chalky blue/Inert	x	-
KSM-SHELL-003	Section	Purple	916 (one side)	Pink	205 × 152	Inert	x	-

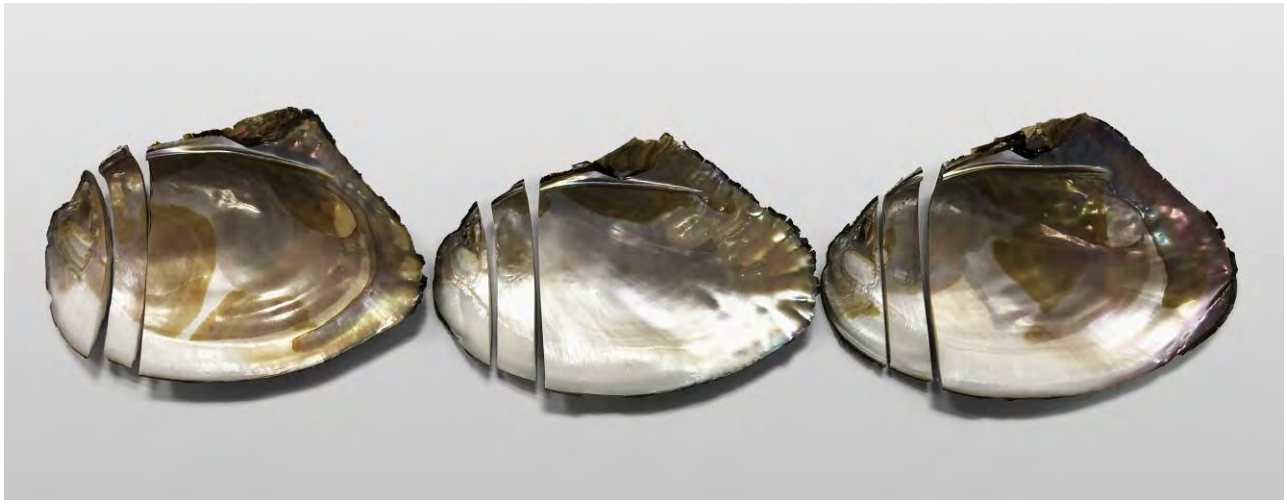

Figure 11. Three shells from Lake Kasumigaura were sliced for chemical composition analysis. The variable color and luster of the mother-of-pearl strongly influence the color of the pearl during cultivation. Photo by Ahmadjan Abduriyim.

bodycolors of the Kasumiga pearls included white, cream, light yellow, pink, purple, orange, and golden with orient. Three shells of the *Hyriopsis* hybrid from which the pearl samples were extracted were selected and sliced into sections for chemical composition analysis (figure 11). Chinese samples (figure 12) were also studied for comparison of chemical properties. These consisted of a *Hyriopsis* hybrid shell and 15 nucleated cultured pearls with 10 mm diameters, collected from the Zhong Shui Pearl Research Institute. These pearls were cultivated at Lake Taihu in Hubei Province.

Figure 12. The Chinese freshwater nucleated cultured pearls in this strand from Lake Taihu, also cultured by the Hyriopsis schegelii × Hyriopsis cumingii *hybrid, are 10 mm in diameter and show a color range and luster similar to Kasumiga pearls. Photo by Ahmadjan Abduriyim.*

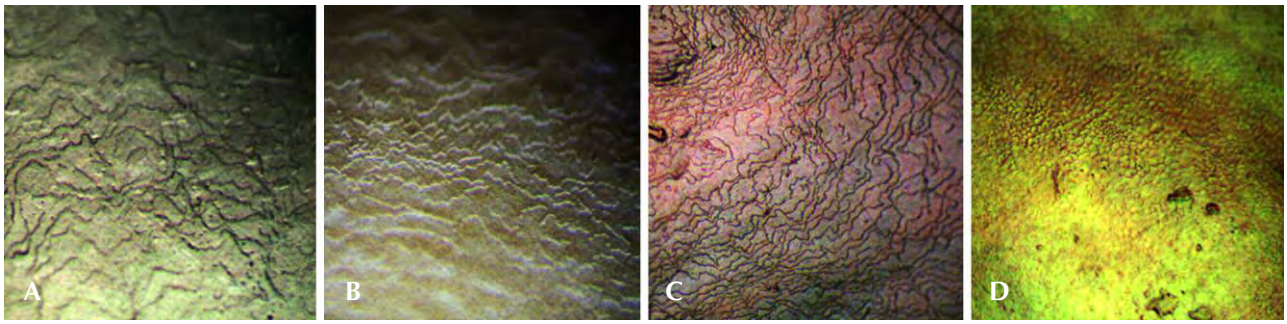

Figure 13. The surface nacreous structure of Kasumiga pearls. A: Cream-colored pearls show a rough, thick growth feature of aragonite platelets. B–C: Thin, parallel platelets can be seen in pink and purple pearls. D: A prismatic layer and brownish yellow pigment covered the nacreous layer of a golden pearl with orient. Photos by Ahmadjan Abduriyim; field of view 400 µm.

The 25 pearls and three shells from Lake Kasumigaura were observed visually and microscopically for their surface growth structure and color. Their fluorescence reactions were recorded under 4-watt long-wave and short-wave ultraviolet light from a System Eickhorst MultiSpec UV-AC lamp. UV-Vis-NIR spectroscopy was performed on the surface of each sample using a Shimadzu UV-2600 spectrophotometer in diffuse reflection mode, with a resolution of 1 nm, in the 200–1000 nm range. The internal structure of the pearls was observed using a Faxitron CS-100 2D real-time X-ray microradiography (RTX) unit (90 kV and 100 mA X-ray excitation).

Raman spectra were obtained by a Horiba Jobin Yvon XploRA Plus Raman microscope equipped with a 532 nm Nd:YAG laser. The laser beam was focused through the 300 µm aperture with a 10× objective lens. The measurements were recorded on LabSpec6 software using a grating of 1800 gr/mm and spectral resolution of ±2.5 to 3.5 cm^{-1} between 100 and 1800 cm^{-1}. The instrument was calibrated with a Si 520 nm reference.

Semiquantitative chemical analysis was performed using a Shimadzu EDX-8000 energy-dispersive spectrometer (EDS) equipped with an X-ray microprobe. Trace elements were measured by means of laser ablation–inductively coupled plasma–mass spectrometry (LA-ICP-MS) analysis using a Thermo Scientific iCAP RQ quadrupole ICP-MS with a ESI UP 213 Nd-YAG laser, a repetition rate of 7 Hz, an energy density of 10 J/cm^2, and a spot diameter of 40 µm. The carrier gas was a mixture of helium and argon. All of the isotope ratio signals were detected, and an analytical precision (relative standard deviation 1 sigma) within 10% was achieved for all trace elements except P, which fell within 20%. Three to eight spots on each pearl sample and section of sliced shell were ablated, and the averaged data were calibrated. Microanalytical carbonate standards MACS-1 and MACS-3 pressed-powder pellets and NIST glass 610 were used as external standards.

RESULTS AND DISCUSSION

Shape and Size. Cultured pearls from Lake Kasumigaura are produced in various shapes including round, semi-round, oval, and baroque, usually with very good luster. The most common shapes are round and semi-round. Larger pearls over 16 mm have been successfully produced, but the size typically ranges between 11 and 15 mm.

Hue and Surface Structure. Cream pearls show weak luster and overtone, with irregular, interrupted, or distorted growth layers of aragonite crystals that are observed under magnification. In the studied samples, they were formed of layers of thick aragonite crystal platelets and a few black or brown organic sediments on the surface (figure 13A). Pink pearls are well produced by the *Hyriopsis* hybrid, showing strong luster and smooth surface reflection. They have compactly arranged layers of aragonite single crystals (figure 13B). The intensity of the pink color is determined by (1) the content of pale pigment inside the conchiolin that is a protein consisting of nacre, (2) the thickness of the aragonite single crystals, and (3) the overtone produced from the way the aragonite platelets are layered. The volume of pigment secreted differs according to the age of the shell and the water temperature, and it tends to increase when mussels are strong and healthy. Control of the shell's physiology during cul-

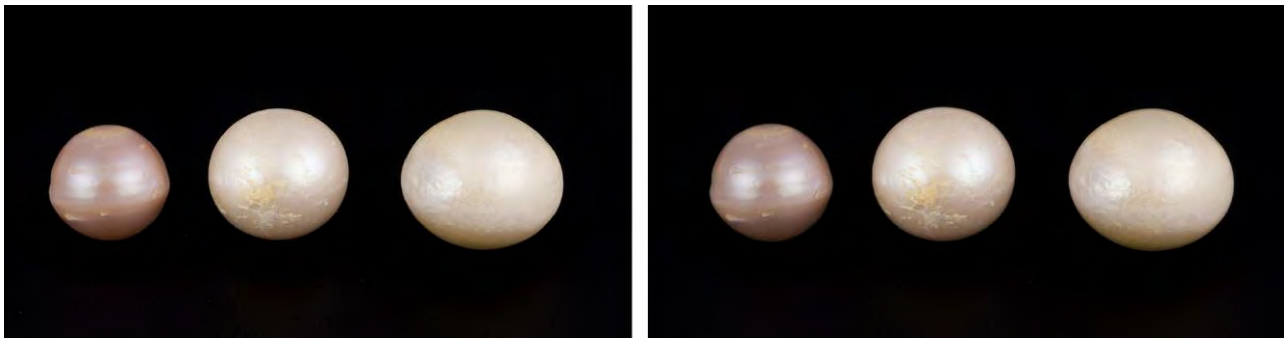

Figure 14. Pink Kasumiga pearls are shown before (left) and after (right) a fading test in these calibrated photos. The pearls were placed under a 100W tungsten lamp at less than 100°C for 30 minutes. The pink color has faded very slightly. Photos by Tetsuya Chikayama.

turing is the key factor to the thickness and quality of the aragonite crystal layers (Komatsu et al., 1989).

Some pink pearls are vulnerable to heat (Komatsu et al., 1989), and their color may fade slightly after one hour of exposure to strong incandescent light and heat at about 100°C (see figure 14, calibrated images before and after). Purple pearl samples showed a more violetish hue than the pink material, but with a somewhat lower luster. They contained smoothly piled growth layers of aragonite crystals with no interstitial extraneous substance (figure 13C).

Orange samples showed a very bright yellowish orange and sometimes orange color. Observation of the cross-section revealed the sheet-laminated aragonite platelets and layers of yellow-brown pigment that had grown into the compact concentric structure (figure 15). In the inner part of the pearl, where the bead nucleus was removed to observe the initial growth structure on the nacre surface, an organic substance produced during the initial growth phase and a columnar nacre were observed. The nacre displayed four cycles of growth layers divided by white boundaries until it reached the pearl surface. This indicates a four-year culturing period, with growth interrupted in cold seasons and resuming in warmer seasons (again, see figure 15). Their color did not fade with exposure to heat.

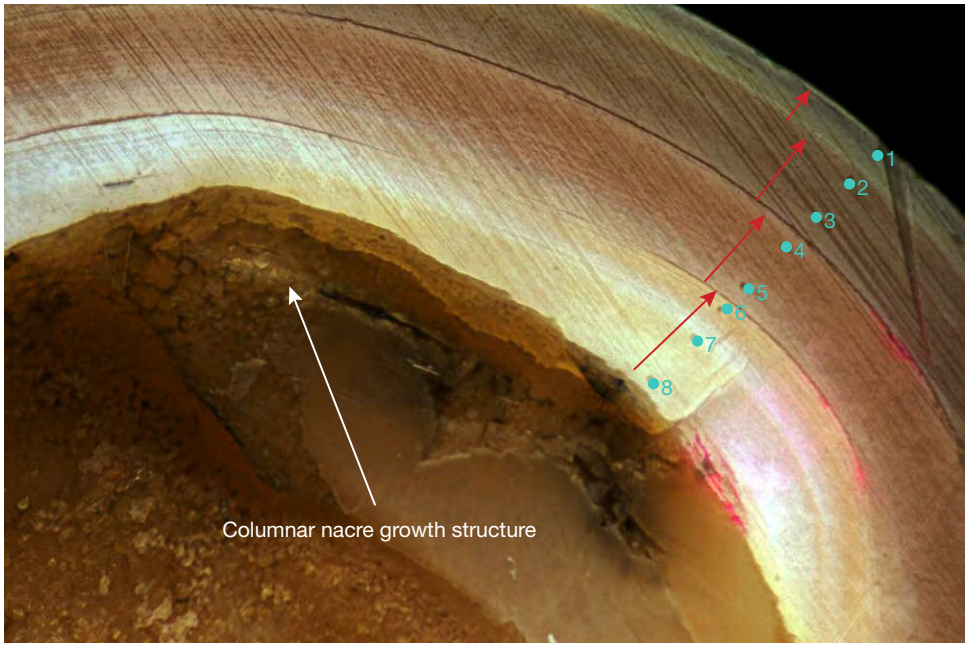

Figure 15. A light orange pearl (sample KSM-Ora-half-024) was cut in half and its bead nucleus was removed. The sheet nacreous layers show four different boundaries (marked by red arrows), indicating a growth period of four years (red arrow). The inner part of the nacreous layer close to the bead nucleus shows a columnar growth structure of aragonite (confirmed by 705 and 1085 cm^{-1} peaks in the Raman spectrum). Blue circles indicate the LA-ICP-MS analysis spots. Photo by Ahmadjan Abduriyim.

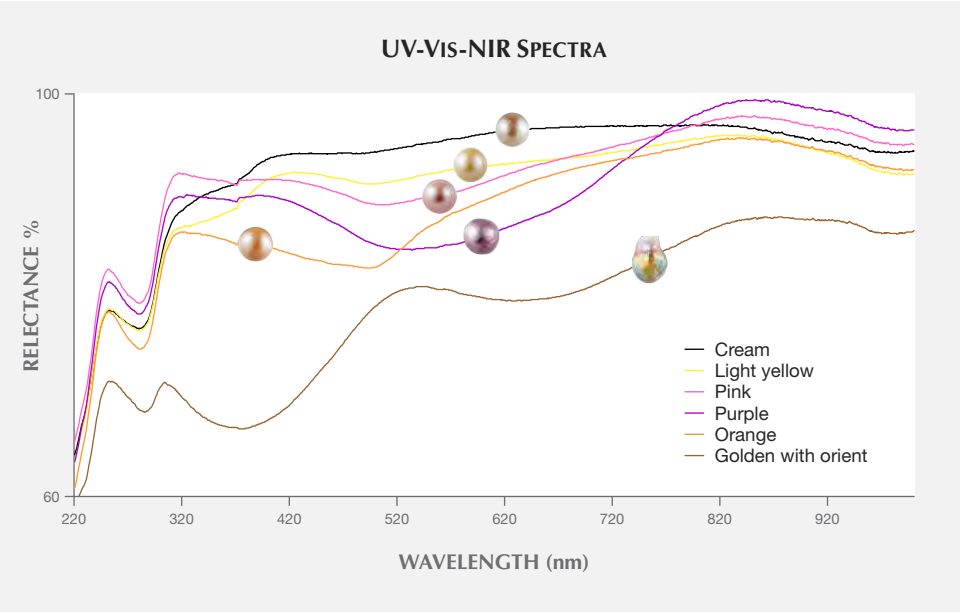

Figure 16. These UV-Vis-NIR reflectance spectra of six Kasumiga pearls—cream, light yellow, orange, pink, purple, and golden with orient—show increasing absorption from 484 to 526 nm with greater saturation of color from white to purple. The golden pearl with orient presents two broad absorption bands, at 320 to 460 nm in the UV to blue range and at 580 to 820 nm in the orange to near-infrared range.

It was learned that golden pearls with orient were actually pink-purple pearls covered with thin yellow-brown organic prismatic layers, just several dozen microns thick, across the surface (figure 13D). The golden color with orient (rainbow-like iridescence) seen on the surface is supposedly produced from an overtone mixture of laminated pink-purple aragonite crystals, an overlaid organic layer formed by abundant secretion from the shells in the growth period just before harvesting, and prismatic aragonite layers. In general, golden pearls with orient are characterized by very strong orient.

UV Fluorescence. Cream to light yellow pearl samples showed weak chalky green-blue fluorescence under long-wave UV light, whereas pink-purple pearls and golden pearls with orient showed weak chalky green fluorescence. Under short-wave UV light, the reaction became much weaker. The fluorescence appeared evenly distributed when the pearls were evenly colored. Orange pearls showed almost no fluorescence under both short-wave and long-wave UV.

UV-Vis-NIR Reflection Spectroscopy. The reflection spectra of pearls in each color are shown in figure 16. Cream pearls showed no distinct absorption except for a vague absorption band around 484 nm, while the absorption center was shifted to 498 nm in the light yellow pearls and appeared as a weak but broad absorption band. On the other hand, the purplish pink pearls colored by pigment contained in the nacre showed a large absorption band centered at around 506 nm, which became intense as the color became more saturated, with an increase in absorption between 415 and 820 nm. Study of the pearls with strong purple color revealed that general absorption between 415 and 820 nm appeared greater and the absorption band centered at 526 nm became stronger. Orange pearls showed a stronger absorption band near 498 nm, similar to light yellow pearls. The strong yellow pearls displaying rainbow iridescence that are rarely produced from the *Hyriopsis* hybrid showed two characteristic absorption regions. One was between the ultraviolet and the visible range at 320–460 nm with a maximum at 373 nm, and the other was in the visible range at 580–820 nm with a maximum at 640 nm.

As noted above, these reflection spectra showed an absorption band centered around 484–526 nm, indicating a feature characteristic to orange, pink, and purple pearls cultured from *Hyriopsis* hybrid mollusks. The absorption intensity increased with color saturation. In contrast, golden pearls with orient showed a different type of spectrum. Its golden yellow bodycolor with strong rainbow iridescent layers was supposedly produced by the absorptions in the blue and red regions between the UV and the visible range. Also, these pearls showed thick yellow-brown organic layers and prismatic layers that were formed close to the pearl surface, whereas the orange, pink, and purple pearls may be colored by pigment contained in their nacre. The author will continue to test a large number of samples to draw a detailed conclusion of the coloring pigment in pearls from Lake Kasumigaura.

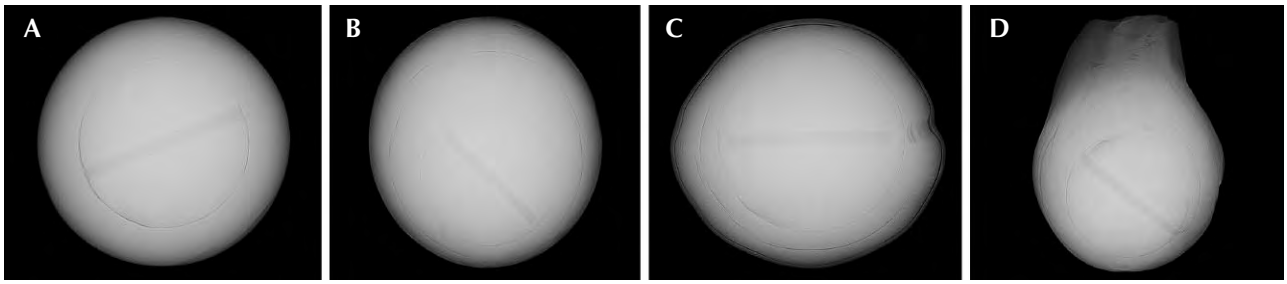

Figure 17. Microradiographic images of undrilled shell-nucleated cultured pearls from Lake Kasumigaura. A drill hole seen within the bead nucleus of the round and semi-round pearls showed the thickness of the nacre, ranging from approximately 2 to 3 mm (A–C). The baroque-shaped pearl (D) had an approximately 8.7-mm-thick nacre in its long axis. Photos by Kwanreun Lawanwong.

Microradiography. X-ray images of an orange round (sample KSM-Ora-014), a pink near-round (KCM-Pink-013), a purple near-round (KCM-Pur-017, showing circular growth structure), and a rainbow golden baroque (KSM-GY-022) cultured pearl from Lake Kasumigaura are shown in figure 17. All the samples tested with X-ray were confirmed to contain a drilled bead, and the organic layer distributed along the boundary between the bead and nacre was very thin. The pearls shown in images A, B, and C had a similar nacre thickness, typically averaging 2 to 3 mm. Near-round pearls tended to grow a thicker nacre on one side, 1 mm on the thinner side and 5.6 mm on the thicker side. The thickest nacre observed in the baroque pearls reached approximately 8.7 mm. In the nacreous growth layer of all the pearl samples, three boundaries of organic layers were confirmed, revealing a culturing period of three years or more.

Raman Spectrum. Raman spectra of pearls with the six representative colors (cream, light yellow, pink, purple, orange, and golden with orient) are shown in figure 18. Each spectrum displays a series of peaks related to the aragonite crystal lattice at 138, 148, 187,

Figure 18. Raman spectra of six colors of Kasumiga pearl showed aragonite-associated peaks at 138, 148, 187, 210, 268, and 280 cm^{-1}; a doublet peak at 701 and 705 cm^{-1}; a weak single peak at 1462 cm^{-1}; a strong aragonite peak at 1085 cm^{-1}; and polyene-related peaks at 1017, 1132, 1295, and 1522 cm^{-1}.

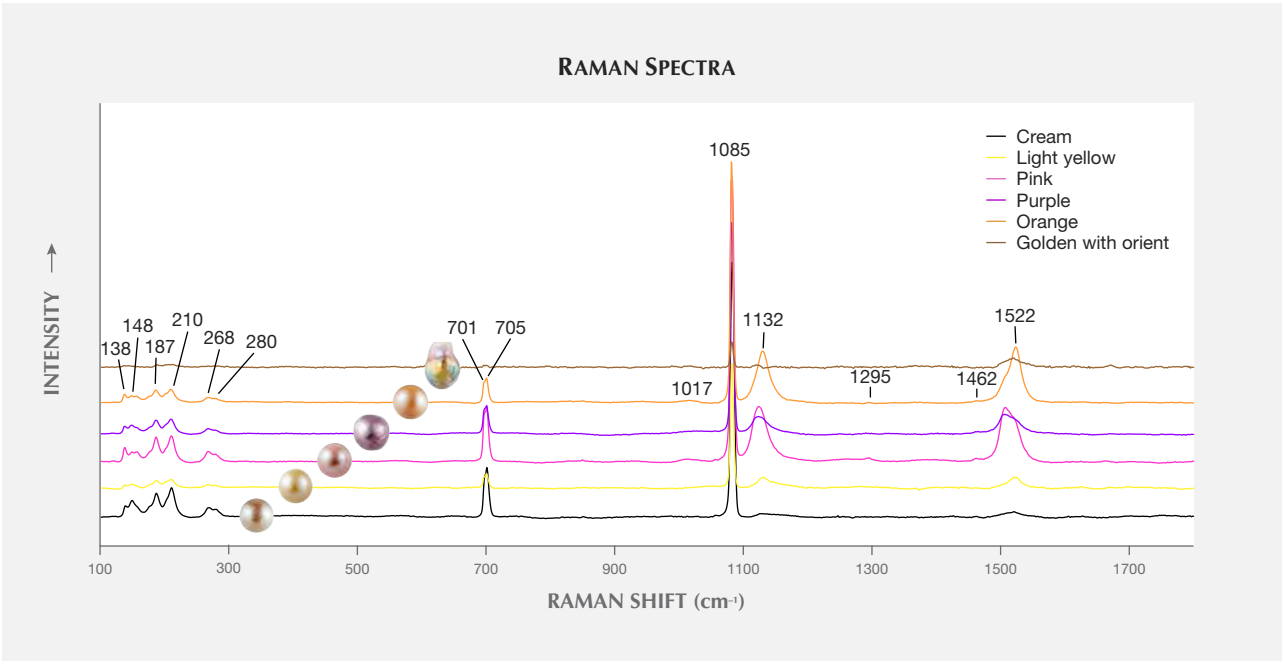

210, 268, and 280 cm^{-1}; a strong peak at 1085 cm^{-1} that indicates symmetric stretching of (CO_3^{2-}); a doublet at 701 and 705 cm^{-1} from plane stretching; and a weak peak at 1462 cm^{-1}. Peaks related to the pigment (polyene, an organic compound) were confirmed at 1017, 1295, 1132, and 1522 cm^{-1} (Karampelas et al., 2007; Sturman et al., 2014). The peaks at 1132 (C-C single-bond stretching vibration) and 1522 cm^{-1} (C=C double-bond stretching vibration) tended to be weaker in cream and light yellow pearls and stronger in pink, orange, or purple pearls. The peaks at 1017 and 1295 cm^{-1} did not appear in the paler pearls with cream and light yellow color. The spectrum background in the golden pearls with orient was generally high, with weaker main peaks at 1085 and 701 cm^{-1} that indicated an aragonite crystal, confirmation that the outermost nacreous growth layers on these iridescent pearls were prismatic layers formed of aragonite, not calcite. A pigment-related peak at 1522 cm^{-1} was also clearly observed.

Chemical Composition. X-ray fluorescence analysis can nondestructively measure a pearl's composition of major and trace elements to assist in the determination of some mollusk species and the culturing environment. This semiquantitative technique is also advantageous in identifying the composition of a historical or highly valuable pearl that cannot be subjected to destructive tests. In X-ray fluorescence analysis of the 25 pearl samples, CaO was detected as the main component, but organic components and water cannot be detected by this technique. A small amount of Na was detected, with an Na_2O content of 1.50–5.90 wt.%. Trace elements Mn, Fe, and Sr were detected, with MnO = 0.06–0.40 wt.%, Fe_2O_3 = bdl–0.02 wt.%, and SrO = 0.10–0.14 wt.%. The elements Mg and K showed values close to the detection limit of the EDX-8000 spectrometer (detection limits: MgO = 0.067 wt.%, K_2O = 0.016 wt.%, and Fe_2O_3 = 0.014 wt.%, respectively). Among these elements, Mn showed higher content in freshwater than saltwater pearls, whereas Sr tended to have higher concentration in saltwater pearls, consistent with previous studies (Wada and Fujinuki, 1976). The chemical composition results from energy-dispersive X-ray fluorescence (EDXRF) analysis indicate a slightly lower concentration compared with the results from LA-ICP-MS analysis, based on the different reference standards used in this study.

To investigate trace-element distribution using LA-ICP-MS, we ablated the surface of all 25 pearls, the section of one pearl, and the section of three *Hyriopsis* hybrid shells with a laser spot 40 μm in diameter, collecting analytical data on three to eight spots on each sample. The average of each detected trace element is shown in table 2.

From the LA-ICP-MS analysis on the pearls in each color and the shell from Lake Kasumigaura, minor and trace amounts of 18 elements in total (^{7}Li, ^{11}B, ^{23}Na, ^{24}Mg, ^{27}Al, ^{31}P, ^{39}K, ^{45}Sc, ^{47}Ti, ^{55}Mn, ^{57}Fe, ^{59}Co, ^{60}Ni, ^{63}Cu, ^{66}Zn, ^{69}Ga, ^{88}Sr, and ^{137}Ba) were consistently detected. In all the pearls tested, Na, Mn, Sr, and Fe showed rather high concentrations, ranging from 3100 to 9700 ppmw (avg. 7363 ppmw) for Na, 790–5800 ppmw (avg. 1146 ppmw) for Mn, 800–1540 ppmw (avg. 836 ppmw) for Sr, and 920–1290 ppmw (avg. 702 ppmw) for Fe. P was detected as another element of high content, between 147 and 870 ppmw. Other elements such as Mg, Al, and K showed low concentrations, between 6 and 432 ppmw. B, Ti, and Zn were below 22 ppmw, while Li, Sc, Co, Ni, Cu, and Ga were below 10 ppmw. Interestingly, Al and Ti were only detected in the outer layer (the prismatic growth area) of shell. In the analysis on the cross-section of a nacreous pearl (sample KSM-Ora-024), the nacre from the pearl's surface to the inner side of the columnar nacre layer close to the bead nucleus showed no distinct element partition gradient except the enrichment of Na, Mg, and Fe in the columnar aragonite layer close to the bead nucleus area. Pearls produced from the *Hyriopsis* hybrid in Lake Kasumigaura contain less Li, Na, Mg, and Sr but much more Mn than the Japanese saltwater akoya cultured pearls from Ehime and Nagasaki Prefectures, showing the characteristic feature of freshwater species (past study data by the author). From these analysis results, there was no consistent relationship between the color of the pearls and the type and amount of transition metal elements. Thus it is reasonable to think the principal cause of color of the nacre, in the pearls or the shells, is organic pigment.

A bivalve shell is generally composed of three layers of ostracum (outer, middle, and inner). These are divided into tissue structures that include prismatic, columnar, nacreous, foliated, crossed lamellar, and complex crossed lamellar structure (Boggild, 1930; Kobayashi, 1971; Barthelat et al., 2009). The mollusk shell of the *Hyriopsis* hybrid from Lake Kasumigaura consists of an outer shell layer with prismatic structure and middle and inner shell layers with nacreous structure. As shown in the Raman analysis above, however, the *Hyriopsis* hybrid shell consists of prismatic and nacreous structures, both made of aragonite (figure 19). The shell of the Japanese akoya oyster con-

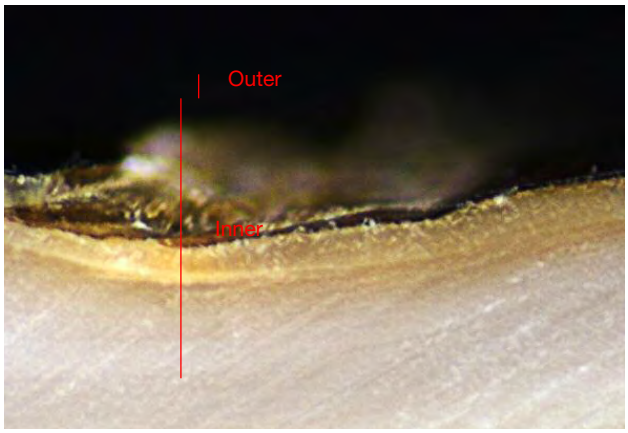

Figure 19. The shell of the Hyriopsis *hybrid from Lake Kasumigaura consists of an outer shell layer with prismatic structure and a middle and inner shell layers with nacreous structure. Photo by Ahmadjan Abduriyim.*

sists of a prismatic structure made of calcite and a nacreous structure made of aragonite (Nakahara, 1994; Wada, 1999; Liu and Li, 2015). The trace-element partition of the *Hyriopsis* hybrid shell from Lake Kasumigaura revealed high Na and Fe contents and the trace elements Al, Ti, Co, Ni, Cu, and Zn in the outer shell layer (prismatic structure) and high Mn in the nacreous structure. To find out the relationship between the ostracum of a shell and the trace-element contents, the factors in the secretion function in a tissue or in ostracum that control the content of trace elements should be analyzed in the future. The content of trace elements such as B, Mg, and P seemed to be somewhat lower in the shell than in the pearls.

Large amounts of Chinese freshwater bead-cultured pearls showing Kasumiga-like colors have recently been supplied to the global market. We analyzed 15 beaded freshwater pearls in each color (cream, light yellow, pink, purple, and orange) and the cross-section of a *Hyriopsis* hybrid shell from Hubei to compare the features of trace elements.

LA-ICP-MS analysis detected distinctly higher amounts of Ba and Ga in the Chinese pearls of all six colors and in the shell. The content ranges of other metallic elements such as B, Mg, K, Mn, Fe, Sr, Co, Ni, Cu, and Zn were similar to those of Kasumiga pearls. The analyzed chemical data were plotted on the chemical fingerprint diagram in figure 20 using a combination of the trace elements Ba and Ga to differentiate the freshwater pearls and shells of the *Hyriopsis* hybrid from both Japan and China. Ba and Ga values for the freshwater pearls and the *Hyriopsis* hybrid shell from Kasumigaura were concentrated in the lower region and clearly distinguished from the Chinese counterparts from Lake Taihu without overlap. Despite the use of the same species of *Hyriopsis* hybrid oysters in both countries, they showed different concentrations of heavy metal ions (Ba^{2+}, Ga^{2+}) in both the pearls and the shells, presumably in direct proportion to that of the aquatic habitat, as those ions are contained in extracellular fluid in the mantle. The application of this diagram to freshwater pearls and shells from China or other countries is subject to validation in future studies.

Future Outlook for the Kasumiga Pearl Industry. Since the late 1980s, the mass production and inexpensive price of Chinese freshwater cultured pearls has transformed the Japanese pearl industry. Although it is almost impossible to compete with China in the present circumstances, a few farmers are dedicating their efforts to improving culturing techniques, growing shells with great care, and strictly monitoring water quality, prioritizing quality over mass production. Kasumiga pearls started attracting attention from Europe and the United States in the 1990s but are scarcely sold in Japan's domestic market. Improvements in the quality of the pearls, as well as stronger marketing and branding, are critical to eliminating cheap Kasumiga products and maintaining a higher price point.

Figure 20. LA-ICP-MS analysis on 25 pearls and three shells from Lake Kasumigaura, along with 15 pearls and one shell from Lake Taihu in China, plotted according to Ga vs. Ba. There is clear separation of both samples from the two locations. Kasumiga pearls and shells had lower Ga and Ba contents overall, while these elements were enriched in Chinese pearls and shell.

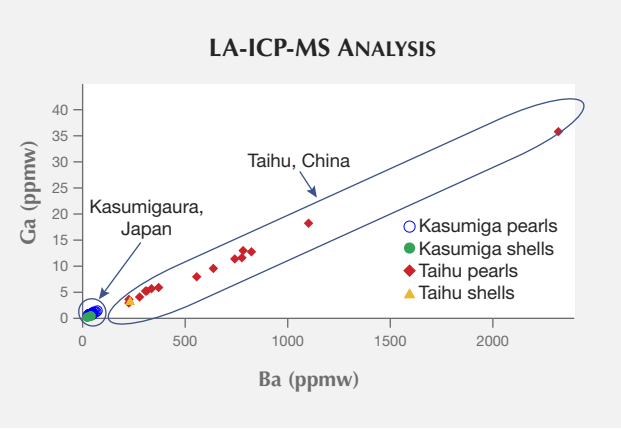

TABLE 2. Chemical composition (in ppmw) of trace elements of freshwater pearls and shells from Lake Kasumigaura (Japan) and Lake Taihu (China), analyzed by LA-ICP-MS.

Lake Kasumigaura, Japan: Pearl	Sample	^{7}Li	^{11}B	^{23}Na	^{24}Mg	^{27}Al	^{31}P	^{39}K	^{45}Sc	^{47}Ti	^{55}Mn	^{57}Fe	^{59}Co	^{60}Ni	^{63}Cu	^{66}Zn	^{69}Ga	^{88}Sr	^{137}Ba
Cream	KSM-W-001	0.09	17.08	3555	43.09	bdl	463	28.492	0.18	bdl	2510	1111	0.415	2.02	0.687	bdl	0.86	1172	45.93
	KSM-W-002	0.11	17.7	3696	148.1	bdl	466	44.157	0.212	bdl	777	1105	0.381	1.73	2.464	bdl	0.56	1175	24.94
	KSM-W-003	0.09	16.15	4149	125.7	bdl	686	37.816	0.146	bdl	1079	1254	0.439	1.99	4.577	11.4	0.74	1131	31.47
	KSM-W-004	0.07	14.55	3188	84.14	bdl	531	62.453	0.161	bdl	4156	1112	0.414	1.81	0.922	1.6	1.02	1201	49.81
Light yellow	KSM-MW-005	0.12	13.76	4166	59.69	bdl	629	58.306	bdl	bdl	1355	1098	0.395	2.04	2.805	14.4	0.96	1275	48.93
	KSM-MW-006	0.13	15.41	3487	84.24	bdl	680	62.176	0.182	bdl	5671	1103	0.365	1.91	1.99	0.44	1.06	1045	51.45
	KSM-MW-007	0.07	14.03	3697	77.91	bdl	562	40.634	bdl	bdl	2158	1093	0.439	2.16	0.822	2.33	0.69	1083	38.1
	KSM-MY-008	0.09	14.3	3463	78.56	bdl	689	36.484	0.129	bdl	5551	1120	0.467	1.96	1.876	2.68	1.1	1090	48.7
Pink	KSM-Pink-009	0.07	15.28	3873	26.94	bdl	455	41.937	0.13	bdl	1014	1026	0.393	1.71	0.482	bdl	0.54	816	30.19
	KSM-Pink-010	0.06	12.68	3574	96.37	bdl	581	29.377	bdl	bdl	1919	994	0.363	1.83	0.652	bdl	0.83	1080	42.37
	KSM-Pink-011	0.09	12.9	3845	86.37	bdl	593	44.679	0.125	bdl	1318	979	0.363	1.7	0.708	bdl	0.79	1163	44.27
	KSM-Pink-012	0.05	13.83	3198	85.52	bdl	505	29.224	bdl	bdl	1695	898	0.316	1.56	0.492	bdl	0.74	974	39.42
	KSM-Pink-013	0.12	13.16	3977	91.76	bdl	623	40.78	bdl	bdl	1401	980	0.363	1.95	0.853	bdl	0.97	1179	46.08
Orange	KSM-Ora-014	0.07	12.97	4191	63.18	bdl	558	35.091	bdl	bdl	1725	1011	0.428	2.18	0.568	bdl	0.7	1245	32.57
Purple	KSM-Pur-015	0.1	15.56	4047	90.35	bdl	840	49.78	0.1	bdl	3155	1170	0.43	2.35	1.004	6.37	0.81	1457	40.92
	KSM-pPur-016	0.09	15.34	3648	86.06	bdl	791	33.17	bdl	bdl	3098	1069	0.383	2.02	0.855	5.83	0.74	1338	38.29
	KSM-Pur-017	0.1	14.85	4139	138.8	bdl	715	75.731	bdl	bdl	4357	1098	0.403	2.28	1.467	6.68	1.22	1436	58.83
	KSM-Pur-018	bdl	21.07	7436	158.8	bdl	802	24.305	bdl	bdl	1091	913	0.323	1.89	1.059	6.85	1.27	1129	52.82
	KSM-Pur-TD	bdl	17.73	8731	146.3	bdl	750	20.116	bdl	bdl	913.4	858	0.221	1.6	1.055	7.81	0.99	1058	46.04
Golden with orient	KSM-GY-019	0.06	14.3	5164	58.61	bdl	310	18.732	bdl	bdl	821.8	563	bdl	0.92	0.653	11.5	0.84	775	43.02
	KSM-GY-020	0.09	13.88	3696	242.3	bdl	872	24.169	bdl	bdl	3176	1042	0.391	1.94	10.83	1.93	1.3	1459	68.6
	KSM-GY-021	bdl	11.5	4108	53.79	bdl	330	36.186	bdl	bdl	636	544	bdl	0.8	0.908	3.48	0.84	560	46.91
	KSM-GY-022	0.09	12.44	3575	165.2	bdl	814	42.906	bdl	bdl	2483	1036	0.418	2.07	14.34	0.78	1.57	1461	73.25
	KSM-GY-023	bdl	16.3	4260	71.93	bdl	317	32.398	bdl	bdl	1911	520	bdl	0.82	1.362	9.95	0.75	662	47.05
Light orange KSM-Ora-half-024	Outer part of nacreous layer of pearl, spot 1	bdl	17.22	7024	175.1	bdl	392	13.423	0.438	bdl	1401	603	0.258	1.17	0.756	10.8	1.33	1000	72.01
	Near the inner layer, spot 2	0.08	13.24	6953	175.4	bdl	376	45.249	0.266	bdl	378.2	579	0.203	0.96	0.847	14.2	0.64	780	33.35
	Near the inner layer, spot 3	bdl	11.05	7023	128.6	bdl	300	49.173	bdl	bdl	293.3	542	0.14	1.14	0.719	5.93	0.52	695	26.26
	Near the inner layer, spot 4	bdl	12.06	6974	53.61	bdl	229	70.857	bdl	bdl	391.8	550	0.175	1.12	0.781	7.34	0.49	659	23.06
	Near the inner layer, spot 5	bdl	14.12	8420	118.8	bdl	257	30.94	bdl	bdl	361.3	638	0.24	1.11	0.646	8.16	0.48	710	22.06
	Near the inner layer, spot 6	bdl	16.73	8926	174.6	bdl	342	6.3969	0.21	bdl	302.8	627	0.246	1.21	0.869	12.3	1.35	996	55.41
	Near the inner layer, spot 7	bdl	15.61	9528	361.5	bdl	237	31.584	0.432	bdl	519.3	654	0.177	1.35	0.77	15	0.75	876	39.66
	Inner part of the layer (near bead, spot 8)	0.11	17.43	9800	432.7	bdl	245	60.375	0.498	bdl	423	735	0.268	1.33	0.825	7.94	0.98	941	42.42
Lake Kasumigaura, Japan: Shell	Sample	^{7}Li	^{11}B	^{23}Na	^{24}Mg	^{27}Al	^{31}P	^{39}K	^{45}Sc	^{47}Ti	^{55}Mn	^{57}Fe	^{59}Co	^{60}Ni	^{63}Cu	^{66}Zn	^{69}Ga	^{88}Sr	^{137}Ba
KSM-SHELL-001 Cut surface position	Outer part of shell spot 1 (prismatic)	0.24	5.815	12872	47.5	28.25	267	62.625	bdl	13.5	395.2	810	0.335	2.12	5.078	9.91	0.49	883	32.42
	Spot 2	bdl	4.525	9144	27.67	13.2	155	77.46	bdl	4.34	972.1	625	0.191	1.27	1.249	4	0.56	722	29.22
	Spot 3	bdl	4.244	7279	12.26	bdl	147	28.027	bdl	bdl	797.3	474	0.16	1.07	0.252	0.25	1.32	556	65.81
	Inner part of shell, spot 4	bdl	3.365	6143	33.01	bdl	191	92.327	bdl	bdl	1574	403	0.14	0.81	0.226	bdl	0.3	731	22.94

Lake Kasumigaura, Japan: Shell	Sample	^{7}Li	^{11}B	^{23}Na	^{24}Mg	^{27}Al	^{31}P	^{39}K	^{45}Sc	^{47}Ti	^{55}Mn	^{57}Fe	^{59}Co	^{60}Ni	^{63}Cu	^{66}Zn	^{69}Ga	^{88}Sr	^{137}Ba
KSM-SHELL-002 Cut surface position	Outer part of shell spot 1 (prismatic)	bdl	3.096	9891	42.07	10.2	385	25.178	bdl	12	427.9	801	bdl	1.69	26.95	20.4	0.58	563	18.79
	Spot 2	0.05	4.157	6744	40.12	bdl	375	44.251	bdl	bdl	517.2	689	0.104	0.97	0.507	3.98	0.23	475	11.1
	Spot 3	0.13	4.456	6751	60.67	bdl	372	72.393	bdl	bdl	610.4	707	bdl	1.09	0.424	4.83	0.28	490	14.6
	Spot 4	0.1	4.831	6358	81.53	bdl	366	74.44	bdl	bdl	677.5	727	bdl	1.23	0.345	1.84	0.62	632	23.13
	Spot 5	0.08	5.001	6747	45.03	bdl	371	91.306	bdl	bdl	949.9	693	bdl	1.64	0.311	4.33	0.3	514	19.85
	Spot 6	0.09	5.391	5143	34.76	bdl	368	83.539	bdl	bdl	705.1	594	bdl	0.64	4.424	86.2	0.3	577	19.04
	Spot 7	0.09	5.502	4844	27.95	bdl	367	107.76	bdl	bdl	780.2	516	bdl	bdl	0.126	4.35	0.36	617	21.15
	Inner part of shell, spot 8	0.11	5.389	4436	43.82	bdl	368	118.64	bdl	bdl	1240	501	bdl	0.85	9.511	0.2	0.24	632	22.39
KSM-SHELL-003 Cut surface position	Outer part of shell spot 1 (prismatic)	0.06	3.44	13519	73.72	139.6	410	104.13	bdl	21.8	1065	894	0.52	3.2	7.756	14.2	1.02	1096	53.14
	Spot 2	0.05	10.25	9069	87.25	bdl	258	30.605	bdl	5.83	1165	703	0.217	1.61	1.202	0.92	0.75	1092	37.03
	Spot 3	bdl	11.57	8097	35.83	bdl	197	75.058	0.332	bdl	1192	631	0.179	1.36	0.266	0.68	0.41	746	22.43
	Spot 4	0.05	7.965	7943	27.97	bdl	211	39.239	bdl	bdl	1435	571	0.201	0.92	0.391	bdl	0.35	823	21.99
	Inner part of shell, spot 5	bdl	9.947	7154	21.84	bdl	206	70.981	bdl	bdl	1641	592	0.193	1.61	0.537	0.65	0.73	961	36.01
Lake Taihu, China: Pearl	Sample	^{7}Li	^{11}B	^{23}Na	^{24}Mg	^{27}Al	^{31}P	^{39}K	^{45}Sc	^{47}Ti	^{55}Mn	^{57}Fe	^{59}Co	^{60}Ni	^{63}Cu	^{66}Zn	^{69}Ga	^{88}Sr	^{137}Ba
Pink	CN-FW-P1	bdl	14.71	7050	131.1	bdl	433	41.481	bdl	bdl	1693	1137	0.563	1.89	1.037	3.87	11.9	1108	768
Cream	CN-FW-P2	0.27	11.88	6381	150.3	bdl	472	39.228	bdl	bdl	2390	1098	0.519	1.98	1.594	1.71	4.24	802	271.2
Light yellow	CN-FW-P3	bdl	13.6	6757	72.75	bdl	346	109.53	bdl	bdl	1144	1132	0.477	1.9	0.418	1.36	6.25	1042	365.6
Pink	CN-FW-P4	bdl	12.58	6379	63.22	bdl	397	30.397	bdl	bdl	1316	1019	0.456	1.71	1.617	4.71	3.86	812	216.8
Cream	CN-FW-P5	bdl	10.8	5765	122.3	bdl	442	41.533	bdl	bdl	2034	997	0.426	1.59	0.864	0.98	3.17	806	217.1
Light yellow	CN-FW-P6	0.05	10.89	5758	148.7	bdl	419	81.917	bdl	bdl	2386	1034	0.474	1.82	1.639	1.36	5.51	967	299.3
Purple	CN-FW-P7	bdl	16.76	6523	60.73	bdl	601	61.337	bdl	bdl	1250	1197	0.554	2.28	1.416	0.61	5.97	795	332.4
Cream	CN-FW-P8	bdl	13.81	5978	122.8	bdl	583	39.319	bdl	bdl	2889	1054	0.45	1.66	0.563	3.93	13.1	1151	819.1
Light yellow	CN-FW-P9	bdl	13.52	6992	143.5	bdl	387	55.757	bdl	bdl	4333	1107	0.408	1.68	0.652	5.63	36.1	1318	2314
Purplish pink	CN-FW-P10	0.21	12.49	8411	111	bdl	453	85.281	bdl	bdl	393.7	1187	0.441	1.73	0.87	5.42	5.45	767	307.5
Cream	CN-FW-P11	bdl	15.94	7359	236.9	bdl	588	102.86	bdl	bdl	2653	1167	0.513	2.07	1.288	3.76	13.1	1112	777
Light yellow	CN-FW-P12	bdl	12.06	5943	108.9	bdl	405	130.33	bdl	bdl	2959	979	0.381	1.76	1.566	bdl	9.72	1025	630.6
Purple	CN-FW-P13	bdl	10.45	6528	96.14	bdl	439	48.445	bdl	bdl	2063	908	0.396	1.57	0.814	3.22	18.5	883	1094
Cream	CN-FW-P14	bdl	12.26	6930	131.4	bdl	457	76.369	bdl	bdl	2136	1102	0.456	1.64	0.602	1.67	11.7	1104	735.9
Orange	CN-FW-P15	bdl	11.24	6335	116.5	bdl	391	29.85	bdl	bdl	2388	956	0.379	1.84	1.12	0.21	8.18	1001	552.9
Lake Taihu, China: Shell	Sample	^{7}Li	^{11}B	^{23}Na	^{24}Mg	^{27}Al	^{31}P	^{39}K	^{45}Sc	^{47}Ti	^{55}Mn	^{57}Fe	^{59}Co	^{60}Ni	^{63}Cu	^{66}Zn	^{69}Ga	^{88}Sr	^{137}Ba
China-SHELL-001 Cut surface position	Outer part of shell, spot 1 (prismatic)	bdl	12.64	8841	116.8	10.31	198	159.33	bdl	bdl	2731	612	0.394	4.81	5.613	10.7	6.73	862	459.7
	Spot 2	0.11	4.768	8203	35.81	29.72	195	57.733	bdl	bdl	1029	572	0.171	1.08	1.588	3.34	4.89	514	274.9
	Spot 3	0.1	4.543	7499	17.38	bdl	122	55.342	bdl	bdl	588.4	479	0.191	1.16	0.993	6.32	2.06	463	115.6
	Spot 4	bdl	5.235	5815	26.38	bdl	144	67.59	bdl	bdl	814	744	0.144	0.76	0.774	3.58	2.03	745	135
	Spot 5	bdl	2.767	5354	38.84	bdl	165	96.771	bdl	bdl	5291	315	0.104	0.73	0.726	0.21	3.23	837	225.5
	Inner part of shell, spot 6	0.08	3.87	7186	20.57	bdl	112	77.982	bdl	bdl	2190	432	0.13	0.83	0.46	bdl	2.79	711	150.7
Detection limits		0.05	1.95	9.73	0.46	4.03	32	3.24	0.1	3.15	0.33	27.8	0.1	0.52	0.29	0.2	0.1	0.36	0.1

bdl=below detection limit

CONCLUSIONS

The production of nucleated freshwater cultured pearls from Lake Kasumigaura has subsided in recent years, but large Kasumiga pearls with thick nacre and strong luster in pink or purple colors are highly valued in the international market. In this study, the author visited the Toda Shinju pearl farm at the Ono River, which empties into Lake Kasumigaura, to harvest pearls and shells directly and analyze them. The pearls were analyzed by means of absorption and Raman spectroscopy, observation of internal structure, and quantitative compositional analysis for major and trace elements.

The freshwater nucleated cultured pearls collected from *Hyriopsis* hybrid shells were divided into six groups of representative colors: cream, light yellow, pink, purple, orange, and golden with orient. The nacreous growth layer in the cream and light yellow pearls showed thick layers of aragonite platelets and laminated irregularity with low tone, and a vague absorption band between 480 and 500 nm in the visible region of the UV-Vis-NIR reflectance spectrum. Pink, purple, and orange pearls demonstrated the nacre's very fine crystalline structure with neat lamination and very good luster. They showed a strong absorption center in the range between 480 and 530 nm, which increased in intensity as the color tone and saturation of the pearl became stronger, marking the characteristic increment in a wider range between 415 and 820 nm. The surface of the golden pearls with orient was covered with a thin prismatic layer of aragonite that was rich in yellow-brown organic substance, and these pearls were characterized by strong orient. They showed two absorption regions in the visible range, one at 320–460 nm centered at 373 nm and the other at 580–820 nm centered at 640 nm. Raman spectroscopy detected a pigment contained in the nacre.

Kasumiga pearls generally do not undergo treatments such as bleaching and dyeing, and the samples showed very weak chalky green-blue fluorescence or no reaction under UV irradiation, providing proof of natural color.

Semiquantitative analysis of the Kasumiga pearls detected a main component of CaO, followed in descending order by Na, Mn, Sr, and Fe. LA-ICP-MS analysis detected 18 minor and trace elements, of which Na, Mn, Sr, and Fe were in the highest concentration (over 1000 ppmw). P, Mg, Al, and K were in the second-highest group (several hundred to several dozen ppmw). B, Ti, and Zn were under 22 ppmw, while Li, Sc, Co, Ni, Cu, and Ga were detected in trace amounts (under 10 ppmw). Al and Ti were only distributed in the prismatic aragonite growth layer on the outer part of the mollusk shell. All the metallic elements detected were confirmed to be unrelated to the color of the pearls.

In Lake Taihu, China, large volumes of freshwater beaded cultured pearls using *Hyriopsis* hybrid shells of the same species used at Lake Kasumigaura have been produced for the international market. Chemical analysis by LA-ICP-MS demonstrated that chemical fingerprinting using the Ba to Ga ratio was effective in distinguishing freshwater nucleated pearls from these two countries.

ABOUT THE AUTHOR

Dr. Abduriyim (tgs@gemscience.tokyo) is president of Tokyo Gem Science LLC and the director of GSTV Gemological Laboratory, also in Tokyo.

ACKNOWLEDGMENTS

The author would like to thank Mr. Ryuichi Toda from Toda Shinju for facilitating our visit to examine their culturing process at Lake Kasumigaura. Mr. Takayoshi Nishida from Belpearl provided current marketing information on Kasumiga pearls. The author also thanks the Miyuki Co., Ltd for offering study specimens from China, as well as colleague Yumi Eguchi in GSTV Gemological Laboratory and Nick Sturman and Kwanreun Lawanwong in GIA's Bangkok laboratory for assisting with the X-ray data collection and providing helpful discussions.

REFERENCES

Akamatsu S., Li T., Moses T., Scarratt K. (2001) The current status of Chinese freshwater cultured pearls. *G&G*, Vol. 37, No. 2, pp. 96–109, http://dx.doi.org/10.5741/GEMS.37.2.96

Barthelat F., Rim J.E., Espinosa H.D. (2009) A review on the structure and mechanical properties of mollusk shells – Perspectives on synthetic biomimetic materials. In B. Bhushan and H. Fuchs, Eds., *Applied Scanning Probe Methods XIII: Biomimetics and Industrial Applications*. Springer-Verlag, Berlin and Heidelberg, Germany, pp. 17–44.

Boggild O.B. (1930) The shell structure of the mollusks. *Kongelige Danske Videnskabernes Selskabs Skrifer*, Vol. 9, No. 2, pp. 233–326.

Karampelas S., Fritsch E., Mevellec J.-V., Gauthier J.-P., Sklavounos S., Soldatos T. (2007) Determination by Raman scattering of the nature of pigments in cultured freshwater pearls from the mollusk *Hyriopsis cumingi*. *Journal of Raman Spectroscopy*, Vol. 38, No. 2, pp. 217–230, http://dx.doi.org/10.1002/jrs.1626

Kobayashi I. (1971) Internal shell microstructure of recent bivalvian molluscs. *Science Reports of Niigata University*. Series E, Vol. 2, pp. 27–50.

Komatsu H., Hirama K., Kogawa H. (1989) Consideration about chromophore mechanism of 6 kinds of fresh-water pearls with the typical color tone. *Journal of the Gemmological Society of Japan*, Vol. 14, No. 1-4, pp. 46–47 (in Japanese).

Liu X.J., Li J.L (2015) Formation of the prismatic layer in the freshwater bivalve *Hyriopsis cumingii*: the feedback of crystal growth on the organic matrix. *Acta Zoologica*, Vol. 96, No. 1, pp. 30–36.

Nakahara H (1994) Surface patterns and inner structures of mollusk shells. *Journal of the Surface Science Society of Japan*, Vol. 15, No. 3, pp. 184–188 (in Japanese).

Statistics of fishery and cultivation (2000) *Almanac of Fishery Agency*. Ministry of Agriculture, Forestry and Fisheries, Tokyo.

Strack E. (2006) *Pearls*. Ruhle-Diebener-Verlag, Stuttgart, Germany, 707 pp.

Sturman N., Homkrajae A., Manustrong A., Somsa-ard N. (2014) Observations on pearls reportedly from the Pinnidae family (pen pearls). *G&G*, Vol. 50, No. 3, pp. 202–215, http://dx.doi.org/10.5741/GEMS.50.3.202

Toyama T. (1991) Freshwater pearl—Status of, and future. *Pearls of the World II*, Les Joyaux special edition, Shinsoshoku Co., Tokyo, pp. 119–126.

Wada K. (1974) Biomineralogy and pearl culture-1. *Journal of the Gemmological Society of Japan*, Vol. 1, No. 1, pp. 19–23 (in Japanese).

——— (1999) *Science of Pearl—Mechanism of Formation and Method to Distinguish*. Shinjyu Shuppan Co., Tokyo, 336 pp.

Wada K., Fujinuki T. (1976) Biomineralization in bivalve molluscs with emphasis on the chemical composition of the extrapallial fluid. In N. Watabe and K.M. Wilbur, Eds., *The Mechanisms of Mineralization in the Invertebrates and Plants*. University of South Carolina Press, Columbia, pp. 175–190.

Ward F. (1985) Pearls. *National Geographic*, Vol. 168, No. 2, August, pp. 192–223.

For online access to all issues of GEMS & GEMOLOGY from 1934 to the present, visit:

gia.edu/gems-gemology

GEMOLOGICAL CHARACTERIZATION OF SAPPHIRES FROM YOGO GULCH, MONTANA

Nathan D. Renfro, Aaron C. Palke, and Richard B. Berg

Yogo Gulch in central Montana is one of the most important gem deposits in the United States. Although very little material has been recovered there in recent years, it has produced several million carats of rough sapphire over the course of its history (Voynick, 2001). These stones, known for their vibrant untreated blue color and high clarity, have always commanded a price premium, especially in sizes larger than 0.75 ct. This paper offers a thorough gemological characterization of Yogo sapphire, which may be unfamiliar to many gemologists. Fortunately, Yogo sapphires are unique and experienced gemologists can easily separate them from gem corundum of different geographic origins throughout the world, making it possible to determine the provenance of important stones from this deposit.

Over more than 120 years, mines in Yogo Gulch, Montana, have produced millions of carats of rough sapphire. Much of that has yielded very small finished stones, and faceted stones over 1 ct are highly prized (figure 1). The largest known Yogo sapphire crystal was found in 1910 and weighed 19 ct (Howard, 1962a) The shape of Yogo rough is often in the form of flat tabular crystals that offer a very low yield. Large stones over 1 ct are almost exclusively collector stones, with the provenance having a significant impact on value. While there are other significant sources of gem-quality sapphire in Montana—including Rock Creek, Missouri River, and Dry Cottonwood Creek—Yogo sapphires are unique among these and other sapphire deposits worldwide (figure 2). Virtually all of the material produced has a desirable even blue to violet or purple color, often with higher clarity than sapphires from other deposits (Yaras, 1969) (figure 3). Yogo sapphires do not require heat treatment, offering a virtual guarantee of their untreated nature. They also possess a unique trace-element chemistry and an inclusion suite that makes them easily recognizable to the experienced gemologist.

In Brief

- Sapphires from Yogo Gulch are generally small, and finished stones larger 1 ct are rare.
- Yogo sapphires range in hue from blue to purple with purple stones representing about 3% of total production. They do not require heat treating and are often relatively free of inclusions.
- A unique chemistry profile and inclusion suite makes it possible to separate them from sapphires from other deposits.

HISTORY

In 1895, the Yogo sapphire deposit was accidentally discovered by a gold prospector named Jake Hoover. Hoover sought financial backing from two friends—local banker S.S. Hobson and Dr. Jim Bouvet, a veterinarian from Chicago—and the three formed a mining partnership. While recovering gold from his sluice, Hoover found many shiny blue pebbles and sent them to Dr. George Kunz of Tiffany & Co. in New York for identification. These were confirmed to be sapphires, and a cigar box full of the blue pebbles was purchased by Tiffany for $3,750. In contrast, Hoover only recovered $700 in gold that season (approximately 35 troy ounces; Woodward and Hanley, 2013). Since the sapphires proved to be more profitable than the gold, Hoover and his partners focused

See end of article for About the Author and Acknowledgments.
GEMS & GEMOLOGY, Vol. 54, No. 2, pp. 184–201,
http://dx.doi.org/10.5741/GEMS.54.2.184
© 2018 Gemological Institute of America

Figure 1. This suite contains more than 36 carats of Yogo sapphires. Courtesy of RareSource. Photo by Robert Weldon/GIA.

their attention on mining for sapphires at Yogo Gulch. In 1896, James Ettien discovered a sapphire-bearing weathered **dike** (for boldfaced terms, please refer to the Glossary) and staked a mining claim on it (Howard, 1962b). This claim was purchased in late 1896 by Hoover and his associates for $2,450.

In 1897, the death of Jim Bouvet brought the introduction of two new partners, Matthew Dunn and

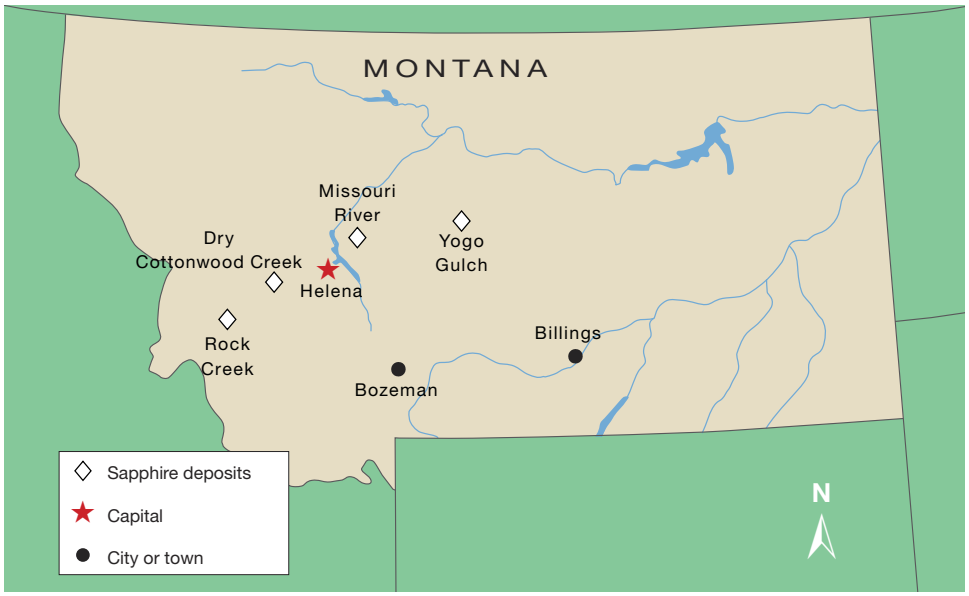

Figure 2. The major gem sapphire deposits in the state of Montana. The sapphire deposit at Yogo Gulch is the only primary deposit in Montana.

George A. Wells, and the foursome formed the New Mine Sapphire Syndicate (Voynick, 2001). Other claims in the area began to appear as news of the sapphire deposit spread. John Burke and Pat Sweeny staked a claim further west on Yogo Creek that would later be known as the American mine (Woodward and Hanley, 2013).

The following year saw the arrival of a group of London gem merchants, as Johnson, Walker, and Tolhurst Ltd. acquired the majority interest in the New Mine Sapphire Syndicate. Annual production increased to more than 400,000 carats before 1900, with approximately a quarter of that production being gem quality. The remainder found a market for industrial use as abrasives or watch bearings (figure 4). By 1901, the London group had acquired the remaining share of the New Mine Sapphire Syndicate from Hoover's partners (Woodward and Hanley, 2013). This mine at the eastern end of the deposit would become known as the English mine. Charles

Figure 3. This suite of rough and cut Yogo sapphires shows the wide range of blue to violet or purple hues and light to dark saturation combinations that can be found in Yogo sapphires. The largest faceted stone is a 1.44 ct cushion cut. Photo by Kevin Schumacher, courtesy of Bill Vance.

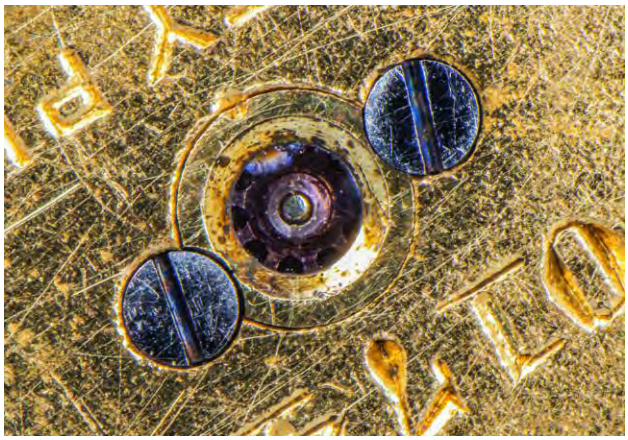

Figure 4. Many of the "industrial-grade" Yogo sapphires that were too thin to cut as gemstones were used for watch bearings and abrasives. The natural sapphire bearing in this American Waltham Watch Co. movement, which measures 1.28 mm in diameter, is likely not from the Yogo deposit. Photomicrograph by Nathan Renfro.

Gadsden (figure 5), another Englishman who would become a significant figure in Yogo's history, arrived in 1902 and supervised the English mine until it closed in 1929.

Mining claims on the western end of the dike that were staked by Burke and Sweeny were purchased by the American Sapphire Company of New York, which began operations in 1905. This became known as the American mine (figure 6). Within a few years, the company reorganized as the Yogo American Sapphire Company and was ultimately acquired by the New Mine Sapphire Syndicate in 1914 at Gadsden's recommendation. Even though the mine was not reopened at that time, Gadsden rewashed the dump piles from the American mine, recovering most of the purchase price of $80,000 (Howard, 1962b).

World War I would halt the production of Yogo sapphires, as miners were needed to extract metals to support the war effort. By 1921, activity at Yogo had returned to pre-war levels, but this early productive period in Yogo sapphire mining was about to end. After a flood in 1923 destroyed much of the English mine operation's infrastructure, production declined significantly. This natural disaster and competition from synthetic sapphires were devastating for sapphire mining at Yogo Gulch. In 1927, the last year of production from this era, the deposit yielded a reported $4,850 of sapphire (Woodward and

Figure 5. Left: Charles Gadsden and his wife Margaret managed the English mine from 1902 until its closure in 1929. Photo courtesy of Stephen Droullard. Right: A plaque installed at the "tollgate" in Yogo Gulch marks the Gadsdens' significance in the history of the Yogo deposit. Photo by Nathan Renfro.

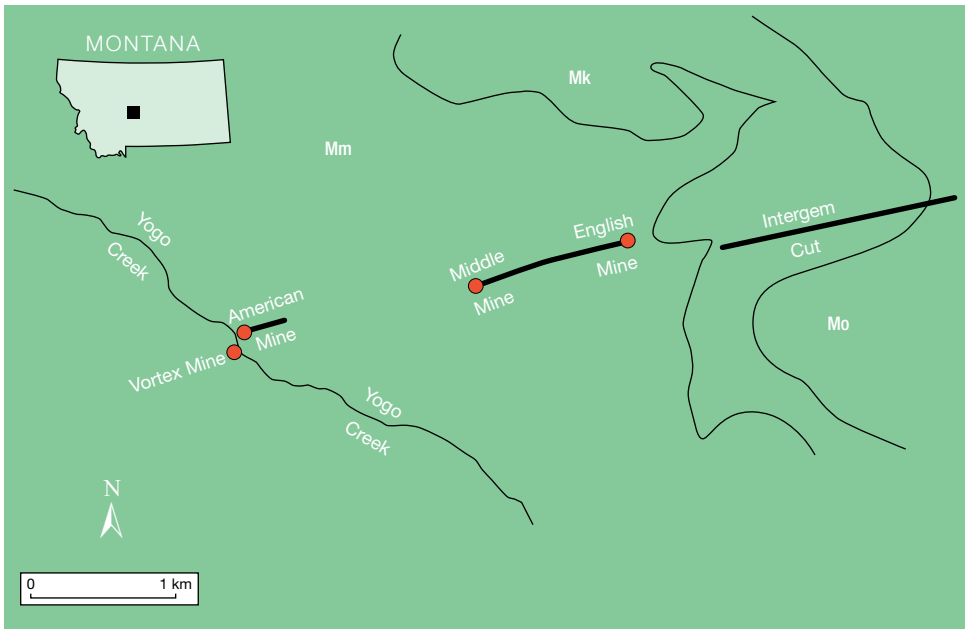

Figure 6. The Yogo dike system. The thick line demarcates the Yogo dike. Geological formations shown on the map are the Mississippian-age Madison Formation (Mm), the Kibbey Formation (Mk), and the Otter Formation (Mo), all belonging to the Madison Group. Modified from Dahy (1991) and Mychaluk (1995).

Hanley, 2013). The English mine had a successful and profitable run and even uncovered a 19 ct rough stone, still the largest Yogo sapphire ever recorded. That stone was cut into four gems, the largest of which weighed 8.5 ct (Howard, 1962a). Nevertheless, the mine was officially closed in 1929 (Howard, 1962b).

The New Mine Sapphire Syndicate struggled to find a buyer for a number of years, but in 1949 a group of investors led by Thomas P. Sidwell began lengthy negotiations to purchase the mine. This group formed the Yogo Sapphire Mining Corporation (which was eventually reorganized in 1956, once again as the New Mine Sapphire Syndicate) and purchased the mine for $65,000. After somewhat unsuccessful attempts at mining and with financial and legal problems mounting, the mine was purchased in 1965 by Siskon Inc., a Nevada-based construction firm, for $75,000. Siskon then leased the property to Arnold Baron, who had some success cutting and selling sapphires but ran into problems mining the dike, which turned out to be more complex than previously thought (Voynick, 2001). After two years, when Baron decided that the mining cost was prohibitive and chose not to purchase the property, Siskon put it up for sale. The property was reportedly purchased for $585,000 (Voynick, 2001) by a group of Californians including Herman Yaras and Ray Von Felden, who formed Sapphire Village Inc. This deal was comprised of 1,780 acres along the sapphire-bearing dike and included the old British and American mines and the surrounding land (Leiper, 1969). In addition to developing the mine, the new owners created Sapphire Village, in which a portion of the property was subdivided into small lots, up to one-third of an acre in size, that had rights to excavate a limited amount of rock from an area of virgin dike (Leiper, 1969). By 1973, Chikara Kunisaki formed the Sapphire International Corporation, which bought the assets of Sapphire Village Inc. and began one of the most serious mining efforts on the Yogo dike since the English mine (Voynick, 2001). At a cost of nearly $5 million, he installed a 3,000-foot tunnel in the old American mine that became known as the "Kunisaki Tunnel." In the fall of 1976, operations at Sapphire International ceased with another failed attempt at profitably mining Yogo sapphires. In 1977, another player entered the Yogo sapphire game. Victor di Suvero leased the Kunisaki property under the name Sapphire-Yogo Mines, Inc. Di Suvero also started a marketing and distribution company, Sapphire Trading Co., Inc., which in 1978 began what was slated to be an extensive marketing campaign aimed at bringing Yogo sapphires into the spotlight ("The $1 million sapphire campaign," 1978). Unable to make the payments and with funding running out, Di Suvero relinquished the lease in 1979 (Voynick, 2001).

The next turn in the Yogo tale saw the sale of the Kunisaki property in 1980 to mining engineer Harry Bullock for $6 million and the formation of American Yogo Sapphire, Ltd. In 1982, the company changed its name to Intergem, Ltd., and began marketing Yogo sapphires as "Royal American Sap-

phires," guaranteeing them to be free of the heat treatment that was relatively common among sapphires from other deposits. By 1984, Intergem's marketing campaign seemed to be working, with sales that year of over $3 million. But in 1985, Intergem was no longer able to make their payments to Sapphire International, which had become Roncor Inc., and in 1986 the property was once again under the ownership of Chikara Kunisaki (Voynick, 2001).

In the late 1980s, consulting geologist and gemologist Delmer Brown had brought the Yogo sapphire deposit to the attention of AMAX Exploration Inc. president William Lodder (Voynick, 2001), who began a 22-month lease-purchase agreement with Roncor in March 1993. After nearly two years of mining and exploration, AMAX determined it was not cost effective to purchase the mine from Roncor for the approximately $10 million asking price, and retired from mining the Yogo dike in 1995 (Voynick, 2001). After Roncor took over the Yogo property again, Silver Standard Resources and an associated company named Pacific Sapphire Company Ltd. entered a lease deal with Roncor, but they were not successful. Their funds ran out and their lease option with Roncor expired in 2001 (Woodward and Hanley, 2013).

On the heels of Intergem, Lanny Perry and Chuck Ridgeway, both of whom had worked for Sapphire International in the 1970s, were out prospecting when they discovered a new exposure of sapphire-bearing dike. By 1985 they went commercial with their mining claims and formed Vortex Mining with additional partners Pete Ecker and Paul Davis Jr. By 1987 Vortex Mining began underground operations, with a shaft that reached a depth of 280 feet (Woodward and Hanley, 2013).

Although Roncor conducted some small-scale mining, even uncovering an 11 ct crystal in the summer of 1992 (Voynick, 1995), Vortex Mining operated the only active commercial mine in the late 1990s, producing 45,000 carats of cuttable rough per year (Voynick, 2001). Operations expanded, and a company called Small Mine Development (SMD) partnered with the Vortex mine, establishing a joint venture known as Yogo Creek Mining. SMD added a 3,000-foot spiral decline reaching 475 feet and installed a wash plant capable of processing 100 tons of ore per day (Woodward and Hanley, 2013). This wash plant was later removed after Yogo Creek Sapphire Mining closed its operations in November 2004, once mining became uneconomical (Laurs, 2005).

By 2005, another deal was struck with Lanny Perry, who reacquired ownership of the Vortex mine. Perry had been acquainted with a miner named Mike Roberts while working in Alaska, and Roberts became interested in the Vortex property. He traded his Alaska gold mine to Perry in 2008 and set up Roberts Yogo Company (Kane and Hughes, 2012). Roberts successfully operated the mine until 2012, when he was killed in an accident at the Vortex mine (Nixon, 2016).

The current chapter in Yogo's long history brings in a longtime jeweler and friend of Mike Roberts'. Don Baide, owner of the Gem Gallery in Bozeman, Montana, bought the mine from Roberts' wife in 2017 (Branstrator, 2017) and is operating as Yogo Mining LLC. Once the property is brought into compliance, mining operations can resume at the Vortex mine. Only time will tell what else is in store for the Yogo sapphire deposit.

LOCATION AND GEOLOGY

Around 350 million years ago (Ma), the part of Montana that would someday produce some of the world's finest sapphires was a warm, shallow sea. Microscopic organisms lived and died in this primordial pool, and their remains filtered down and littered the ocean floor. Their inanimate husks accumulated and eventually solidified into **limestone**. This rock became the Mission Canyon Formation of the Mississippian-age Madison Group. This formation is around 275 meters thick in central Montana and forms many of the scenic features at Yogo Gulch. Around 50 Ma the warm, ancient seas in Montana had long since dried up and another geological act was set to begin. Far below the surface, something was stirring in the earth's **mantle**, which had started to melt in places, producing magmas that rose to the surface and erupted in a fiery turmoil. This hadean activity produced numerous volcanic formations throughout Montana that form the Central Montana Alkalic Province. Among these volcanic formations, at a place that would come to be known as Yogo Gulch, was an unassuming dike that intruded into Mississippian-aged limestone and **shales** of the Madison Group in Judith Basin County, about 75 km southwest of the city of Lewiston. This is the geological story of how this small dike, in a remote location in central Montana, came to produce legendary blue sapphires.

The Yogo dike was emplaced at 48.2 Ma (Gauthier, 1995) and occurs in multiple discrete segments for a total length of about 10 kilometers. These multiple segments suggest multiple intrusion events as well as possible later-stage faulting. The dike ranges

Figure 7. This underground image of the Yogo dike, as seen from the Vortex mine, shows it to be approximately 30 cm thick. Photo by Nathan Renfro.

from <1 meter to about 6 meters wide (figure 7). Sapphires occur in low concentration (0–70 ct/ton; Mychaluk, 1995) in the Yogo dike itself, where current mining efforts are focused. Descriptions of the dike's geology here are based on the authors' firsthand observations at the mine as well as previous studies (Brownlow and Komorowski, 1988; Dahy, 1988, 1991; Mychaluk, 1992, 1995; Gauthier, 1995).

The dike rock is classified as a type of **lamprophyre**, a term that describes a group of ultrapotassic

volcanic rocks composed primarily of large crystals of mica and/or amphibole. The Yogo lamprophyre is more properly called a **ouachatite**, a specific type of lamprophyre that is predominantly composed of phenocrysts (large crystals) of mica and **clinopyroxene** set within a groundmass of fine-grained mica and clinopyroxene with minor **analcime**, calcite, corundum, and other trace accessory minerals. Also occurring in the lamprophyre are light-colored globular structures sometimes called **leucocratic ocelli**, which range in size up to about 1 cm and consist of carbonates (calcite and dolomite) along with analcime and/or zeolite minerals. In addition to the leucocratic ocelli, lamprophyric magma will occasionally pick up foreign bits of rock along their ascent to the earth's surface. These foreign rocks are called **xenoliths** (figure 8). While such xenoliths are rare, the most common ones in the Yogo dike are composed of plagioclase feldspar, clinopyroxene, and pyrope-almandine-grossular garnet. Importantly, Dahy (1988, 1991) reported the finding of a corundum-bearing plagioclase/clinopyroxene xenolith, which suggests that Yogo sapphires were derived from a similar source as garnet/clinopyroxene/feldspar xenoliths.

Figure 8. This sample of lamprophyre from Yogo Gulch contains a small sapphire crystal about 4 mm in length and several leucocratic ocelli. Photo by Robison McMurtry; courtesy of Katie McPherson, Montana Yogo and Agate.

In November 2017, two of the authors (NR and AP) had the opportunity to visit the Vortex mine, which had been recently purchased by Don Baide. Extensive underground workings in this portion of the Yogo dike were largely developed by Small Mine Development, LLC in 2000 (Woodward and Hanley, 2013) and were later worked by Mike Roberts when he owned Vortex. At the Vortex mine, the dike ranges up to about 12 inches (30 cm) in thickness. The rest of the dike, owned by the Roncor Corporation, is much wider. The contact with the country rock limestone is generally sharp, but the dike was seen to pinch and swell and cut off in many places, and occasionally it was clearly offset by later faulting. The Yogo dike is a fairly tough and competent rock, so the most profitable ore being pursued at the Vortex mine is the portion of the dike that has been altered and broken down to allow sapphires to be recovered more easily. This alteration may have occurred due to interaction of the magma with karstic groundwater during its intrusion into the Mission Canyon limestone. In many places the dike is completely unaltered and cohesive and appears dark gray to black. In other areas, the dike is so heavily altered that it is easily broken apart and appears orange, likely due to secondary production of iron (oxy)hydroxides. In these sections the dike rock has a clayey consistency, suggesting that the original minerals in the lamprophyre have been broken down by interaction with circulating fluids and largely turned into clay minerals.

Genesis of Yogo Sapphires. One of the most prominent features of rough Yogo sapphires is the **etched** appearance of the crystal surfaces (figure 9). This has long been recognized as evidence that the sapphires were out of equilibrium with the lamprophyre that transported them to the surface. In other words, the sapphires are foreign crystals, or **xenocrysts**, and did not crystallize directly from the lamprophyre. This means, unfortunately, that the sapphires have been removed from the rocks in which they originally formed, and so geologists have mostly had to search for clues within the sapphires themselves to understand their formation conditions.

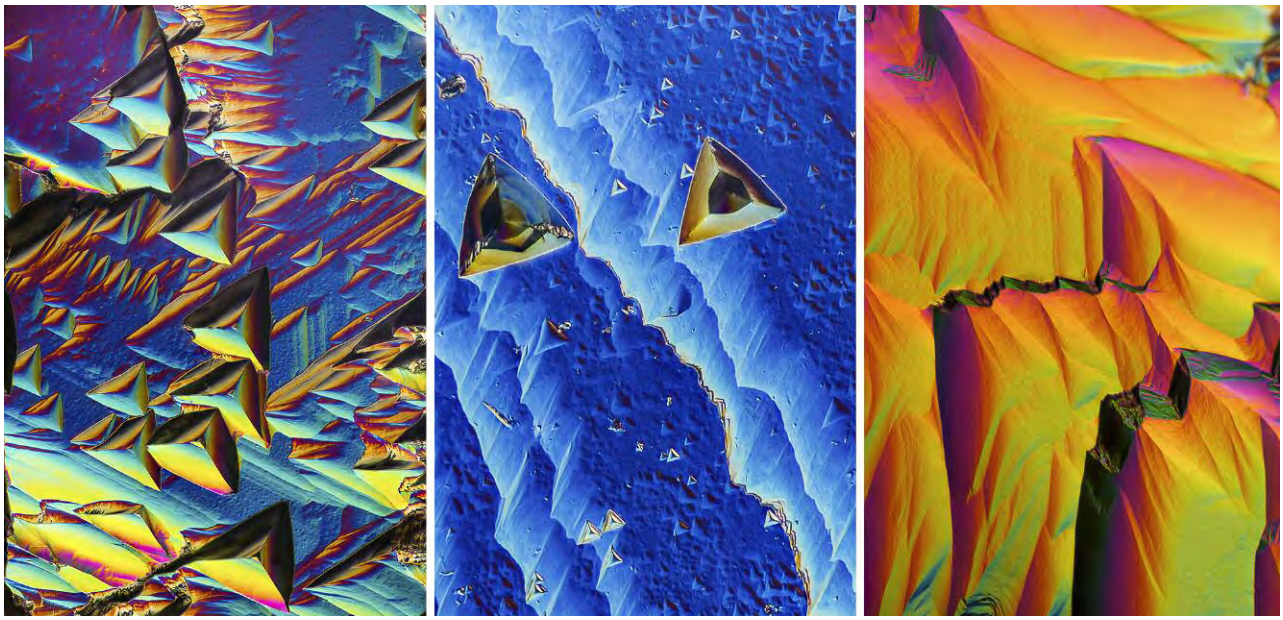

Figure 9. The surfaces of rough Yogo sapphires often show an etched appearance, as seen here using differential interference contrast microscopy, suggesting they were not in equilibrium with the lamprophyre that transported them to the earth's surface. Photomicrographs by Nathan Renfro (left and right) and Aaron Palke (center). Fields of view 0.95 mm (left), 0.48 mm (center), and 0.48 mm (right).

Several hypotheses have been advanced to explain the genesis of Yogo sapphires. Meyer and Mitchell (1988), Mychaluk (1992), and Gauthier (1995) favored the hypothesis that the sapphires are xenocrysts that originated in Al-rich metamorphic rocks and were sampled by the lamprophyre as it made its way to the earth's surface. Alternatively, Clabaugh (1952) suggested that the sapphires formed by metamorphism of Al-rich rocks by the hot lamprophyre as they were picked up and brought to the surface. While the sapphires have mostly been separated from their original host rocks, Dahy (1988, 1991) discovered a rare sapphire crystal in a plagioclase-pyroxene xenolith. This xenolith is similar to the garnet-plagioclase-pyroxene xenoliths studied by Gauthier (1995) and used for geothermobarometry measurements that indicated formation at 1.2–2.0 GPa (~40–70 km depth) and around 811–857°C. Cade and Groat (2006) found garnet inclusions in the sapphires to be consistent with group II mantle **eclogites**. However, the common occurrence of plagioclase feldspar inclusions in Yogo sapphires is inconsistent with an origin in mantle eclogites. Finally, Dahy (1991) suggested that Yogo sapphires formed through a **peritectic melting** reaction when the Yogo lamprophyre pooled at the base of the crust and partially melted Al-rich **pelitic rocks**.

A recent study by Palke et al. (2016) pointed out the similarity between the light-colored globular structures ("leucocratic ocelli"; figures 8 and 10) in the Yogo lamprophyre and the negative-crystal-shaped inclusions found in the Yogo sapphires (see "Inclusions" section below). Both are composed predominantly of analcime and calcite. Based on their analysis, Palke et al. (2016) proposed that Yogo sapphires crystallized when the lamprophyre intruded into the earth's lower crust and partially melted a preexisting aluminum-rich rock there, forming corundum through a peritectic melting reaction. This is similar to the model of Dahy (1991), except that Palke et al. (2016) suggested the protolith was an **anorthosite** or **troctolite** rather than a pelitic rock. In this model, the analcime-calcite inclusions in the sapphires are actually considered to be **carbonatite** melt inclusions, and they are interpreted to have the same origin as the leucocratic ocelli in the lamprophyre. Both features are believed to have originally been a single carbonatite melt produced when the lamprophyre partially melted carbonated and hydrated lower crustal anorthosites, troctolites, or some other plagioclase feldspar-rich rock (Palke et al., 2016). In this model, the Yogo sapphires may not have crystallized directly from the magma that transported them to the surface, but the lamprophyre is directly responsible for their formation, as it served as a heat source for the partial melting event that led to the formation of these sapphires. The important

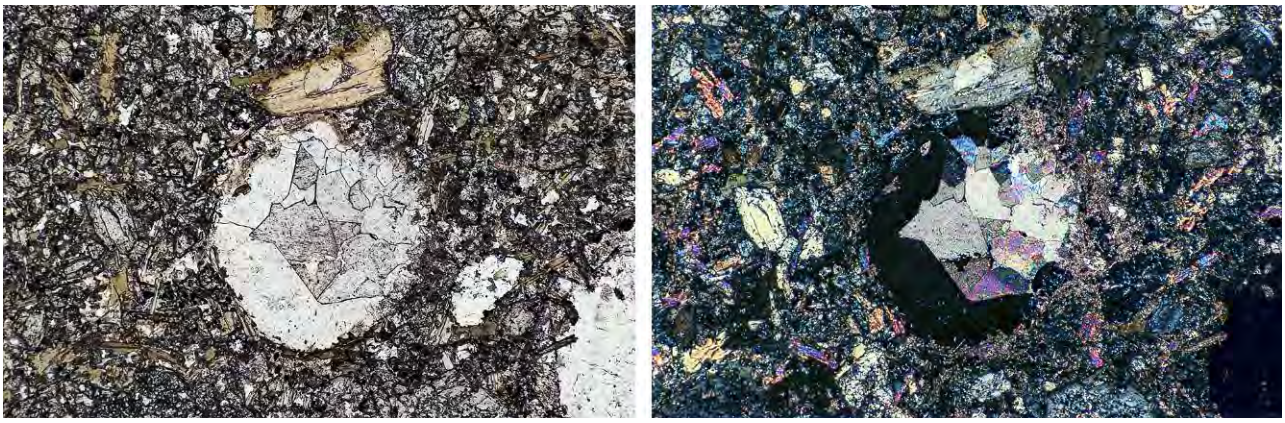

Figure 10. Leucocratic ocelli, shown in plane-polarized light (left) and cross-polarized light (right), are composed primarily of calcite near the core and analcime near the rim. Photomicrographs by Aaron Palke; field of view 2.88 mm.

distinction of this model is that while the Yogo sapphires can be considered xenocrysts in the lamprophyre, they were not accidentally incorporated since their genesis was intimately linked to the passage of the lamprophyre through the earth's crust.

One important aspect of this model is that, given the frequency of both silicate and carbonatite melt inclusions—in other words, inclusions of magma—Yogo sapphires can be considered igneous sapphires. As Palke et al. (2016) pointed out, this is at odds with their generally "metamorphic" trace-element signatures according to most of the commonly used corundum trace-element classification schemes. Other studies have also shown that such trace-element classification schemes often produce inconsistent results (e.g., Palke et al., 2017). It seems such classification should be used cautiously.

MATERIALS AND METHODS

For this study, a large number of rough and faceted Yogo sapphires from a variety of sources were examined. The largest rough sample weighed over 8 ct, while most weighed well under 1 ct. Numerous samples from the GIA Museum collection were used for trace-element chemistry measurements and UV fluorescence observation. Samples containing prominent inclusions were sourced from private collections. Also examined was a sample of Yogo sapphire in place in its host rock.

Standard gemological instruments were used to measure refractive index, birefringence, specific gravity, pleochroism, and visible absorption spectra. A standard combination long-wave (365 nm) and short-wave (254 nm) ultraviolet lamp was used for fluorescence observations. Microscopic observation was performed using a Nikon Eclipse LV100 compound microscope with an observed magnification of up to 1000× and differential interference contrast capabilities, outfitted with a Nikon DS-Ri2 camera for recording images. Also used were a Nikon SMZ25 stereomicroscope equipped with dual fiber-optic illuminators, darkfield and brightfield illumination, polarizing filters, and a Nikon DS-Ri2 camera with an observed magnification of up to 157.5×.

For spectroscopic measurements, we carefully selected a 4 mm Yogo sapphire that was free of inclusions and obvious color zoning. The sample was then fabricated into an optically oriented wafer with two polished sides oriented parallel to the optic axis. This sample preparation allowed polarized spectra measurements on both the ordinary and extraordinary rays (Thomas et al., 2014). Inclusions were identified using a Renishaw InVia Raman system with a 514 nm laser. Infrared absorption spectra were collected with a Thermo Nicolet 6700 FTIR spectrometer. Polarized UV-Vis-NIR absorption spectra were collected using a Perkin Elmer Lambda 950 spectrometer. Raman mapping of the 694 nm "*R*-line" was performed using a Thermo DXR2xi Raman imaging microscope with a 532 nm laser. Laser ablation–inductively coupled plasma–mass spectrometry (LA-ICP-MS) analyses were conducted on a Thermo Scientific iCap-Q ICP-MS with plasma RF power of 1400 W coupled with a New Wave Research UP-213 laser ablation unit with a frequency-quintupled Nd:YAG laser (213 nm wavelength with 4 ns pulse width). Laser conditions consisted of a 55 µm diameter spot size, a fluence of 10±1 J/cm^2, and a 15 Hz repetition rate using internally developed corundum standards (Stone-Sundberg et al., 2018).

RESULTS AND DISCUSSION

Gemological Properties. In general, sapphires from geologically similar deposits show overlapping properties, often making it difficult to determine the precise geographic origin. For example, a sapphire from Madagascar and a sapphire from Kashmir, India, can have a similar appearance, physical properties, chemistry, and inclusions. There can be significant overlap in the gemological characteristics between Sri Lankan and Burmese sapphires, often making geographic origin determination of such stones difficult if not impossible. Yogo sapphires, however, are unlike any other. Their inclusions and trace-element chemistry are distinct enough that when either is consistent with known Yogo sapphire reference data, a given stone is almost certainly from the Yogo deposit.

Yogo sapphires generally have light to dark blue colors and are generally flattened tabular crystals that yield small faceted stones. Violet to purple hues and color-change stones (blue to violet or purple) are occasionally encountered, but these account for less than 3% of production (see, e.g., figure 13) (Mychaluk, 1995). Most faceted Yogo sapphires are less than 1 ct, and faceted stones over 2 ct are extremely rare.

Typical refractive index measurements for Yogo sapphires range between 1.760 and 1.771, with a birefringence of 0.008–0.009, and specific gravity averages 3.99–4.00. All of these properties are consistent with gem corundum from other sources.

Inclusions/Microscopic Observations. For the gemologist, microscopic examination may be the most powerful tool to confirm that a sapphire is from the Yogo deposit. While sapphires from this deposit are generally eye clean, when inclusions are present, they are often diagnostic of this geographic origin. Unlike many other blue sapphires, Yogo sapphires are nearly always free of needle-like, oriented **rutile** inclusions known as "silk." However, it is extremely rare (but not impossible) for a Yogo sapphire to exhibit small patches of rutile silk in the form of small acicular needles, flakes, and particles, which are often called "rutile dust" by gemologists. In the authors' observations of hundreds of Yogo sapphires, only one was found to have silk, and only then in a very small amount (figure 11). This stone was reported to have been mined at the Vortex mine, and chemical analysis confirmed its origin.

The most common types of inclusions are thin-film **decrepitation halos**, also be referred to as "stress halos," surrounding solid **protogenetic** inclusions of rutile, feldspar, apatite, garnet, metal sulfides, and rarely **monazite** (figure 12A–H). The protogenetic rutile crystals are often rounded and black to reddish orange in color. They can also occur as elongated lathe-like brownish green protogenetic crystals. Pyrope-almandine-grossular garnets are also distinctive inclusions, because of their unusual chemistry, that can be encountered in Yogo sapphires. They generally appear brownish orange and can range from quite pale to very saturated in color depending on their size.

Other common inclusions are distinctive whitish **negative crystals** filled with a polycrystalline mixture of carbonate minerals and analcime (figure 12, I and J). Gübelin and Koivula (2008) were the first to report and identify these inclusions in Yogo sapphire.

Figure 11. Silk is almost never encountered in Yogo sapphires but is a possibility, as this extremely rare example from the Vortex mine shows. Photomicrographs by Nathan Renfro, courtesy of James Rambur. Fields of view: 1.75 mm (left) and 1.26 mm (right).

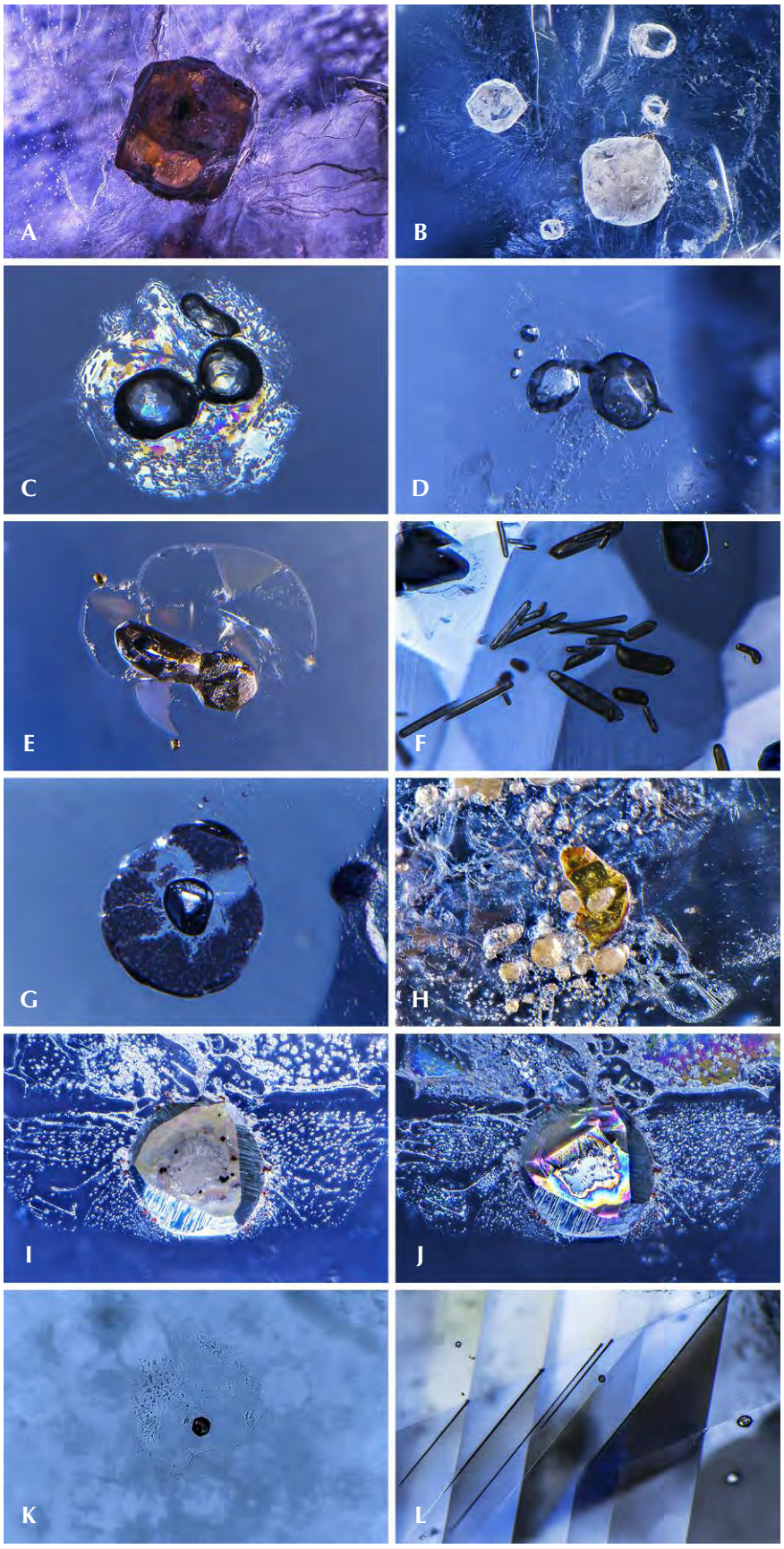

Figure 12. Protogenetic crystals of pyrope-almandine-grossular garnet vary in color from dark brownish orange (A) to light brown (B), depending on their size and resulting optical density. Rounded, protogenetic, transparent, colorless crystals in Yogo sapphires are often apatite (C) or feldspar (D). Rutile crystals can be seen as elongated rods with a dark brownish green color (E) and as black opaque rounded crystals with tension cracks and healed fringes that result from the igneous growth environment (F) and not from heat treatment. Other inclusions that may be encountered are iron sulfides, which often have a black opaque decrepitation halo (G), and rarely yellowish monazite (H). Negative crystals filled with analcime and calcite are shown in darkfield illumination (I) and reflected light displaying thin-film interference colors (J). Glassy melt inclusions with contraction bubbles are occasionally seen in Yogo sapphires (K), consistent with their igneous origin. Yogo sapphires are also occasionally twinned and contain intersection tubules (L). Photomicrographs by Nathan Renfro (A–J, L) and Aaron Palke (K).

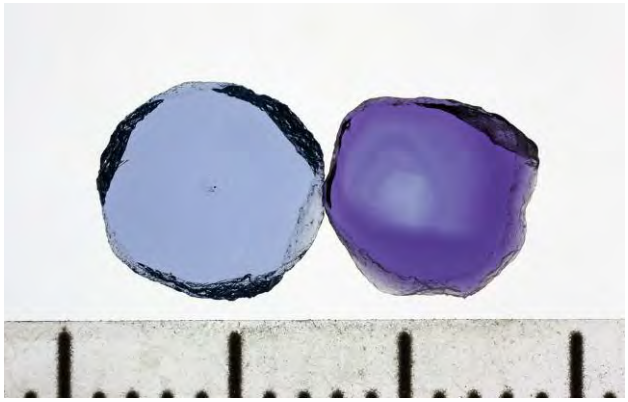

Figure 13. The blue Yogo tablet on the left shows a uniform color, while the purple Yogo tablet on the right shows diffuse angular purple color zoning. Photo by Nathan Renfro (scale is in mm).

These features have been interpreted as originally trapped within the sapphires as blebs of carbonatite melt that later crystallized after entrapment into analcime and carbonate minerals. Glassy silicate melt inclusions (figure 12K) are also relatively common and an indicator of the igneous origin of Yogo sapphires (Palke et al., 2016). The observer may occasionally find pronounced lamellar twinning with **intersection tubules** (figure 12L).

Many blue sapphires from other deposits around the world show some degree of color zoning when examined with diffuse transmitted light. Another defining characteristic of blue Yogo sapphires is their distinct lack of color zoning. Violet to purple Yogo sapphires, however, may show a minimal amount of color zoning (figure 13).

When examined using long-wave UV light, blue Yogo sapphires typically show no reaction or a weak red fluorescence due to trace amounts of chromium, while violet to purple stones generally show a medium red fluorescence reaction due to higher levels of chromium (figure 14).

Spectra. Yogo sapphires have a typical UV-Vis-NIR spectrum with moderate to high iron and an absorption band at 580 nm, caused by the Fe^{2+}-Ti^{4+} intervalence charge transfer, that is responsible for the blue color (Hughes et al., 2017) (figure 15).

The mid-infrared absorption spectrum offers a potentially diagnostic clue to Yogo origin. Yogo sapphires often, but not always, show a weak absorption peak at a wavenumber of approximately 3220 cm^{-1} (figure 16). In the authors' experience, this feature may be present in sapphires from other Montana deposits (Rock Creek, Missouri River, and Dry Cottonwood Creek), but it is generally uncommon in sapphires from sources outside of Montana. This feature may serve as an important indicator of Montana origin and may be useful in identifying Yogo Gulch as the origin.

Chemistry. Yogo sapphires have a distinct trace-element signature that can provide an additional means of distinguishing them. LA-ICP-MS trace-element measurements indicated ranges of 73–146 ppma Mg, 77–131 ppma Ti, 3–19 ppma V, 3–470 ppma Cr, 1060–3110 ppma Fe, and 11–21 ppma Ga. These values generally overlap with the ranges reported by Peucat et al. (2007) and Palke et al. (2016), although our measurements indicate slightly lower average Mg values and slightly higher than average Ti and Fe. This difference is due to the use of internally developed corundum standards in this study, as opposed to the

Figure 14. This parcel of Yogo sapphires shows a wide variation in UV fluorescence. Purple to violet stones generally fluoresce stronger than blue stones. Photos by Nathan Renfro (scale is in mm).

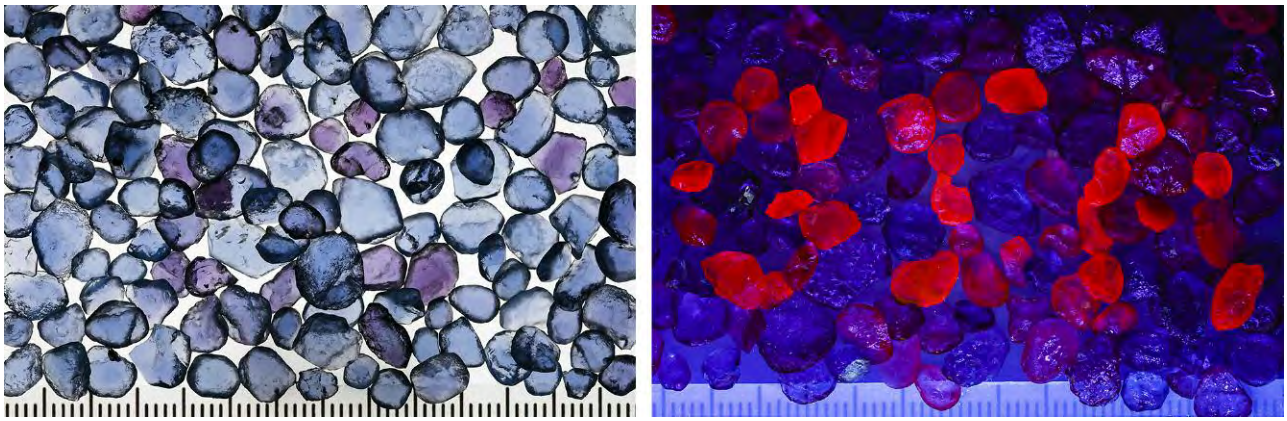

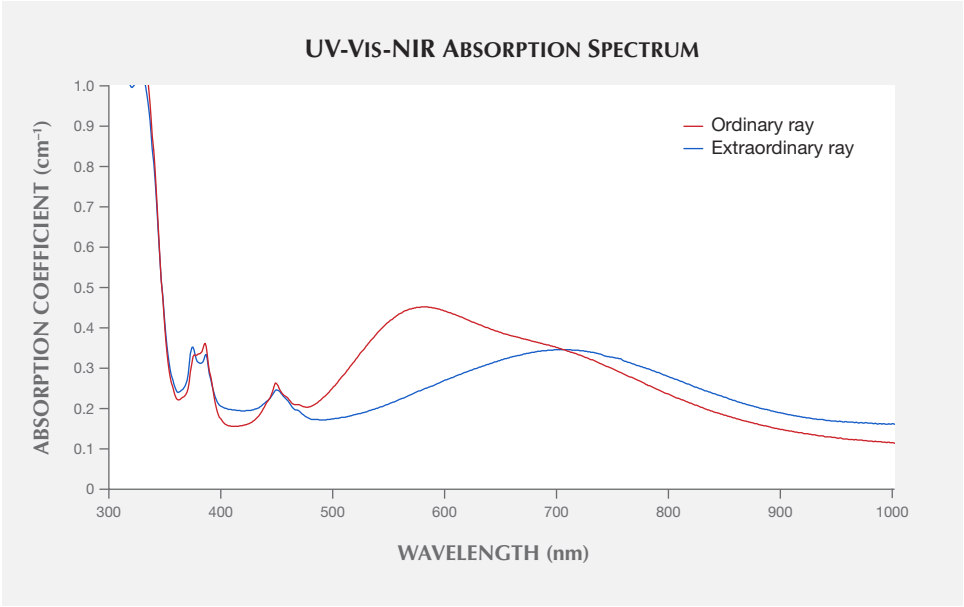

Figure 15. The polarized UV-Vis-NIR spectrum of a blue Yogo sapphire shows strong iron-related absorption at 377, 388, and 450 nm in both the ordinary (red trace) and extraordinary (blue trace) rays, while the cause of color results from the Fe^{2+}-Ti^{4+} intervalence charge transfer band in the ordinary ray (red trace) at 580 nm. Note the absence of a strong absorption band around 870 nm, which typically indicates igneous origin for sapphires.

NIST glass standards used in most other studies (Stone-Sundberg et al., 2018). The ranges and averages of trace-element concentrations for Yogo sapphires are reported in table 1, which also contains trace-element concentrations for a variety of economic deposits. The full analytical results for each individual analysis can be found in supplementary table S1 (https://www.gia.edu/doc/SU18-characterization-of-sapphires-from-yogo-table.pdf).

However, Yogo sapphires have a unique trace-element signature and in almost all cases can be easily distinguished using appropriate trace-element plots (figure 17). Specifically, Yogo sapphires can be separated by their generally higher concentrations of Mg and Ti. While some Sri Lankan sapphires analyzed here overlap with Yogo sapphires at their lower range of Mg and Ti concentrations, Yogo material always has much higher concentrations of Fe (figure 17). While this represents only a small sampling of sapphires from worldwide deposits, the unusual trace element signature of Yogo sapphires should allow clear identification by LA-ICP-MS measurements. In fact,

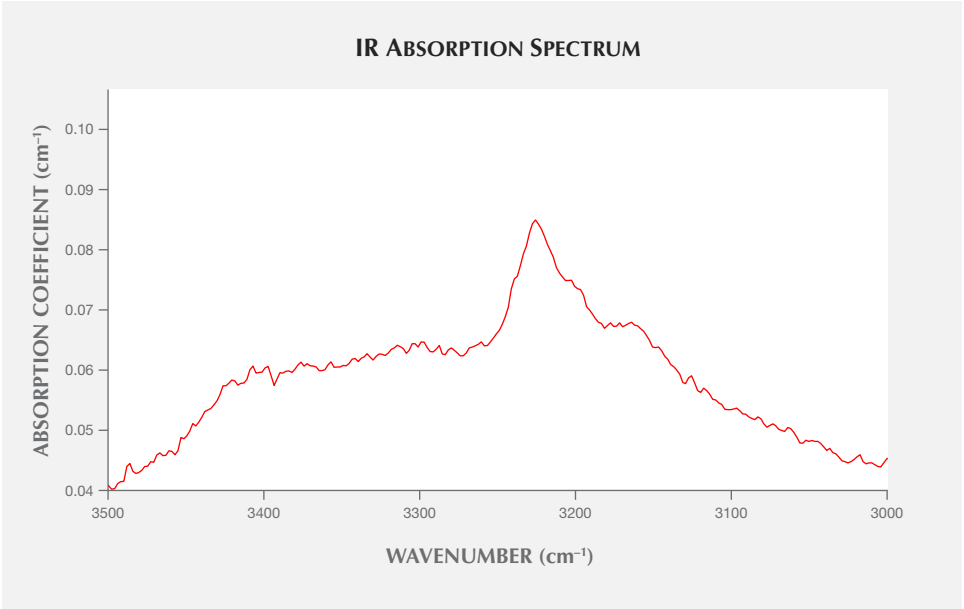

Figure 16. Sapphires from Montana, including both Yogo and the secondary deposits at the Missouri River, Dry Cottonwood Creek, and Rock Creek, often show a unique absorption feature at approximately 3220 cm^{-1}. While this feature is not exclusively diagnostic for Yogo sapphire, it is highly suggestive of a Montana origin.

TABLE 1. Comparison of trace-element compositions of sapphires from Yogo Gulch and other deposits*.

	No. of samples: No. of analyses	Mg	Ti	V	Cr	Fe	Ga
Yogo Gulch	20:60	99 (73–146)	101 (77–131)	9 (3–19)	56 (3–470)	1440 (1060–3110)	14 (11–21)
Montana secondary deposits (Rock Creek and Missouri River)	19:57	32 (18–51)	30 (10–61)	3 (1–6)	10 (1–39)	1715 (978–2750)	14 (11–18)
Umba, Tanzania	17:54	32 (11–98)	29 (12–148)	11 (5–32)	54 (2–158)	1560 (676–3580)	17 (4–30)
Sri Lanka (locality unknown)	19:54	47 (2–116)	149 (5–1060)	18 (1–143)	27 (3–89)	539 (44–1250)	21 (4–53)
Inverell, Australia	9:27	6 (2–15)	49 (15–160)	5 (2–11)	7 (1–39)	2003 (754–4650)	51 (38–69)

**Reported in ppma. Averages are shown first with the full range given next in parentheses. Full analytical results are available in supplementary table S1 (https://www.gia.edu/doc/SU18-characterization-of-sapphires-from-yogo-table.pdf).*

the corundum locality that might have the most consistently similar trace-element chemistry is the Thai/Cambodian ruby mines. This is, of course, excepting chromium, which is consistently enriched in Thai/Cambodian rubies (although some Yogo sapphires do have similar levels of Cr). The similarities in trace-element chemistry, rough crystal morphology, and inclusions have led to speculation that Yogo sapphires and Thai/Cambodian rubies might have formed through very similar geological processes (Hughes et al., 2017; Palke et al., 2018). In addition to the subset of ordinary corundum trace elements reported in table 1, Co and Ni have also been found in Yogo sapphires (Z. Sun, pers. comm., 2017). Co and Ni were found in our samples from below the detection limit to 0.16 ppma and 0.81–16.3 ppma, respectively. Additionally, Emmett et al. (2017) performed a detailed colorimetric analysis of Yogo sapphires using highly accurate SIMS data. Those authors showed that Si is ubiquitously found in Yogo sapphires. Their study also showed that the Yogo sapphires' rich cornflower blue color can only be explained by their incorporation of Si^{4+}, which couples with much of the Mg^{2+} present, leaving enough Ti^{4+} to couple with Fe^{2+}. This produces blue

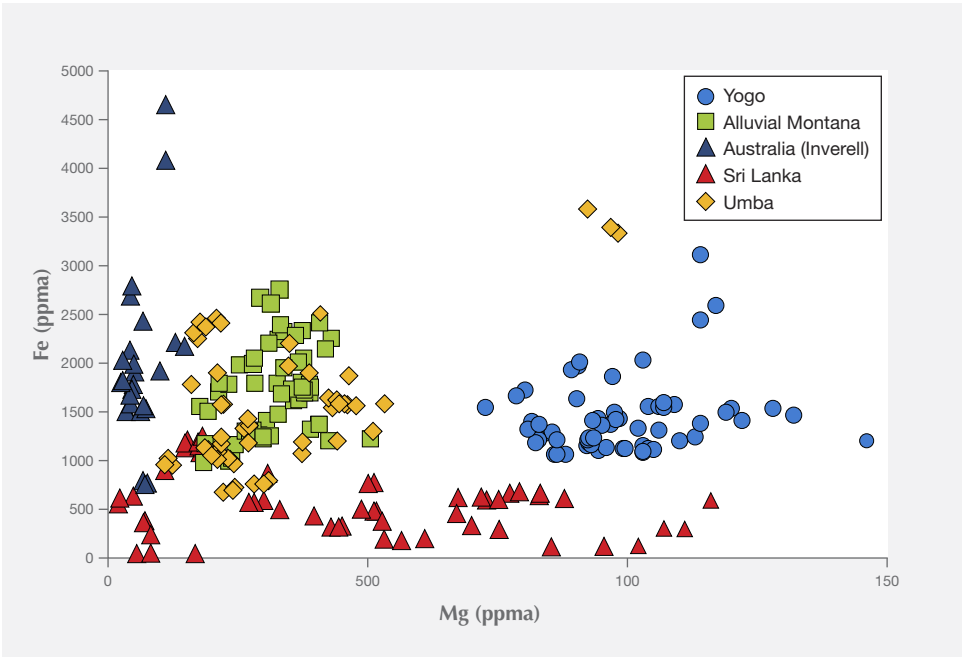

Figure 17. Plot of Mg vs. Fe (in ppma) of Yogo sapphires compared to a select group of other economically important sapphires. This generally covers the range of sapphire trace-element chemistry. Yogo sapphires have a unique chemical signature that can be used in addition to inclusions to positively identify their origin.

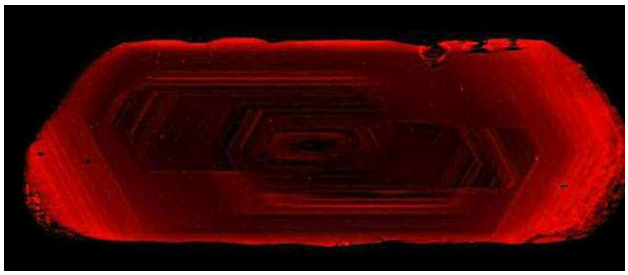

Figure 18. Raman photoluminescence mapping produced this image, which shows the relative distribution of chromium in a Yogo sapphire viewed perpendicular to the c-axis. Chromium is concentrated in the outer portion of the crystal and is not particularly homogeneous throughout. Field of view approximately 4 mm.

Figure 19: The flat tabular shape of the Yogo rough often dictates the production of stones under 1 ct in weight. Photo by Robison McMurtry.

coloration due to the Fe^{2+}-Ti^{4+} intervalence charge transfer.

Raman Mapping. Even though one of the characteristic features of Yogo sapphires is a lack of blue color zoning, violet to purple stones may show visible color zoning due to an uneven distribution of chromium. The heterogeneous distribution of Cr was further explored in one of the blue samples from this study using photoluminescence mapping of the 694 *R*-line. The Raman imaging microscope was used to map the relative chromium distribution in the sample used to collect the UV-Vis-NIR spectrum. This sample was an oriented wafer with two windows polished parallel to each other and parallel to the optic axis (figure 18).

CONCLUSIONS

While Yogo sapphires (figure 19) may not be as well-known as those from other deposits such as Sri Lanka and Myanmar (formerly Burma), they are truly unique among gem corundum. They can be readily recognized by their inclusions and trace-element

Figure 20. With activities resuming at Yogo Gulch, the industry may see more contemporary jewelry designs using the deposit's sapphires. The suite shown here incorporates the blue material that made Yogo famous, along with the purple stones that remain a rarity. The center stone of the ring weighs 1.36 ct. Photo by Kevin Schumacher, courtesy of Bill Vance.

chemistry. Because they do not require heat treatment to improve their color, the origin alone offers the consumer reasonable confidence that their stone has not been heat treated or otherwise artificially altered. While the Yogo sapphire deposit has been known for more than a century, mining efforts have often been met with failure. And since the deposit is quite large, time will tell how much of an impact Yogo sapphires will have on the gem trade and jewelry design (figure 20) in the future.

ABOUT THE AUTHORS

Mr. Renfro is manager of colored stones identification, and Dr. Palke is a senior research scientist, at GIA in Carlsbad, California. Dr. Berg is research geologist at the Montana Bureau of Mines and Geology at Montana Tech of the University of Montana in Butte.

ACKNOWLEDGMENTS

Samples containing prominent inclusions were sourced from the inclusion collection of John I. Koivula and from James Rambur, a gem cutter in Montana. Edward Boehm provided the Yogo sapphire necklace photographed in figure 1. A sample of Yogo sapphire in place in its host rock was sourced from Katie McPherson, who owns a small claim on the Yogo dike. Gem dealer and gemologist Bill Vance provided numerous samples of rough and cut stones for examination. Will Heierman from the Corundum website also provided many Yogo sapphires for trace element and inclusion analysis. The authors also are appreciative for the helpful comments and discussion from Don Baide, John Emmett, Richard Hughes, Robert Kane, and Ziyin Sun, which significantly improved the manuscript.

GLOSSARY

Anorthosite: A rock composed dominantly of plagioclase feldspar (>90%).

Analcime: A hydrated sodium aluminum silicate with the chemical formula $NaAlSi_2O_6H_2O$.

Carbonatite: A magma composed mostly of molten carbonate minerals.

Clinopyroxene: A monoclinic chain silicate, the most common species of which is diopside ($CaMgSi_2O_6$).

Decrepitation halo: A small fracture concentrically centered on an inclusion formed when the inclusion expanded against and fractured the host mineral, likely due to decompression or heating.

Dike: A (sub)volcanic formation formed by the intrusion and solidification of magma into preexisting rock in a narrow, (sub)vertical sheet.

Eclogite: A rock composed dominantly of pyrope-almandine garnet and Na-rich clinopyroxene. Eclogites are generally noted for their lack of plagioclase feldspar and typically form through metamorphism of mafic rocks at very high pressures, usually in the earth's mantle or in very thick sections of the crust.

Etching: Dissolution that occurs on the surface of a crystal when it is out of equilibrium and becomes soluble within its host rock.

Intersection tubules: Hollow tubes formed in the corundum at the intersections of twinning planes. In corundum, these tubules often contain the aluminum hydroxide mineral boehmite.

Lamprophyre: An ultrapotassic volcanic rock composed primarily of large crystals of mica and/or amphibole.

Leucocratic ocelli: Light-colored globular structures often found in lamprophyres and other similar volcanic rocks. They are generally composed of calcite and analcime with traces of other minerals.

Limestone: A sedimentary rock dominantly composed of calcium carbonate ($CaCO_3$). Limestones generally form through the gradual accumulation of the skeletal remains of marine organisms onto the seafloor over time.

Mantle: The layer of the earth below the crust from about 35 to 3,000 km deep. The mantle is compositionally distinct from the earth's crust, with the mantle more Mg- and Fe-rich and Si-depleted and the crust enriched in Si, Na, and K.

Monazite: A light rare earth phosphate with the general formula $(Ce,La,Nd)PO_4$.

Negative crystal: A void with the morphology and crystallographic alignment of the host sapphire that can be filled with foreign included material. Solids, liquids, and gases may all be present in negative crystals.

Ouachatite: Pronounced "wash-e-tite," this is a specific type of lamprophyre, predominantly composed of phenocrysts (large crystals) of mica and clinopyroxene set within a groundmass of fine-grained mica and clinopyroxene with minor analcime, calcite, corundum, and other trace accessory minerals

Pelitic rock: Rocks formed through the accumulation and solidification of mud or silt.

Peritectic melting: A melting reaction in which one of the solid crystalline phases will break down into a liquid component and an entirely different crystalline phase. This is in contrast to "ordinary" melting reactions in which single crystalline phases melt directly into a liquid phase.

Protogenetic: Referring to an inclusion whose formation significantly predates that of the host mineral.

Rutile: Titanium oxide, TiO_2. Notably, Yogo sapphires are nearly always free of needle-like, oriented rutile ("silk").

Shale: A sedimentary rock formed by the accumulation and solidification of mud. Shales are largely composed of clays, quartz, and other minerals.

Troctolite: A rock composed predominantly of plagioclase feldspar, with lesser amounts of olivine and minor pyroxene.

Xenocryst: A single crystal picked up by a magma during its ascent to the earth's surface. Xenocrysts are generally out of equilibrium with the surrounding magma and show signs of corrosion or etching on their surfaces.

Xenolith: A rock picked up by a magma during its ascent to the earth's surface. Such rocks are foreign to the igneous rocks in which they are found. Xenoliths are useful to geologists trying to understand the composition of the deep earth.

REFERENCES

Branstrator B. (2017) Montana retailer acquires, reopens Yogo sapphire mine. *National Jeweler*, www.nationaljeweler.com/diamonds-gems/supply/5758-montana-retailer-acquires-reopens-yogo-sapphire-mine

Brownlow A.H., Komorowski J.-C. (1988) Geology and origin of the Yogo sapphire deposit, Montana. *Economic Geology*, Vol. 83, No. 4, pp. 875–880, http://dx.doi.org/10.2113/gsecongeo.83.4.875

Cade A., Groat L.A. (2006) Garnet inclusions in Yogo sapphires. *G&G*, Vol. 42, No. 3, p. 106.

Clabaugh S.E. (1952) Corundum deposits of Montana. U.S. Geological Survey Bulletin 983 (https://pubs.er.usgs.gov/publication/b983).

Dahy J.P. (1988) The geology and igneous rocks of the Yogo sapphire deposit and the surrounding srea, Little Belt Mountains, Judith Basin County, Montana. Master's thesis, Montana College of Mineral Science and Technology.

——— (1991) Geology and igneous rocks of the Yogo sapphire deposit, Little Belt Mountains, Montana. In D.W. Baker and R.B. Berg, Eds., *Guidebook of the Central Montana Alkalic Province*. Montana Bureau of Mines and Geology Special Publication 100, pp. 45–54.

Emmett J., Stone-Sundberg J., Guan Y., Sun Z. (2017) The role of silicon in the color of gem corundum. *G&G*, Vol. 53, No. 1, pp. 42–47, http://dx.doi.org/10.5741/GEMS.53.1.42

Gauthier G. (1995) Mineralogy, geochemistry, and geochronology of the Yogo dike sapphire deposit, Montana. Master's thesis, University of British Columbia.

Gübelin E.J., Koivula J.I. (2008) *Photoatlas of Inclusions in Gemstones*, Vol. 3. Opinio Publishers, Basel, Switzerland, pp. 228–229.

Howard D.L. (1962a) No ghosts at Yogo! (part 1). *Lapidary Journal*, Vol. 16, No. 1, pp. 65–77.

——— (1962b) No ghosts at Yogo! (part 2). *Lapidary Journal*, Vol. 16, No. 2, pp. 228–241.

Hughes R., Manorotkul W., Hughes B. (2017) *Ruby and Sapphire: A Gemologist's Guide*. RWH Publishing/Lotus Publishing, Bangkok.

Kane R., Hughes R. (2012) In Memoriam: Mike Roberts of the Roberts Yogo sapphire mine. www.ruby-sapphire.com/mike-roberts-yogo-sapphire.htm

Laurs B. (2005) Gem News International: Historic U.S. sapphire and benitoite mines close. *G&G*, Vol. 41, No. 3, p. 276.

Leiper H. (1969) "Five miles of sapphires": Famous Yogo Montana sapphire mine to be reopened. *Lapidary Journal*, Vol. 22, No. 10, pp. 1278–1286.

Meyer H.O.A., Mitchell R.H. (1988) Sapphire-bearing ultramafic lamprophyre from Yogo, Montana: a ouachitite. *Canadian Mineralogist*, Vol. 26, pp. 81–88.

Mychaluk K.A. (1992) Geology of the Vortex mine, Utica, Montana. Bachelor's thesis, University of Calgary.

——— (1995) The Yogo sapphire deposit. *G&G*, Vol. 31, No. 1, pp. 28–41, http://dx.doi.org/10.5741/GEMS.31.1.28

Nixon L. (2016) All that glitters is not gold. *Montana Magazine*, No. 259, pp. 48–53.

The $1 million sapphire campaign (1978) *Jewelers' Circular Keystone,* Vol. 149, No. 10, p. 111.

Palke A.C., Renfro N.D., Berg R.B. (2016) Origin of sapphires from a lamprophyre dike at Yogo Gulch, Montana, USA: Clues from their melt inclusions. *Lithos*, Vol. 260, pp. 339–343, http://dx.doi.org/10.1016/j.lithos.2016.06.004

Palke A.C., Wong J., Verdel C., Avila J.N. (2018) A common origin for Thai/Cambodian rubies and blue and violet sapphires from Yogo Gulch, Montana, USA? *American Mineralogist*, in press.

Peucat J.E., Raffault P., Fritsch E., Bouhnik-Le Coz M., Simonet C., Lasnier B. (2007) Ga/Mg ratio as a new geochemical tool to differentiate magmatic from metamorphic blue sapphires. *Lithos*, Vol. 98, No. 1-4, pp. 261–274, http://dx.doi.org/10.1016/j.lithos.2007.05.001

Stone-Sundberg J., Thomas T., Sun Z., Guan Y., Cole Z., Equall R., Emmett J. (2018) Accurate reporting of key trace elements in ruby and sapphire using matrix-matched standards. *G&G*, Vol. 53, No. 4, pp. 438–451, http://dx.doi.org/10.5741/GEMS.53.4.438

Thomas T., Rossman G.R., Sandstrom M. (2014) Device and method of optically orienting biaxial crystals for sample preparation. *Review of Scientific Instruments*, Vol. 85, No. 9, 093105, http://dx.doi.org/10.1063/1.4894555

Voynick S.M. (1995) Yogo sapphires: A 1995 update. *Rock and Gem*, Vol. 25, pp. 50–81.

——— (2001) *Yogo: The Great American Sapphire*. Mountain Press Publishing Company, Missoula, MT.

Woodward L.A., Hanley J.D. (2013) *Yogo Sapphire Mine, Montana: History of a World-Class Gem Deposit*. Running Wolf Press, Lewistown, MT.

Yaras H. (1969) Precious Yogo sapphires will again gleam among the world's precious jewels. *Lapidary Journal*, Vol. 23, No. 1, pp. 178–180.

CHARTS

Features of Synthetic Diamonds

Sally Eaton-Magaña and Christopher M. Breeding

CVD- and HPHT-grown synthetic diamonds occur in a variety of colors depending on the growth conditions and post-growth treatments. While their final faceted appearances may be similar, the crystals produced from the two techniques are usually quite different.

In the last few years, the influx of synthetic diamonds into the market has sparked tremendous interest in the laboratory growth of this beautiful and fascinating gemstone. The chart provided here offers a summary and reference guide for the growth parameters and characteristics of both rough and faceted samples grown by the two major methods of synthetic diamond production: high-pressure, high-temperature (HPHT) growth and chemical vapor deposition (CVD) growth. It also provides the major gemological and spectroscopic features used to identify these lab-grown diamonds. The last few years have seen numerous advancements in synthetics: the rapid evolution in CVD technology, the ability to produce 10+ carat HPHT synthetics, and the proliferation of HPHT-grown colorless melee diamonds.

The far left column of the chart focuses on features of melee-sized lab-grown diamonds (those less than 0.2 ct), while the far right column presents photos and photomicrographs of large (greater than 5 ct) faceted

See end of article for About the Authors.
Gems & Gemology, Vol. 54, No. 2, pp. 202–204,
http://dx.doi.org/10.5741/GEMS.54.2.202
© 2018 Gemological Institute of America

synthetics. The top two rows are assigned to HPHT synthetics and linked by the blue background. The third and fourth rows discuss CVD synthetics and are distinguished by the dark blue background. The bottom row concentrates on fancy-color synthetic diamonds, both CVD- and HPHT-grown. Fancy-color synthetics can be either as-grown or have color due to post-growth treatments.

The center portion of the chart focuses on growth methods and gemological traits. Important methods of identification include strain observation through crossed polarizers, fluorescence imaging with high-energy UV, and observation of distinctive inclusions.

The panels depicting long-wave and short-wave fluorescence and phosphorescence of synthetics show that the phosphorescence response can be quite subtle to not discernible at all. They also demonstrate that the response is more pronounced with short-wave UV than long-wave. For example, the phosphorescence response in HPHT synthetics to short-wave UV can vary from pronounced to undetectable, indicating that this observation is not always reliable for determining synthetic origin.

Similarly, the observation of strain through crossed polarizers is often useful to identify HPHT synthetics, as the vast majority do not show birefringence (although at least one exception has been encountered; Summer 2016 Lab Notes, pp. 417–418). This is quite distinct from the strain patterns seen in CVD synthetics and naturals.

Although this chart cannot be comprehensive and cover all aspects of HPHT and CVD synthetics, or fully qualify where exceptions exist, we hope it serves as a useful reference for the reader. The chart is intended to be representative of synthetic diamond materials and technology currently encountered in the market and in gemological laboratories. As synthesis technology continues to evolve, it is likely that some features will shift in the coming years. For more information on synthetic diamonds, please see the suggested reading list below.

ABOUT THE AUTHORS
Dr. Eaton-Magaña and Dr. Breeding are senior research scientists at GIA in Carlsbad, California.

ADDITIONAL READING

Angus J.C. (2014) Diamond synthesis by chemical vapor deposition: The early years. *Diamond and Related Materials*, Vol. 49, pp. 77–86, http://dx.doi.org/10.1016/j.diamond.2014.08.004

Angus J.C., Hayman C.C. (1988) Low-pressure, metastable growth of diamond and "diamondlike" phases. *Science*, Vol. 241, No. 4868, pp. 913–921, http://dx.doi.org/10.1126/science.241.4868.913

Breeding C.M., Shigley J.E. (2009) The "type" classification system of diamonds and its importance in gemology. *G&G*, Vol. 45, No. 2, pp. 96–111, http://dx.doi.org/10.5741/GEMS.45.2.96

Butler J.E., Mankelevich Y.A., Cheesman A., Ma J., Ashfold M.N.R. (2009) Understanding the chemical vapor deposition of diamond: Recent progress. *Journal of Physics: Condensed Matter*, Vol. 21, No. 36, pp. 364201-1–364201-20, http://dx.doi.org/10.1088/0953-8984/21/36/364201

Deljanin B., Alessandri M., Peretti A., Åström M. (2015) NDT breaking the 10 carat barrier: World record faceted and gem-quality synthetic diamonds investigated. *Contributions to Gemology*, No. 15, pp. 1–7.

D'Haenens-Johansson U.F.S., Edmonds A.M., Green B.L., Newton M.E., Davies G., Martineau P.M., Khan R.U.A., Twitchen D.J. (2011) Optical properties of the neutral silicon split-vacancy center in diamond. *Physical Review B*, Vol. 84, No. 24, pp. 245208-1–245208-14, http://dx.doi.org/10.1103/PhysRevB.84.245208

D'Haenens-Johansson U.F.S., Moe K.S., Johnson P., Wong S.Y., Lu R., Wang W. (2014) Near-colorless HPHT synthetic diamonds from AOTC Group. *G&G*, Vol. 50, No. 1, pp. 30–45, http://dx.doi.org/10.5741/GEMS.50.1.30

D'Haenens-Johansson U.F.S., Ardon T., Wang W. (2015) CVD synthetic gem diamonds with high silicon-vacancy concentrations. *Conference on New Diamond and Nano Carbons*, Shizuoka, Japan, May 2015.

D'Haenens-Johansson U.F.S., Katrusha A., Moe K.S., Johnson P., Wang W. (2015) Large colorless HPHT-grown synthetic gem diamonds from New Diamond Technology, Russia. *G&G*, Vol. 51, No. 3, pp. 260–279, http://dx.doi.org/10.5741/GEMS.51.3.260

Eaton-Magaña S., D'Haenens-Johansson U.F.S. (2012) Recent advances in CVD synthetic diamond quality. *G&G*, Vol. 48, No.

2, pp. 124–127, http://dx.doi.org/10.5741/GEMS.48.2.124
Eaton-Magaña S., Shigley J. (2016) Observations on CVD-grown synthetic diamonds: A review. *G&G*, Vol. 52, No. 3, pp. 222–245, http://dx.doi.org/10.5741/GEMS.52.3.222
Eaton-Magaña S., Shigley J., Breeding C.M. (2017) Observations on HPHT-grown synthetic diamonds: A review. *G&G*, Vol. 53, No. 3, pp. 262–284, http://dx.doi.org/10.5741/GEMS.53.3.262
Kitawaki H., Abduriyim A., Okano M. (2008) Identification of melee-size synthetic yellow diamonds in jewelry. *G&G*, Vol. 44, No. 3, pp. 202–213, http://dx.doi.org/10.5741/GEMS.44.3.202
Liang Q., Yan C.-S., Meng Y., Lai J., Krasnicki S., Mao H.-K., Hemley R.J. (2009) Recent advances in high-growth rate single-crystal CVD diamond. *Diamond and Related Materials,* Vol. 18, No. 5–8, pp. 698–703, http://dx.doi.org/10.1016/j.diamond.2008.12.002
Martineau P.M., Lawson S.C., Taylor A.J., Quinn S.J., Evans D.J.F., Crowder M.J. (2004) Identification of synthetic diamond grown using chemical vapor deposition (CVD). *G&G*, Vol. 40, No. 1, pp. 2–25, http://dx.doi.org/10.5741/GEMS.40.1.2
Nad S., Gu Y., Asmussen J. (2015) Growth strategies for large and high quality single crystal diamond substrates. *Diamond and Related Materials,* Vol. 60, pp. 26–34, http://dx.doi.org/10.1016/j.diamond.2015.09.018
Shigley J.E., Moses T.M., Reinitz I., Elen S., McClure S.F., Fritsch E. (1997) Gemological properties of near-colorless synthetic diamonds. *G&G*, Vol. 33, No. 1, pp. 42–53, http://dx.doi.org/10.5741/GEMS.33.1.42
Shigley J.E., Abbaschian R., Clarke C. (2002) Gemesis laboratory-created diamonds. *G&G*, Vol. 38, No. 4, pp. 301–309, http://dx.doi.org/10.5741/GEMS.38.4.301
Shigley J.E., McClure S.F., Breeding C.M., Shen A.H.-T., Muhlmeister S.M. (2004) Lab-grown colored diamonds from Chatham Created Gems. *G&G*, Vol. 40, No. 2, pp. 128–145, http://dx.doi.org/10.5741/GEMS.40.2.128
Sumiya H., Satoh S. (1996) High-pressure synthesis of high-purity diamond crystal. *Diamond and Related Materials,* Vol. 5, No. 11, pp. 1359–1365, http://dx.doi.org/10.1016/0925-9635(96)00559-6
Wang W., Moses T., Linares R., Shigley J.E., Hall M., Butler J.E. (2003) Gem-quality synthetic diamonds grown by a chemical vapor deposition (CVD) method. *G&G*, Vol. 39, No. 4, pp. 268–283, http://dx.doi.org/10.5741/GEMS.39.4.268
Wang W., Hall M.S., Moe K.S., Tower J., Moses T.M. (2007) Latest-generation CVD-grown synthetic diamonds from Apollo Diamond Inc. *G&G*, Vol. 43, No. 4, pp. 294–312, http://dx.doi.org/10.5741/GEMS.43.4.294
Wang W., Doering P., Tower J., Lu R., Eaton-Magaña S., Johnson P., Emerson E., Moses T.M. (2010) Strongly colored pink CVD lab-grown diamonds. *G&G*, Vol. 46, No. 1, pp. 4–17, http://dx.doi.org/10.5741/GEMS.46.1.4
Wang W., D'Haenens-Johansson U.F.S., Johnson P., Moe K.S., Emerson E., Newton M.E., Moses T.M. (2012) CVD synthetic diamonds from Gemesis Corp. *G&G*, Vol. 48, No. 2, pp. 80–97, http://dx.doi.org/10.5741/GEMS.48.2.80
Watanabe K., Lawson S.C., Isoya J., Kanda H., Sato Y. (1997) Phosphorescence in high-pressure synthetic diamond. *Diamond and Related Materials,* Vol. 6, No. 1, pp. 99–106, http://dx.doi.org/10.1016/S0925-9635(96)00764-9
Welbourn C.M., Cooper M., Spear P.M. (1996) De Beers natural versus synthetic diamond verification instruments. *G&G*, Vol. 32, No. 3, pp. 156–169, http://dx.doi.org/10.5741/GEMS.32.3.156

For online access to all issues of GEMS & GEMOLOGY from 1934 to the present, visit:

gia.edu/gems-gemology

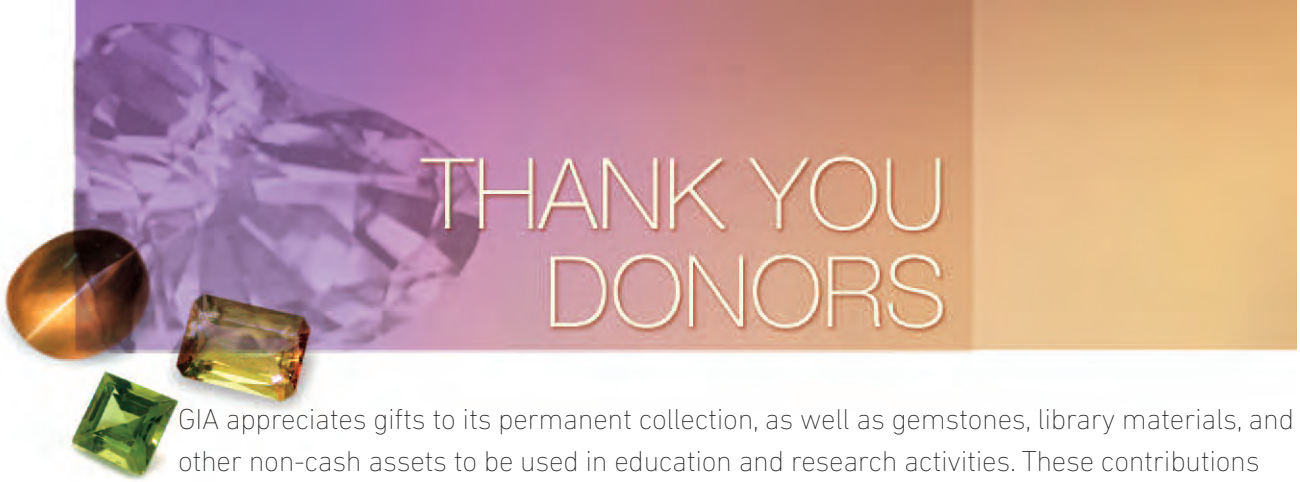

THANK YOU DONORS

GIA appreciates gifts to its permanent collection, as well as gemstones, library materials, and other non-cash assets to be used in education and research activities. These contributions help GIA further its public service mission while offering donors philanthropic benefits. We extend sincere thanks to all 2017 contributors.

CIRCLE OF HONOR*

$100,000 and higher

Dr. Suman Agrawal
Robert and Marlene Anderson
K.C. Bell
Thomas Cacek
In Memory of Nicholas Scott Golden
Hauser Family In Memory of Joel and Barbara Hauser
Dr. James Y. Hung
Kazanjian Beverly Hills
Bill Larson
Dr. Geoffrey A. Smith

2017 DONORS

$10,000 to $49,999

Dr. J.K. Agrawal
Dr. Suman Agrawal
In Memory of Dr. V. Premanand
Thomas M. Schneider

$5,000 to $9,999

Maximilian Art Foundation

$2,500 to $4,999

Jeffery Bergman
Al Gilbertson
Dr. James Y. Hung

$1,000 to $2,499

Meg Berry
Lester N. Doulis
Lennox King-Sun Li
Pokot Gems Ltd.
Sanwa Pearl & Gems Ltd.

$500 to $999

Sidney Schlusselberg

Under $500

Al-Rumayyan
Anne Margaret
Anonymous
René Brus
Lillian Cole, Twelfth Street Booksellers
Marge Dawson
In Memory of Joel and Barbara Hauser
Jack Hobart
In Memory of Joan Goebel Holmes
Jaroslav Hyršl
Jewelry Television
Jasmine Karger
Kazanjian Beverly Hills
Betty Sue King, King's Ransom/Pearl Goddess
Bill Larson
Glenn Lehrer
Linda MacNeil, Artist/Jeweler
In Memory of Erina Matuls, Emilia Nikwewicz, and Wlise Whetstone
In Memory of Craig Nass
Ponderosa Mine
Nathan Renfro
In Memory of Dorothy M. Smith
Starla Turner

If you are interested in making a donation and receiving tax benefits information, please contact:

MCKENZIE SANTIMER
call: (760) 603-4150
email: mckenzie.santimer@gia.edu

* All are cumulative donations

G&G Lab Notes

Editors
Thomas M. Moses | Shane F. McClure

Large Faceted Gem-Quality AFGHANITE

Afghanite is a blue mineral named in 1968 after its discovery in Badakhshan Province, Afghanistan. It is often found in association with lapis lazuli and sodalite (R.V. Gaines et al., *Dana's New Mineralogy*, John Wiley & Sons, New York, 1997, p. 1634). It has a chemical formula of $(Na,Ca,K)_8(Si,Al)_{12}O_{24}(SO_4,Cl,CO_3)_3{\cdot}H_2O$ (Gaines et al., 1997). Since 2003, there have been only a few mentions in the literature of gem-quality afghanite (Winter 2003 GNI, pp. 326–327; Spring 2008 GNI, pp. 79–80; Fall 2011 GNI, p. 235; Spring 2015 GNI, p. 83), with no reports of finished faceted stones larger than 1.5 ct. Five gem-quality samples ranging in size from 2.87 to 7.25 ct have been reported; however, all five were cabochons and contained numerous inclusions of lazurite (Winter 2003 GNI, pp. 326–327).

For these reasons, the 1.91 ct transparent faceted oval brilliant afghanite recently submitted to the Carlsbad lab for an identification report was truly exceptional (figure 1). The only inclusions in the stone were minor fractures. To date, it is the largest facet-grade afghanite on record in the GIA gem identification department. Standard gemological testing revealed that the stone was doubly refractive and uniaxial, with an RI of 1.522 to 1.530 and a specific gravity (SG) of 2.52. These results are consistent with the published properties of afghanite (Gaines et al., 1997). Additionally, an early report on gem-quality afghanite notes that "an interesting feature of afghanite that should prove useful in its identification is its strong, bright orange fluorescence to long-wave UV radiation," a property that this remarkable stone exhibited (Winter 2003 GNI, p. 326–327). Further confirmation of the stone's identity was obtained by using Raman spectroscopy, which yielded a spectrum that matched that of known afghanite samples.

Figure 1. An exceptionally large and clean 1.91 ct faceted oval brilliant afghanite was recently submitted to GIA's Carlsbad lab.

Hollie McBride

BERYL and Glass Assemblage Imitating Emerald

Assemblages of various materials have long been used as imitations of precious stones, with records dating back to Pliny the Elder's *Natural History* (79 AD). Assembled stones commonly consist of two or more pieces of materials joined together in a parallel, layered fashion. Natural gem materials, such as spinel or garnet, are often used for the crown for the dual benefit of their durability and natural inclusions. The pavilion is typically composed of attractively colored, inexpensive materials such as glass or synthetic sapphire.

A unique assembled 3.35 ct imitation emerald composed of five glass segments surrounding a rectangular beryl core (figure 2) was submitted to the New York lab. Microscopic observation revealed multiple nonparallel cement planes in the pavilion (figure 3, left). The crown was shown to be separated from the pavilion in a single piece, whereas the pavilion was composed of four asymmetrical exterior segments surrounding a sub-rectilinear pyramidal core. The core material contained inclusions typical of natural beryl, such as dark dendritic flakes (figure 3, right) and fingerprints. Large gas bubbles and internal chips were observed within the cement layers that accumulated at the beryl core's corners. Standard gemological testing produced consistent RIs of 1.61 on both the crown and the four segments that made up the pavilion, an SG of 2.99, and weak white fluorescence in the cement planes in long- and short-wave UV light. Under cross-polarized light,

Editors' note: All items were written by staff members of GIA laboratories.

Gems & Gemology, Vol. 54, No. 2, pp. 206–218.

© 2018 Gemological Institute of America

Figure 2. Face-up, the assemblage displayed natural inclusions underneath the table. Large bubbles are also visible at the corners of the beryl core, a warning sign for the observant viewer.

the outer material was singly refractive and displayed interference patterns along the interior join planes (figure 4). When immersed, the coloration was shown to be derived from the surrounding sections and joined by a colorless cement. This was further supported by ultraviolet/visible/near-infrared (UV-Vis-NIR) spectroscopy, which yielded a spectrum similar to manufactured green glass samples from our database. Raman microscopy of the crown and four pavilion segments produced amorphous spectra typical of glass. In addition to amorphous mounds, beryl peaks were detected in the core material, confirming prior suspicions.

Figure 4. Face-up view under cross-polarized light displaying the inert reaction of the outer material and interference planes outlining the beryl core. Field of view 14.52 mm.

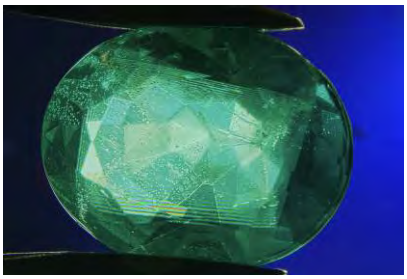

Figure 3. Left: All four glass sections of the pavilion assemblage are visible in reflected light. The small triangular segment is a protrusion from the opposite side. Field of view 3.57 mm. Right: Metallic dendritic films supporting the natural provenance of the beryl core. Also visible are planar bubbles within the cement layer. Field of view 2.90 mm.

Interestingly, the four glass segments in the pavilion assemblage are interlocked in a fashion that reveals a possible explanation of how the stone was manufactured. Based on visual observations, it appears the pavilion was constructed by a laborious multistep cut-and-glue process (figure 5). As a result of the iterant cutting, the first segment shares five sides that are parallel to the faces of the beryl core (four pyramidal faces and one basal). The number of faces parallel to the core decreases by one for each added glass segment. The asymmetry of the segments, parallel faces, and precise angles that match the sides of the core support the proposed model of ordered assembly.

Figure 5. Diagram showing the proposed model of the complex assembly of the composite stone. Final faceting is shown for simplicity. A: The first glass segment (green) is attached to the beryl core (gray). B: Both the core and the first segment are cut to make a flat surface for the second segment. C: The second segment (teal) is attached. D: The segments are again cut. E: The third segment (blue) is attached. F: The assemblage is shown rotated 180° for clarity. All current pieces are cut to create the surface for the final piece. G: The fourth and final segment (purple) is attached. H: Omitted for simplicity, the assembled pavilion would likely be polished flat to make room for the crown. Lastly, the crown (pink) is attached. The diagram was generated using Onshape CAD software.

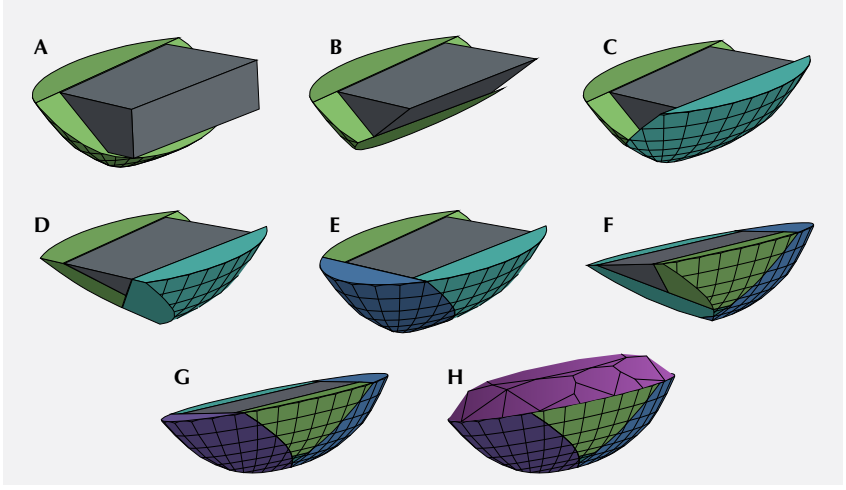

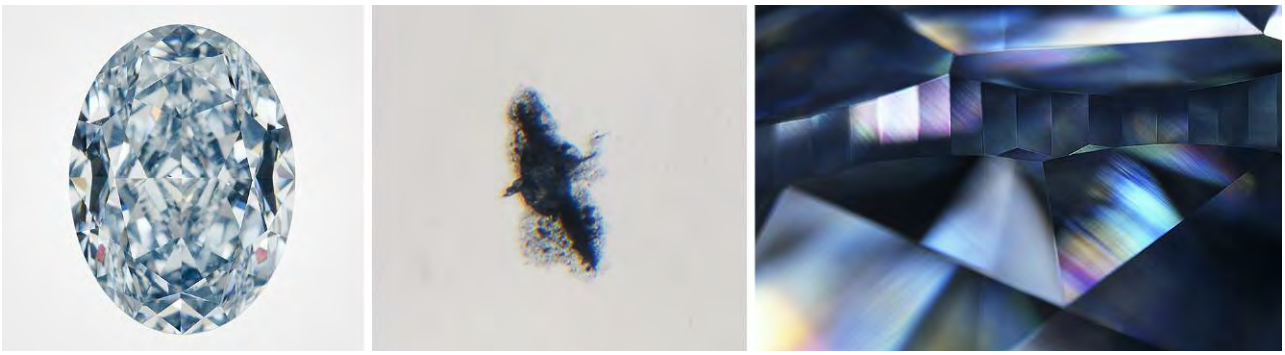

Figure 6. This 17.09 ct HPHT-treated blue diamond (left) has ragged-looking graphitization around an inclusion (center, field of view 0.76 mm) and high-order interference colors when viewed with crossed-polarizing filters (right, field of view 7.19 mm).

The authors were not able to find any records of this type of assembled stone, and it was the first time one has been submitted to GIA's New York or Carlsbad laboratories. Since all exposed surfaces were glass, it is assumed that the stone was fabricated relatively recently due to the sharp facet junctions and lack of wear. It is intriguing that an antiquated technique is updated in modern times, serving as a cautionary tale of the ingenuity counterfeiters employ.

Tyler Smith and Augusto Castillo

Large HPHT-Treated Blue Type IIb DIAMOND

Over the past two decades, high-pressure, high-temperature (HPHT) treatment has emerged as a prominent technology for changing the color of diamonds. It is best known for removing brown coloration from natural type IIa material to yield colorless or, rarely, pink diamonds. Similarly, HPHT treatment can be used to reduce the brown color component of gray or brownish natural type IIb (boron-bearing) diamonds, thereby increasing the underlying blue color. Improvements to equipment and methods continue to push the capabilities of HPHT processing.

GIA's New York lab recently encountered a notably large HPHT-treated Fancy Intense blue oval-cut diamond (figure 6, left). At 17.09 ct, this is the largest HPHT-treated blue diamond graded by GIA to date. For comparison, the average size of most submitted HPHT-processed blue diamonds lies in the 1 to 5 ct range. HPHT treatment can be challenging to detect with standard gemological tools, but in this case the ragged-looking graphitization around an inclusion and the appearance of moderate to high-order interference colors under crossed polarizers were helpful clues (figure 6, center and right). Advanced testing methods (e.g., infrared spectroscopy and photoluminescence spectroscopy) confirmed that the stone was HPHT treated.

Additionally, this diamond had a striking blue color zonation (figure 7, left) that is thought to be unrelated to HPHT treatment. A region of strong blue color is separated from an almost colorless region by a sharp division with octahedral plane {111} orientation. Color zonation is not uncommon in natural type IIb diamonds, though it is seldom so sharp and planar (J.M. King et al., "Characterizing natural-color type IIb blue diamonds," Winter 1998 *G&G*, pp. 246–268). The stronger blue region likely contains more uncompensated boron. It also exhibits more intense greenish blue fluorescence/phosphorescence in DiamondView images (figure 7, right). The color boundary might reflect a change in defect incorporation during diamond growth.

Evan M. Smith, Paul Johnson, and Kyaw Soe Moe

One Natural Melee Diamond Found in Large Batch of HPHT Synthetic Melee

Over the last decade, the production methods used to create synthetic dia-

Figure 7. Color zonation (left) becomes more noticeable when viewed through the pavilion. The stronger blue-colored region corresponds with bright greenish blue fluorescence in the DiamondView (right, field of view 5.8 mm). Note that the DiamondView image is taken from the opposite side of the diamond.

Figure 8. Out of a parcel of 1,102 diamond melee received at GIA's New York lab for testing, 1,092 were identified as HPHT synthetic melee.

mond melee have improved substantially, along with the quality of the specimens themselves. The increase in the amount of synthetic melee submitted—both disclosed and undisclosed—to GIA's laboratories for identification has exponentially increased since GIA began offering its Melee Analysis Service in 2016. Parcels of melee are often submitted with a mixture of naturals and synthetics. Typically, a few synthetics are detected in batches of natural melee diamonds, known in the trade as "salting" (e.g., S. Eaton-Magaña and J.E. Shigley, "Observations on CVD-grown synthetic diamonds: A review," Fall 2016 *G&G*, pp. 222–245).

GIA's New York laboratory received a batch of 1,102 melee diamonds with a total weight of 9.67 carats for the melee analysis service. The tested melee ranged from 0.98 to 1.52 mm in diameter. Preliminary testing using GIA's fully automated screening device referred 1,093 for further testing, while nine were found to be outside of the service criteria. Further analysis using detailed spectroscopic analysis confirmed 1,092 (figure 8) out of the 1,093 to be HPHT synthetics. Fourier-transform infrared (FTIR) absorption spectroscopy performed on the referred melee revealed an absorption band at approximately 2800 cm^{-1} from trace boron in the diamond lattice, classifying these melees as type IIb (boron-bearing), typical of HPHT synthetic diamonds. Due to the relatively high concentrations of boron, these melee diamonds showed a clear blue hue, which is very different from most of the melee diamonds we have tested.

Further examination using photoluminescence (PL) spectroscopy showed no detectable peaks of nickel, often a catalyst used to grow HPHT synthetic diamonds (e.g., Spring 2017 Lab Notes, pp. 95–96). These spectra were in fact atypical of HPHT synthetic diamonds. Distinctive HPHT growth patterns were observed in the DiamondView (figure 9) along with strong phosphorescence following exposure to short-wave UV radiation (figure 10).

One sample out of 1,093 was confirmed as a natural diamond. Infrared absorption spectroscopy indicated this stone was type Ia, with a hydrogen peak at 3107 cm^{-1}. DiamondView imaging displayed a typical blue fluorescence and no detectable phosphorescence, both typical for a natural type Ia diamond.

It is interesting to note that only one natural was found in this parcel of melee. This has been the largest percentage of undisclosed synthetic melee that GIA has seen. The majority of the HPHT synthetic melee had no detectable traces of Ni, demonstrating the importance of advanced testing to identify these melees.

Stephanie Persaud, Wuyi Wang, Paul Johnson, and Ivana Petriska Balov

Figure 9. This diamond shows characteristic growth patterns of HPHT-grown material.

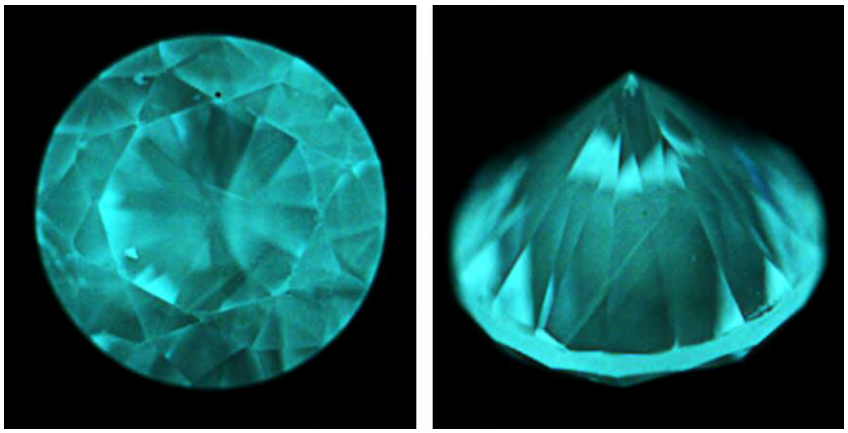

Figure 10. These HPHT-grown synthetic diamond melee, from the parcel of 1,102 specimens, display strong phosphorescence following exposure to short-wave UV radiation.

A Repaired Diamond

A 1.38 ct marquise-cut diamond (figure 11) was submitted to the Carlsbad lab for colored diamond grading services. It was initially noted that large fractures and a large cavity were present on the table. Careful examination of the stone with a gemological microscope revealed that it had previously broken in half and been repaired with an unknown adhesive. The first clue was a large fracture from the crown to the pavilion that showed a sizeable gap present throughout the stone. Furthermore, the facets the fracture passed through all showed slight to moderate misalignment, which cannot happen during polishing (figure 12). Finally, large trapped air bubbles could be seen in the fracture when viewed at an angle. These clues proved that the diamond had broken and been put back together again, though not perfectly. Polish lines on the pavilion facets showed a pattern that would line up if not for the fracture separating them, demonstrating that the breakage occurred after the diamond had been at least partially polished. Beyond that, it is impossible to tell when the damage occurred.

Figure 11. A face-up photo of the repaired diamond.

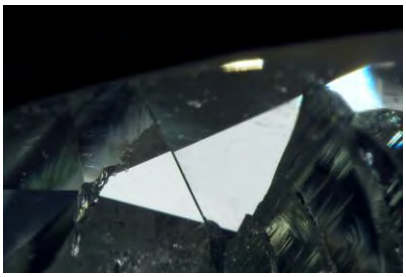

Figure 12. A bezel facet of the repaired diamond as seen in reflected light. The wide fracture can be seen cutting across the facet, and the upper edge of the facet does not form a straight line. Field of view 3.3 mm.

Diamonds have been adhered together with glue to form a diamond-diamond doublet (E. Barrie and E. Biermans, "A different type of deception: 'Diamond-diamond' doublet," HRD Antwerp, 2014, www.hrdantwerp.com/en/news/a-different-type-of-deception-diamond-diamond-doublet), but a broken diamond that has been repaired was not something previously reported by GIA. The fracture in the item was not a flat, straight surface but very irregular, indicating that it was not two separate diamonds glued together to make a larger diamond, but rather a repair. Since the item was simply two pieces of diamond joined together, it was not eligible to receive a diamond grading report. None of the 4Cs apply to a composite such as this (e.g., the carat weight of the item was actually the sum of the weights of two diamonds plus the weight of the adhesive). The decision to repair a diamond in this manner is unusual. Careful gemological examination will, however, reveal the repair work done.

Troy Ardon

A Cat's-Eye Rock Consisting of JADEITE and Amphibole

The Hong Kong laboratory recently examined a translucent variegated green bead exhibiting chatoyancy (figure 13). The 1.42 ct bead, measuring approximately 5.62 mm in diameter, displayed two different shades of green on opposite sides. A distinct cat's-eye band was readily visible across the darker green region with fiber-optic illumination, whereas no chatoyancy was observed in the lighter green region on the reverse side.

Microscopic observation revealed that the darker green side consisted of parallel fibrous crystals (figure 14, left). Light reflecting off these oriented crystals produced a chatoyant band perpendicular to the length of the

Figure 13. This 1.42 ct translucent variegated green bead displays a distinct chatoyant band on the darker green side (left). No chatoyancy was observed on the lighter green side (right).

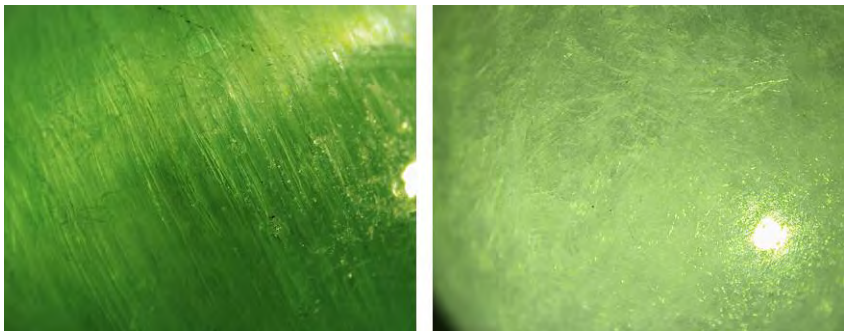

Figure 14. Left: Parallel fibrous amphibole crystals were the cause of chatoyancy in this green bead; field of view 11.34 mm. Right: Tight interlocking grains were visible in the lighter green jadeite region; field of view 3.80 mm. Both observed with fiber-optic illumination.

crystals. On the lighter green side, tight interlocking grains were observed (figure 14, right). Raman spectroscopy detected the presence of richterite, an amphibole with the general formula $Na_2CaMg_5Si_8O_{22}(OH)_2$, in the darker green region and jadeite in the lighter green region.

While it is not unusual to encounter a rock consisting of jadeite and amphibole (G. Shi, "Mineralogy of jadeitite and related rocks from Myanmar: a review with new data," *European Journal of Mineralogy*, Vol. 24, No. 2, 2012, pp. 345–370), it is fascinating to see such a rock being fashioned into an attractive variegated green bead exhibiting chatoyancy.

Bona Hiu Yan Chow

Two Natural "Horse Conch" PEARLS

GIA's Hong Kong laboratory recently examined two strongly saturated reddish orange non-nacreous pearls weighing 126.20 ct and 4.89 ct, and measuring 40.80 × 23.70 × 20.96 mm and 10.53 × 8.55 × 7.68 mm, respectively. The client who submitted the pearls also provided the shell from which they were reportedly extracted (figure 15). While such information must be treated with a degree of caution, our client also stated that the shell and pearls were handed to him by a fisherman who claimed to have found them in the waters off Isla Mujeres, near Cancun, Mexico. The shell measured approximately 47 × 24 × 24 cm and appeared pinkish orange with an orangy brown periostracum. Its large size, characteristic shape, pinkish orange color, and fine slender flame structures enabled us to identify it as a member of the *Triplofusus* genus, most likely *Triplofusus papillosus or Triplofusus giganteus*, sometimes referred to as *Pleuroploca gigantea* (E. Strack, *Pearls*, Rühle-Diebener-Verlag GmbH & Co., Stuttgart, Germany, 2006, p. 108; Fall 1994 Lab Notes, p. 195). These are all names that have been used to describe the Florida horse conch, though differences of opinion on the correct nomenclature applicable exist (D.P. Berschauer, "What's in a name – the Florida horse conch," *The Festivus*, Vol. 49, 2017, pp. 110–116). The *Triplofusus* genus is part of the Fasciolariidae subfamily which is a very diverse group of marine gastropods. The parallel line patterned *Pleuroploca trapezium* is another member of the Fasciolariidae subfamily said to produce unusual horse conch pearls (H. Bari and D. Lam, *Pearls*, Skira Editore S.p.A, Milan, 2009, pp. 70–73).

Figure 15. Two natural "horse conch" pearls and the shell from which they were reportedly extracted.

The larger of the two pearls displayed an uneven coloration with some lighter areas blending into a more saturated reddish orange. The smaller pearl was more homogeneous in appearance. The flame structures appeared spiky on the smaller pearl but were fine and elongated on the larger pearl (figure 16). Real-time microradiography revealed small void-like features in the center of the smaller pearl and toward the tapered

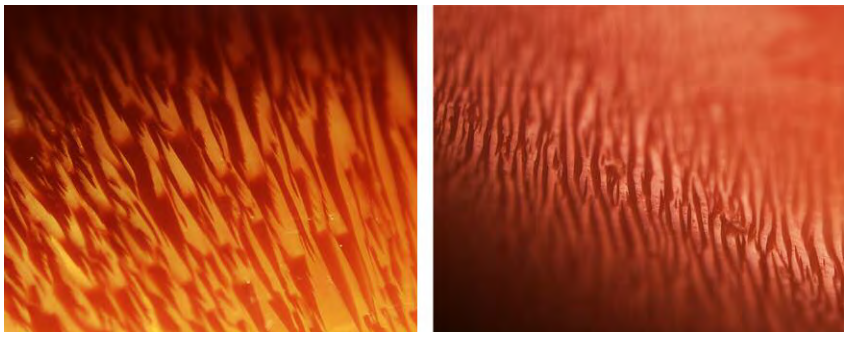

Figure 16. Short spiky flame structure on the 4.89 ct pearl (left, field of view 3.74 mm), and fine, elongated flame structure on the 126.20 ct pearl (right, field of view 2.83 mm).

end of the larger pearl. Such voids are not uncommon in the pearls of a number of porcelaneous pearl-producing mollusks. GIA has recorded similar features in examples from species of *Tridacna*/*Hippopus*, *Strombus gigas*, *Cassis*, and *Melo*. While the flame structures bore some similarities to those seen in *Strombus gigas* (conch) pearls, their strong reddish orange color and internal structures aligned more closely with horse conch pearls. Raman spectroscopy using 514 nm laser excitation detected aragonite peaks at 702, 706, and 1086 cm^{-1}, as well as peaks at 1130 and 1520 cm^{-1} attributed to naturally occurring polyenic pigments responsible for the strong reddish orange color. The natural coloration was further supported by the presence of numerous polyenic-related peaks in the PL spectrum (figure 17) collected with the same laser excitation.

Figure 17. The PL spectrum of the 4.89 ct horse conch pearl displayed numerous peaks associated with naturally occurring polyenic pigments.

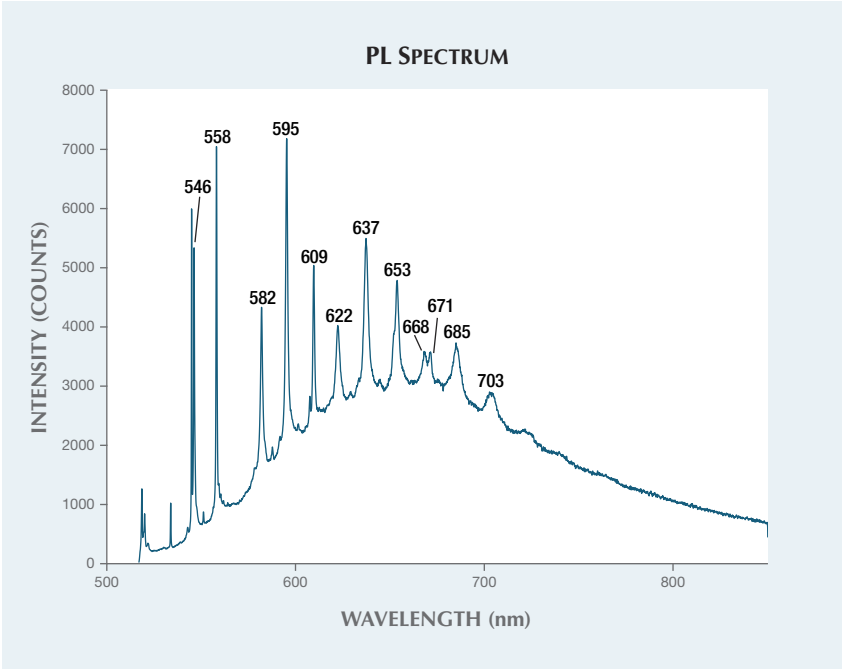

Although GIA handles a wide range of pearls originating from different mollusk species, horse conch pearls are among the rarest examined. It was, therefore, very rewarding to handle the 126.20 ct pearl and its smaller partner together with the shell from which they reportedly originated.

Bona Hiu Yan Chow

Unique Star SAPPHIRE with Transparent Core

GIA's Tokyo laboratory recently examined a 34 ct oval cabochon of unique appearance. This cabochon consisted of a transparent yellow pseudohexagonal core in an opaque metallic-looking area (figure 18). Spot RIs on both areas were 1.76, and SG was 4.04. This appearance of a transparent yellow window with an opaque metallic surrounding area is reminiscent of pallasitic peridot, an olivine nodule enclosed in nickel-ion alloy of stony-iron meteorites (see J. Sinkankas et al., "Peridot as an interplanetary gemstone," Spring 1992 *G&G*, pp. 43–51). However, no surface discontinuity between these two parts can be found with close observation under reflected light. Furthermore, this metallic-looking area exhibited

Figure 18. This 34 ct sapphire cabochon has a yellow pseudohexagonal window surrounded by metallic-looking material that displays asterism.

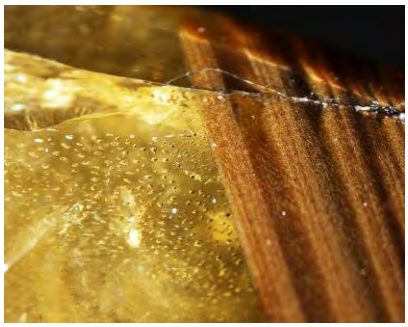

Figure 19. The sapphire's yellow core includes negative crystals and healed fissures (left) and the metallic-looking part (right) has dense needles. Field of view 3.38 mm.

six-rayed asterism. Under the microscope, negative crystals in a plane and healed fissures were found in the transparent area; densely packed needle-like inclusions, some crystals, and stained fissures were seen in the opaque area (figure 19). In addition to the microscopic observations, advanced testing of the yellow part revealed that this specimen was a natural corundum. The metallic appearance and asterism were caused by the strong reflection from the dense needle-like inclusions (figure 19), some of which were flat. These needles were identified as hematite and ilmenite by Raman spectroscopy. The slightly elevated SG of this specimen might have been caused by the abundance of these inclusions, since the SGs of both hematite and ilmenite are higher than that of corundum.

As previously documented (e.g. T.N. Bui et al., "From exsolution to 'gold sheen': A new variety of corundum," *Journal of Gemmology*, Vol. 34, No. 8, 2015, pp. 678–691; N. Narudeesombat et al., "Golden sheen and non-sheen sapphires from Kenya," Gem and Jewelry Institute of Thailand, July-August 2016, pp. 282–288; Winter 2016 Lab Notes, pp. 413–414), sapphires with golden shimmer caused by hematite needles are known as "golden sheen" or "Zawadi" sapphires in the trade. As with rutile needles in common star sapphires, hematite needles intersecting at 60 degrees can cause six-rayed asterism. Golden sheen sapphires sometimes have densely included parts, but such a distinct zoning of transparent and densely included parts has not been documented. This unique appearance may indicate a certain crystallizing condition of sapphires.

Yusuke Katsurada

Cabochons Fashioned from the SHELL of *Crassostrea Virginica*

Crassostrea virginica, the so-called Eastern or American oyster, is a commercial seafood widely distributed along the east coast of the United States to the Gulf of Mexico ("Indian River Lagoon Species Inventory," Smithsonian Marine Station at Fort Pierce, 2008, https://www.sms.si.edu/irlspec/Crassostrea_virginica.htm). Connecticut, Virginia, and Mississippi have all designated the Eastern oyster as their official state shell, and cabochons cut from this bivalve are the official state gemstone of Louisiana (http://legis.la.gov/Legis/Law.aspx?d=103557). These specimens are marketed under the trade name LaPearlite.

The Carlsbad laboratory received ten LaPearlite cabochons together with a shell for examination (figure 20). The cabochons exhibited low domes and flat bases and ranged from 1.65 to 6.12 ct. They measured from 6.85 × 6.60 × 3.80 mm to 14.40 × 10.30 × 5.30 mm and possessed non-nacreous surfaces, with the majority displaying a natural brownish yellow banded structure typical of shell formation. Microscopic examination revealed that the main white surface and subsurface structure varied from a patchwork of nondirectional cells or segments to a broad mottled appearance within individual specimens, as well as from specimen to specimen.

Figure 20. The ten cabochon-cut gems examined are shown alongside the valves of C. virginica *(Eastern or American oyster). The interior and exterior valves shown belong to one oyster. Samples courtesy of Anne Dale.*

Figure 21. Left: A 3.09 ct cabochon showed various surface structures consisting of a non-directional patchwork of cells near the center to a broad mottled appearance in the outer area, together with natural brownish layers of shell formation. Right: Higher magnification of another cabochon's surface revealed a distinct patchwork structure. Both samples displayed a whitish sheen on the surface when illuminated with a fiber-optic light. Fields of view 11.90 mm (left) and 5.24 mm (right).

These structures exhibited a reflective whitish sheen when illuminated by a fiber-optic light or other bright oblique lighting, creating a shimmery phenomenon (figure 21). A similar patchwork pattern has been noted on scallop pearls and shells of the Pectinidae family (K. Scarratt and H.A. Hänni, "Pearl from the lion's paw scallop," *Journal of Gemmology*, Vol. 29, No. 4, 2004, pp. 193–203). Under long-wave UV radiation (365 nm), the white portions of all the cabochons and the shell were inert, while the yellow portions showed a weak to moderate yellow fluorescence, and the shell's dark purple adductor muscle scar exhibited a weak red fluorescence.

Raman spectroscopic analysis with a 514 nm argon-ion laser subsequently verified that the white and yellow portions of the cabochons and shell were calcite with peaks at 280, 712, 1085, and 1437 cm^{-1}. No peaks indicating the possible presence of pigments were detected in the yellow areas. Moreover, Raman spectra collected on the shell's dark purple adductor muscle scar produced aragonite peaks at 703 and 1085 cm^{-1} along with several relatively weak broad pigment-related bands (figure 22). PL spectra collected with 514 nm laser excitation on the same areas showed clear triple bands at approximately 620, 650, and 680 nm (figure 23). The PL spectra and fluorescence reaction indicate the purple color is associated with the pigment porphyrin (Y. Iwahashi and S. Akamatsu, "Porphyrin pigment in black-lip pearls and its application to pearl identification," *Fisheries Science*, Vol. 60, No. 1, 1994, pp. 69–71; L.H. Arma et al., "Red fluorescence lamellas in calcite prismatic layer of *Pinctada vulgaris* shell (Mollus, bivalvia)," *Optical Materials Express*, Vol. 4, No. 9, 2014, pp. 1813–1823). None of the studied cabochons showed purple areas to examine for comparison. Interestingly, the Raman spectra obtained from the white and purple areas of the same mollusk that were previously referenced in the literature (K. Scarratt et al., "A note on a pearl attached to the interior of *Crassostrea virginica* (Gmelin, 1791) (an edible oyster, common names, American or Eastern oyster)," *Journal of Gemmology*, Vol. 30, No. 1/2, 2006, pp. 43–50) differed slightly from the findings in this work. The samples in this submission were also analyzed by energy-dispersive X-ray fluorescence (EDXRF) chemical analysis and showed low levels of manganese (Mn), confirming their saltwater environment.

As with all shell mollusks, *C. virginica* is capable of producing pearls. However, the cabochons in this study provided useful gemological and spectroscopic information for future refer-

Figure 22. Raman spectra collected using 514 nm laser excitation on the white and purple areas of the interior of the C. virginica *valve. The white area shows calcite peaks at 280, 712, 1085, and 1437 cm^{-1}, and the purple area shows aragonite peaks at 703 and 1085 cm^{-1}, along with several broad pigment-related bands.*

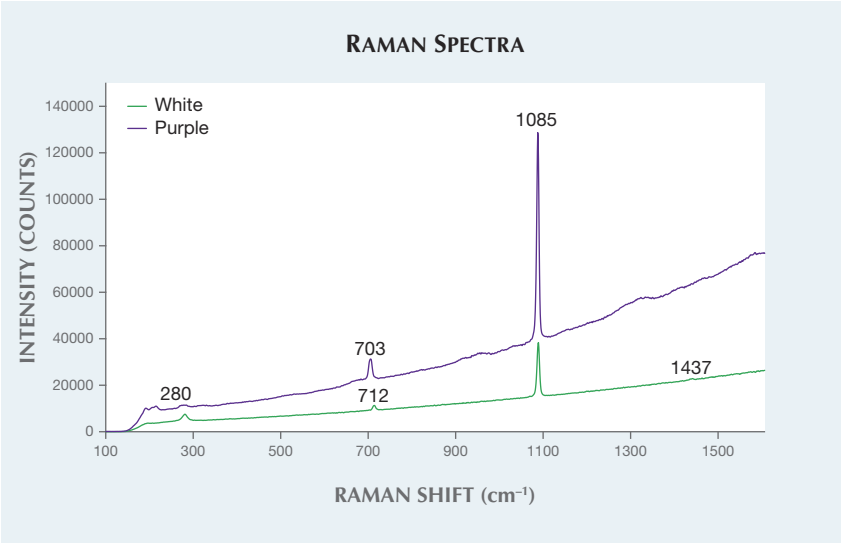

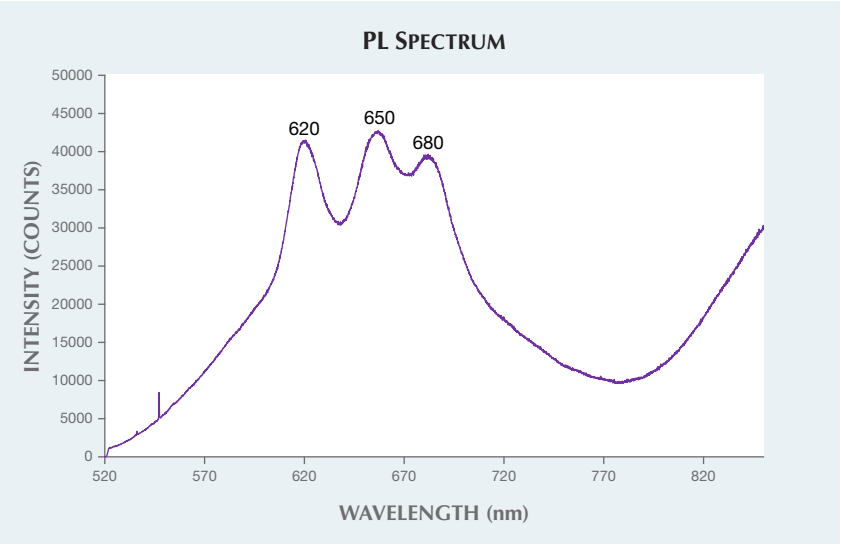

Figure 23. A PL spectrum collected using 514 nm laser excitation on a purple area on the interior of a C. virginica *valve displays clear triple bands at approximately 620, 650, and 680 nm related to the porphyrin pigment.*

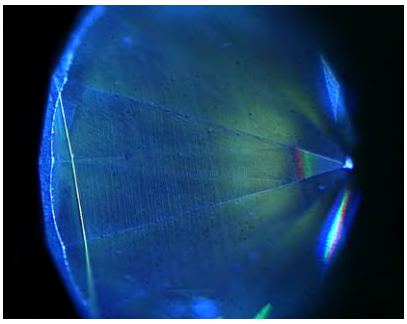

Figure 25. All three irradiated CVD synthetics displayed very weak fluorescence in the DiamondView, as seen in the 1.14 ct sample shown here. All showed the characteristic striations of CVD growth.

ence that can no doubt assist with identifying the composition of pearls produced by the mollusk (C.P. Idyll, "The pearls of Margarita," *Americas*, Vol. 19, No. 8, 1967, pp. 8–14). Although the samples could be mistaken for agate at first glance, owing to their distinctive banding, it would soon be apparent that they were pieces of fashioned shell. The samples demonstrate how creative work can turn nature's beauty into an attractive gemological material.

Artitaya Homkrajae

Three Irradiated CVD SYNTHETIC DIAMONDS

While laboratory-irradiated diamonds are often submitted for grading reports, irradiated synthetics with a green-to-blue color are still a rare occurrence. Before the submissions described here, GIA's laboratory had examined only three irradiated CVD synthetics (Fall 2014 Lab Notes, pp. 240–241; Fall 2015 Lab Notes, pp. 320–321) and two irradiated HPHT synthetics. So it was interesting when the Carlsbad laboratory received three irradiated CVD synthetics, apparently from the same client.

All three synthetics showed very similar features in terms of color (equivalent to Fancy Deep green-blue; figure 24), clarity (equivalent to VVS_2), and weight (1.12 ct, 1.14 ct, and 1.34 ct), along with comparable features detected by fluorescence imaging (figure 25) and spectroscopy (figure 26).

The Vis-NIR and IR absorption spectroscopy and the PL spectroscopy were nearly identical among the three specimens, indicating that they were probably grown and treated under similar if not identical conditions. The IR

Figure 24. These 1.12 ct, 1.14 ct, and 1.34 ct laboratory-irradiated CVD synthetic diamonds all have similar appearance, with color grades equivalent to Fancy Deep green-blue.

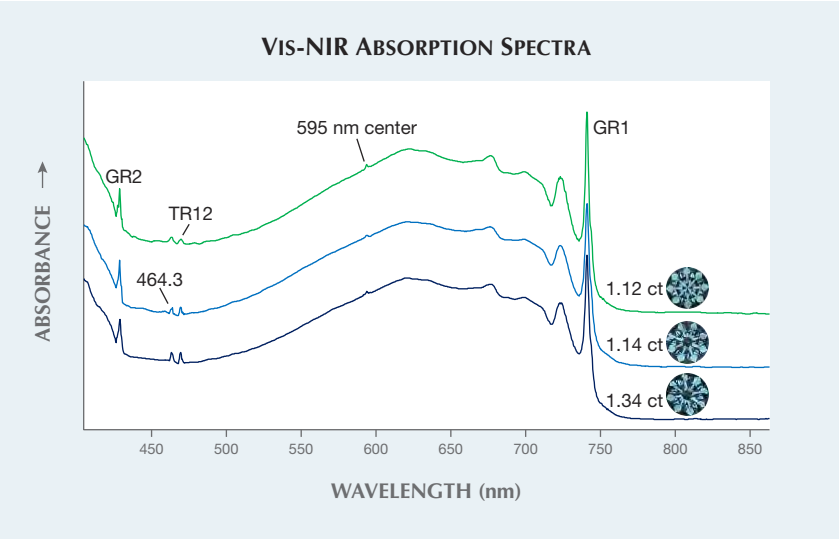

Figure 26. Radiation-related features dominate the CVD synthetic diamonds' Vis-NIR absorption spectra when collected at liquid nitrogen temperature. Features include the GR1 at 741.2 nm, the 595 nm center at 594.2 nm, the TR12 center at 469.9 nm, a radiation-related peak at 464.3 nm, and the GR2 at 429 nm.

absorption spectra showed very weak 3107 cm^{-1} and 1344 cm^{-1} peaks. Based on the integrated area of the 1344 cm^{-1} peaks (I. Kiflawi et al., "Infrared absorption by the single nitrogen and A defect centres in diamond," *Philosophical Magazine B*, Vol. 69, No. 6, 1994, pp. 1141–1147), we determined the single N concentration as about 0.4–0.5 ppm for all three samples. The Vis-NIR absorption spectra showed typical features for irradiated diamonds: the TR12 (a radiation-related feature tentatively ascribed to a divacancy/di-interstitial defect at 469.9 nm), the 595 nm center, and GR1 [V^0] at 741.2 nm (figure 26). PL spectra showed a weak SiV^- doublet at 736.6 and 736.9 nm along with a very strong GR1 center. PL spectroscopy also indicated the presence of the H2 peak at 986.2 nm and the lack of the 596/597 nm doublet that is normally seen in as-grown CVD synthetics and generally disappears with post-growth treatment. This combination, along with the 3107 cm^{-1} peak in the IR spectra, suggests these diamonds were HPHT treated before irradiation.

Owing to their extreme rarity and individuality, creating a set of matching natural-color diamonds can be quite challenging. In contrast, synthetic diamonds can demonstrate uniformity in features and appearance due to the manufacturer's ability to control the growth conditions, defect concentrations, and the subsequent treatment parameters.

Sally Eaton-Magaña

Large Pinkish Orange CVD Synthetic Diamond

Natural diamonds with intense pink-orange color are very rare, particularly in large sizes. GIA's New York lab recently tested a pinkish orange CVD synthetic diamond, submitted by Unique Lab Grown Diamond Inc. in New York, that showed some outstanding gemological features.

This square cut weighed 5.01 ct (9.45 × 9.10 × 6.05 mm) and was color graded as Fancy Intense pinkish orange (figure 27). The color was distributed evenly throughout. A few small feathers and pinpoints were observable under the microscope at about 20× magnification, and the clarity was equivalent to SI_1. Infrared absorption spectroscopy revealed this was a type IIa diamond, with nitrogen concentration below the instrument's detection limit. A clear and sharp peak detected at 3123 cm^{-1} is a well-known specific feature of CVD synthetic diamond. The absorption spectrum in the UV-Vis region indicated that the observed bodycolor was caused by a very strong and broad absorption band around 520 nm (figure 28). This band can be introduced to a CVD diamond during its growth. It creates a color effect similar to the one from the ~550 nm band in natural pink diamonds. There is no report of the ~520 nm band being introduced to a CVD synthetic diamond after its initial growth. In PL spectroscopy, clear emissions at 737 nm from SiV^- and 503 nm from the H3 defect were recorded. In addition, strong emissions at 575 and 637 nm from NV centers were detected. As a result, this synthetic diamond showed strong orange-red fluorescence in DiamondView imaging. Unlike other large CVD-grown diamonds, this diamond's fluorescence images hardly revealed the multiple growth layers responsible for its significant thickness. Instead, the multiple growth layers with subtle boundaries could only be detected in high-resolution cathodoluminescence (CL) images.

Based on all spectroscopic features, we believe that this CVD synthetic diamond was not treated by

Figure 27. This CVD-grown diamond, weighing 5.01 ct and Fancy Intense pinkish orange in color, stands out among all CVD synthetics GIA has tested so far.

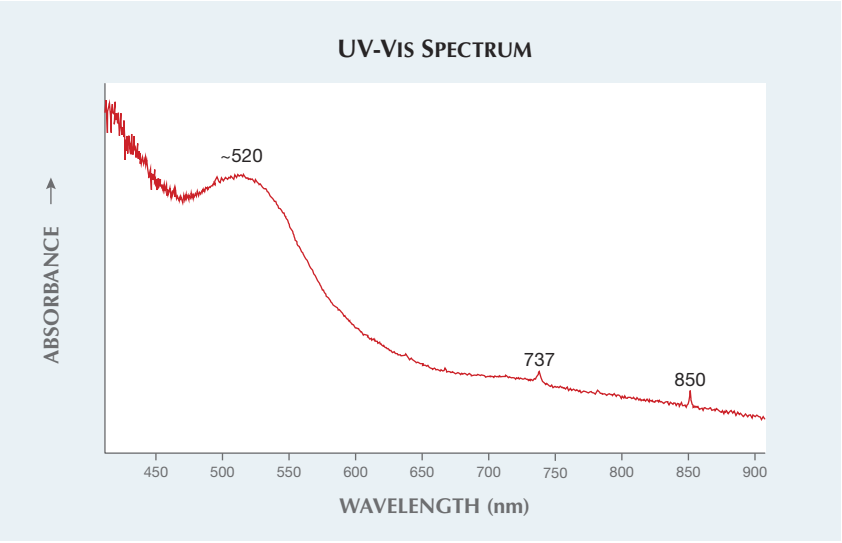

Figure 28. The UV-Vis spectrum of this CVD synthetic revealed that its intense pinkish orange bodycolor was caused by a strong and broad absorption band around 520 nm.

HPHT annealing after its growth for color improvement, though heating to a moderate temperature could not be entirely ruled out. The combination of size, color, and clarity made this the most remarkable CVD synthetic diamond GIA has tested so far.

Wuyi Wang and Tom Moses

15 Carat HPHT Synthetic Diamond

The Carlsbad laboratory recently examined an HPHT synthetic diamond that is now the largest faceted lab-grown diamond examined by GIA. The specimen was a cushion modified brilliant weighing 15.32 ct, with grades equivalent to I_1 clarity and H color (figure 29). The largest previously reported fully faceted synthetic diamonds were a 10.02 ct emerald-cut HPHT-grown (equivalent to E-color; Summer 2016 Lab Notes, pp. 195–196) and a 10.08 ct emerald-cut HPHT-grown diamond (equivalent to Fancy Deep blue; Winter 2016 Lab Notes, p. 416). The 15.32 ct synthetic contained large metallic flux inclusions (figure 30) as well as numerous fractures. Examination under crossed polarizers revealed no strain patterns, except for small strain fields around the metallic flux inclusions.

The infrared absorption spectrum showed no detectable boron or nitrogen, indicating that the sample was type IIa. DiamondView imaging did reveal blue phosphorescence, which is characteristic of boron impurities (figure 31, right), but any boron present was below the detection level of the FTIR spectrometer. PL spectroscopy

Figure 29. This 15.32 ct cushion modified brilliant, with grades equivalent to H color and I_1 clarity, is the largest HPHT synthetic diamond graded by GIA.

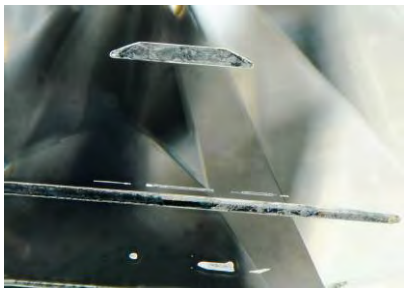

Figure 30. The metallic flux inclusions present in the synthetic diamond. Several rod-shaped structures can be seen, as well as an inclusion with a trapezoidal shape. Field of view 4.79 mm.

taken with the 514 nm laser revealed the presence of the negative silicon vacancy defect at 737 nm; the neutral nitrogen-vacancy center was also seen at 575 nm. The nickel-related doublet at 882/884 nm was seen in the 830 nm PL spectrum. EDXRF revealed the presence of iron and cobalt which, together with the nickel feature in the PL, gives insight into the flux mixture used to grow this specimen.

Due to their growth method, HPHT synthetics generally show very distinct growth patterns when examined in the DiamondView. While they can show dramatic differences in fluorescence color, these are generally seen within angular zones that radiate from the center and extend through the volume of the specimen. In contrast, CVD synthetic diamonds are grown as layers. The start/stop events of the CVD reactor result in distinct changes in diamond chemistry that are visible in DiamondView fluorescence images; the changes in fluorescence color are usually parallel due to the layered growth. Therefore, it was quite interesting to see DiamondView fluorescence patterns in which the pavilion section toward the culet far more closely resembles the layers seen in CVD growth than the cross-pattern color zoning often seen in HPHT synthetics (figure 31). The fluorescence zoning commonly found in HPHT-grown material can be seen towards

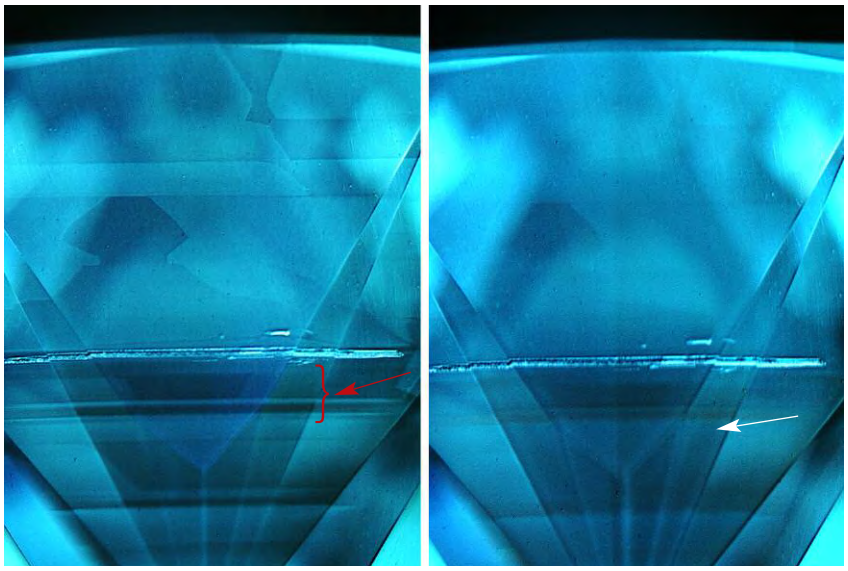

Figure 31. Left: This DiamondView fluorescence image of the HPHT-grown diamond's pavilion shows a combination of apparent layered growth, along with the more common cross-pattern morphology seen in HPHT synthetics. The area of the pavilion shown here also indicates the region of PL mapping. The red arrow indicates the regions that showed a high concentration of nickel, silicon, and NV center defects compared to the remainder of the mapped region. Above this more heavily doped layer is the metal rod inclusion also seen in figure 30. Right: The patterning in the corresponding phosphorescence image closely resembles the fluorescence image. A thin layer of material showing orange (~580 nm) phosphorescence is indicated by the white arrow.

the girdle section of this sample. PL mapping at liquid nitrogen temperatures was used to verify the DiamondView observations and detect the distribution of defects through the synthetic diamond (for more on the PL mapping collection technique see L.C. Loudin, "Photoluminescence mapping of optical defects in HPHT synthetic diamond," Summer 2017 *G&G*, pp. 180–189). We mapped the PL spectra of the region shown in figure 31 using 532, 633, and 785 nm laser excitations. One of the layers (red arrow in figure 31) in particular showed greatly elevated concentrations of nickel (as the 883/884 nm doublet; average concentration in this area was 5× greater than the average intensity of the doublet in other portions of the mapped pavilion), silicon (as the SiV^- defect at 737 nm; 10× greater), and NV centers (NV^0 at 575 nm [2× greater] and NV^- at 637 nm [2.5× greater]). This particular layer also showed orange phosphorescence in the DiamondView, assumed to be centered at approximately 580 nm (U.F.S. D'Haenens-Johansson et al., "Large colorless HPHT synthetic diamonds from New Diamond Technology," Fall 2015 *G&G*, pp. 260–279), in addition to the more common blue phosphorescence.

The specific growth process that creates the apparent layers in this HPHT synthetic is unknown, but it may be a necessary condition to grow synthetic material in such large sizes. The manufacturer may use successively larger seeds in separate growth runs or alter the pressure or temperature conditions within a single growth experiment. It should be noted that this growth feature, while layered in appearance, is quite different from CVD growth layers, which have sharp boundaries and are often differently colored. The chemistry collected on the layered portion was consistent with HPHT growth and not CVD growth; the chemistry was also consistent between the layered portion and the cross-patterned portion of growth. Therefore, a CVD seed was not used to grow this specimen. Similar layers were observed in the DiamondView images of the 10.08 ct blue HPHT synthetic (unpublished data). However, the size of this most current specimen demonstrates that the growth technologies and processes are continuing to improve and continuing to impress.

Troy Ardon and
Sally Eaton-Magaña

PHOTO CREDITS
Robison McMurtry—1, 11, 24, 29; Jian Xin (Jae) Liao—2, 6 (left), 27; Tyler Smith—3 (left), 4; Augusto Castillo—3 (right); Evan Smith—6 (center and right), 7; Sood Oil (Judy) Chia and Towfiq Ahmed—8, 10; Stephanie Persaud—9; Troy Ardon—12; Tony Leung—13; Bona Hiu Yan Chow—14; Johnny Leung—15; Sharon Tsz Huen Wu—16; Shunsuke Nagai—18; Makoto Miura—19; Diego Sanchez—20; Artitaya Homkrajae—21; Sally Eaton-Magaña—25; Jonathan Muyal—30.

©2018 GIA. GIA® and Gemological Institute of America® are registered trademarks of Gemological Institute of America, Inc.

Not all gems come from under the ground.

The Gemological Institute of America® supports communities where gems are mined, working with the Nelson Mandela Centre of Memory to build libraries in Africa and helping artisanal miners understand the quality of their discoveries with our Gem Guide. These initiatives help make it possible for regional populations to take a more active role in the industry and ultimately help their community look forward to a brighter future. Our contributions are one of the many reasons why GIA® is the world's foremost authority on diamonds, colored stones and pearls.

Learn more about the many facets of GIA at GIA.edu

GIA®

The World's Foremost Authority in Gemology™

Ensuring the Public Trust Through Nonprofit Service Since 1931

BENEFICIATION EDUCATION INSTRUMENTS LABORATORY RESEARCH

Karen V. Smit and Steven B. Shirey

Diamonds Help Solve the Enigma of Earth's Deep Water

Water is carried down into Earth at subduction zones by the process of plate tectonics. Much of the water escapes close behind the subduction zone, promoting melting of the mantle and giving rise to the volcanic chains in the Pacific Ocean basin known as the Ring of Fire, and many other volcanoes elsewhere. But can water be carried even further into the mantle? How would we even know? Why is it important, and what are the effects of such deep water storage? Diamonds can give us the answers to these questions. Recent discoveries of water-containing mineral inclusions and even free water held at high pressures in diamonds tell us that water is carried into Earth's deep interior—perhaps as deep as 700 km.

Why Do Earth Scientists Want to Know the Water Content at Great Depths?

Water, Water Everywhere... Everyone can see how abundant water is at Earth's surface from our oceans. But because water can fit into mineral structures at high pressure and the volume of Earth's mantle is so large, there could be at least another ocean's worth of water stored in the minerals of the mantle. To know precisely how much water and in what form it was stored would help scientists understand where the water for our oceans came from, how much water returns to the mantle through plate tectonics, and how the stored water affects the properties of the mantle.

Water in the deep earth is not always a free fluid phase, and many minerals instead have water incorporated in the crystal structure as hydrogen bonded to oxygen. Common mantle minerals such as majorite, bridgmanite, Mg-Al spinel, and olivine (and its high-pressure equivalents wadsleyite and ringwoodite), are "nominally anhydrous," but experiments show that they have the capacity to carry and host water in such a form in their structures.

Once in the mantle, water has many important effects on the properties of the mantle. Water affects the temperature at which the mantle begins to melt, along with its physical properties such as viscosity and density. In turn, these properties influence the strength of the mantle rock (its resistance to being deformed). It therefore becomes important for our understanding of the mobility and melting of mantle rock in the deep Earth to know how much water is down there. Water-rich fluids—i.e., water solutions wherein a variety of elements, compounds, and gases may be dissolved—are also a very effective way to transport other elements between different parts of Earth. Specifically, subduction fluids can transfer elements from the surface to diamond-stable portions of Earth and may even be a critical ingredient for growing diamonds.

How Is Water Distributed, and How Does It Get into the Deep Earth? The mantle transition zone (410–660 km) is thought to be a major sink for water in the mantle (Smyth, 1987). The two key minerals that make up the transition zone, wadsleyite and ringwoodite, have been shown experimentally to host an abundance of water, up to about 3.3 wt.% and 2.2 wt.% H_2O, respectively (Kohlstedt et al., 1996). Seismic images show that oceanic slabs—containing the water that was not released at shallower levels—are recycled into the mantle by subduction and can sit within the transition zone (van der Hilst et al., 1997). So both a delivery and storage mechanism for water exists for the mantle transition zone.

The water content in the lower mantle (below 660 km) is likely not as high as it is in the transition zone. Experiments show that the minerals in the lower mantle do not have a high water-carrying capacity (Inoue et al., 2010; Schmandt et al., 2014). When some oceanic slabs are subducted past the transition zone and into the lower mantle, it is expected that any water would be released upward into the overlying mantle. However, a lower mantle diamond from the Juína area of Brazil was found to contain brucite ($Mg(OH)_2$) in association with ferropericlase ($(Mg,Fe)O$) (Palot et al., 2016). Water in the brucite structure likely originated as a H_2O-bearing fluid film around the ferropericlase inclusion. This diamond preserved an inclusion that indicates that some water transport beyond the transition zone is possible.

Evidence for Mantle Water from Minerals Found in Superdeep Diamonds

Water as a Solidified Fluid: Samples of High-Pressure Ice. Direct observations of water-rich fluids in superdeep diamonds (see box A) are rare and have only been reported in two studies. At atmospheric pressure, H_2O occurs as a liq-

Gems & Gemology, Vol. 54, No. 2, pp. 220–223.

© 2018 Gemological Institute of America

uid, but at higher pressures (and relatively cool temperatures compared to mantle temperatures), H_2O occurs as two different forms of ice, known as Ice VI and Ice VII (figure 1).

Ice VI was found in fibrous diamonds from the Democratic Republic of the Congo with a remnant pressure of 1.9 GPa (Kagi et al., 2000), where 1 GPa is 1 gigapascal or 10,000 times atmospheric pressure. Ice VII was found in diamonds from Orapa (Botswana), Shandong (China), and Namaqualand (South Africa) at pressures ranging from 7 GPa to 28 GPa, which is equivalent to 220 to 880 km (Tschauner et al., 2018). Amazingly, once these water-rich fluids are trapped as inclusions in diamond, they retain some high pressure even after eruption to the earth's surface. As the diamond cools down to ambient conditions (25°C, 100 kPa), the trapped H_2O recrystallizes as Ice VI or Ice VII (figure 1).

Hydrous fluids have previously been found trapped as thin films around shallower lithospheric diamonds (again, see box A; Nimis et al., 2016). But the presence of Ice VII in superdeep diamonds confirms the presence of a free fluid phase at pressures corresponding to the transition zone and lower mantle. As discussed with the finding of hydrous ringwoodite (below), these H_2O-rich fluids could represent the fluid-rich diamond-forming environment, or they could be indicative of the ambient water content of the deep Earth. A likely scenario is that H_2O-rich fluids are introduced into the deep Earth through subduction, consistent with the compositions of many superdeep diamonds that indicate an affinity with subducted oceanic slabs. This suggests that these fluid-rich regions of the transition zone occur locally around subducted slabs. Only further work on other superdeep inclusion-bearing diamonds from worldwide localities will show if this is the case, or how widespread such water contents are. But the highly diverse nature of the host diamonds that have been studied already suggests that these ices may be much more common than thought—we just need to look more carefully.

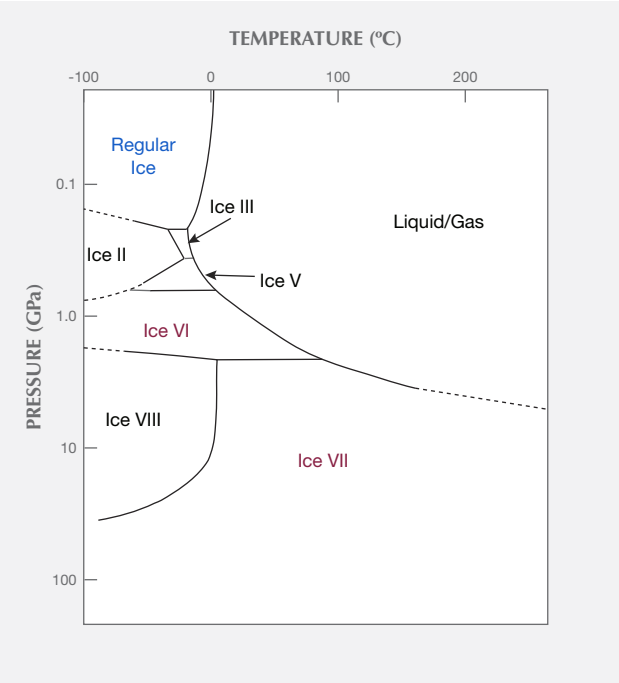

Figure 1. Phase diagram showing the stability fields of H_2O as liquid and ice at high pressures (modified from Lobban et al., 1998). Superdeep diamonds form at temperatures between 1300 and 1500°C (beyond scale of diagram) where H_2O occurs as a liquid. As the diamond cools at the earth's surface, H_2O trapped within the diamond retains its original high pressure and recrystallizes as the high-pressure form of solid H_2O known as Ice VII.

Water Isn't Always a Free Fluid Phase: Examples of Mineral-Hosted Water. Ringwoodite is a high-pressure form of olivine (Mg_2SiO_4) that occurs in the lower half of the mantle transition zone, where it comprises around 60% of the total mineralogy. We know this from experimental work that simulates the high-pressure conditions deep within Earth. Until 2014, ringwoodite had only been found in highly shocked meteorites. This is because at surface pressures, ringwoodite—even when confined to its diamond host—is notoriously unstable and reverts to olivine at lower pressure.

Unchanged ringwoodite from deep in Earth was found for the first time as a 30 µm inclusion trapped within a diamond from Juína, Brazil (figure 2; see also Pearson et al., 2014). Even more remarkable was that this tiny ringwoodite grain was able to provide the first direct measurement of the water content of the most common mineral in the mantle transition zone. Water content was measured using nondestructive infrared spectroscopy (IR) while the inclusion was still trapped at high remnant pressure within the diamond. When the scientists attempted to remove the inclusion from the diamond for additional measurements, it self-destructed by exploding!

By comparing the intensity of the water peaks in the IR spectrum with those from synthetic ringwoodite with known amounts of water, the natural ringwoodite inclusion was estimated to contain around 1.4 wt.% H_2O. This value could represent either a locally water-enriched portion of the mantle transition zone, perhaps associated with the fluids that formed the diamonds, or the water content of the mantle transition zone as a whole. It is interesting to note that if this water content is applied to the whole mantle transition zone, the total water content would be approximately 2.5 times the volume of water in Earth's oceans (Nestola and Smyth, 2015).

The Tip of the Iceberg: Much Further Work Is Needed. Wadsleyite, another potential water carrier, has not yet been observed as an inclusion in diamond. This is the high-pressure

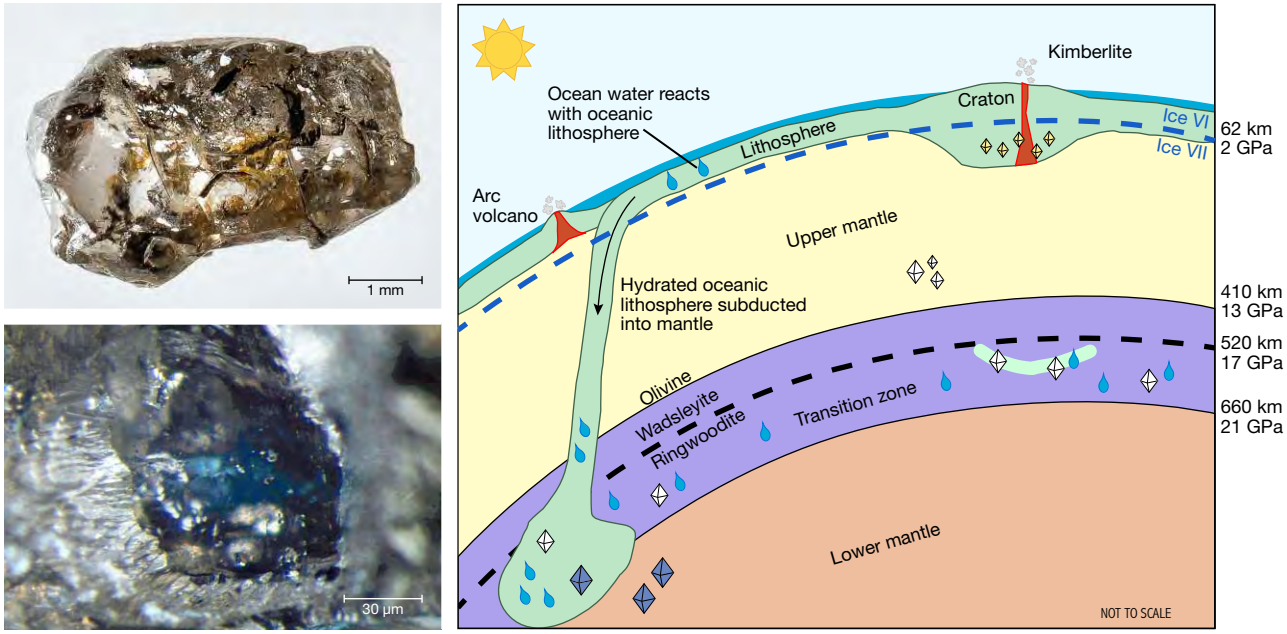

Figure 2. Ringwoodite is the high-pressure form of the mineral olivine (Mg_2SiO_4) that occurs between 520 and 660 km below the surface of the earth in the transition zone. The first terrestrial observation of this mineral was in a diamond from Juína, Brazil (top left). Water content in this 30 µm inclusion (bottom left) is around 1.4 wt.%, indicating that the global transition zone could contain at least 2.5 times the amount of water as Earth's oceans. The majority of diamonds come from the cratonic lithosphere (indicated here as yellow diamonds). Superdeep diamonds (indicated here as white and blue diamonds) are rarer and originate from greater depths, often from the transition zone, which extends between 410 and 660 km.

phase of olivine that is found between 410 and 520 km, just slightly shallower than ringwoodite (figure 2). Finding wadsleyite, along with more occurrences of ringwoodite, and analyzing their water contents will give a better understanding of the mantle transition zone's average water-carrying capacity. Expectations are that wadsleyite will carry at least

Box A: Diamond in the Earth's Mantle

Natural Diamond Formation. Natural diamonds typically form 150–200 km below the surface of the earth. Diamond formation does not occur everywhere at these depths, but only below the oldest continents that have been stable for billions of years; these areas are known as *cratons*. This is because these old cratons all have thick continental roots with cool temperature profiles conducive to diamond formation. Diamonds that form within these continental roots are known as *lithospheric diamonds* and are carried up to the surface of the earth by rare volcanic eruptions known as *kimberlites*. Other diamonds form much deeper in the earth, below these continental roots. So-called *superdeep diamonds* form at depths greater than 200 km in areas of the mantle known as the *transition zone* (410 to 660 km below the earth's surface) and *lower mantle* (> 660 km). After formation they are transported to shallower depths in the mantle, likely through mantle convection cells, and then also brought to the surface by kimberlite eruptions.

Inclusions in Superdeep Diamonds Are Direct Samples of the Deep Earth. Diamonds often trap tiny pieces of their surrounding rocks as they grow. These trapped inclusions are the only direct samples we have to study the composition of the deep earth. In the absence of mineral inclusions in diamond, the way to study the earth's composition at depth is through experimental work: subjecting minerals to high pressures in the lab to see what their properties are. This experimental work has given us a good understanding of the mineral phase transitions in the deep earth, but inclusion-bearing diamond remains an unparalleled tool to uncover the earth's properties at depth.

as much water as ringwoodite. Will water in these minerals turn out to be ubiquitous? Is the earth even wetter than we thought?

Further evidence for water in mineral inclusions in many more superdeep diamonds must be sought. An easy way to start is through nondestructive infrared spectroscopy of diamonds and their inclusions, specifically looking for water and ice peaks (see Kagi et al., 2000 for example spectra). Even some lithospheric diamonds are thought to form from water-rich fluids (Stachel and Luth, 2015; Smit et al., 2016), yet observation of water in these diamonds is incredibly rare (Nimis et al., 2016). Could it be that these high-pressure ices are much more common than we thought? Could the discovery of Ice VII in Earth's diamonds revolutionize our thinking about ice storage at high pressure in other planets of our size range, such as Mars or Venus? In any case, these secrets will be revealed by more work on diamonds.

REFERENCES

Inoue T., Wada T., Sasaki R., Yurimoto H. (2010) Water partitioning in the Earth's mantle. *Physics of the Earth and Planetary Interiors*, Vol. 183, No. 1-2, pp. 245–251.

Kagi H., Lu R., Davidson P., Goncharov A.F., Mao H.K., Hemley R.J. (2000) Evidence for ice VI as an inclusion in cuboid diamonds from high P-T near infrared spectroscopy. *Mineralogical Magazine*, Vol. 64, No. 6, pp. 1089–1097.

Kohlstedt D.L., Keppler H., Rubie D.C. (1996) The solubility of water in α, β and γ phases of $(Mg, Fe)_2SiO_4$. *Contributions to Mineralogy and Petrology*, Vol. 123, pp. 345–357.

Lobban C., Finney J. L., Kuhs W. F. (1998) The structure of a new phase of ice. *Nature*, Vol. 391, pp. 268–270.

Nestola F., Smyth J.R. (2015) Diamonds and water in the deep Earth: a new scenario. *International Geology Review*, Vol. 58, No. 3, pp. 263–276.

Nimis P., Alvaro M., Nestola F., Angel R.J., Marquardt K., Rustioni G., Harris, J.W. (2016) First evidence of hydrous silicic fluid films around solid inclusions in gem-quality diamonds. *Lithos*, Vol. 260, pp. 384–389.

Palot M., Jacobsen S.D., Townsend J.P., Nestola F., Marquardt K., Miyajima N., Harris J.W., Stachel T., McCammon C.A., Pearson D.G. (2016) Evidence for H_2O-bearing fluids in the lower mantle from diamond inclusion. *Lithos*, Vol. 265, pp. 237–243.

Pearson D.G., Brenker F.E., Nestola F., McNeill J., Nasdala L., Hutchison M.T., Matveev S., Mather K., Silversmit G., Schmitz S., Vekemans B., Vincze L. (2014) Hydrous mantle transition zone indicated by ringwoodite included within diamond. *Nature*, Vol. 507, No. 7491, pp. 221–224.

Schmandt B., Jacobsen S.D., Becker T.W., Liu Z., Dueker K.G. (2014) Dehydration melting at the top of the lower mantle. *Science*, Vol. 344, No. 6189, p. 1265.

Smit K.V., Shirey S.B., Stern R.A., Steele A., Wang W. (2016) Diamond growth from C–H–N–O recycled fluids in the lithosphere: Evidence from CH_4 micro-inclusions and $\delta^{13}C$–$\delta^{15}N$–N content in Marange mixed-habit diamonds. *Lithos*, Vol. 265, pp. 68–81.

Smyth J.R. (1987) β-Mg_2SiO_4–A potential host for water in the mantle. *American Mineralogist*, Vol. 72, pp. 1051–1057.

Stachel T., Luth R.W. (2015) Diamond formation – where, when and how? *Lithos*, Vol. 220-223, pp. 200–220.

Tschauner O., Huang S., Greenberg E., Prakapenka V.B., Ma C., Rossman G.R., Shen A.H., Zhang D., Newville M., Lanzirotti A., Tait K. (2018) Ice-VII inclusions in diamonds: Evidence for aqueous fluid in Earth's deep mantle. *Science*, Vol. 359, No. 6380, pp. 1136–1139.

van der Hilst R., Widiyantoro S., Engdahl E.R. (1997) Evidence for deep mantle circulation from global tomography. *Nature*, Vol. 386, No. 6625, pp. 578–584.

For online access to all issues of GEMS & GEMOLOGY from 1934 to the present, visit:

gia.edu/gems-gemology

Mushroom in Copal

Copal is widely popular among gem collectors due to its eclectic inclusion scenes. As a fossilized tree resin, copal can contain a wide range of flora, fauna, and inorganic materials. It is not uncommon to find spiders, termites, leaves, and petals inside this resinous gem. In a 19.83 ct brownish orangy yellow copal, the author recently observed a remarkably well-preserved mushroom that was easily seen with the naked eye and had a cap that was just over 5.5 mm in diameter. Stalks of broken mushrooms, miscellaneous plant materials, and gas bubbles were also found in this specimen. Interestingly, copal was also used for many years by some indigenous peoples in Mexico and Central America as incense for ceremonial purposes such as the sacred mushroom ceremony. The mushroom inclusion in this copal, reportedly from Mexico, may have a more significant meaning for the people of Mesoamerica that goes beyond a gemological standpoint (figure 1).

Rebecca Tsang
GIA, Carlsbad

Figure 1. This copal from Mexico contained a remarkably well-preserved eye-visible mushroom inclusion. Photomicrograph by Nathan Renfro; field of view 9.59 mm.

Gilalite Altered to Cuprite in Quartz

In 2004, gem-quality quartz that contained blue to green inclusions of the hydrated copper silicate mineral gilalite was found in Paraíba, Brazil. This material was sold as "Medusa quartz," so named for the medusa phase of a jellyfish, which has an umbrella-like shape similar to these brightly colored inclusions. One specimen of this material contained an unusual red inclusion with the same umbrella shape (figure 2). This red inclusion revealed a surface-reaching crack. Microscopic examination showed a granular texture in the red areas. Raman analysis identified the red mineral as the copper oxide cuprite. It was apparent that the gilalite had been altered by secondary fluids that entered the crack. Neighboring gilalite inclusions were pristine and unaltered. The underside of the umbrella-like structure also revealed a blue ring, indicating that the inclusion had not completely altered (figure 3). The high-contrast blue and red colors seen in this particular sample of Medusa quartz make it a most intriguing inclusion specimen.

Nathan Renfro and John I. Koivula
GIA, Carlsbad

About the banner: The surface of a synthetic rock crystal quartz is shown in contrasting color using modified Rheinberg contrast. Three colored filters highlight different crystallographically oriented sets of crystal faces. Photomicrograph by Nathan Renfro; field of view 12.50 mm.
Editors' note: Interested contributors should contact Nathan Renfro at nrenfro@gia.edu and Jennifer-Lynn Archuleta at jennifer.archuleta@gia.edu for submission information.

Gems & Gemology, Vol. 54, No. 2 pp. 224–232.

© 2018 Gemological Institute of America

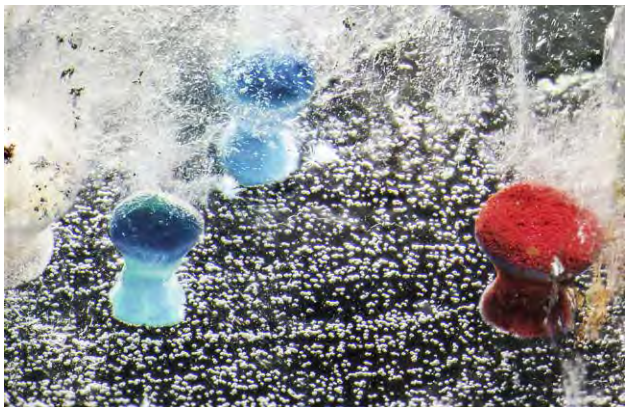

Figure 2. This quartz from Paraíba, Brazil, contains inclusions of the hydrated copper silicate mineral gilalite, with one inclusion altered to the red copper oxide mineral cuprite due to a crack that allowed secondary fluids to attack and alter the inclusion. Photomicrograph by Nathan Renfro; field of view 5.49 mm.

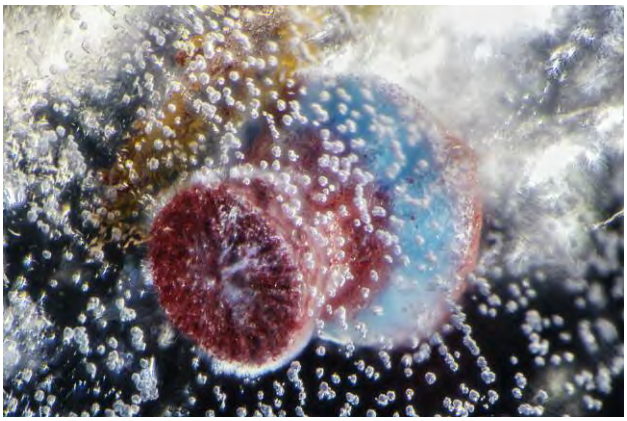

Figure 3. The red cuprite inclusion shows a blue ring of gilalite where there was incomplete alteration to cuprite. Also note the granular structure of the cuprite. Photomicrograph by Nathan Renfro; field of view 2.41 mm.

Uncommon Parallel Color Zoning in a Chameleon Diamond

As their name suggests, chameleon diamonds are a kind of thermo- and photosensitive colored diamond that change hue with gentle heating or when left in darkness for an extended period of time. A diamond must meet the following criteria to qualify for chameleon testing at GIA: a green or greenish component in the bodycolor, yellow or orange fluorescence under both long-wave and short-wave UV light, and persistent yellow phosphorescence following exposure to short-wave UV light. After heating or an extended stay in darkness, the green component of the stone disappears and gives way to a yellowish orange hue. The mechanism responsible for this change is not well understood.

The infrared spectrum of chameleon diamonds typically shows them to be type Ia with moderate nitrogen concentration. The dominant feature in the visible-light spectrum is a broad absorption band centered at 480 nm. Viewed face-up, most diamonds appear to have an even bodycolor to the unaided eye, but magnification reveals that the vast majority of diamonds with the 480 nm band defect show distinct color zoning with an amorphous distribution of color.

GIA's Carlsbad laboratory recently graded a Fancy Light grayish greenish yellow 1.06 ct round brilliant chameleon diamond that displayed this typical color zoning, but in a very distinctive pattern. Rather than the usual formless color distribution, the green color in this diamond was neatly confined to parallel bands (figure 4). The color-change effect caused by heating was correspondingly limited to these bands (figure 5). It is worth noting that the characteristic chameleon fluorescence and phosphorescence of this diamond were likewise confined to parallel zones as revealed by DiamondView imaging (figure 6). Al-

Figure 4. Parallel bands of green color in the 1.06 ct chameleon diamond at room temperature. Photomicrograph by Nathan Renfro; field of view 3.21 mm.

Figure 5. The green color changed to yellowish orange after about 15 seconds of gentle heating. Photomicrograph by Nathan Renfro; field of view 3.21 mm.

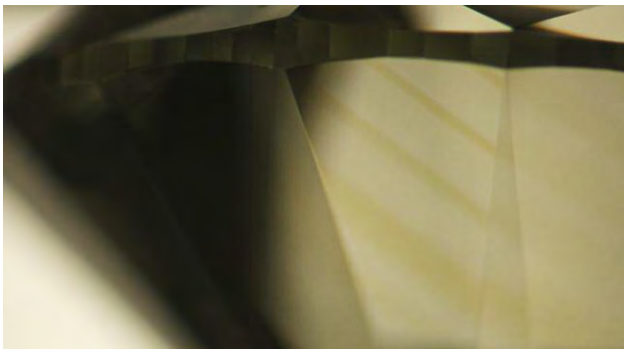

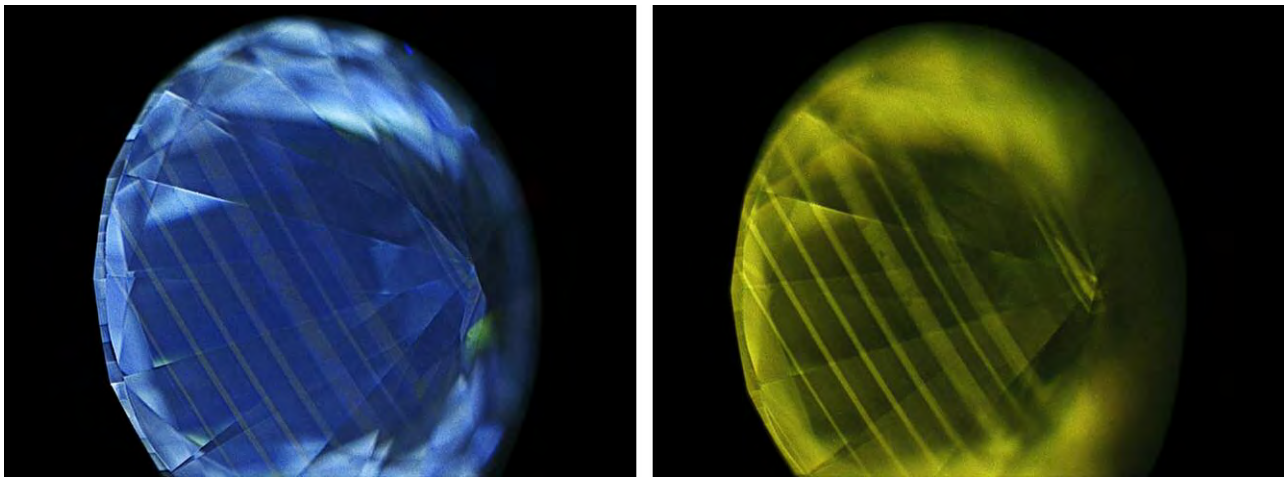

Figure 6. DiamondView images showing characteristic chameleon fluorescence (left) and phosphorescence (right) zoned in parallel bands. Images by Hollie McBride.

though parallel features are not rare in diamonds due to the inherent planes of weakness within their crystal structure, it is uncommon to see this pattern in chameleon stones. We took the opportunity to capture video of the chameleon effect in this distinctive stone while heating it in real time, something GIA has not previously endeavored. View the video at www.gia.edu/gems-gemology/summer-2018-microworld-uncommon-parallel-color-zoning-in-a-chameleon-diamond.

Hollie McBride
GIA, Carlsbad

Merelaniite Inclusions in Tanzanite

Tanzanite, the blue to violet transparent variety of the mineral zoisite, was discovered in Tanzania around 1967. Since tanzanite seldom contains significant inclusions, the authors were surprised to examine a tanzanite cabochon that contained myriad dense whisker-like inclusions. The whiskers were cylindrical in shape, typically gently curved along their length, and displayed a metallic luster. At first glance, the whiskers were interpreted to be composed of graphite, as it is one of the more common opaque black mineral inclusions found in tanzanite. However, the elongate, curvilinear morphology suggested they were likely something else.

Merelaniite, a new molybdenum-essential member of the cylindrite group, was recently identified by coauthor JAJ and colleagues and approved in 2016 by the Commission of New Minerals, Nomenclature and Classification (CNMNC) of the International Mineralogical Association (IMA). The new mineral is sporadically found in specimens from the tanzanite mines near Merelani, Tanzania. It can be associated with a wide variety of minerals from the Merelani mines and has also been noted as being enclosed in calcite, quartz, chabazite, fluorapatite, prehnite, and zoisite. All the specimens identified so far have been obtained from secondary mineral markets, and the exact geological location of any specimen known to contain merelaniite is so far undocumented and unknown. Merelaniite occurs individually and in clusters as dark gray metallic whiskers of circular cross-section. The whiskers are composed of crystal lamellae that are tightly rolled in a "scroll-like" manner similar in appearance to the related mineral cylindrite (J.A. Jaszczak et al., "Merelaniite, $Mo_4Pb_4VSbS_{15}$, a new molybdenum-essential member of the cylindrite group, from the Merelani tanzanite deposit, Lelatema Mountains, Manyara region, Tanzania," *Minerals*, 2016, Vol. 6, No. 4, 115).

This tanzanite cabochon sample revealed similar whisker-like inclusions accompanied by growth blockages, dark platy crystals, and fractures. The whiskers varied in diameter and length, and tended to branch out intermittently. The length was generally over a millimeter (figure 7). Growth blockages were fluid filled and also contained

Figure 7. Merelaniite whisker inclusions in the tanzanite cabochon. Photomicrograph by Augusto Castillo; field of view 3.57 mm.

Figure 8. A growth blockage results from the suspension of zoisite growth when the crystal is interrupted by a foreign body. In this case, the foreign body is a merelaniite whisker. Photomicrograph by Tyler Smith; field of view 1.99 mm.

dark solids (figure 8). The presence of intact liquid inclusions was a strong indicator that this tanzanite had not undergone heat treatment. Small granular crystals were observed in between fractures associated with the whisker inclusions. Raman spectroscopy confirmed these opaque whisker-like inclusions to be merelaniite, and platelets that were associated with the whiskers might be unwound layers of merelaniite.

Coincidentally, two unusual specimens of tanzanite crystals containing merelaniite whiskers were found by one of the coauthors (JAJ) among a gem and mineral dealer's stock at one of the mineral shows held in Tucson, Arizona, in February 2018. Also relatively unusual is that these crystals were still on matrix composed primarily of calcite and graphite (figure 9).

The occurrence of merelaniite in tanzanite is very rare. This is the first time GIA has identified this new mineral in gem-quality tanzanite.

Augusto Castillo and Tyler Smith
GIA, New York

John A. Jaszczak (jaszczak@mtu.edu)
Michigan Technological University
Houghton, Michigan

Microlite Crystals in Topaz from Pakistan

Microlite, $NaCaTa_2O_6(OH)$, is a typical mineral of highly developed lithium pegmatites, known from many localities worldwide. It always forms yellow to orange octahedral crystals. It was already known as inclusions in quartz from Pakistan (J. Hyršl and G. Niedermayr, "Einschlüsse im 'Allerweltsmineral' quarz," *Mineralien-Welt*, Vol. 18, No. 2, 2007, pp. 44–55), but much more beautiful are microlite inclusions in topaz (figure 10), examples of which were sold in Tucson in January 2018. Shigar Valley in northern Pakistan was reported as the locality. Both minerals were confirmed by Raman spectroscopy.

Topaz forms loose, very light brown crystals up to about 2 cm, and microlite forms sharp transparent orange octahedrons in sizes up to about 1.5 mm. The inclusions grew both on the surface and inside the topaz crystals (figure 11). Several topaz crystals were faceted, and the stones

Figure 9. A merelaniite-included tanzanite crystal (2.2 cm tall, left) on a matrix of calcite and graphite. The calcite also contains merelaniite inclusions. The close-up field of view (right) is 6.55 mm wide. Photos by J.A. Jaszczak.

Figure 10. A 16 mm topaz crystal and an 8.69 ct faceted topaz, both with microlite inclusions, from Pakistan. Photo by J. Hyršl.

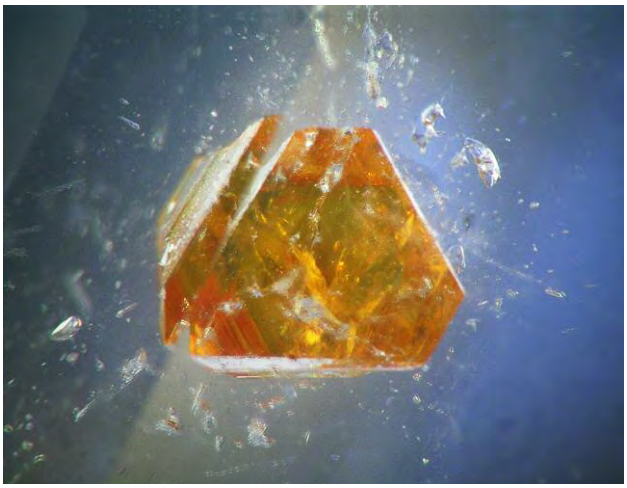

Figure 11. A microlite crystal, measuring 1 mm across, in a topaz from Pakistan. Photo by J. Hyršl.

host some of the most aesthetically pleasing inclusions found during the several last years.

Jaroslav Hyršl
Prague

Perettiite-(Y) and Tusionite Inclusions in Phenakite from Myanmar

Every year about 100 new minerals are described, but few have been discovered as inclusions in gemstones (e.g., carmichaelite in chrome pyrope from Arizona and protoenstatite in labradorite from Oregon). In 2015, a new mineral—perettiite-(Y)—was described as inclusions in phenakite crystals from pegmatites by Khetchel village in the Molo area near Momeik, about 100 km northeast of Mogok (R.M. Danisi et al., "Perettiite-(Y), $Y_2^{3+}Mn_4^{2+}Fe^{2+}[Si_2B_8O_{24}]$, a new mineral from Momeik, Myanmar," *European Journal of Mineralogy*, Vol. 27, No. 6, pp. 793–803). It was named after Swiss gemologist Adolf Peretti, head of the GemResearch Swisslab, who found the first specimens.

Perettiite-(Y) has a very unusual composition, $Y_2Mn_4Fe[Si_2B_8O_{24}]$. It forms strongly tapered yellow needles up to several millimeters long; only very rarely do they form beautiful bundles (figure 12, left). Several other inclusions were also found in phenakite from the same locality, including the very rare tin borate tusionite, which forms groups of mica-like yellow plates (figure 12, right). Phenakite itself is also unusual, because it often forms

Figure 12. Left: Perettiite-(Y) bundle in phenakite from Khetchel, Myanmar; image width 3.8 mm. Right: Tusionite plates in phenakite from Khetchel; image width 2.5 mm. Photomicrographs by P. Škácha.

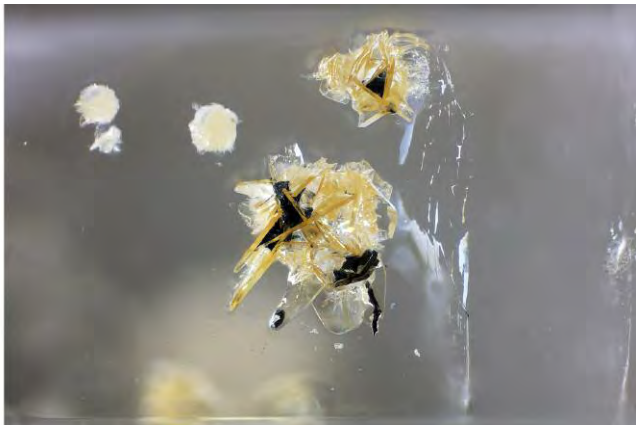

Figure 13. Phenakite twin, measuring 1.35 cm high, with a "drill bit" termination and perettiite-(Y) inclusions. Photo by J. Hyršl. From the author's collection.

twins with very strange "drill bit" termination (figure 13). Unfortunately, perettiite-(Y) and tusionite inclusions (figure 14) are extremely rare, found in just a few pieces in a thousand phenakite crystals, so cut stones will remain a valuable collector's rarity (figure 14).

Jaroslav Hyršl

A Horse-Shaped Inclusion in Pink Sapphire from Mozambique

Recently, GIA's Bangkok lab received a 0.58 ct pink sapphire with a unique inclusion. Microscopic observation revealed needles, platelets, and particles, all of which are common inclusions found in Mozambican ruby and pink sapphire. The most interesting inclusion was found near the stone's girdle. The crystal, which resembled a horse, was identified as phlogopite (figure 15). The most common mineral inclusions in Mozambican rubies are crystals of

Figure 14. Phenakite with tusionite (left) and perettiite-(Y) inclusions (right). The specimen on the left weighs 1.77 ct, and the one on the right weighs 2.31 ct. Photo by J. Hyršl. From the author's collection.

amphibole and mica (V. Pardieu et al., "Rubies from the Montepuez area (Mozambique)," 2013, www.gia.edu/gia-rubies-from-montepuez-area; V. Pardieu et al., "GIA lab reports on low-temperature heat treatment of Mozambique ruby," 2015, www.gia.edu/gia-news-research-low-temperature-heat-treatment-mozambique-ruby). Most of the mica inclusions are margarite or muscovite, typically with a lighter color and pseudohexagonal shape. Phlogopite is another end member of the mica series, but with a very different chemical composition from muscovite. To our knowledge, phlogopite mica has not been reported in Mozambican rubies or pink sapphires.

Charuwan Khowpong
GIA, Bangkok

Figure 15. The horse-shaped inclusion of phlogopite mica identified by Raman analysis. Photomicrograph by Charuwan Khowpong; field of view 2.40 mm.

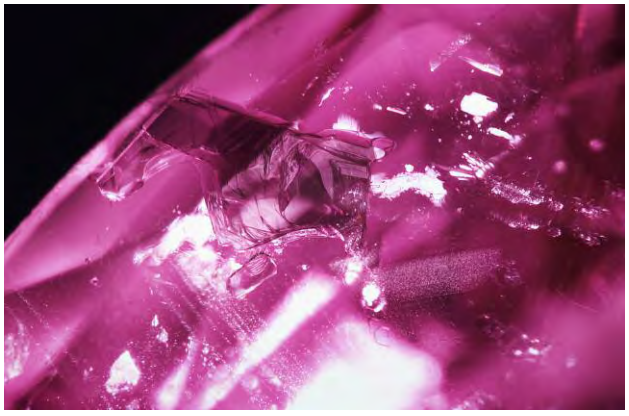

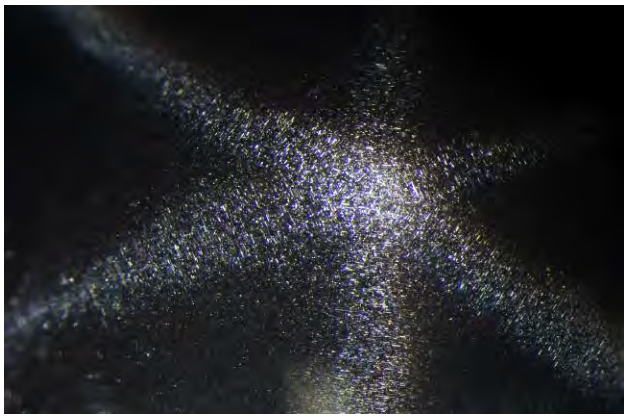

Figure 16. Fine needles create a six-rayed star in an untreated spinel. Photomicrograph by E. Billie Hughes; specimen courtesy of Global Spinel Gems.

Star Spinel with Four and Six Rays

Lotus Gemology receives submissions of star stones on a regular basis, so when we first saw the specimen shown here, it appeared to be one among many of our usual stones to test. Upon closer examination, however, we realized it was not a star sapphire, but something much more rarely seen: star spinel.

Upon first glance at the cabochon's dome, the stone displays one six-rayed star (figure 16), similar to what we see in star corundum. But if we look on the sides of the stone, we can also see a four-rayed star (figure 17). These stars are both created from numerous dense, short needle-like particles. Once we examined a small polished area on the cabochon's base, we found that there are actually two distinct types of exsolution products in the stone. On the right side of figure 18, we can see the tiny, dense needles and particles that form both types of stars. In the center of the image we can see much larger, less densely dispersed platelets that resemble confetti.

Figure 17. When viewed in a different position, the spinel also displays a four-rayed star. Photomicrograph by E. Billie Hughes; specimen courtesy of Global Spinel Gems.

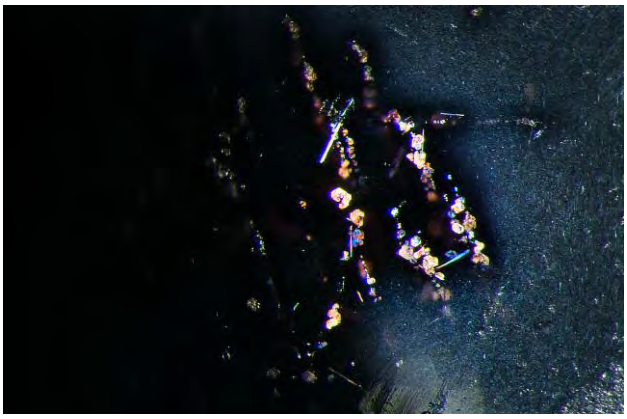

Figure 18. In the center of the image we can see larger reflective platelet inclusions in the untreated star spinel. On the right-hand side, we see much finer dense needles that form both six-rayed and four-rayed asterism. Photomicrograph by E. Billie Hughes; specimen courtesy of Global Spinel Gems.

E. Billie Hughes
Lotus Gemology, Bangkok

Wollastonite in Devitrified Glass, Imitating Horsetail Inclusions in Demantoid Garnet

A 13.12 ct transparent yellowish green gemstone with a beautiful internal scene was examined by the author. The specimen exhibited numerous elongated colorless crystals radiating from the center (figure 19), much like the horsetail inclusions of chrysotile that one would expect to find in Russian demantoid garnets. Standard gemological testing yielded surprising results: a single refractive index of 1.520, specific gravity of 2.50, and medium chalky green fluorescence under short-wave UV light. The specimen was inert to long-wave UV light. These properties indicated that the yellowish green cabochon stone was glass, whereas the masses of needle-like crystals (figure 20) were identified as calcium silicate wollastonite by Raman spectroscopy. Wollastonite inclusions have been reported as an indicator of the devitrification process (Winter 2017 Micro-World, pp. 469–470).

Other advanced techniques, including energy-dispersive X-ray fluorescence (EDXRF) and Fourier-transform infrared (FTIR) and Raman spectroscopy, were also carried out to confirm the cabochon's identity. FTIR and Raman spectroscopy showed a distinct and characteristic pattern of artificial glass. The nonquantitative EDXRF offers no

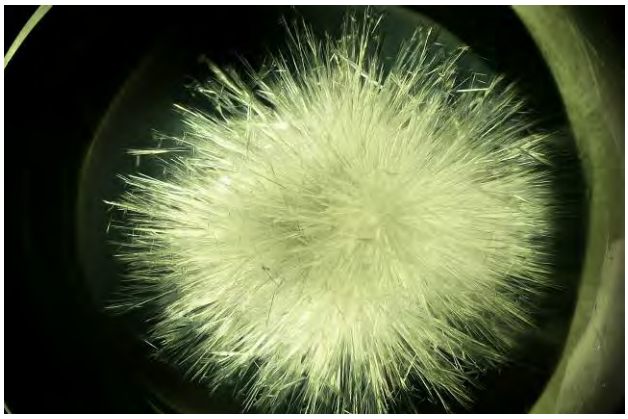

Figure 19. A yellowish green glass with numerous wollastonite needles radiating from the center, similar to the horsetail inclusions found in demantoid garnets. Photomicrograph by Ungkhana Atikarnsakul; field of view 14.4 mm.

additional value, as the elements detected are also present in demantoid garnets.

Although this is not the first time that wollastonite inclusions have been found in devitrified glasses, they formed in an interesting pattern in this yellowish green gemstone.

Ungkhana Atikarnsakul
GIA, Bangkok

Quarterly Crystal: Wurtzite Phantom in Quartz

Transparent colorless rock crystal quartz is a strong, durable mineral that makes a favorable host for a wide variety of inclusions (see the three-volume *Photoatlas of Inclusions in Gemstones* for examples). The geographic source of the crystal pictured in figure 21 is British Columbia, Canada. At 1,140 ct and 86.38 mm in length, this large example of rock crystal plays host to several near-surface opaque black hexagonal to trigonal crystals as large as 5.0 mm.

Figure 20. Close-up view of the wollastonite crystals. Photomicrograph by Ungkhana Atikarnsakul; field of view 4.8 mm.

Figure 21. Measuring 86.38 mm and weighing 1,140 ct, this quartz crystal from British Columbia contains a three-sided phantom composed of an abundance of opaque black wurtzite inclusions. Photo by Robison McMurtry.

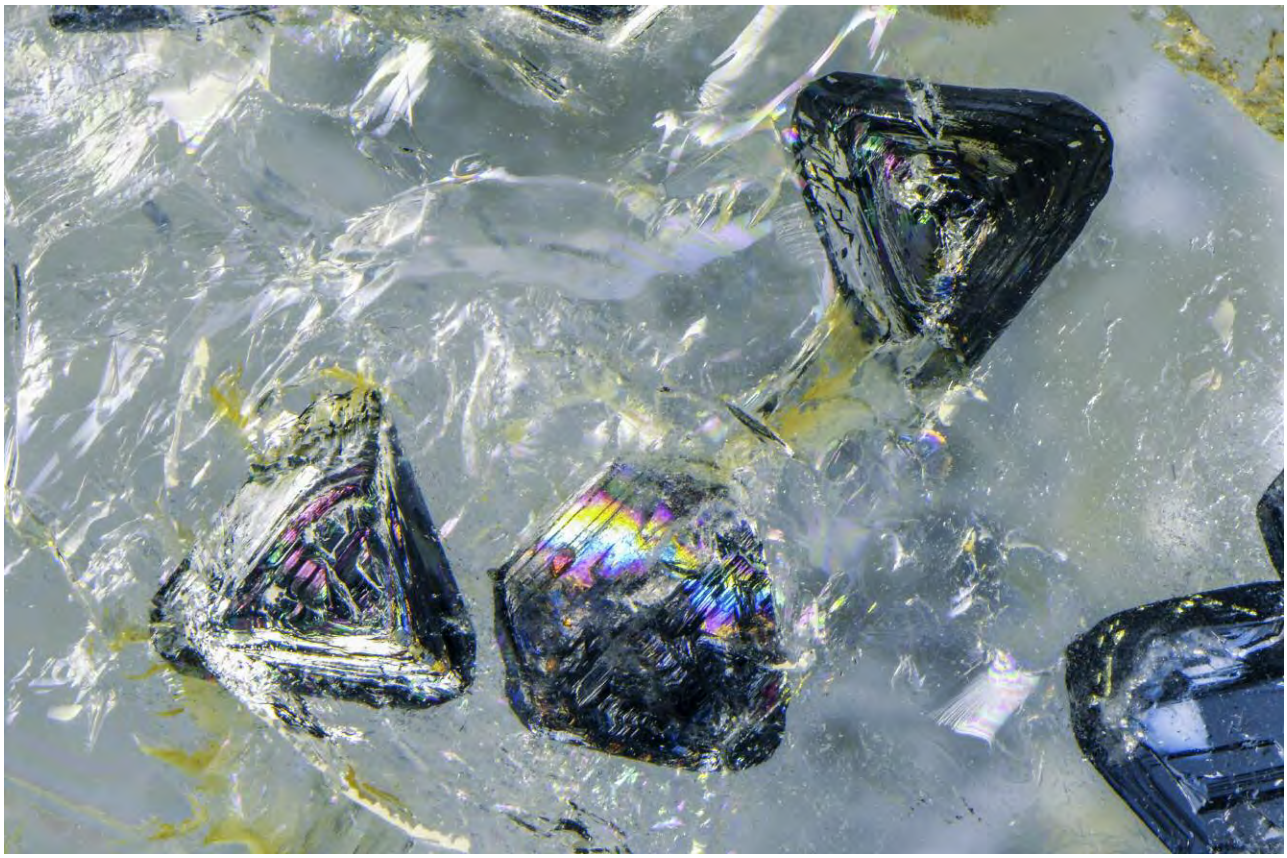

Figure 22. The crystals in this phantom plane in quartz were identified by Raman analysis as wurtzite. Photomicrograph by Nathan Renfro; field of view 19.2 mm.

As shown in figure 22, the micromorphology of the numerous inclusions, forming a three-sided phantom, suggests that they might be the zinc iron sulfide wurtzite. Laser Raman microspectrometry confirmed the identification of the inclusions as wurtzite. The euhedral inclusions were situated in the quartz crystal in the form of directional phantoms that developed through the directional deposition of the wurtzite on three consecutive surfaces of the quartz, which then continued to grow, enveloping the wurtzite as inclusion planes tracing the form of the original quartz host. From what we can determine, this is the first time that wurtzite has been found as an inclusion in any gem material. Because of wurtzite's relationship to sphalerite, some inclusions previously identified as sphalerite may actually be wurtzite.

John I. Koivula

For More on Micro-World

To see video of the chameleon effect in a Fancy Light grayish greenish yellow diamond, as featured in this section, please visit www.gia.edu/gems-gemology/summer-2018-microworld-uncommon-parallel-color-zoning-in-a-chameleon-diamond

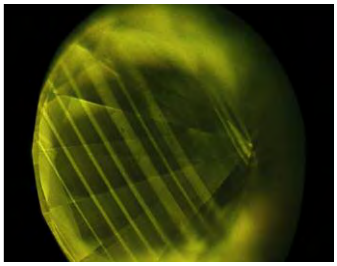

G&G

Gem News International

Contributing Editors

Emmanuel Fritsch, *University of Nantes, CNRS, Team 6502, Institut des Matériaux Jean Rouxel (IMN), Nantes, France* (fritsch@cnrs-imn.fr)

Gagan Choudhary, *Gem Testing Laboratory, Jaipur, India* (gagan@gjepcindia.com)

Christopher M. Breeding, *GIA, Carlsbad* (christopher.breeding@gia.edu)

COLORED STONES AND ORGANIC MATERIALS

Discovery of color-change chrome grossular garnets from Ethiopia. Ethiopia has become a significant producer of opal, sapphire, and emerald in recent years. In addition, reports of gem-quality green garnets have started to emerge (B. Williams et al., "Tsavorite reportedly from Ethiopia," *Journal of Gemmology*, Vol. 35, No. 8, 2017, pp. 702–704).

Todd Wacks (Tucson Todd's Gems, Tucson, Arizona, and Vista, California) recently submitted three rough and one faceted garnet (figure 1, stones 1, 2, 3, and 4) to GIA in Carlsbad for scientific examination. He purchased the garnets from Inna Gem, which reported that the garnet mine is located near the town of Wbi and the new Dubuluk emerald deposit (Spring 2017 GNI, pp. 114–116). The stones showed obvious color change from yellow-green under daylight-equivalent lighting to orange-brown under incandescent illumination. This is similar to the color-change behavior reported for some color-change garnets from Sri Lanka (Spring 2017 GNI, pp. 137–138).

Standard gemological testing revealed a refractive index (RI) of 1.740 on the faceted stone. Hydrostatic specific gravity (SG) of all garnets in this study ranged from 3.62 to 3.68. Fluorescence was inert to long-wave and short-wave UV light. Rotating the stones 360° between a pair of crossed polarizing filters revealed an anomalous double refraction. Using a handheld spectroscope, faint absorption bands at 480–490 and 570–590 nm were observed. Microscopic examination showed fingerprints composed of two-phase inclusions, iron-stained and cloudy fractures, long thin etch channels, unidentified transparent crystals, and zoned greenish brownish yellow areas. These properties are consistent with grossular (grossular-andradite) garnets (I. Adamo et al., "Tsavorite and other grossulars from Itrafo, Madagascar," Fall 2012 *G&G*, pp. 178–187; M.L. Johnson et al., "Gem-quality grossular-andradite: A new garnet from Mali," Fall 1995 *G&G*, pp. 152–166.).

Laser ablation–inductively coupled plasma–mass spectrometry (LA-ICP-MS) analyses were performed to obtain the chemical composition of these garnets using a Thermo Fisher iCAP Qc ICP-MS coupled with an ESL NWR213 nm laser ablation unit. USGS glass standards GSD-1G and GSE-1G and NIST glass standard 610 were used as external standards. ^{29}Si was used as an internal standard. The analyses were performed in the same region where spectroscopic data was collected for stones 3, 4 (Ethiopian garnets), 5 (non-Ethiopian tsavorite), and 6 (non-Ethiopian demantoid) (see www.gia.edu/gems-gemology/summer-2018-gemnews-discovery-of-color-change-chrome-grossular-garnets-from-ethiopia). The Ethiopian garnets are predominantly composed of 87.24–91.60% grossular, 6.03–8.19% andradite, 1.04–2.80% spessartine, 1.29–0.55% uvarovite, 0.71–0.82% pyrope, and 0.03–0.05% goldmanite (again, see stones 1–4 at the link provided above). The dominant chromophore is Cr^{3+} at about 0.19–0.43 wt.%, with an almost negligible contribution from V^{3+}. This contrasts significantly with most tsavorite grossular garnets, whose color is dominantly derived from V^{3+} with a lesser contribution from Cr^{3+} (Adamo et al., 2012).

UV-Vis-NIR spectra (figure 2) were collected and corrected for reflection loss. These spectra were then used to quantitatively calculate the color of the garnets at a wide range of path lengths and under different lighting conditions. In addition to two of the Ethiopian grossular garnets, UV-Vis spectra were also collected on the non-Ethiopian tsavorite (stone 5) and the non-Ethiopian demantoid (stone 6) for comparison. The chemistry of stones 5 and 6 is also reported online; see the link above. The calculated color panels of stones 3–6 under daylight-equivalent lighting (CIE D65 illumination) and incandescent light (CIE A illumination) are shown in figure 3, which shows the pos-

Editors' note: Interested contributors should send information and illustrations to Stuart Overlin at soverlin@gia.edu or GIA, The Robert Mouawad Campus, 5345 Armada Drive, Carlsbad, CA 92008.

Gems & Gemology, Vol. 54, No. 2, pp. 233–254.

© 2018 Gemological Institute of America

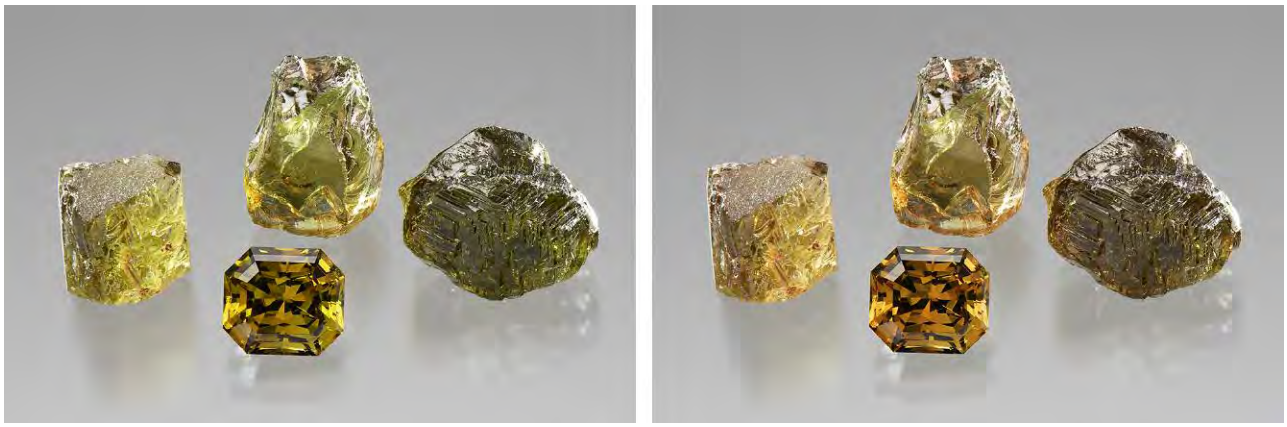

Figure 1. Left: Three rough garnets (left to right, stones 2, 3, and 4) and one faceted garnet photographed in an LED light source with 6000K color temperature (a daylight-equivalent light simulator). Right: The same stones photographed in an LED light source with 3100K color temperature (an incandescent light simulator). The 2.705 ct faceted stone measures 8.08 × 7.18 × 5.49 mm. Photos by Kevin Schumacher.

sible colors these four garnets would exhibit with different path lengths (defined by stone thickness) and the approximate corresponding carat weight of a well-proportioned round brilliant (for details of this calculation, see Z. Sun et al., "Vanadium- and chromium -bearing pink pyrope garnet: Characterization and quantitative colorimetric analysis," Winter 2015 *G&G*, pp. 348–369). Ethiopian grossular stone 4 showed a stronger color change and a higher chromium component than Ethiopian grossular stone 3. Stone 6 showed a more yellowish green than stone 5 due to the demantoid's higher Fe component, which absorbs more blue light than in tsavorite (again, see figure 2).

One way to judge the quality of a color-change stone is to plot the color panel pair in the CIE 1976 color circle. Good color-change pairings show a large hue angle difference, a small chroma difference, and large chroma values (Z. Sun et al., "How to facet gem-quality chrysoberyl: Clues from the

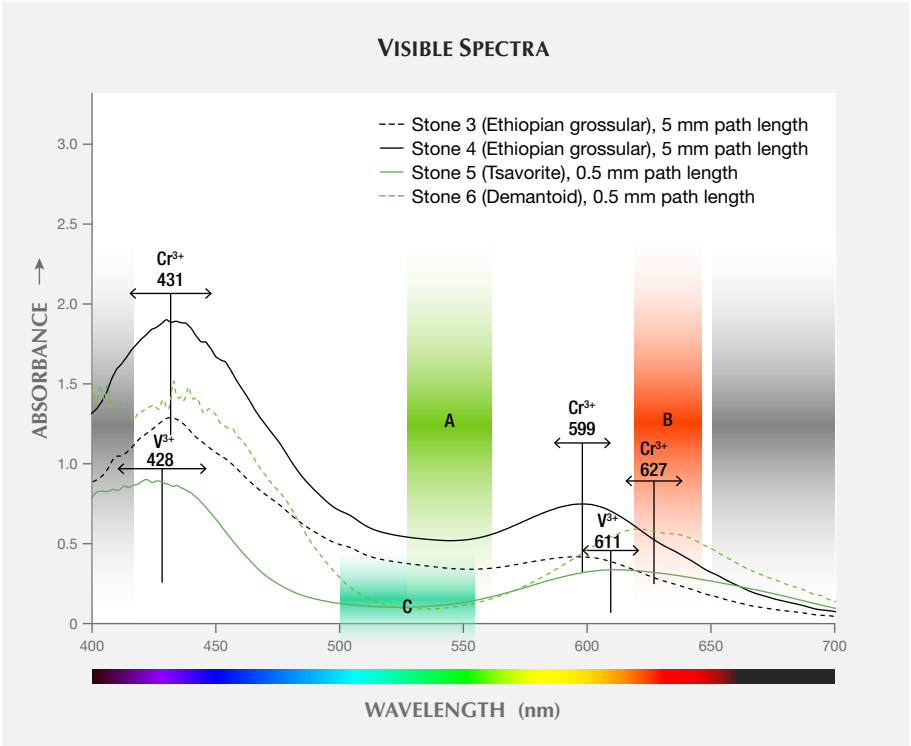

Figure 2. The calculated visible absorption spectra (corrected for reflection loss) of garnets 3, 4, 5, and 6 with various path lengths. Transmission window A is centered at 545 nm. Transmission window B is between 620 and 650 nm; transmission window C is centered at 520 nm. In Ethiopian grossular stones 3 and 4, the absorption bands at 431 and 599 nm are caused by Cr^{3+}. In stone 5 (non-Ethiopian tsavorite) the absorption bands at 428 and 611 nm are caused by V^{3+}. In stone 6 (non-Ethiopian demantoid) the absorption bands at 431 and 627 nm are caused by Cr^{3+} (Adamo et al., 2009). The human eye is not color sensitive above 650 nm or below 420 nm wavelength (gray color zoning in the graph). The transmission in these ranges cannot contribute to the color seen. Please note that the y-axis units are in true absorbance and not absorbance coefficients.

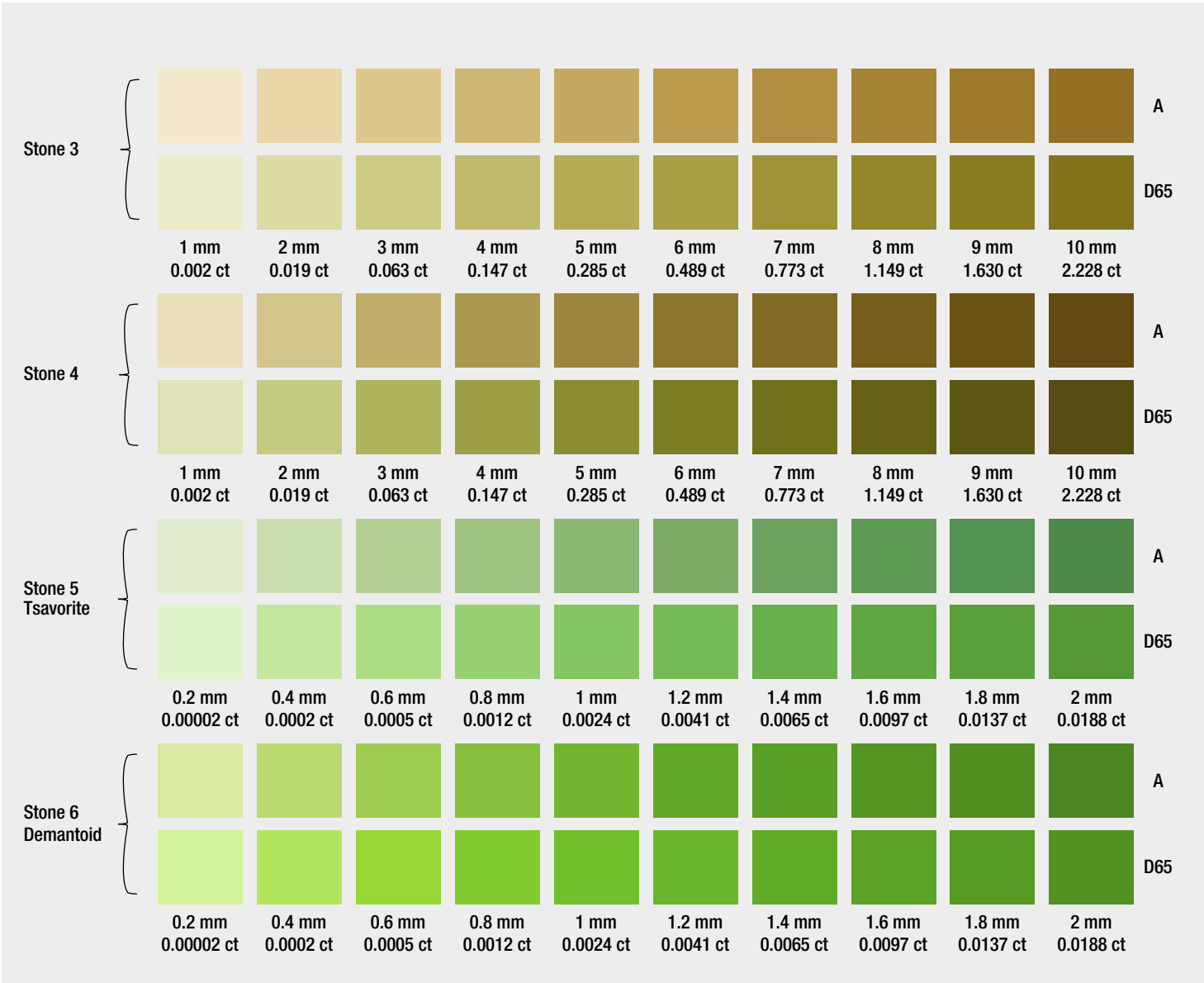

Figure 3. The color panels of four garnets (stones 3, 4, 5, and 6) under CIE A (incandescent) and CIE D65 (daylight-equivalent) illumination are quantitatively reproduced. The garnets' colors are shown at different light path lengths (defined by stone thickness). For each sample, the top and bottom rows represent the color under incandescent light (A) and daylight-equivalent light (D65), respectively. For calculation methods, please see Sun et al. (2017).

relationship between color and pleochroism, with spectroscopic analysis and colorimetric parameters," *American Mineralogist*, Vol. 102, No. 8, 2017, pp. 1747–1758). The color coordinates of the four stones in daylight-equivalent (D65) and incandescent (A) illumination were plotted in the CIE 1976 color circle (see the link above). Ethiopian grossular stone 4 had the largest hue angle difference among the four stones and a relatively small chroma difference. The non-Ethiopian tsavorite and demantoid both had a very small hue angle difference that was close to zero but with large chroma difference.

One interesting observation is that the Cr^{3+} absorption band shifted significantly from 627 in demantoid (stone 6) to 599 in the Ethiopian grossulars (stones 3 and 4; all stone samples contained little V). This shift opens a transmission window B in the red region shown in figure 2. To our knowledge, color-change behavior has not been reported in tsavorite or demantoid. This is because the absorption bands of V^{3+} at the 610 region in tsavorites (green grossular) or of Cr^{3+} at the 627 nm region are dominated by Cr^{3+} in demantoids and prevent the transmission of red light in these stones. In other words, there is no transmission win-

TABLE 1. Vanadium and chromium concentration of grossular garnets, obtained by LA-ICP-MS.

Ethiopian grossular from this study	
Oxide (wt.%)	
V_2O_3	0.01–0.02
Cr_2O_3	0.19–0.43

dow in the red for tsavorite or demantoid. However, these Ethiopian grossulars have little V^{3+}, and the Cr^{3+} absorption is shifted away from the red region, which allows for significant transmission of red light through these stones. This creates a transmission window that produces significantly different color for the Ethiopian grossular in incandescent illumination versus daylight. To the authors' knowledge this was the first group of color-change gem-quality chrome grossular garnet reported.

Ziyin Sun, Aaron C. Palke, Nathan D. Renfro, Heidi Breitzmann, Dylan Hand, and Jonathan Muyal
GIA, Carlsbad

Green-blue Maxixe-type beryl. Recently, a transparent greenish blue pear-shaped mixed-cut sample (figure 4) was submitted for identification to the Gem Testing Laboratory in Jaipur. The 54.21 ct specimen (40.00 × 20.14 × 12.63 mm) was relatively clean to the unaided eye. Its RI of 1.582–1.590, birefringence of 0.008 with a uniaxial negative optic sign, and hydrostatic SG of 2.71 suggested a beryl, which was later confirmed with Fourier-transform infrared (FTIR) and Raman spectroscopy. The specimen's natural origin was established by zones of fine growth tubes, planes of dendritic platelets (usually ilmenite, although not identified here) oriented along the basal plane, and birefringent crystals.

Identification of the stone as beryl was straightforward, but its unusual color and striking dichroism invited further study. It displayed deep blue and yellow as the two principal colors (figure 5); the deep saturated blue resembled the color

Figure 4. This 54.21 ct green-blue specimen was identified as Maxixe-type beryl. Photo by Gagan Choudhary.

of top-quality sapphires. Such strong dichroism was reminiscent of Maxixe-type beryls, although their dichroic colors are usually deep blue and colorless. Careful examination of the specimen showed a deep saturated blue o-ray and a yellow e-ray. Maxixe-type beryls are known to display deep blue color absorption along the o-ray direction (R. Webster, *Gems*, 5th ed., Butterworth-Heinemann, London, 1994, pp. 124–127) and colorless along the e-ray direction. An opposite pattern of deep blue (e-ray) and pale greenish blue (o-ray) absorptions was reported previously in an aquamarine by this author (Fall 2014 GNI, pp. 244–245).

Further analysis with UV-Vis-NIR spectroscopy confirmed the cause of color. Polarized spectra (figure 6) revealed a series of bands between 500 and 700 nm along the o-ray direction, but only a broad absorption feature at ~690 nm along the e-ray; these features are typically associated with the radiation-induced color centers observed in Maxixe-type beryl (see I. Adamo et al., "Aquamarine, Maxixe-type beryl, and hydrothermal syn-

Figure 5. The Maxixe-type beryl in figure 4 displayed an intense dichroism, with a deep saturated blue o-ray (left) and a yellow e-ray (right). A combination of these blue and yellow components resulted in a greenish face-up appearance. Photos by Gagan Choudhary.

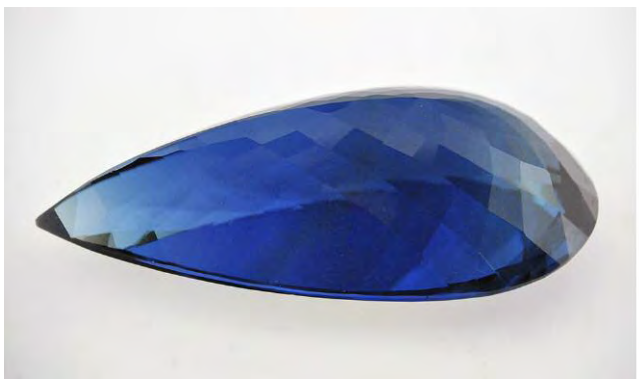

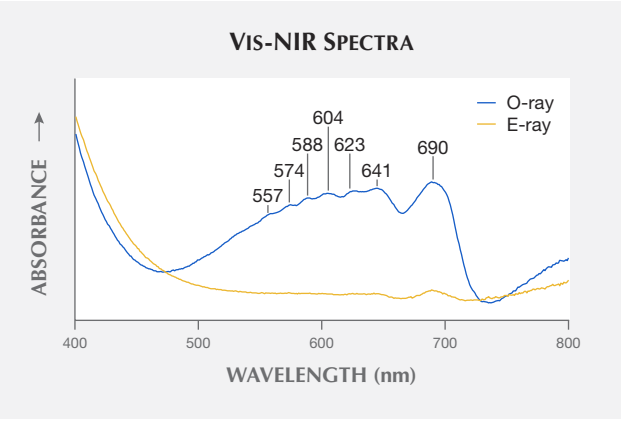

Figure 6. Polarized Vis-NIR spectra of the green-blue Maxixe-type beryl displayed a series of bands between 500 and 700 nm (o-ray) that are associated with radiation-induced color centers.

Figure 7. Left to right: 16.73 ct, 14.50 ct, 17.03 ct, and 27.75 ct trapiche-like amethysts. The four cabochons were cut with the base perpendicular to the c-axis (optic axis). Photo by Diego Sanchez.

thetic blue beryl: Analysis and identification," Fall 2008 *G&G*, pp. 214–226).

Gemological properties along with absorption spectra and the pleochroic color directions were sufficient to establish the identity of this submitted specimen as Maxixe-type beryl. This was the first time we had encountered a green-blue Maxixe-type beryl, although there exists a previous report of such a beryl (see K. Nassau et al., "The deep blue Maxixe-type color center in beryl," *American Mineralogist*, Vol. 61, 1976, pp. 100–107). On the basis of pleochroic colors, it can be deduced that the greenish face-up appearance of this specimen was due to the overlap of blue and yellow color components. The supplier of the specimen informed us that the specimen is reportedly from Mozambique.

Gagan Choudhary (gagan@gjepcindia.com)
Gem Testing Laboratory, Jaipur, India

Trapiche-like amethyst from Brazil. Minerals such as corundum, beryl, tourmaline, and quartz, which belong to either the trigonal or the hexagonal crystal system, can show a trapiche-like texture with a hexagonal core and six extended arms when viewed down the c-axis. Four trapiche-like amethyst cabochons (figure 7) were submitted to GIA's Carlsbad laboratory by L. Allen Brown (All That Glitters, Methuen, Massachusetts) for scientific examination. Each was characterized by a hexagonal black core and six brownish arms with pale purple color zoning in between. Magnification revealed that the black core was composed of dense metallic dendritic inclusions (figure 8, left). The brown color of the arms was caused by numerous tufts of tiny inclusions (figure 8, right), some of which resembled either brushes or bullets.

Raman spectra were collected with a Renishaw inVia Raman microscope system. The confocal capabilities of the

Figure 8. Left: Metallic dendritic inclusions compose the hexagonal black core in the amethysts; field of view 19.27 mm. Right: Brownish and yellowish brush-like and bullet-like fibrous inclusions in the trapiche-like arms; field of view 2.34 mm. Photomicrographs by Jonathan Muyal.

Figure 9. A 12-rayed black star sapphire, weighing 3.6 ct, with one set of golden rays and another set of silver rays producing two different-colored stars. Photo by Simon Bruce-Lockhart.

system allowed inclusions beneath the surface to be analyzed. The black core was identified as an FeS_2 (iron sulfide) mineral, likely pyrite. The brownish tiny inclusions in arms could not be identified but were likely goethite (E.J. Gübelin and J.I. Koivula, *Photoatlas of Inclusions in Gemstones*, Vol. 2, Opinio Verlag, Basel, Switzerland, p. 558) based on appearance and occurrence in quartz matrix.

The texture of trapiche-like amethysts is often caused only by the distribution of color-inducing elements (K. Schmetzer and B. Williams, "Gem-quality amethyst from Rwanda: Optical and microscopic properties," *Journal of Gemmology*, Vol. 36, No. 1, 2018, pp. 26–36). The fact that the texture was caused by two sets of distinctly colored inclusions makes these four gemstones unique.

Ziyin Sun, Jonathan Muyal, and Dylan Hand

Twelve-rayed star sapphire from Thailand. The Thai city of Chanthaburi is a well-known international trading hub for colored gemstones but was once an important corundum mining center. In recent decades, mining activity in the area has decreased, but there are still several smaller-scale operations active. The 3.6 ct 12-rayed black star sapphire shown in figure 9 was mined in 2017 in Bang Kha Cha (or Bang Kaja), a mining locality near Chanthaburi.

Thailand's gemstone deposits typically produce blue, green, and yellow sapphires (and combinations of these colors). The deposits in eastern Thailand also produce a peculiar sapphire variety: black star sapphire. This variety is found in other basalt-related deposits like Australia, but they rarely match the size, quality, and abundance that the Thai stones are famous for.

The black color is due to a very high concentration of Fe-rich particles, identified as hematite and ilmenite. This high density of particles completely masks the bodycolor of the stone. When strongly illuminated from the back, glimpses of the bluish green bodycolor in this gem can be seen. If the platy, Fe-rich particles are oriented in the correct way, they result in a six-rayed star pattern. This star is often yellowish golden in color.

Another common inclusion in corundum is rutile needles. When they are abundant and correctly oriented in the crystal, this might also result in a six-rayed pattern, often with a whitish silvery color. In some cases, both of these patterns overlap, creating a 12-rayed star with one set of golden-yellow rays and one set of silver-white rays. The stone in figure 9 is an excellent example of this phenomenon, displaying well-centered, sharp asterism with two different-colored stars.

Wim Vertriest
GIA, Bangkok

Simon Bruce-Lockhart
Chanthaburi, Thailand

Update on trace-element chemical characteristics of golden sheen sapphire. GIA's Tokyo laboratory recently examined 23 sapphires displaying a "golden sheen" effect, reportedly from Kenya (e.g., T.N. Bui et al., "From exsolution to 'gold sheen': A new variety of corundum," *Journal of Gemmology*, Vol. 34, No. 8, 2015, pp. 678–691). Bui et al. (2015) were the first to describe gemological characteristics of golden sheen sapphires from Kenya; updated characteristics of inclusions, UV-Vis-NIR spectra, and chemistry of golden sheen material was published the following year (N. Narudeesombat et al., "Golden sheen and non-sheen sapphires from Kenya," The Gem and Jewelry Institute of Thailand, July-August 2016, pp. 282–288; Winter 2016 Lab Notes, pp. 413–414). Here we update the gemological and chemical characteristics of the recently examined material, and compare the information with various sapphire sources including other golden sheen sapphire data previously documented.

We examined 15 cabochons, three faceted, and five rough stones (figure 10). The samples were semi-transparent to opaque, with a blue and yellow bodycolor and weight range of 1.75 to 34.00 ct. The cabochons displayed a "golden sheen" effect and/or golden six-ray asterism. For the polished samples, standard gemological testing revealed RI values of 1.760 to 1.770 and hydrostatic SG values of 3.98–4.01, except for one densely included stone with an SG of 4.04 (see Lab Notes this issue, pp. 212–213). These SG values suggested that they were all corundum. The rough stones showed SG values of 3.82–4.01 and the Raman signatures of corundum.

The inclusions were similar to those in other golden sheen sapphires described by Bui et al. (2015) and Narudeesombat et al. (2016). Characteristics included dense clouds composed of brownish needles and platelets displaying a golden sheen effect. Raman analysis identified the needles as ilmenite and hematite, although their Raman signals

Figure 10. Eighteen of the 23 golden sheen sapphires examined for their trace-element chemical characteristics. The largest stone weighs 34 ct. Photo by Shunsuke Nagai.

were weak because of their thinness. Some showed six-ray asterism caused by reflection from dense clouds of oriented needles. Inclusion-free zones like the center stone and rough stones in figure 1 contained mineral crystals and healed fissures with negative crystals (see Lab Notes, pp. 212–213). Various euhedral to subhedral mineral inclusions (figure 11) were confirmed as hematite, diaspore, and zircon. Hematite was found as needles and euhedral crystals; these euhedral hematite crystals coexisted with goethite (figure 11B). Some carbonate minerals such as siderite ($FeCO_3$) and dawsonite [$NaAlCO_3(OH)_2$] were found as irregular inclusions with a vein-like appearance, although their primary or secondary origin was unknown (figure 11C, D). Additionally, magnetite and mica (paragonite and muscovite series) were identified.

Quantitative LA-ICP-MS analysis of trace elements on the 23 samples—90 spots in total—is summarized in table 1 and figure 12. Six of the samples had both blue and yellow bodycolors, and only one had a single yellow bodycolor (again, see figure 10). The other 16 contained numerous inclusions and fractures, and were not clear in color distribution. Chemical analyses were conducted on three spots for each blue, yellow, and included zone. The blue zones had high Fe content ranging 2630 to 3486 ppma and low to medium V content of 0.13 to 0.37 ppma. Their Ti concentration was higher than their Mg content. Ga/Mg ratios for the blue zones varied from 3.50 to 25.35. The yellow zones showed similar Fe, V, and Ga contents as the blue zones, with high Fe (2923 to 3846 ppma), low to medium V (0.13 to 0.40 ppma), and Ga/Mg ratios of 7.78 to 10.06. Included zones also showed similar concentrations of all elements as the blue and yellow zones, although some spots tended to be slightly high in Fe, Ti, Al, and Ga. Enrichment in these elements probably indicates compositions of dense inclusion phases, because most of the inclusion phases were Fe-Ti oxides such as hematite and ilmenite, as documented by Bui et al. (2015) and Narudeesombat et al. (2016). *G&G* previously published that other trace elements, such as Zr, Nb, Ta, W, Th, and U, were enriched in the included zones of some golden sheen sapphires (again, see Winter 2016 Lab Notes, pp. 413-414). Only Ta and U were detected in our samples. Elements such as Na and K that can be considered to be related to inclusions were also detected in some spots on included zones.

TABLE 1. Average and range of trace-element concentration of gold sheen sapphires (in ppma).

Sample	Mg	Ti	V	Cr	Fe	Ga	Ga/Mg ratio
Blue zone (6 samples, 18 spots)	5.88 (1.70–9.29)	13.13 (11.00–19.51)	0.24 (0.13–0.37)	bdl	3258 (2841–3486)	37.67 (31.88–45.04)	10.06 (3.50–25.35)
Yellow zone (7 samples, 21 spots)	8.00 (1.95–15.99)	19.38 (9.26–40.22)	0.26 (0.13–0.40)	bdl	3404 (2923–3846)	39.83 (34.32–46.31)	9.08 (2.65–22.90)
Included zone (17 samples, 51 spots)	8.49 (1.95–23.24)	21.56 (3.63–52.5)	0.10 (bdl–0.56)	bdl	3477 (2630–4552)	39.92 (31.78–53.23)	7.78 (2.29–24.89)

Detection limits: 0.049 for Mg, 0.335 for Ti, 0.035 for V, 0.409 for Cr, 5.28 for Fe, and 0.010 for Ga. bdl: below detection limit.

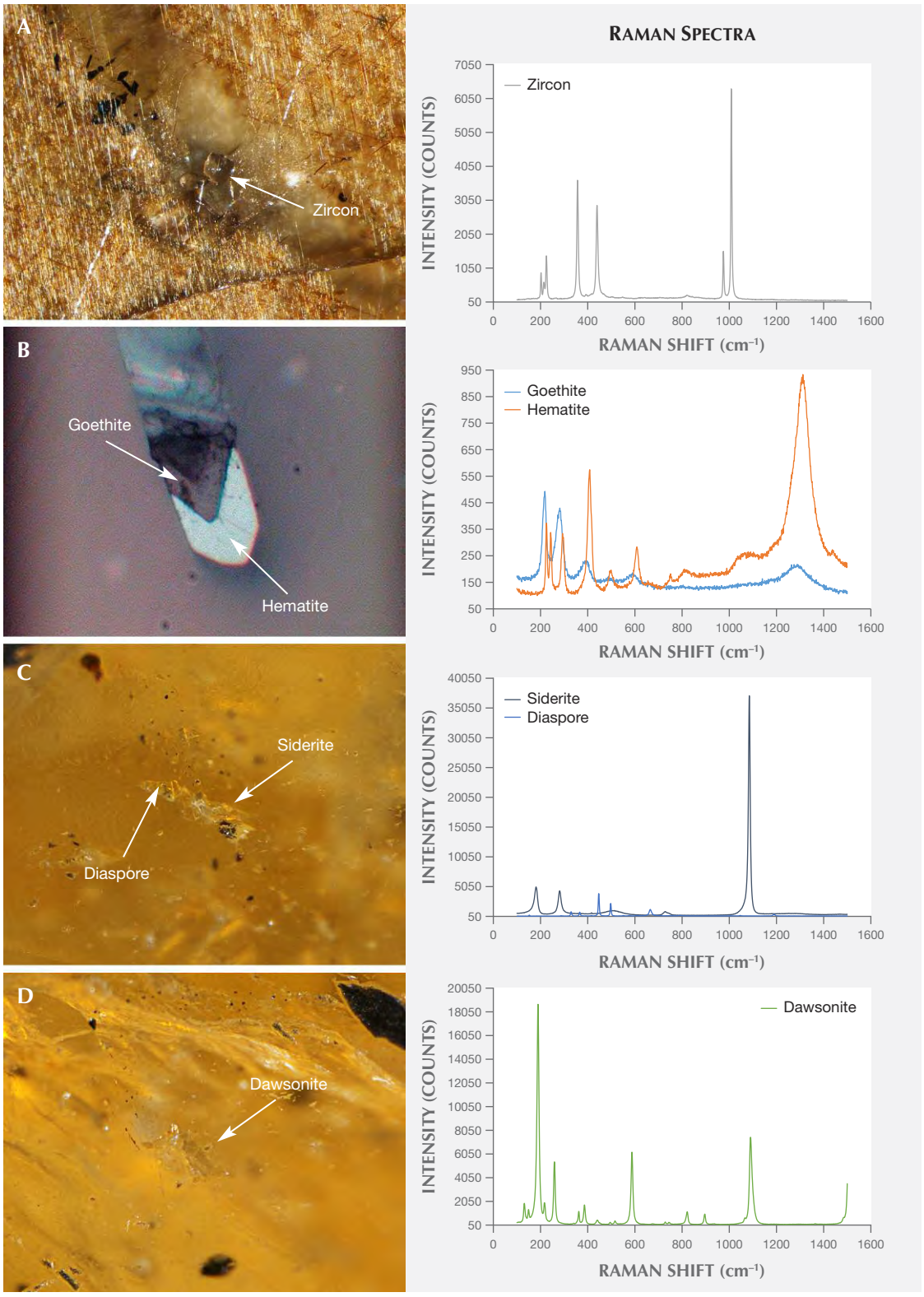

Figure 11. Photomicrographs (left) and Raman spectra (right) of micro-inclusions in golden sheen sapphires: zircon inclusion with intersecting needles (A), hematite and goethite inclusion (B), diaspore and siderite inclusion (C), and dawsonite inclusion (D). Darkfield illumination (A, C, and D) and reflected light (B). Photomicrographs by Makoto Miura; fields of view 1 mm (A), 0.06 mm (B), and 0.8 mm (C and D).

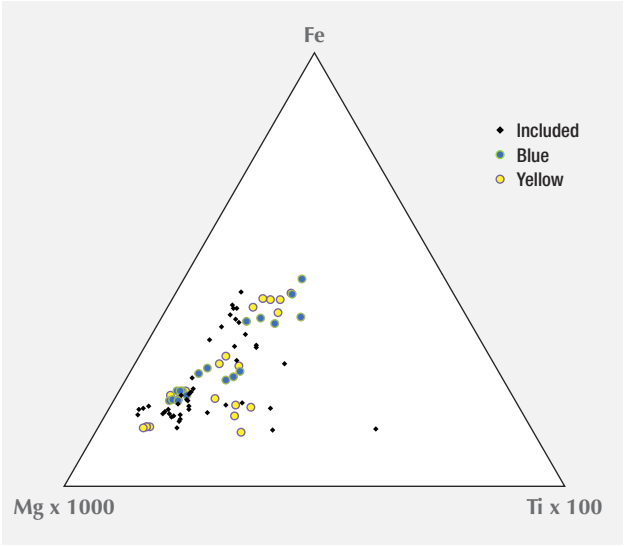

Figure 12. This ternary diagram shows the relationships between Fe, Mg, and Ti in golden sheen sapphires. Note that most of samples have similar Fe, Mg, and Ti content. Some of the yellow and included zones are rich in Mg and Ti.

While golden sheen sapphires are reportedly mined in northeastern Kenya, there is no other published chemical data available from this region. We compared our chemical characteristics with those of other samples documented in the Winter 2016 Lab Notes entry; metamorphic sapphires from Sri Lanka, Myanmar, and Madagascar; and basalt-related sapphires from Thailand, Australia, Nigeria, Kenya, and Cambodia (figure 13). Compositional data for metamorphic and basalt-related sapphires are from previously published articles (J.J. Peucat et al., "Ga/Mg ratio as a new geochemical tool to differentiate magmatic from metamorphic blue sapphires," *Lithos*, Vol. 98, 2007, pp. 262–274; V. Pardieu et al., "Sapphires from the gem rush Bemainty area, Ambatondrazaka (Madagascar)," *GIA News from Research*, Feb. 24, 2017; W. Soonthorntantikul et al., "An in-depth gemological study of blue sapphires from the Baw Mar mine (Mogok, Myanmar)," *GIA News from Research*, Feb. 24, 2017; Fall 2017 GNI, pp. 380–382). As shown in figure 13, the samples in this study were similar to other golden sheen sapphires in Fe, Ga, and V contents. The Fe concentration and high Ga/Mg ratio (table 1) were far from those of metamorphic sapphires but close to those of some basalt-related sapphires. Kenya, where golden sheen sapphires may occur, has two known types of sapphire deposits; one is associated with alkali basalts from the Gregory Rift, an eastern branch of the African Rift Valley, and the other is associated with syenite (Peucat et al., 2007). Both types of sapphire showed a high Fe concentration and Ga/Mg ratio, which are similar to the chemical data in this study.

The similarities in inclusions and trace-element composition between our samples and other golden sheen sapphires indicate that they possibly come from the same origin. A wide variety of inclusions observed in golden sheen sapphires suggests the specific condition during the formation processes. The presence of hematite inclusions especially implied formation in a highly oxidized environment. Further gemological studies are required to construct the database for origin determination.

Makoto Miura, Yusuke Katsurada, and Kazuko Saruwatari
GIA, Tokyo

DIAMONDS

D-color natural IIa diamond with walstromite inclusion. Nondestructive testing methods such as Raman, photoluminescence (PL), and infrared spectroscopy have been

Figure 13. Log plots of chemical variations of Fe vs. Ga contents (expressed in ppma) in golden sheen sapphires. Only blue sapphire data was plotted.

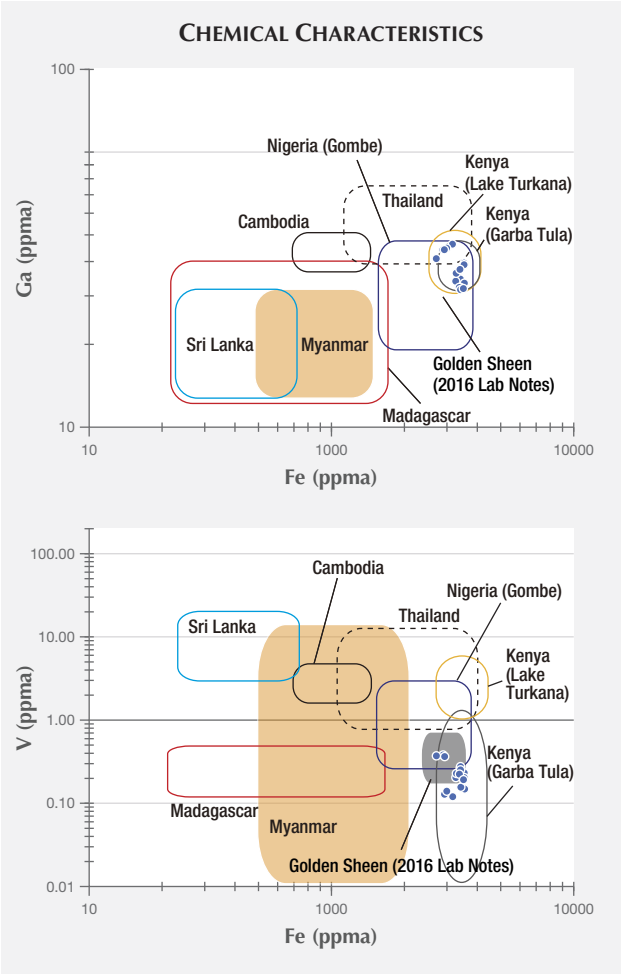

widely applied to identify diamond and its inclusions. The $NV^{0/-}$ (nitrogen-vacancy) and V^0 (vacancy) centers are used as a probe to confirm whether the color of a type IIa diamond is natural or caused by high-pressure, high temperature (HPHT) treatment or irradiation (Fall 2016 Lab Notes, pp. 299–301; D. Fisher et al., "The vacancy as a probe of the strain in type IIa diamonds," *Diamond and Related Materials,* Vol. 15, No. 10, 2006, pp. 1636–1642).

Recently, the National Gemstone Testing Center (NGTC) laboratory in Shenzhen received a 3.0 ct diamond for identification. The stone was a standard round brilliant cut with D color, SI_2 clarity, and a diameter of 9.2 mm. When exposed to DiamondView imaging, the diamond exhibited medium blue fluorescence. It was identified as type IIa because no nitrogen- or boron-related absorptions were detected in the 800–1400 cm^{-1} range and at 2802 cm^{-1}. Nitrogen-vacancy centers NV^0 (575 nm) and NV^- (637 nm) were not detected, either.

Magnification revealed some mineral inclusions and fan-shaped fractures (figure 14). Part of the fissure was filled with black material. We identified the inclusion in figure 14 as $CaSiO_3$-walstromite and confirmed that the black fracture contained graphite using a Renishaw inVia micro-Raman confocal microscope equipped with a green solid laser (532 nm) focused through a 50× short-working-distance objective (figure 15). As the most abundant Ca-bearing mineral inclusion found in super-deep diamonds, $CaSiO_3$-walstromite is believed to derive from $CaSiO_3$-perovskite. Perovskite-structure minerals are predominant in the earth's lower mantle more than 600 km below the surface. The presence of $CaSiO_3$-walstromite and Ca-silicate inclusions is a strong indication of superdeep origin (C. Anzolini et al., "Depth of formation of superdeep diamonds: Raman barometry of $CaSiO_3$-walstromite inclusions," *American Mineralogist*, Vol. 103, No. 1, 2018, pp. 69–74).

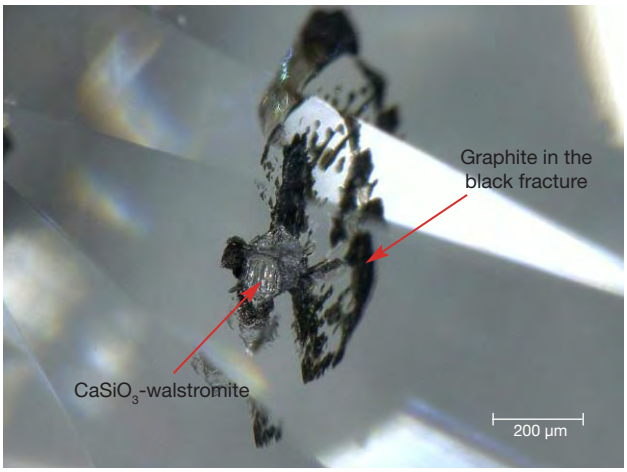

Figure 14. A $CaSiO_3$-walstromite inclusion (100 µm) in a 3.0 ct diamond with fan-shaped black fractures. Graphite (less than 10 µm) was identified in the black fracture. Photomicrograph by Ying Ma.

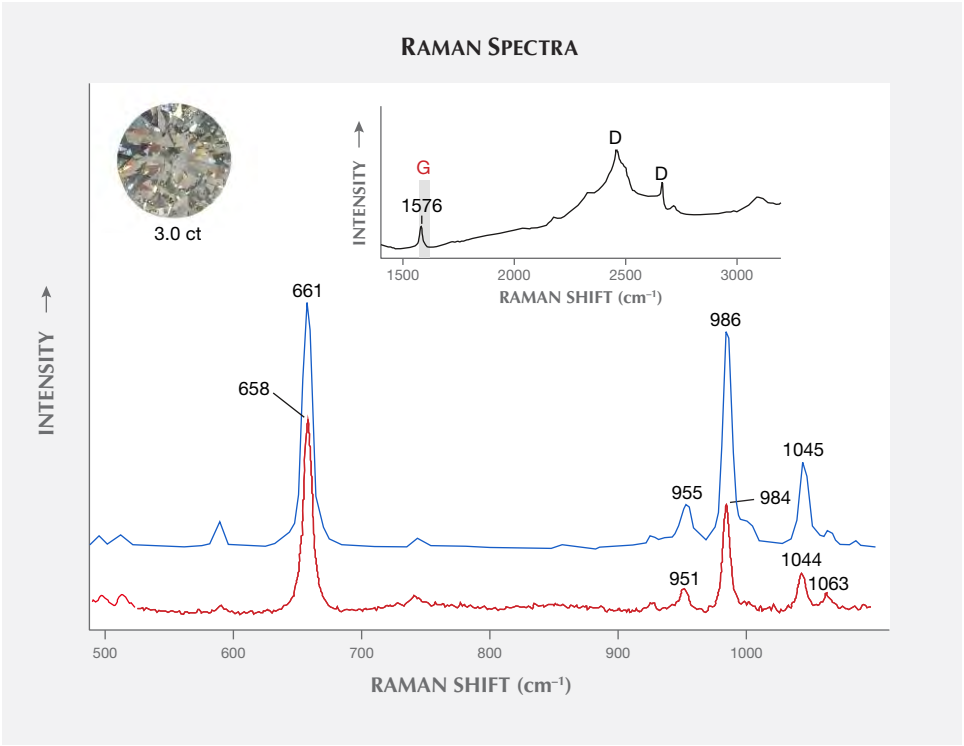

Figure 15. In these Raman spectra, the blue line represents a reference spectrum for $CaSiO_3$-walstromite (Smith et al., 2016, supplementary materials; 500–1100 cm^{-1}). The red trace is from $CaSiO_3$-walstromite in the 3.0 ct diamond (500–1100 cm^{-1}) in the inset photo. The black line shows that the fissure is filled with black graphite; the peak at 1576 cm^{-1} is the G band of graphite, and the D peaks belong to diamond.

Figure 16. In this DiamondView image of the 3.0 ct diamond, the black arrow indicates the site of dislocation networks. Image by Ying Ma.

The 3.0 ct diamond was similar to CLIPPIR (Cullinan-like, Large, Inclusion-Poor, Pure, Irregular, and Resorbed) diamonds (E.M. Smith et al., "Large gem diamonds from metallic liquid in Earth's deep mantle," *Science*, Vol. 354, No. 6318, pp. 1403–1405). Many CLIPPIR diamonds are of top color grades and type IIa, originating from a depth between 360 and 750 km. Dislocation networks, a relatively common feature in type IIa diamonds, were also found (figure 16). Dislocation networks in diamond are interpreted to be equivalent to the polygonized structure of dislocations in other minerals that have been deformed and subsequently annealed (H. Kanda et al., "Change in cathodoluminescence spectra and images of type II high-pressure synthetic diamond produced with high pressure and temperature treatment," *Diamond and Related Materials*, Vol. 14, No. 11-12, 2005, pp. 1928–1931; K. De Corte et al., "Overview of dislocation networks in natural type IIa diamonds," Fall 2006 *G&G*, pp. 122–123). High-temperature experimental treatment of synthetic type II diamond can also reproduce dislocation structures (H. Kanda et al., 2005; D. Fisher et al., "Brown colour in natural diamond and interaction between the brown related and other colour-inducing defects," *Journal of Physics: Condensed Matter*, Vol. 21, No. 36, 2009, 364213).

CLIPPIR diamonds sometimes exhibit infrared absorption at 3107 cm^{-1}; this is a nitrogen-bearing (VN_3H) defect (J.P. Goss et al., "Identification of the structure of the 3107 cm^{-1} H-related defect in diamond," *Journal of Physics: Condensed Matter*, Vol. 26, No. 14, 2014, 145801). This diamond has no clear signature of infrared absorption at 3107 cm^{-1} or NV centers (PL: 575 and 637 nm). We believe that the cause of this is an extremely low level of nitrogen, below the detection limits of the instrument (figures 17 and 18). The lack of nitrogen in type IIa diamond is associated with less color in the diamond. This diamond has a strong V^0-GR1 center (741, 745 nm) and no $NV^{0/-}$(575 nm) and V^0 (637 nm) centers (figure 18).

The $CaSiO_3$-walstromite inclusion in this 3.0 ct diamond indicates a natural diamond from a very deep origin.

Ying Ma, Huihuang Li, Xiaoxia Zhu, Ting Ding, Taijin Lu, and Zhili Qiu
National Gemstone Testing Center (NGTC)
Shenzhen, China

RESPONSIBLE PRACTICES

Gemstones and Sustainable Development Knowledge Hub. In 2016, the Tiffany & Co. Foundation awarded the University of Delaware (UD) $350,000 over the course of two years to promote responsible practices in the colored gemstone

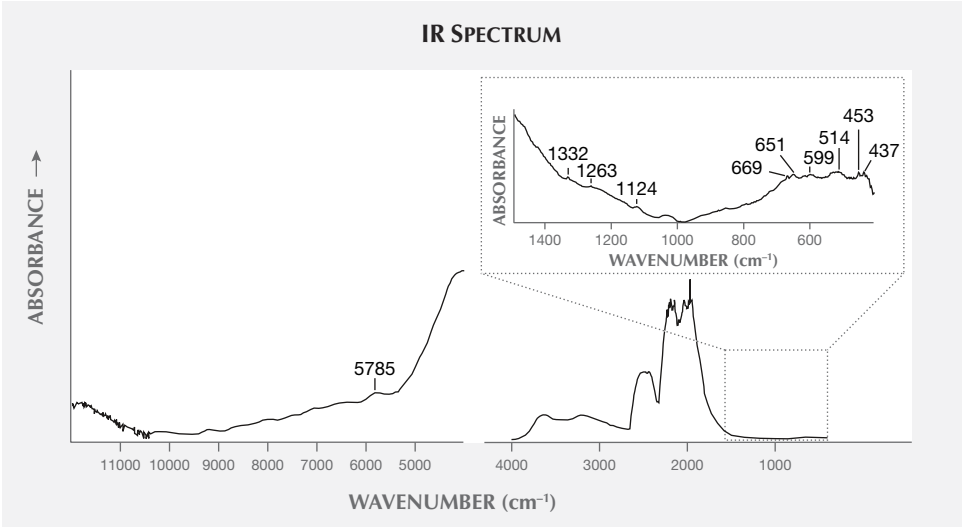

Figure 17. The diamond's infrared spectrum shows no detectable nitrogen-related absorption in the 800–1400 cm^{-1} range. The diamond absorption peak is at 1332 cm^{-1}, while the peaks at 5785, 1263, 1124, and 437–669 cm^{-1} are unknown.

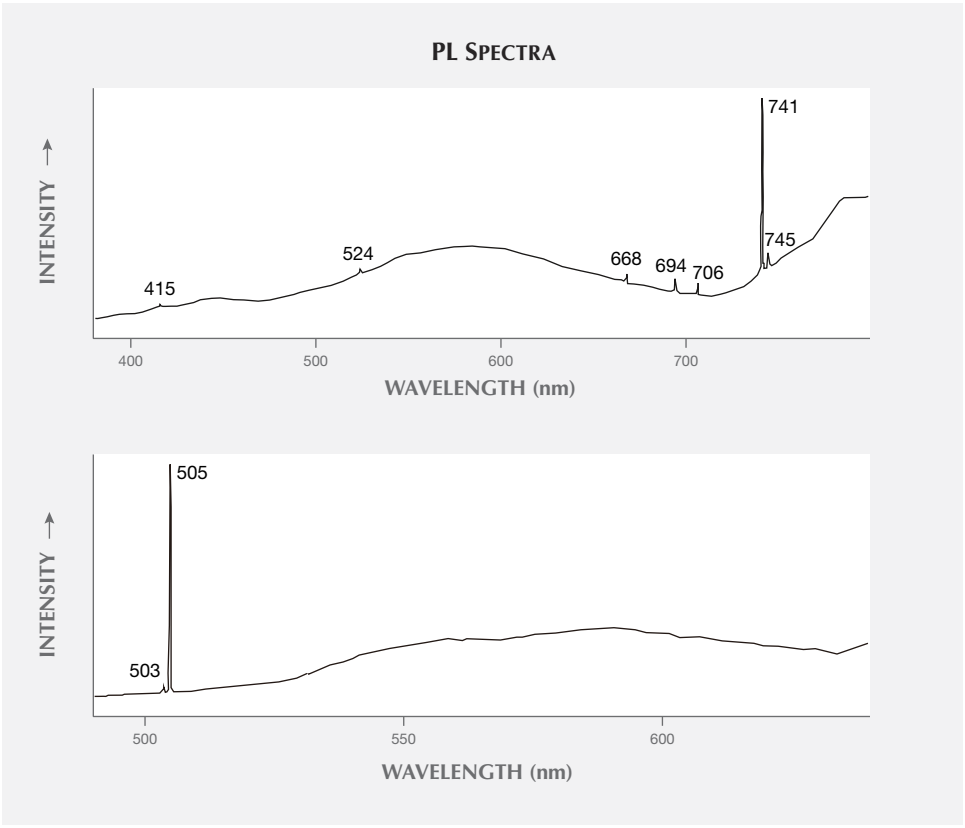

Figure 18. The diamond has a strong V^0-GR1 center (741, 745 nm) and a weak $(NVN)^0$ center (503 nm). The NV^0 (575 nm) and NV^- centers (637 nm) were not detected at liquid nitrogen temperature at either 325 nm (top) or 473 nm (bottom) laser excitation. The designation of the 505, 524, 668, 694, and 706 nm bands is unknown.

supply chain. Out of this grew the Gemstones and Sustainable Development Knowledge Hub, a collaboration between UD, the University of Queensland, and the University of Lausanne. The Hub's goals are to perform research and to connect with initiatives identified by industry, academic, and mining communities as essential to the supply chain. The Hub's website, www.sustainablegemstones.org, is an excellent resource for those interested in learning about and buying sustainable and ethical stones. The areas addressed by the Hub are colored stone mining and geology, processing and manufacturing (including cutting), gender analysis of supply chains, and economic development impact.

Figure 19. Gem cutters in Jaipur were issued masks, provided by AGTA, as part of the safety measures put in place after the Hub's assessment. Photo courtesy of Lynda Lawson.

As of June 2018, the Hub had launched two projects. The pilot project, initiated in Jaipur, India, in early 2018, is a study of the health issues associated with gemstone manufacturing and their solutions. This effort is in partnership with the American Gem Trade Association (AGTA) and Workplace Health Without Borders (WHWB). As part of this program, dust and silica were monitored and cost-effective best practices for improving conditions were evaluated. From these observations, educational materials on silica exposure prevention and other safety precautions, such as the distribution of face masks (figure 19), were created. Noise levels have also been measured, and information on hearing loss, along with disposable hearing protection, has been disseminated. Future steps will involve measuring whether the methods that have been implemented (e.g., wetting to minimize dust and wet mopping of cutting shops) are adequate or if further measures must be taken.

Figure 20. The women miners in Madagascar use the gem testing kit, which includes tweezers, a bowl, a loupe, a dichroscope, and a scoop. Photo courtesy of Lynda Lawson.

The second project is a continuation of the work performed by Lynda Lawson, one of the Hub's research associates, and focuses on miner education in Madagascar. Women miners in the region of Atsimo-Andrefana were taught field gemology essentials and provided with tools for identification (figure 20), even learning to make and use a simple dichroscope. The women were also taught basic lapidary skills, allowing them to make their own jewelry for sale. In the most recent training, the miners have been taught to identify characteristics of stones that are easily confused, such as topaz and quartz; women who had taken previous courses acted as peer coaches. The women have maintained their skills and tools, and the project has been extended through the end of 2018. Future steps will include working with the women to find more profitable markets for the small stones they find (primarily pink, purple, and orange sapphires).

An additional Hub grant was awarded to "Minerals and Society," an interdisciplinary graduate certificate program due to launch at UD in 2020. The program, which will be offered online and on campus, will be designed for members of the jewelry industry along with geologists, economists, and government employees. The program's signature project will be the Jewelry Development Index (JDI), a project first developed at the 2017 Jewelry Industry Summit in Tucson, Arizona. The JDI's goal is to measure the gem and jewelry industry's impact on the economic and social well-being of the countries in which they operate while establishing replicable examples of responsible activity and transparency. UD will begin to develop the JDI in the fall of 2018.

For more information on these programs, please go to www.gia.edu/gems-gemology/summer-2018-gemnews-gemstones-and-sustainable-development-knowledge-hub.

Jennifer-Lynn Archuleta and Aaron Palke
GIA, Carlsbad

Gemstone Guidebook Project. *Selecting Gem Rough: A Guide for Artisanal Miners* was researched, photographed, written, and produced by GIA and distributed in Tanzania through a joint venture between GIA and the nongovernmental organization Pact. It is an educational tool to help artisanal and small-scale miners understand the value of rough gem material. The pilot program was launched in four villages in the Tanga/Umba area of northern Tanzania in the first half of 2017. The sites were selected by Pact staff, who also helped deliver the content and monitor the impact of the training. The region produces a variety of garnets (figure 21), sapphire, tourmaline, and zircon.

Figure 21. A miner in northern Tanzania examines rhodolite rough from a local deposit. Photo by Robert Weldon/GIA.

Figure 22. Gemologist Marvin Wambua (right) shows women miners how to use the white tray to sort gem rough. Photo by Robert Weldon/GIA.

The guidebooks, written in Swahili and showing different types of gem rough found in the area, were distributed to the Tanzanian miners along with small white trays. These trays are used to sort gem rough in reflected or transmitted light (figure 22), which allows stones of higher quality to be separated.

The pilot program reached approximately 200 miners. Participants were surveyed afterward on the effectiveness of the training, and many reported a better understanding of gem quality. Women miners in particular said the training gave them a greater sense of financial independence, indicating that they might be more likely to sell rough on their own rather than rely on men. Using the responses to the survey, Pact calculated that for every $1 invested in the program there was a $12 social return on investment.

In their impact report, GIA and Pact identified areas that might benefit from this resource. GIA has decided to proceed with the project, with plans to include a number of gem localities throughout Tanzania. This expansion is expected to take place in late 2018 and in 2019.

Jennifer-Lynn Archuleta

SYNTHETICS AND SIMULANTS

Observation of etched surface micro-features on HPHT synthetic diamonds using laser confocal microscopy. China is the world's largest HPHT synthetic diamond producer, with an annual output of more than 3,000 tons of rough industrial diamonds. The production technology of HPHT synthetic diamond is quite mature, and most Chinese HPHT synthetic diamonds use the hexahedral static pressure method. The diamond crystals grow out of high-purity graphite through a high-temperature and high-pressure process, and then the superfluous graphite is removed by acid cleaning (Z. Song et al., "Identification characteristics of large near-colourless HPHT synthetic diamond from China," *Journal of Gems and Gemmology*, Vol. 18, No. 3, 2016, pp. 1–8).

Acid cleaning of HPHT synthetic diamond is usually done with 90% H_2SO_4 and 10% HNO_3. This process can remove graphite and metal impurities that remain on the diamond surface and in crevices (L. Yin et al., "Micromechanism of the artificial diamond's growth," *Journal of Synthetic Crystals*, Vol. 29, No. 4, 2000, pp. 386–387). During the growth process, the metal catalyst and graphite are in close contact with diamond and continuously participate in crystal growth.

To the best of our knowledge, no research has been done on the surface characteristics of HPHT synthetic diamonds after acid cleaning, which can reveal the growth features of HPHT diamond. In this study, 39 HPHT synthetic diamonds produced in China were observed using laser confocal microscopy (LCM). The laser confocal microscopy measures the surface topography of the sample moving focused laser spots over the sample with a galvanometer scanner. The strongest-intensity scanning points in each vertical scan layer are recorded and used to construct the 3-D topography through a pixel-by-pixel method (W.-C. Liu et al., "A self-designed laser scanning differential confocal microscopy with a novel vertical scan algorithm for fast image scanning," *IFAC-PapersOnLine*, 2017, Vol. 50, No. 1, 2017, pp. 3221–3226). Therefore, the laser confocal microscope can overcome the problem of depth of field and observe the surface characteristics of materials clearly.

The characteristics of the structure after acid cleaning are observed on the surface of an HPHT synthetic diamond and on the inside of the crystal. An HPHT synthetic diamond was cut into thin slices and then washed by acid, exposing its internal structure (figure 23). Metal catalysts and a small amount of graphite remain in diamond crystals

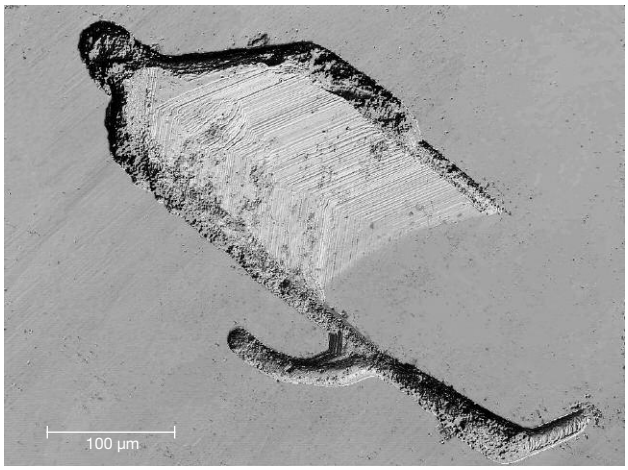

Figure 23. Laser confocal microscopy (LCM) shows traces of metallic catalyst and step-like growth marks in an HPHT synthetic diamond's interior. Photo by Xuxu Wu.

during growth, leaving holes in the interior. Due to the lack of raw material for growth in the hole, a step-like structure was left in the space that was not fully filled with crystallized diamond.

The fine structure of the step-like growth can be expressed by using the 3D scanning function of the laser confocal microscope. The images built in the three-dimensional coordinate system can show the depth and spatial relationship of the microstructures (figure 24). The irregularly etched structures, the depth of voids left by metal catalysts, range from 5 to 17 µm.

After acid cleaning, HPHT synthetic diamonds will display step-like irregular pits and lines on the surface (figure 25). The triangular growth structures of HPHT synthetic

Figure 24. 3D scanning of micro-features by LCM shows the depth change and relative spatial relation. Image by Xuxu Wu.

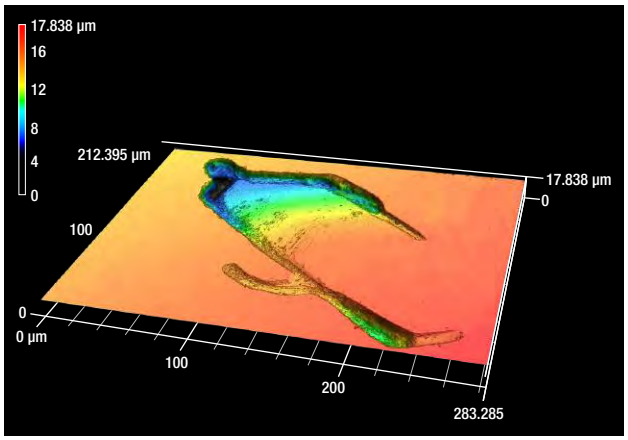

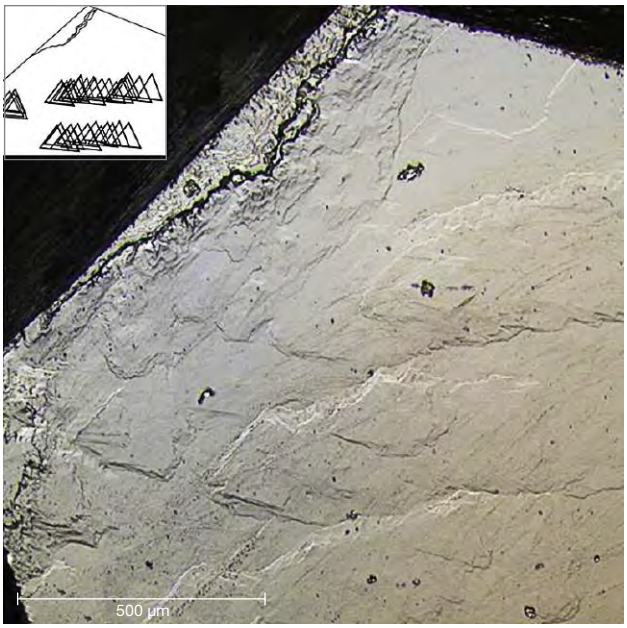

Figure 25. Step-like irregular pits and lines on the surface of the HPHT synthetic diamond. The inset shows a simulation of the sample's stacked triangular growth structure. Photo by Xuxu Wu.

diamonds are stacked on the surface with slight displacement. Rectilinear line marks on the surface of HPHT synthetic diamonds (figure 26) are also very common, and may be traces of the displacements that develop between small

Figure 26. The surface of this HPHT synthetic diamond presents several groups of parallel lines. Photo by Xuxu Wu.

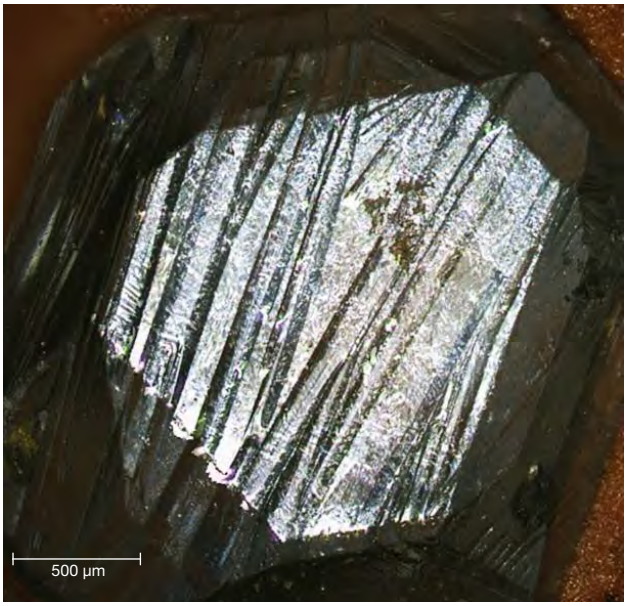

Figure 27. Two white jade bracelets weighing 62.305 g (left) and 69.422 g (right) with dark color patches similar to the natural skin of some nephrite pebbles. Photo by Jianjun Li.

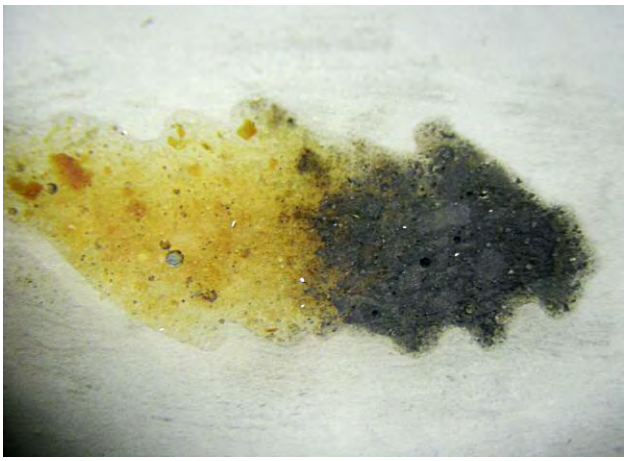

Figure 28. Many gas bubbles and spherical pores formed from burst bubbles can be seen in the brown and black areas. Photo by Jianjun Li; field of view 13 mm.

crystals due to compression during the growth process.

Characteristic patterns observed on the surface of HPHT synthetic diamonds are related to metal catalysts and diamond particles, revealing the order of growth of synthetic diamonds. The step-like structure with the same angle is very common. The etched microstructure caused by metal catalysts usually displays irregular patterns. The several groups of parallel straight lines could be caused by the displacement and friction between a large number of tiny diamonds in the growth chamber. LCM is very reliable at revealing surface micro-features on HPHT synthetic diamonds, and it should be more widely applied to gemological research.

Contributors' note: This study was partially supported by the National Natural Science Foundation of China (grants 41473030 and 41272086).

Xuxu Wu, Taijin Lu, Shi Tang, Jian Zhang, Zhonghua Song, Hua Chen, and Jie Ke
NGTC, Beijing
Mingyue He
China University of Geosciences, Beijing

TREATMENTS

Nephrite bracelet with filled cavity. Nephrite, also called tremolite, is treasured by the Chinese for its fine texture and superior toughness. White nephrite pebbles with some areas of orange or brown skin are called *zi yu*. Mutton-fat nephrite jade with a natural dark brown, brown, and/or brown-yellow oxide skin is rare and considered premium quality. This skin forms due to natural weathering, and the pebble is polished within river currents. In China, nephrite enthusiasts often aspire to own mutton-fat *zi yu* jewelry. White jade that is artificially polished into pebbles and partially dyed is often seen in China as an imitation of mutton-fat jade with brown and/or orange skin. Therefore, many traders treat the white primary ore into dyed brown-orange pebbles by artificially dyeing the material. A great deal of white jade with partially dyed color is marketed as mutton-fat *zi yu* in the Chinese market.

Recently, China's National Gold & Diamond Testing Center (NGDTC) laboratory received from a client two bracelets with filled cavities that mimicked mutton-fat nephrite with dark brown skin. This treatment process is quite different from the traditional surface staining.

Shown in figure 27 are two bracelets weighing 62.305 and 69.422 g. The white portions were pure with very fine texture. The deep brown parts, which resembled the black skin on some nephrite, were distributed along large fissures, and the sharp color boundaries were accompanied by brown and yellow materials. The black material penetrated the body of the 62.305 g bracelet (figure 28).

Standard gemological tests were carried out to identify the two bracelets and the deep brown and orange-yellow parts. With the owner's permission, a dark brown portion was sampled with a knife to obtain small scrapings, which were mixed with KBr powder to form a tablet. Next, infrared spectra were collected using a Nicolet Nexus 470 infrared spectrometer with a resolution of 8 cm^{-1} and 64 scans per sample.

With a PIKE Technologies UpIR diffuse reflection accessory, reflectance infrared spectra were collected on the white parts of the bracelets. The instrument resolution and scan count were the same as those described above. The reflection spectrum was corrected using the Kramers-Kronig method.

The sample's spot RI was 1.61; the SG ranged between 2.95 and 2.96, consistent with nephrite. The white body of the bracelets presented very weak blue-white fluorescence under a 5-watt long-wave UV lamp (365 nm) and was inert under short-wave UV (254 nm). Because of a poor surface

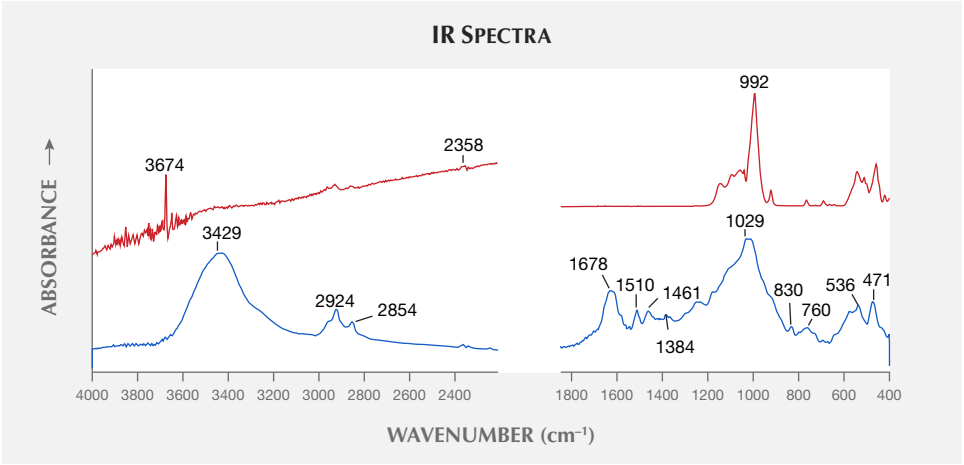

Figure 29. Infrared spectra of the white (red line) and brown (blue line) areas of the bracelets are significantly different, with fingerprints that represent the vibration of the -OH (3674 cm^{-1}) and the -CH_2- groups (2924 and 2854 cm^{-1} peaks), respectively. The spectra have been vertically offset for clarity.

polish, the refractive index of the brown-black part could not be measured. The dark parts showed no fluorescence.

Under the gemological microscope, the white bodies presented a cryptocrystalline texture, with some obscure white areas. Dark brown patches on the bracelets appeared compact, with a slightly weak luster and grainy texture. The dark patches on the inner wall of one bracelet contained many spherical pores and gas bubbles of different sizes (again, see figure 28). This feature is common in glass or plastic imitation gemstones, but has never been found in nephrite. Spherical pores are formed from bubbles close to the surface that burst during the polishing process. The brown or dark brown dendritic pattern often found in fractures of natural nephrite (Z. Yin et al., "Nephrite jade from Guangxi Province, China," Fall 2014 *G&G*, pp. 228–235) was not observed. Magnification showed that the orange-yellow and dark brown patches were artificially filled.

One of the authors reported on a "filled nephrite" in 2005 (J. Li, "The identification of impregnated nephrite," *Australian Gemmologist*, Vol. 22, No. 7, pp. 310–317). After careful testing, a serious mistake in that report has subsequently been identified: the direct transmission FTIR spectra with absorption bands or peaks between 3060 and 2850 cm^{-1} were incorrectly attributed to the epoxy resin filler. The nephrite in that report was not actually filled at all. Until now, the authors have not found a nephrite that has been bleached and filled with polymer like the B-jadeite jade. The author of the earlier study and a coauthor of the present study (JL) no longer believe that direct transmission infrared spectroscopy detects the treatment of nephrite jade. The author tried to collect direct transmission infrared spectra through the deep brown patches of the two bangles, but experiments show that these areas absorbed the mid-infrared light completely.

As shown in figure 29, there was significant difference between the infrared spectra of the white body (collected using reflection mode) and the brown patches (collected with KBr powder). These clearly represent two different materials.

The infrared spectrum (red line in figure 29, right) from the white body of the bracelets has a fingerprint similar to that of Italian nephrite (see I. Adamo and R. Bocchio, "Nephrite jade from Val Malenco, Italy: Review and update," Summer 2013 *G&G*, pp. 98–106), except that the sample does not exhibit the absorption peak of carbonate-associated minerals. This verifies that the white part of the sample is tremolite.

To identify the material in the dark brown part collected with KBr powder (blue line in figure 29, right), we searched databases containing hundreds of spectra libraries purchased by NGDTC using Thermo Scientific OMNIC 9.2 software. Materials with higher degrees of matching included allspice, cellophane, and even opium. This suggests that the dark brown material may be organic. Further advanced testing would be required to conclusively identify the dark brown material.

In the 4000–2000 cm^{-1} range, the white part shows a spectrum peak of 3674 cm^{-1}, attributed to the stretching vibration of the -OH groups in tremolite; the dark brown part shows a strong absorption band centered at 3429 cm^{-1} between 3700 and 3100 cm^{-1}. This band is usually associated with hydroxyl groups in the polymer in organic matter. The 2924 and 2854 cm^{-1} peaks are often attributed to the -CH_2- groups, which often appear in the spectra of organic-filled gems (e.g., E. Fritsch et al., "Identification of bleached and polymer-impregnated jadeite," Fall 1992 *G&G*, pp. 176–187; M.L. Johnson et al., "On the identification of various emerald filling substances," Summer 1999 *G&G*, pp. 82–107). Contamination from human fingerprints or body oils can also lead to absorption peaks within the 3000–2800 cm^{-1} range, but the absorption is generally weaker. The spectrum of the white part of the sample has a very weak absorption in this region, probably due to human body fat contamination or wax residue left after polishing.

This evidence indicates that the dark brown and orange parts of the samples are fillers. But this filling is obviously different from that in B-jade, where polymer is flooded between the grain boundaries. The filling in these two nephrite bracelets looks more like that in single-crystal gems. Therefore, we propose that the nephrite used in these bracelets had severe pits or cavities, and fillers were

used to fill them and make the surface look smooth. The authors want to alert the trade and consumers to this new treatment, whose detection requires access to gemological instruments. Therefore, bringing your nephrite jewelry to a gem laboratory can help avoid unnecessary loss.

Jianjun Li and Guihua Li
National Gold & Diamond Testing Center
Shandong Province, China

Haixia Chen
Gemstone and Materials Technology Institute
Hebei Geoscience University, China

Separating glass-filled rubies using the DiamondView. The treatment of gemstones using various filler materials is not new. In the case of corundum, silica glass was often observed filling rubies from approximately 1980 to the early 2000s, when it was largely replaced by high-lead-content glass in early 2004 (S.F. McClure et al., "Identification and durability of lead glass–filled rubies," Spring 2006 *G&G*, pp. 22–34) which has since become the mainstream artificial filler in corundum. The Lai Tai-An Gem Lab in Taipei recently examined a pair of rubies (figure 30) that were quickly determined to be glass filled with the assistance of DiamondView imaging. In our experience, the DiamondView detects the presence of glass, although it does not distinguish between different types of glasses. This note shows how the DiamondView can be used to observe the presence and, perhaps more importantly, the degree of filling in rubies.

The two heart-shaped cabochons weighed 6.81 and 6.89 ct and measured approximately 10.78 × 13.55 × 5.39 mm and 11.36 × 13.10 × 5.47 mm, respectively. Each semitransparent stone exhibited a purplish red color and fluoresced a strong red to long-wave ultraviolet radiation while exhibiting a weak red reaction to short-wave ultraviolet irradiation. Standard gemological testing showed spot RIs of 1.76, and SGs of 3.94 and 3.93, respectively, which were lower than regular values and raised suspicion that the stones were filled, while advanced analysis by energy-dispersive X-ray fluorescence (EDXRF) and FTIR spectroscopy

Figure 30. A pair of rubies that were determined to be glass filled, partly with the assistance of DiamondView imaging. Photo by Lai Tai-An Gem Lab.

and Raman microscopy revealed data consistent with ruby. Magnification with a gemological microscope revealed natural fluid and fingerprint inclusions, but some evidence of a filler was also observed in the fractures.

Under the DiamondView's visible light settings, some surface-reaching filler features and filled "cavities" were also revealed. Notable differences in the surface reflectance between the filling material and surrounding corundum (figure 31) were clearly evident. After exposure to the DiamondView's short-wave UV radiation, the treated nature of both rubies was even more apparent as the reaction not only showed the obvious cavities but the extent of the filler (in blue) running throughout the stones (figure 32). The 6.81 ct ruby revealed an even greater degree of filling than its twin, especially on the base where a greater concentration of filling material was noted.

As the DiamondView results prove, filler materials penetrate or remain on the fractures of the treated material (ruby in this case) under certain treatment conditions. Hence, some filling treatments may be revealed more clearly when exposed to the ultra-short-wave energy of the DiamondView. Chemical analysis of a filled area using EDXRF detected Si and Ba as the major elements. Minute

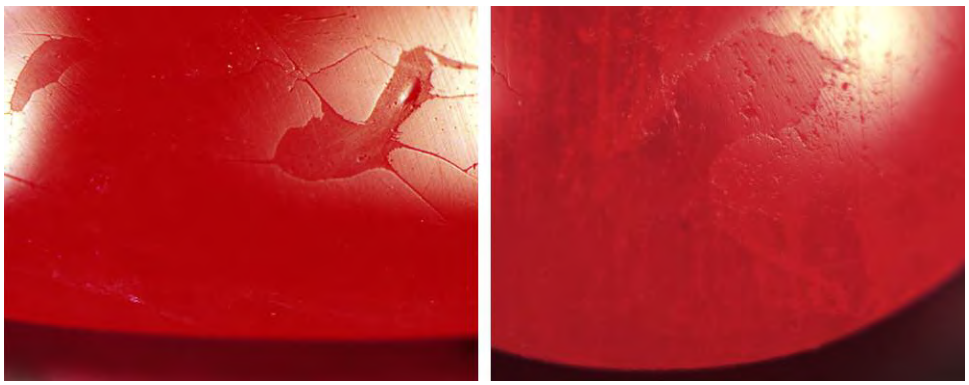

Figure 31. Notable differences in the reflectance of the glass filling and corundum host were seen in the DiamondView's visible light mode.

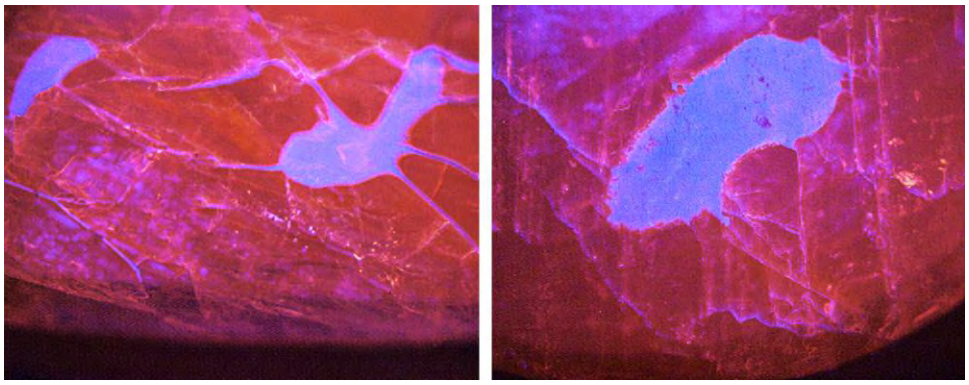

Figure 32. In contrast to figure 31, the DiamondView's operational mode clearly revealed the glass-filled cavities as well as the extent of the glass (shown in blue) running throughout the rubies.

levels of Pb were also obtained. The results proved the filler was a glass composed of these elements, which were not detected when other filler-free areas were analyzed.

Artificial glass is frequently used as a filling material in gemstones. The variable chemical compositions of these different glasses help improve the appearance (lower visibility of fractures) of the host after treatment. While the vast majority of glasses and other fillers, both organic and inorganic, can be detected with a loupe or microscope, the DiamondView is a useful identification aid should the need arise.

Larry Tai-An Lai (service@laitaian.com.tw)
Lai Tai-An Gem Laboratory, Taipei

Strong fluorescence in B-jade impregnated with wax. Fine-quality jadeite jade is known for its high value in the market. "A," "B," and "C" jade are classifications applied to jadeite that relate to various states of enhancement. However, many in the market may not understand the real meaning of the terms. A-jade shows no indications of having undergone modification through the impregnation with colorless or near-colorless wax, resin, or any other agent. When the material has been treated through bleaching and the impregnation with colorless or near-colorless wax, resin, or any other agent, it is described as B-jade. When it shows indications of having fissures or fractures filled with a color agent, it is defined as C-jade. B and C areas may exist in the same specimen; this is described as B+C-jade. A bangle submitted to the Lai Tai-An Gem Laboratory (figure 33, left) illustrates the common misconception that B jade is only impregnated by resin. In fact, wax-impregnated jadeite jade is also defined as B-jade.

The client who submitted the bangle believed it was resin-impregnated jadeite owing to its suspiciously strong fluorescence reaction. The item possessed an uneven green and white color with a greasy luster and weighed 277.14 ct. It measured approximately 76 mm with a thickness of 9–10 mm. An RI reading of 1.66 was obtained from five

Figure 33. Left: The wax-impregnated jadeite jade bangle submitted for identification. Right: The bangle exhibited strong bluish fluorescence under long-wave UV radiation. Photos by Lai Tai-An Gem Lab.

Figure 34. Microscopic observation revealed obvious acid etching marks, coarse pits, and cobweb-like surface fissures. Photo by Lai Tai-An Gem Lab; field of view 4.6 mm.

random spots on the bangle, and an SG of 3.34 was also recorded. The most interesting feature was an unusually strong reaction under long-wave UV (figure 33, right), indicating it was probably treated and should be examined with more care. This material was determined to be jadeite jade when subsequently tested by FTIR spectroscopy, but the FTIR results also revealed some features other than the jadeite-related peaks.

FTIR analysis confirmed that the jadeite bangle was heavily impregnated with wax. The absorption peaks at 2850, 2920, and 2965 cm^{-1} differed from those expected in resin-impregnated material—which usually exhibits peaks at 3061 and 3040 cm^{-1}—and they were intense and sharp enough to indicate that a significant quantity of wax had been applied. Microscopic examination revealed obvious acid etching marks, coarse pits, and cobweb-like surface fissures (figure 34). Wax residues were also found within pits and fissures when poked. Additional unseen wax was apparently within the structure according to the wax pattern revealed by FTIR analysis, typical for wax-impregnated B-type jadeite, which clearly explains the strong reaction under long-wave UV.

While the term B-jade is meant to be applied to wax- and/or resin-impregnated material (Laboratory Manual Harmonisation Committee Information Sheet #11, http://www.lmhc-gemology.org/pdfs/IS11_20111215.pdf), many traders misleadingly describe B-type jadeite jade as resin-impregnated only. This leads the unsuspecting buyer to believe that wax-impregnated jadeite jade is A-jade. This case clearly shows that those dealing in jadeite should be aware of the differences between resin- and wax-impregnated materials, even though both are considered B-jade, and understand that confusion may arise if items are not carefully checked.

Larry Tai-An Lai

CONFERENCE REPORTS

IAC conference on responsible gold. Gold: Vortex, Virtues, and Values was hosted by Initiatives in Art and Culture (IAC) at Bohemian National Hall in New York City, April 12–13. Now in its eighth year, the conference has become an annual industry gathering for those looking to evaluate the market, discover exceptional work, and discuss key gold-related issues.

Mark Hanna (Richline Group) opened the conference, stating that it is the leading gold event in the United States and introducing IAC founder **Lisa Koenigsberg**, who discussed the importance of bringing together people from various backgrounds. "Gold is the substance that can rivet our attention because the reality is the thing we ascribe value to in a social compact. Everyone in this room agrees that this has value."

In the kickoff presentation, **Jeffrey Christian** (CPM Group) presented graphs showing that interest rates and gold prices are not correlated but indicated that surplus labor will become a problem due to computer-assisted manufacturing. Christian recommended gold as a way to diversify investment portfolios. In assessing international gold investment demand, he concluded that Indian gold investment is in long-term decline and that Chinese gold investment, while down from 2013, is ultimately rising.

Next was the update from Washington, DC. **Tiffany Stevens** (Jewelers Vigilance Committee) addressed the status of Federal Trade Commission (FTC) guides, which are meant to champion consumers and protect them from unfair competition. Once the guides are issued, the JVC will translate them for the industry. Highlighting hot topics, Stevens addressed service applications of precious metals, advertising and disclosure, and anti-money laundering efforts. **Susan Thea Posnock** (Jewelers of America) discussed the importance of advocacy, touching upon hearings on sales tax fairness that could reflect the changing marketplace. **Elizabeth Orlando** (U.S. Department of State) discussed her team's work with conflict minerals and diamonds, particularly regarding the Kimberley Process and the Dodd-Frank Act. **Mark Hanna** observed that the requirement for new FTC members to review regulations has slowed down the overall process. **Linus Drogs** (AU Enterprises) addressed regulations that dictate what can and cannot be marked "Made in the USA" domestically versus globally.

Andrea Hill (Hill Management Group) reframed the use of technology in business. Hill emphasized the importance of marketing coherently across platforms and offering customers help with the decision-making process. She noted that consumers generally shop online and buy in-store. Making the experience seamless over the phone and approaching marketing from the standpoint of consumer desire are key.

Next, **Brandee Dallow** (Fine Girl Luxury Brand Building & Communications) had a sit-down with jewelry designer **Alexandra Mor**, who is working with Balinese artisans to

promote the tagua nut as a luxury alternative to elephant ivory. Taking innovation to the next level, Mor has created a material out of tagua that can be 3D printed to solve the problem of the nut's limiting size.

Independent consultant **Christina Miller** moderated a session on sustainable jewelry. Miller laid out international commitments regarding responsible sourcing, celebrating the progress made and hoping "to push the needle further" during the gold conference. **Monica Stephenson** (idazzle.com and Anza Gems) spoke on the importance of reinvesting in source communities. **Wing Yau** (WWAKE) discussed sourcing in Colombia, where she has visited model mines. **Blair Lauren Brown** (VERTE Essentials) talked about the 120-year legacy of the Alaskan gold nugget jewelry she works in and how it supports local mining. **Stewart Grice** (Hoover & Strong) noted that the company imports from Peru, Colombia, and Mongolia, bringing gold to the U.S. and either selling it as 24K or karating the materials for use. The premium on fair-mined products goes back directly to the local communities. Third-generation retailer **Robert Goodman** (Robert Goodman Jewelers) discussed his commitment to bringing in designers dedicated to sustainability. **Nina Farran** (Fashionkind) came to the table with a style slant. Fashionkind, which stands for "fashion in humankind," began as a blog before launching a retail platform. The group also spoke of industry collectives driving down prices in sustainable sourcing as consumer education drives the demand for sustainable products.

After the sustainability panel, **Toby Pomeroy** was presented with IAC's inaugural award for Leadership and Responsible Practice in Jewelry. The award recognizes a transformational contribution to the worldwide gem and jewelry industry. A leader in the responsible sourcing movement, Pomeroy also founded the Mercury Free Mining Challenge, which seeks to discover a safe replacement for mercury.

Next, **Jean-Jacques Grimaud** (SolidWorks Sell) delivered a presentation on optimizing the consumer experience through personalization. Technology keeps the customer fully engaged with the product, while brands are able to maintain control of design integrity. Grimaud demonstrated a sample personalized software for ring design that is accessible from a computer, tablet, or phone—all on the cloud.

Thursday's closing panel on blockchain technology was jointly presented by **Mark Hanna**, **Marla Beck Hedworth** (UL), and **Catherine Malkova** (IBM). The overview of blockchain technology included provenance assured by the blockchain ledger, permissions to ensure visibility and security, consensus by all parties to verify transactions, immutability, smart contracts, and finality once an operation is completed. Trustchain is proposed to be a consortium permissioned private blockchain, focused on the provenance of a diamond engagement ring from the diamond and gold mines, tracking the full supply chain from the mine to the end consumer.

In the evening, IAC hosted "A Rising Tide: Women in the Jewelry Industry." **Hedda Schupak** (Centurion) moderated the discussion, and panelists included: designer **Wendy Brandes**, **Brandee Dallow**, **Jenny Luker** (Platinum Guild International), and **Barbara Palumbo** (Adornmentality.com and WhatsOnHerWrist.com). A variety of topics were addressed, including: women's involvement in political movements and willingness to perform unpaid labor to promote change, the increase of more women working independently due to lack of upward mobility in corporate settings, minimal presence of women on industry boards for products directing marketing towards women, and more.

Day two started with "Moda Operandi: A New Business Model for Jewelry." **Mickey Alam Khan** (Mobile Marketer) interviewed **Deborah Nicodemus** (Moda Operandi). The company's online luxury business model is currently based on three channels: trunk shows, boutique business, and the showroom. Of the three models, only the boutique carries inventory.

A panel moderated by **Rob Bates** (JCK) that included **David Bouffard**, **Toby Pomeroy**, **Christina Miller**, **Tiffany Stevens**, and **Elizabeth Orlando** opened by discussing issues related to gold. Orlando detailed the smuggling of artisanally mined gold, money laundering problems, gold's use to support armed groups and cartels, and labor problems such as the U.S. interest in eliminating forced labor, mercury use, deforestation, and wildlife trafficking. Bouffard spoke on Signet's efforts to identify the sources of its gold. After years of coordination and tracking from banks to refineries, Signet now knows where 99% of its gold comes from. The company is on the ground to make sure gold that comes from the legitimate supply chain and that workers are paid fair wages, helping promote a responsible cycle. Stevens described how the JVC office helps the industry combat money laundering. Pomeroy noted that his group is raising a million-dollar prize for a safe alternative to mercury in gold mining. Miller spoke about the Initiative for Responsible Mining Assurance and its work on large-scale mining standards. Five sectors form the current setup: mining companies, purchasing companies, labor unions, NGOs, and mining-affected communities. She concluded by reminding the audience that we rely on mining every day, so as an industry we need to advocate for it to be done responsibly.

Leo and Ginnie de Vroomen, the husband-and-wife designers behind the de Vroomen brand, presented selections from their stunning body of work, including the step-by-step making of a gold repoussé bangle. They use brightly colored gemstones and enamel and a variety of traditional metalsmithing techniques to create sculptural forms.

Enameler **Jane Short** detailed her more than 40 years of enameling. Her enamel is focused on the interplay of color or self-expression. Short presented examples of enamel throughout history, explaining technique and chronicling the creation of an enamel on silver beaker.

Figure 35. Barbara Palumbo, Monica Stephenson, and Sarah Yood participate in the panel "Who's Got the Power? Influencers, Ethics, and the Regulations of Social Media." Photo by Alice Catherine Young.

Next, designer **Jen Townsend**, **Renée Zettle-Sterling** (Society of North American Goldsmiths), and **Lin Stanionis** (University of Kansas) spoke on casting. Townsend and Zettle-Sterling are co-authors of the new book *CAST: Art and Objects Made Using Humanity's Most Transformational Process*, which covers jewelry, architecture, and everyday objects made by casting. They described how life events influenced their designs and later inspired them to write the book to combat the stigma associated with the process. The pages feature exceptional cast work, from ancient jewelry to computer-aided design. Stanionis related how casting is a part of her jewelry design process. She explained her dedication to expressing human experience. Her pieces use organic forms such as rattlesnake vertebrae, bones, cracked eggshells, and leaves. She and her husband also excavate fossils and incorporate elements such as dinosaur bones, memorializing links to the past.

Andrea Hill returned to moderate "Industrial Revolution 4.0: Cultivating and Perpetuating Old World Skills." **Patricia Madeja** (Pratt Institute) noted that our country must do more to appreciate makers. **Ted Doudak** (RIVA Precision Manufacturing) added that there are rules for supply and demand—we should see where the demand is, understand what crafts need to be filled, and encourage those. He also emphasized the importance of valuing artisans by compensating them well and acknowledging their accomplishments. **Rich Youmans** (MJSA), **Katrin Zimmermann** (Ex Ovo), and designer goldsmith **Ann Cahoon** rallied around education and the importance of teaching and apprenticeships outside the family.

"Who's Got the Power? Influencers, Ethics, and the Regulations of Social Media" ended the conference with a follow-up panel from last year. **Sarah Yood** (Jewelers Vigilance Committee), **Barbara Palumbo**, **Wendy Brandes**, and **Monica Stephenson** (figure 35) interacted with the audience, under the moderation of **Peggy Jo Donahue**. Yood explained that the FTC is monitoring social media channels, and action can be taken if material connections between influencers and products are not clearly disclosed. She urged the audience to review the FTC endorsement guides and a new Frequently Asked Questions section on their website regarding the endorsement guides. Other topics included early disclosure of sponsorship on posts, pitching, and the purchasing of fake followers. Stephenson added, "Generosity, plus vulnerability, plus accountability, plus candor, equals trust." The panel also took up the issue of followers, and how the question of how many followers an influencer had was usually brought up before getting to know the influencer. The use of fake and purchased followers has also become rampant.

The excitement around the annual IAC conference was palpable. Attendees anticipated a spectrum of calls to action after the gathering. The networking opportunities and the chance to appreciate gold among like-minded colleagues made for an enjoyable and enlightening experience. To learn more about the conference and other upcoming IAC events, visit www.artinitiatives.com.

Olga González
New York

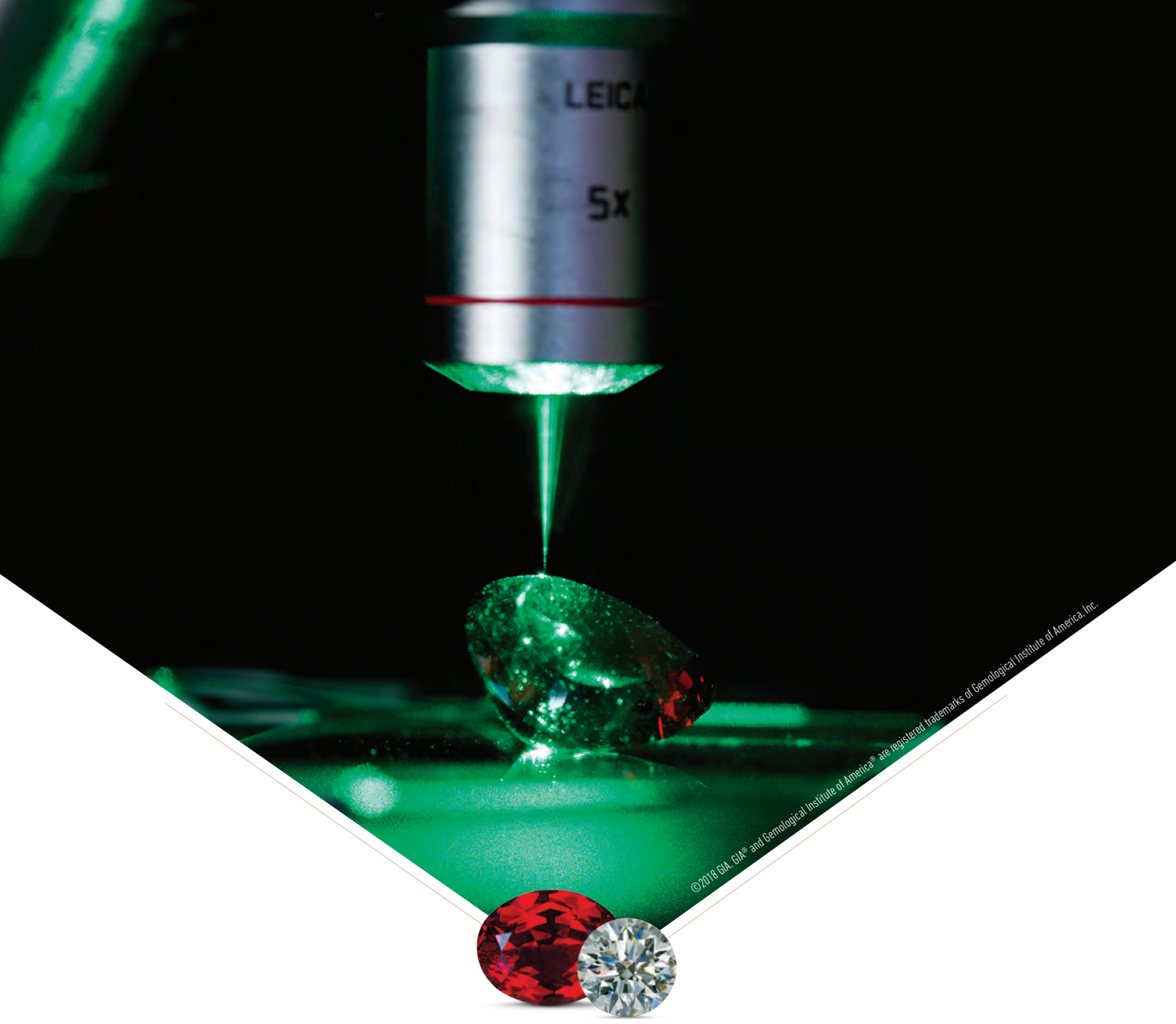

©2018 GIA. GIA® and Gemological Institute of America® are registered trademarks of Gemological Institute of America, Inc.

At GIA, gems endure even more pressure.

Science and discovery underpins everything we do. Since 1931, the Gemological Institute of America® has been unearthing the truth about gems and creating industry standards. With unwavering commitment to accurate and unbiased methodologies, our dedicated research staff advances the knowledge the industry and consumers need to protect confidence in gems and jewelry. Our discoveries are one of the many reasons why GIA® is the world's foremost authority on diamonds, colored stones and pearls.

Learn more about the many facets of GIA at GIA.edu

GIA®

The World's Foremost Authority in Gemology™

Ensuring the Public Trust Through Nonprofit Service Since 1931

BENEFICIATION EDUCATION INSTRUMENTS LABORATORY **RESEARCH**

Features of Synthetic Diamonds

Melee (< 0.2 ct)

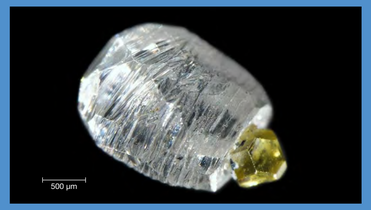

HPHT synthetic diamond crystals as small as a millimeter across are produced in China. Most are grown on {001} cube faces of tiny yellow HPHT synthetic seeds.

Tens of carats of near-colorless HPHT synthetics are grown in single runs and faceted into melee gems like these.

HPHT Synthetics

Cuboctahedral near-colorless HPHT synthetic diamond crystals are commonly grown up to a few carats in size.

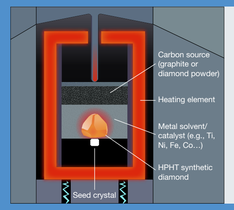

High-pressure, high-temperature (HPHT) growth occurs when a source of carbon (typically graphite) is mixed with a metallic solvent-catalyst in a capsule with diamond seeds.

Pressure: ~5–6 GPa (5–6 × 10⁹ Pa)
Temperature: ~1300–1600°C

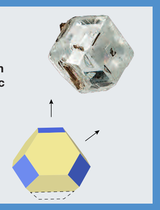

HPHT synthetic diamond is grown using a temperature gradient method where carbon migrates through a molten metal flux to grow cuboctahedral diamond onto a diamond seed plate. The extreme pressures and temperatures are attained using a BARS, belt, toroid, or cubic press. The first reported HPHT synthetic diamonds were grown in 1954 by General Electric.

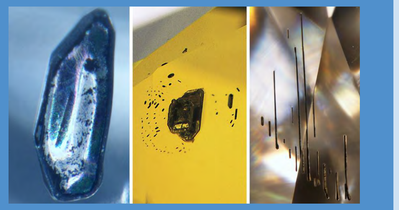

Most inclusions observed in HPHT synthetic diamonds are remnants of the iron/nickel/cobalt metal alloy flux in which the crystal grew. Some samples contain enough trapped flux to be attracted to a magnet.

Large (>5 ct)

This 10.02 ct HPHT synthetic diamond with E color and VS$_1$ clarity is among the largest colorless synthetics seen at GIA. It was faceted from a 32.26 ct crystal.

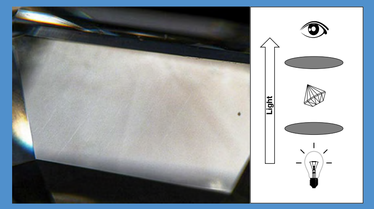

Birefringence (or strain) patterns are mostly absent in HPHT synthetics when viewed between crossed polarizing filters.

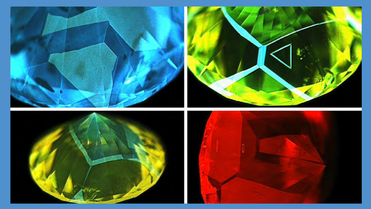

High-energy fluorescence imaging reveals distinctive patterns from cuboctahedral growth sectors in HPHT synthetics.

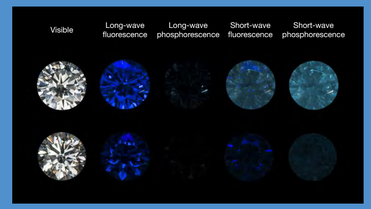

Near-colorless HPHT synthetics may produce blue fluorescence and phosphorescence under UV. Also shown are UV source reflections.

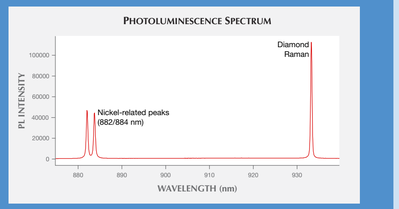

Photoluminescence spectroscopy of HPHT synthetics often reveals optical defects containing nickel due to the metal flux.

Very large HPHT synthetics such as this 15.32 ct sample can show identifying clarity characteristics similar to those of commercial-sized goods.

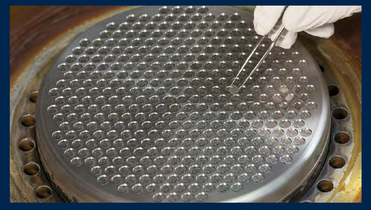

Many small CVD synthetic diamonds can be grown in each run by placing multiple seed plates in the reactor chamber. These small crystals can each be cut to a melee-sized gem. © Fraunhofer IAF.

Faceted CVD synthetic diamond melee like these are often 0.01 to 0.03 ct and near colorless.

CVD Synthetics

When grown, a CVD synthetic diamond is often surrounded by a layer of black non-diamond carbon. A core is usually cut from the center of the tabular crystal; this core is then faceted to create the gem.

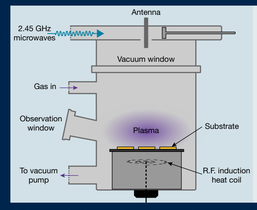

Chemical vapor deposition (CVD) growth occurs layer by layer on the diamond substrate. Gases flow through the reactor and are activated by an energy source—typically microwaves.

Pressure: ~2–20 kPa (2 × 10³ – 2 × 10⁴ Pa)
Temperature: ~800–1000°C

CVD synthetic diamond is grown on a thin plate of single-crystal diamond substrate. The CVD growth process occurs in a vacuum chamber filled with a mixture of gases (hydrogen and methane: H_2 and CH_4). These gases are broken down using a high-temperature plasma, and the released carbon atoms are deposited as diamond on the seed plates. This technique was invented in 1952 by William G. Eversole, and GIA first documented gem CVD synthetics in 2003.

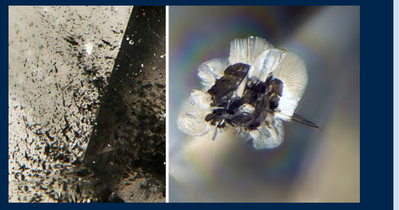

Inclusions in CVD synthetic diamonds are rare but usually occur as small dark particles or crystals that are generally non-diamond carbon.

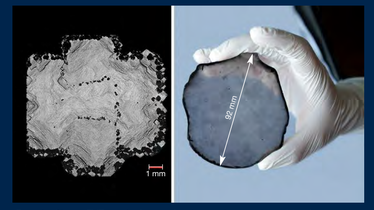

Growth of large CVD synthetics requires large substrate plates. Mosaic growth (left) can "tile" thin plates together to create larger substrates.[1] Ion bombardment of carbon on iridium has been used to grow sizable CVD diamond plates (right).[2]

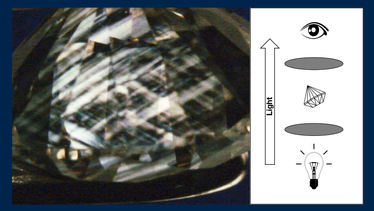

Birefringence (or strain) seen in CVD synthetic diamonds often shows striated patterns similar to those in natural stones.

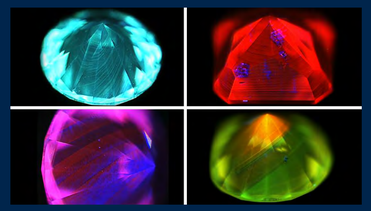

High-energy fluorescence imaging reveals striations, multiple growth layers, and colors uncommon among natural diamonds.

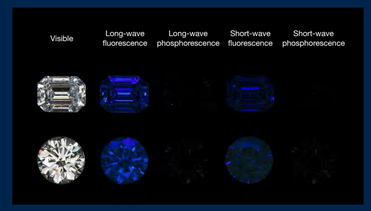

Near-colorless CVD synthetics may show weak blue to green fluorescence and, rarely, very weak phosphorescence. Also shown are UV source reflections.

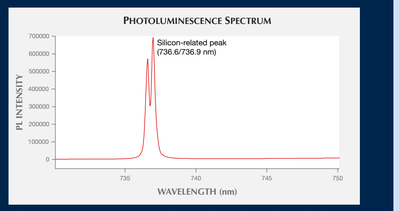

Photoluminescence spectroscopy of CVD synthetic diamonds usually shows distinctive features due to silicon-related impurities.

This 5.19 ct near-colorless type IIa CVD synthetic diamond is one of the largest faceted CVD synthetics seen at GIA.

Fancy-Color Synthetics and Post-Growth Treatment

HPHT synthetics such as these yellow crystals (left) are colored by isolated nitrogen impurities and often cut to very small melee ranging down to 0.005 ct each (right).

HPHT synthetics can be irradiated to green, potentially followed by annealing to turn them pink to red. They can also be grown with boron to create blue color or HPHT annealed to orange.

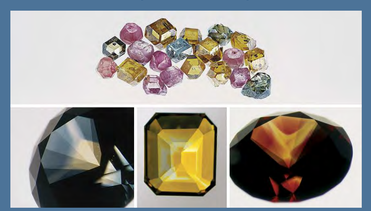

HPHT synthetics form as distinct cuboctahedral crystals (top). When faceted, colored growth sectors exhibit the original growth habits (bottom row).

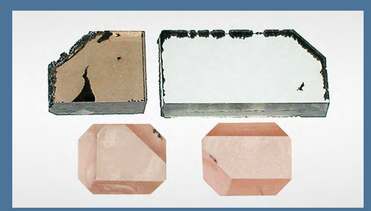

As-grown CVD synthetics are often brown. HPHT annealing removes the brown to create most of the near-colorless material. Irradiation and heating treatments can turn some nitrogen-doped CVD diamonds pink.

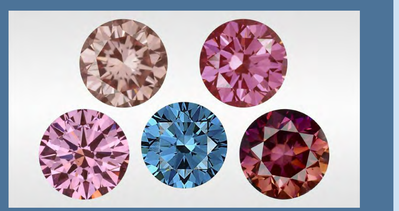

Among fancy-color CVD synthetics, the vast majority are pink due to nitrogen-vacancy centers. A very small number are irradiated to appear blue.

This 10.08 ct deep blue, type IIb synthetic diamond is the largest HPHT-grown blue synthetic seen at GIA. It was grown by New Diamond Technology, Inc. in Russia and is colored by boron impurities.

[1]Tallaire A., Achard J., Silva F., Brinza O., Gicquel A. (2013) Growth of large size diamond single crystals by plasma assisted chemical vapour deposition: Recent achievements and remaining challenges. *Comptes Rendus Physique*, Vol. 14, pp. 169–184.
[2]Schreck M., Gsell S., Brescia R., Fischer M. (2017) Ion bombardment induced buried lateral growth: the key mechanism for the synthesis of single crystal diamond wafers. *Nature Scientific Reports*, Vol. 7, No. 44462.

This chart contains a selection of gemological features of synthetic diamonds. It is intended for reference and not comprehensive. | Published in conjunction with Sally Eaton-Magaña and Christopher M. Breeding (2018), "Features of Synthetic Diamonds," *Gems & Gemology*, Vol. 54, No. 2 | © 2018 Gemological Institute of America

GIA®